Unveiling the Dark Side of the Universe: Unified Dark Energy and the Role of Small-Scale Clustering

Vasco Miguel Cerdeira Ferreira
Doutoramento em Astronomia
Departamento de Física e Astronomia
2021

Orientador
Pedro Pina Avelino, Professor Associado, Faculdade de Ciências da Universidade do Porto

Coorientador
Ismael Alexandre Borges Tereno, Investigador Auxiliar, Faculdade de Ciências da Universidade de Lisboa

Unveiling the Dark Side of the Universe: Unified Dark Energy and the Role of Small-Scale Clustering

by

Vasco Ferreira

A thesis submitted in conformity with the requirements
for the degree of Doctor of Philosophy
Graduate Department of Departamento de Física e Astronomia
University of Porto

Acknowledgements

First and foremost, I would like to thank my supervisors Pedro Avelino and Ismael Tereno, for their constant support, invaluable guidance, and for the many insightful and enlightening discussions. Their contribution have been crucial for accomplishing this thesis, and at so many different levels to my work.

I would like to thank my collaborators Josinaldo Menezes, Lara Sousa, Rui Azevedo, Diogo Castelão, and Alberto Rozas-Fernandez. I am grateful for their helpful input and fruitful discussions. A special thanks to Bruno Barros for his friendship and comradeship. Hopefully we will continue to enjoy chess and snooker (and Cosmology!) together in the future. Many thanks to all the members and staff of the Instituto de Astrofísica e Ciências do Espaço, in particular to the cosmology group, for providing such a friendly and stimulating environment. I would also like to thank Jorge Oliveira and Francesco Renna for reviewing parts of this manuscript.

I am specially grateful to Viktoriya, who not only provided her love and support, but also showed me that there is life outside academia. More than anyone else, I am profoundly grateful to my family, for their love and unconditional support. Thank you for always encouraging me to pursue my dreams.

I acknowledge financial support from the FCT fellowship PD/BD/135229/2017, under the FCT PD Program PhD::SPACE (PD/00040/2012). I acknowledge partial support from project UID/FIS/04434/2013 (FCiências.ID). Funding of this work has also been provided by FCT through national funds (PTDC/FIS-PAR/31938/2017) and by FEDER—Fundo Europeu de Desenvolvimento Regional through COMPETE2020 - Programa Operacional Competitividade e Internacionalização (POCI-01-0145-FEDER-031938).

Abstract

The observational success of the current standard cosmological model presupposes the existence of a dark sector. While it is conventionally assumed to be composed by dark matter and dark energy, so far their properties have only been inferred gravitationally, which precludes a definite conclusion in regard to the number of dark components. In this thesis we explore the possibility of accounting for the phenomenology associated to these dark entities using a single fluid. In particular, we focus on unified dark energy (UDE) models described in terms of a single isentropic perfect fluid. We cover several models belonging to this class of perfect fluids which have been suggested in the literature as UDE candidates, along with further alternatives that we propose in this work. We study their main cosmological properties and determine observational constrains at background and linear level. The scalar field description of perfect fluids is reviewed, with the emphasis being on purely kinetic Lagrangians to account for the dynamics of isentropic perfect fluids. We present a generic mapping between purely kinetic dark energy models and UDE, determined by an appropriate relation between their kinetic terms. We find that isentropic UDE models are severely restricted to behave very similarly to ΛCDM if a standard treatment of perturbations is assumed. This result is widely interpreted as a critical failure of UDE scenarios. We put into question this conclusion and argue that backreaction effects cannot be ignored in the context of UDE. The impact of small scale nonlinear clustering is studied for the generalized Chaplygin gas (GCG) model, taken as a UDE prototype. Considering an ansatz to characterize the level of small scale nonlinear clustering, we show that regions of the GCG parameter space ruled out in linear analysis can be made consistent with observations, provided that the GCG is mostly comprised by collapsed regions at sufficiently early times.

Resumo

O sucesso observacional do actual modelo padrão da cosmologia pressupõe a existência de um sector escuro. Embora convencionalmente se assuma ser constituído por matéria escura e energia escura, até agora as suas propriedades foram apenas inferidas gravitacionalmente, o que impossibilita determinar conclusivamente o número de componentes deste sector. Nesta tese explora-se a possibilidade de usar um único fluído para explicar a fenomenologia associada às componentes escuras. Focam-se, em particular, modelos de energia escura unificada (EEU) definidos por fluídos perfeitos e isentrópicos. Abrangem-se vários modelos pertencentes a esta classe de fluídos perfeitos sugeridos na literatura como EEU, juntamente com outras alternativas que propomos neste trabalho. Estudam-se as suas principais propriedades cosmológicas e determinam-se constrangimentos observacionais de ordem zero e linear. Revê-se a descrição de fluídos perfeitos em termos de campos escalares, sendo dada enfâse a Lagrangeanos puramente cinéticos para descrever a dinâmica de fluídos perfeitos e isentrópicos. Apresenta-se um mapa genérico entre modelos de energia escura descritos por Lagrangeanos puramente cinéticos e EEU, sendo este mapa determinado por uma relação apropriada entre os seus termos cinéticos. Conclui-se que os modelos isentrópicos de EEU têm de se comportar de uma forma idêntica a ΛCDM se um tratamento tradicional das perturbações é assumido. Este resultado é amplamente interpretado como demonstrando o fracasso de cenários de EEU. Põe-se em causa esta conclusão, e argumenta-se que efeitos de reação retroativa não podem ser ignorados no contexto de EEU. O impacto de aglomerados não-lineares em pequena escala é estudado para o gás de Chaplygin generalizado (GCG), assumido como um protótipo de EEU. Considerando um ansatz para caracterizar o nível de aglomeramento não-linear em pequena escala, mostra-se que regiões do espaço de parâmetros do GCG (excluídos na análise linear) podem ser consistentes com as observações se, desde suficientemente cedo, o GCG for maioritariamente constituído por regiões colapsadas.

List of Publications

This thesis resulted in the following three publications:

1. **V. M. C. Ferreira** and P. P. Avelino. "New limit on logotropic unified dark energy models". *Physics Letters B*, 770:213-216, (2017)

2. **V. M. C. Ferreira** and P. P. Avelino. "Extended family of generalized Chaplygin gas models". *Physical Review D* 98, 043515, (2018)

3. **V. M. C. Ferreira**, P. P. Avelino and R. P. L. Azevedo. "Lagrangian description of cosmic fluids: mapping dark energy into unified dark energy". *Physical Review D* 102, 063525 (2020)

   and there is a fourth paper in preparation:

4. **V. M. C. Ferreira**, I. Tereno, D. Castelão, A. Rozas-Fernandez, and P. P. Avelino, "Observational constraints on nonlinear Chaplygin gas cosmologies".

During this period, the PhD candidate also co-authored an additional publication, not included in the thesis:

- P. P. Avelino, **V. M. C. Ferreira**, J. Menezes and L. Sousa. "Phantom Domain Walls". *Physical Review D* 96, 043506 (2017)

Contents

List of Tables

List of Figures

Chapter 1

Introduction

1.1 An expanding Universe

Modern cosmology seeks for the rigorous understanding of the physical nature of the Universe. It is now a mature scientific discipline, built over more than 100 years by the symbiosis between theory and observations. Its inception may be traced back to Albert Einstein and Willem de Sitter, when in 1916 they applied the new theory of gravity (i.e. General Relativity, published by Einstein not long before [1]) to describe the Universe on large scales [2–5]. However, the cosmological solutions that they found did not match the established idea that the Universe was spatially static and eternal; in fact, at that time there was no observational evidence suggesting otherwise[1]. In order to get a static solution Einstein introduced a new term Λ, dubbed cosmological constant, that would work as a repulsive force. Despite the modification in the field equations, the cosmological constant has a noticeable effect only on large scales, meaning that the local predictions of General Relativity (such as Mercury's perihelion advance, or the deflection of light by the Sun) remained unaltered.

The scenario changed in 1929, when Edwin Hubble published his findings on the relationship between the recessional velocity of nearby galaxies and their radial distances [6]. Using the recent Mount Wilson 2.5 meters Hooker telescope, Hubble was able to determine the distance to these galaxies by observing Cepheid variable stars, whose brightness was known to have a regular period (from Henrietta Leavitt's observations on the Magellanic Clouds [7, 8]). In combination with spectroscopic measurements done by Vesto Slipher in 1917 [9], Hubble found that the galaxies's redshift was linearly proportional to their distance. This relation, now known as Hubble's law, was consistent with a spatially expanding Universe, instead of a static one. Spatially expanding cosmologies were first established by Alexander Friedmann [10, 11] and, independently, a few years later Georges Lemaître published his analysis on what he called " Einstein Universe of variable radius " [12]. In the same work, Lemaître also derived Hubble's law from theoretical considerations, and found Einstein's static solution to be unstable (as recognized and further clarified by Eddington

[1] In the early 1920's there was no consensus in the scientific community on the existence of galaxies besides the Milky Way. For example, the Great Debate between Harlow Shapley and Heber Curtis in 1920 concerned the nature of galaxies (then known as spiral nebulae) and the size of the Universe.

in 1930 [13]). All the evidence was now suggesting the we live in a spatially expanding Universe, and the primary motivation for a cosmological constant in Einstein's equations had vanished.

1.2 Hot Big Bang

An immediate consequence of an expanding Universe is that, in the past, galaxies were closer together. Lemaître was the first to suggest that the Universe was once very hot and dense, able to cool down through expansion [14]. This idea was formalized and developed mainly during the 40's by George Gamow [15, 16] and his collaborators [17, 18], in what became known as the Hot Big Bang model. In the seminal work [19], colloquially dubbed as the $\alpha\beta\gamma$ paper[2], they came with the remarkable proposal that the nuclei of light elements (e.g. helium, deuterium or lithium) can be synthesized at very early times, in agreement with their observed abundances in the Universe (consistently with the rate of expansion determined from Hubble). Big Bang Nucleosynthesis (BBN) is a significant and successful prediction, based on well known physics and measured cross-sections for the nuclear reactions.

Yet, another unequivocal consequence of the Universe beginning in a hot and very dense state, is the presence of a black-body radiation coming from all directions, with a present temperature on the order of a few Kelvin [20] (corresponding to photons with a wavelength of about ~ 7 cm). At early times, the Universe was radiation dominated, with the energetic photons preventing the formation of atoms. Thus, the Universe was filled with a dense and opaque plasma, with photons and charged particles (mainly free electrons and protons) in thermal equilibrium, and interacting with each other through Thompson scattering. As the Universe expanded photons became less energetic, and when the Universe was about 1000 times smaller than today, electrons and protons combined to form neutral atoms, a process known as recombination. After this point, photons essentially decoupled (i.e. the scattering rate of photons became smaller than the rate of expansion) and could propagate freely across the Universe, some of them reaching us at the present time. This cosmic microwave background (CMB) radiation was accidentally detected by Arno Penzias and Robert Wilson in 1964, while working at Bell Laboratories [21]. Using a horn-reflector radio antenna, they measured an excess signal which appeared to be isotropic and constant in time, with a temperature of 3.3 ± 1.0 K. It was Robert Dicke and his colleagues at Princeton that interpreted this excess 'noise' as the relic microwave radiation, predicted decades before [22].

The ability of the standard model of hot Big Bang cosmology to account for the measured expansion of the Universe, abundances of light elements, and the CMB (considered the three historical pillars of modern cosmology) discredited alternative cosmological models that were still being considered at that time e.g. the Milne model [23] or the Steady-State theory [24, 25].

[2] A play on the greek letters α, β and γ, after the authors Alpher, Bethe and Gamow.

1.3 Inflation

Despite the empirical evidence presented in the previous sections, the Big Bang model relies on specific and puzzling initial conditions. The so-called Horizon problem, pointed out by Wolfgang Rindler in 1956 [26], is related to the question of why the Universe is so homogeneous and isotropic in the first place. The particle horizon i.e. the maximum distance that light could have traveled since the beginning of time[3], defines a maximal region which could have been in causal contact. However, according to the hot Big Bang model, photons from the CMB coming from opposite directions in the sky (relative to an observer on Earth, detecting the photons today) would not have time to come into thermal equilibrium; simply because these regions were out of causal contact at the epoch of photon decoupling. Moreover, the Horizon problem is also manifest in the BBN: if significant anisotropies were present in the early Universe, the predicted abundances of light elements would be notoriously changed and the agreement with observations could be lost [27].

Another issue concerns the spatial curvature of the Universe. There is *a priori* no theoretical prejudice regarding the large scale geometry of the Universe. Still, in the 1970's observations suggested [28, 29] that the present mean energy density could not differ from the critical density (i.e. the density we should measure if the Universe is flat) by more than 1 or 2 orders of magnitude. The fact that our Universe is so close to being flat only at this stage in the history of its evolution (without any apparent reason) may be regarded as a coincidence problem. In 1979, Dicke and James Peebles draw the attention to what became known as the Flatness problem [30]: if the Universe is not exactly flat, and in order to produce the rate of expansion measured today, an extreme fine-tuning of the value of the energy density and the rate of expansion at early times is required. Therefore, in order for the Big Bang model to retain its predictive capabilities (that matched very well the observations at that time) specific initial conditions would have to be imposed.

The Inflation paradigm, consisting in a period of exponential expansion during the very early stages of the Universe, was proposed by Alan Guth in 1981 [31] as a possible solution to the Horizon and Flatness problems [4]. Different mechanisms to produce this epoch of early accelerated expansion were also put forward by Andrei Linde [33], Alexei Starobinsky [34], Andreas Albrecht and Paul Steinhardt [35] in the following year. The Inflationary epoch increases the horizon size exponentially and is consistent with our observable Universe having originated from a small and causally connected region. This period also accounts, in a natural way, for the observed spatial flatness of the Universe, even if the Universe before Inflation was strongly curved. Furthermore, it can also explain the presence of small primordial inhomogeneities. Quantum fluctuations generated during Inflation can give rise to a nearly scale invariant and gaussian spectrum of density perturbations, responsible for seeding the formation of large scale structures in the late Universe [36]. Observations have so far provided strong hints that a period of Inflation may have occurred in the early

[3] Assuming that the model is valid back to the Big Bang ($t = 0$).

[4] The more exotic Monopole problem can also be addressed by Inflation. Grand Unified Theories attempt to unify the electromagnetic and nuclear (both weak and strong) forces. Generally, these theories predict that the Universe underwent a series of phase transitions through spontaneous symmetry breaking, leading to the production of topological defects. This has important cosmological consequences, in particular the expectation that magnetic monopoles (i.e. zero dimensional topological defects) should have dominated the energy density of the Universe, is in contradiction with observations [32].

Universe (see e.g. [37]).

1.4 The missing mass puzzle

Gravity is the dominant interaction not only on cosmological scales, but also at the level of individual galaxies and clusters of galaxies. By observing the dynamical properties of objects in these gravitationally bound systems, e.g. measuring the velocities of stars in galaxies, or studying the motion of galaxies within clusters, one may estimate their total mass. One can also infer the contribution of luminous matter to the mass of these systems by measuring its luminosity. In general, these two methods are not expected to give the same result: many astronomical bodies do not shine, others may be too faint to be observed. In his series of lectures published in 1904 [38], Lord Kelvin presented one of the first estimates of the contribution of dark bodies to the mass of our galaxy. His calculations showed that some of the galactic mass could be made of invisible matter, albeit not a significant fraction, as pointed out by Henri Poincaré [39] "*Lord Kelvin's method would give us (...) the total number of stars including the dark ones; since his number is comparable to that which the telescope gives, then there is no dark matter, or at least not so much as there is of shining matter*".

The first indication that dark matter may dominate the dynamics on cluster scales was found by Fritz Zwicky in 1933 [40], analyzing the redshifts of galaxies within the Coma Cluster [41]. From the observed number of galaxies, and adopting a reasonable estimation for the physical size of the cluster, he managed to compute the average velocity of the galaxies. However, the observed velocity dispersion was 1 order of magnitude larger than what he expected from his calculations. Zwicky concluded that, in order for the Coma Cluster to be a stable system, its mass should be far greater than what could be inferred from the optical content. Following the same reasoning, a similar mass discrepancy was found by Sinclair Smith for the Virgo Cluster [42]. In the years that followed, the scientific community did not reach a consensus on a satisfactory solution to the problem posed by Zwicky's work [43–45].

Hints for "missing mass" on galactic scales were around already in the 1930's [46, 47]. However, it took a few decades for the emergence of more accurate technology to properly address the question. The development of an image-tube spectrograph by Kent Ford [48], enabled him and Vera Rubin to perform precise measurements of Andromeda's rotational velocity through the Doppler shift of optical emission lines. The results, published in 1970 [49], showed that the rotation curve (i.e. the rotational velocity as a function of the radius) flattens as the radial distance increases. The orbital velocity of stars and hot gas far way from the galactic center were much higher than what one might predict from Newtonian gravity[5] given the density profile inferred from its optical size. This intriguing result was soon found on other galaxies through radio measurements of the 21-cm hydrogen line [50, 51]. Under the assumption that Newtonian theory accurately accounts for the gravitational interaction, the observed flat rotation curves implied the existence of a high fraction

[5] Given the small orbital velocity of stars, as well as the galaxy's weak and approximately static gravitational field (sufficiently far away from any black hole that may reside in the galactic center) the relativistic corrections from General Relativity are expected to be negligible.

of non-luminous mass [52,53].

Eventually it became clear that the "missing mass" observed on multiple scales could share a common origin [54,55], and the hypothesis that dark matter can account for most mass in galaxies and clusters of galaxies began to be broadly accepted by the end of the '70s [56]. So far, if questioned about what dark matter is made of, astronomers could consider several (and the most natural) candidates, e.g. planets, brown dwarfs, or even black holes[6]. However, upper bounds on the cosmological baryonic density derived from the ever more precise measurements of the abundance of light elements resulting from the BBN [57] strongly suggested that most of dark matter is non-baryonic. Furthermore, a high density of baryons was also shown to be in conflict with the absence of CMB anisotropies at the level of $\sim 10^{-4}$ [58] (e.g. in [59] it was reported an upper limit $\lesssim 4.5 \times 10^{-5}$ at the 95% confidence level on the CMB temperature fluctuations).

With growing evidence for the non-baryonic nature of dark matter, some promising candidates were being considered at this time, including neutrinos [60,61], supersymmetric particles [62], or some yet undetected weakly interacting particle beyond the Standard Model of Particle Physics [63–66]. The study of large scale structure formation using numerical simulations provided another important piece of information to characterize the properties of this hypothetical entity. The improvement of N-body simulations, pioneered by William Press and Paul Schechter in 1974 [67], allowed to numerically solve the formation of large structures from the initial density perturbations generated by inflationary models [68–70]. When compared with the 3D galaxy survey available in the 80s [71], cold (i.e. non-relativistic) dark matter particles provided the best reconstruction of the observed cosmic structures [72].

1.5 Late accelerated expansion

By considering a non-baryonic cold dark matter (CDM) component, one could explain the flat rotation curves of galaxies, the dynamics of galaxy clusters, as well as successfully predict the statistical distribution of galaxies. Apparently, it could also be accommodated in the current model of an expanding Universe with an early period of acceleration. However, several internal inconsistencies were being noted. As mentioned before, the inflationary paradigm predicts that the Universe should be very close to being flat. This would mean that, if the Universe is currently dominated by matter, the energy density of matter should be close to the critical density. However, observations in the beginning of 1990's were pointing towards a matter content far lower than that [73–76]. Negatively curved cosmologies were shown to alleviate some of the tensions [77], but, on the other hand, could not be motivated by standard inflationary scenarios. The prevailing standard CDM model was in crisis.

In the late 1960s, a number of authors did consider a cosmological constant in order to explain the excessive number of observed quasars [78–80]. Though the evidence was far from being convincing, these works motivated Yakov Zeldovich [81] to account for a cosmological constant with the energy

[6] These dark matter candidates were later known by the acronym MACHOs (MAssive Compact Halo Objects)

density of vacuum[7]. However, the interpretation of Λ as the vacuum energy leads to a theoretical expectation for its value several orders of magnitude larger than the critical density of the Universe; a conundrum known as the *cosmological constant problem* [85]. Given that in General Relativity all forms of energy contribute to the gravitational field, the presence of a nonzero energy from empty space can not be promptly dismissed.

Notwithstanding the problem attached to the cosmological constant, in the early 90s the possibility that Λ may play a significant role on the dynamics of the Universe on cosmological scales started to be taken seriously [86, 87]. The addition of a cosmological constant to the cosmic budget was shown to fit well the available data, while also being consistent with the inflationary imperative of a spatially flat Universe [88, 89]. Furthermore, a flat ΛCDM model would also imply that the current expansion of the Universe should be accelerating, provided that the contribution of Λ to the total energy density is high enough [90]. Observational evidence for an accelerated Universe was found by two teams in 1998 and 1999 from distance measurements using high redshift supernovae [91,92]. The possibility of unaccounted systematic errors on the SNIa measurements, as well as the results being dependent on the assumed geometry, still raised some skepticism among cosmologists [93–96]. However, the case for a flat ΛCDM model only got stronger in the intervening years, with CMB measurements performed by the BOOMERanG experiment [97]. When combined with SNIa observations, the measured CMB angular power spectrum strongly constrained the curvature of the Universe to be close to zero.

1.6 The standard cosmological model, its challenges, and alternatives

The turn of the millennium witnessed the emergence of a concordance cosmology: the flat ΛCDM model, complemented with an early-time inflationary period, was able to consistently fit all the empirical data available at that time, probing different epochs of the cosmic history. Moreover, other unequivocal predictions of the standard model, e.g. the polarization of CMB photons, and the signature of baryon acoustic oscillations (BAO) in the distribution of galaxies, were soon after detected [98,99]; again, in perfect agreement with the theory. The Wilkinson Microwave Anisotropy Probe (WMAP) spacecraft launched in 2001 to measure the all-sky CMB anisotropies (as well as its polarization), corroborated and improved previous results, being key in establishing the today's standard cosmological model [100–103].

Quite remarkably, the standard model is specified by a set of only six free parameters which need to be inferred from observations. Its underlying assumptions are that: 1) gravity is described by General Relativity, 2) the Universe is approximately homogeneous and isotropic on sufficiently large scales, and 3) the Universe contains particles well described by the standard model of particle physics. According to this picture we can say, with very high confidence, that the present cosmic

[7] A nonzero vacuum energy is an unavoidable consequence of the quantization of fields. The net force due to a change in the vacuum energy between two flat conducting plates predicted by Hendrik Casimir [82] was shown to be consistent with the experiments in 1957 [83]. More recent measurements have verified the Casimir effect at a 5% level [84].

energy budget is roughly composed by $\sim 5\%$ baryonic matter, $\sim 25\%$ CDM, and the remaining $\sim 70\%$ are accounted by the cosmological constant (the contribution from relativistic species is very small). Hence, assuming that the standard model hypotheses hold, we are left with $\sim 95\%$ of the Universe in some dark form that we now very little about. Understanding the physical origin of this dark sector is one of the major challenges in contemporary cosmology.

1.6.1 Dark matter

Guided by observational evidence, only a few things are known about non-baryonic dark matter. For one, since its presence is only inferred through gravitational effects, it must interact very weakly with ordinary matter. Secondly, the particles that made up dark matter must have been non-relativistic since early in the history of the Universe; structure formation would, otherwise, be suppressed on small scales in a way that is incompatible with what is observed. In the meantime, there is no suitable CDM candidate from the standard model of particle physics. The best candidates from the domain of particle physics to represent dark matter are known under the generic name of weakly interacting massive particles (WIMPs), which are predicted by several extensions beyond the standard model [104,105] (see also [106]); so far they have not yet been directly detected [107–109]. Primordial black holes (PBHs) have also been considered as an alternative dark matter candidate since the 70's [110,111], though the interest on the topic gained momentum [112] with the recent detection of gravitational waves emitted from the merging of a binary black hole [113]. Being formed right after the end of inflation, PBHs can evade in this way the tight BBN constraints on the abundance of baryonic matter [114,115].

Instead of some new particle, what is perceived as dark matter could be the result of gravity behaving differently from what we expect when assuming General Relativity (or Newtonian theory in the appropriate conditions). The archetypal example is the MOND paradigm [116,117]: through a phenomenological modification of Newtonian gravity, MOND is able to reproduce the observed rotation curves of galaxies without postulating an "unseen" matter source [118]. However, reproducing the dynamics of the Bullet Cluster with modified gravity alone is somewhat contrived and overly complicated [119], while dark matter is able to provide a more direct explanation [120,121]. More recently, MOND is challenged to explain dark matter deficient galaxies — mass estimations of two ultra-diffuse galaxies in the NGC 1052 Group seem to indicate that dark matter is separable from luminous matter on galactic scales [122,123] (further examples are reported in [124]). Using high-resolution hydrodynamical simulations, two different teams [125,126] have shown that galaxies not dominated by dark matter may be naturally created via tidal interactions, showing no tension with the standard paradigm of galaxy evolution. On the other hand, theories in which dark matter phenomenology is replaced by a modification of gravity, a dark matter-like behavior due to the gravitational field from visible matter should always be present [127]. These two examples provide strong hints of the presence of dark matter at the scale of galaxies and clusters of galaxies (see also [128]).

1.6.2 Dark energy

The cause behind the late accelerated expansion of the Universe is even more enigmatic. The cosmological constant Λ, adopted by the standard cosmological model, is the simplest form of dark energy one can concoct. It is characterized by a negative pressure which does not vary in time, and is smoothly distributed in space. Despite its simplicity, it is difficult to justify the small value of Λ on more fundamental grounds. As far as classical physics is concerned, there is no theoretical constraint on the what value the cosmological constant should take, so it can be taken as a free parameter. On the other hand, Quantum Field Theory predicts a non zero vacuum energy which, according to General Relativity, must source the gravitational field. Ultimately, cosmological observations measure an *effective* cosmological constant, i.e., the sum of a *bare* cosmological constant with all other possible contributions to the energy of empty space. However, as we have mentioned before, the expected vacuum energy density is many orders of magnitude larger than the present critical density of the Universe. Hence, one has to enforce the bare value to cancel almost exactly the large vacuum contribution, resulting on a tiny effective cosmological constant that is compatible with cosmological observations. This extreme case of fine-tuning is now known as the *new* cosmological constant problem, in opposition to the *old* cosmological constant problem (formulated before the evidence for the present accelerated expansion), which requires the effective cosmological constant to be completely negligible for the cosmic expansion [129] (for further details see e.g. [130, 131]).

In the search for alternative models to explain the observational data one implicitly assumes that the old problem is solved. One representative class of dark energy models, dubbed quintessence [132–134], evokes a dynamical canonical scalar field to account for the late time acceleration. Other alternative dark energy models abound (see e.g. the review [135]), which often involve further generalizations in the form of non-canonical scalar field models. The possibility that General Relativity might not hold on large scales is also vastly explored in the literature — in this case, the dark energy phenomenology is substituted by some version of modified gravity theory [136]. Although these approaches modify Einstein equations in different ways, the same phenomenology can, to some extent, be equally well reproduced by these alternatives [137]. Some models also take into account the possibility of interactions (besides gravity) between dark energy and other matter fields [138], which can be motivated in the context of e.g. scalar-tensor theories or $f(R)$ gravity (see [139]). These non-minimal coupling scenarios give rise to the propagation of a fifth force, though suppression mechanisms are envisaged (e.g. chameleon mechanism [140]) in order to avoid local gravity restrictions. However, with the emergence of multi-messenger gravitational wave astronomy [141], several modified gravity models predicting an anomalous propagation of gravitational waves (and consistent with other cosmological data), were ruled out or severely constrained [142, 143]. Nevertheless, given our current knowledge of fundamental physics, one cannot really provide a robust rationale in favor of (or against) any of the alternatives to the ΛCDM, provided that some region of the parameter space in these models proves to be consistent with the observations.

1.6.3 Observational tensions

Although the standard model is extremely successful in explaining a wide number of observations, in more recent years discrepancies on the preferred value of some of its parameters started to emerge. The most statistically significant tensions arise between the inferred values from measurements of the CMB and the results obtained from other low redshift probes, particularly on the value of the present expansion rate [144] (given by the Hubble constant H_0) and the linear density fluctuation power spectrum amplitude [145]. Currently there is a $\gtrsim 4\sigma$ discrepancy between the derived H_0 value from Planck data [146] and what is found from measurements of the distance-redshift relation from SNIa observations [147]. Moreover, constraints on the power spectrum amplitude value from weak-lensing surveys [148–151] also show a persistent $\gtrsim 2\sigma$ disagreement with Planck results.

While the exquisite quality of Planck data provides the most tight constrains on the cosmological parameters to date, these results are also model dependent: the early time observables have to be interpolated to late time quantities assuming a specific cosmological evolution. On the other hand, local measurements are able to probe late time observables independently of the cosmology. Potential unaccounted systematics or selection bias in the data could eventually explain discrepancies between the different probes, although this seems unlikely [144]. Actually, the tensions only got worse as the number and precision of observations continued to improve over the years [152–158]. Hence, these results pose a serious challenge to the concordance model, and might indicate that a paradigm shift [159] is lurking around the corner.

1.7 This thesis: main hypothesis and outline

Within the standard cosmological model, which assumes General Relativity and the Cosmological Principle, the dark sector is separated into two components: CDM, and a cosmological constant. This is however, a quite circumstantial assumption; historically, CDM was required to account for the observed dynamics of galaxies and clusters of galaxies well before the first evidence for the late accelerated expansion of the Universe. Unified Dark Energy (UDE) models are built upon the hypothesis that the entire dark sector can be characterized by a single fluid or field. In this thesis we shall mainly focus our attention on UDE isentropic perfect fluids, described by an equation of state, or, under suitable conditions, by a real scalar field whose dynamics is described by a purely kinetical Lagrangian. We consider various models, derive their properties, and constraint them with current data. The outline of the thesis is the following.

In chapter 2 we provide an overview of the technical details required for the later chapters. We present the necessary concepts from General Relativity, and review essential principles to background cosmology and linear perturbation theory.

In chapter 3 we start by discussing the single dark fluid hypothesis, followed by a review of the generalized Chaplygin gas (GCG) and discussion of its main properties as a representative example of UDE. The GCG model parameters are constrained against SNIa luminosity distances obtained from the Pantheon compilation. We then study the impact of the sound speed on the linear density perturbations and its effect on large scale structure formation. Using the matter power spectrum

data from the clustering of the Sloan Digital Sky Survey DR7 Luminous Red Galaxies we present constraints for GCG cosmologies, including the effect of baryons, updating the analysis of [160]. The logarithmic limit of the GCG is also discussed, following part of Thesis paper 2 [161]. Based on the analysis of our published paper [162], we use the measurements from spiral galaxies rotation curves to constrain the sound speed of the effective dark matter component associated to the high density limit of the modified Chaplygin gas. The final section focus on the logotropic fluid as a UDE model, and includes several results published in Thesis paper 1 [163]. We study its background evolution and discuss the implications of the logotropic UDE sound speed on the linear growth of cosmic structures, as well as on the stability of logotropic dark matter halos.

Chapter 4 deals with the scalar field description of perfect fluids. Starting from a Schutz-Sorkin action, we show that purely kinetic Lagrangians are appropriate to describe the dynamics of isentropic perfect fluids as long as the kinetic term is positive. This first part follows from our discussion in Thesis paper 3 [164]. The Lagrangian descriptions for three isentropic UDE models discussed in chapter 3 are presented. We then consider a one-parameter extension to the GCG Lagrangian, first proposed in our published work Thesis paper 2 [161]. We first examine the non-relativistic regime for this extended family of GCG models. The background evolution is studied, and constraints on the model parameters are also determined using SNIa observations. We then discuss how structure formation is affected for different values of the parameters by examining their impact on the shape of the linear matter power spectrum.

The content of chapter 5 is based on part of Thesis paper 3 [164]. Here we establish a mapping between dark energy models described in terms of pure k-essence Lagrangians and UDE, by defining an appropriate relation between their kinetic terms. We also describe the correspondence between their equation of state parameter and sound speed. We make it more concrete by presenting examples of this mapping, and discuss the implications of constraints on the sound speed in this context.

In chapter 6 we focus on the problem of backreaction. We argue that nonlinearities may have a potential impact and cannot be safely ignored in the analysis of UDE scenarios. We exemplify the role of backreaction effects on the GCG model by considering an ansatz parametrizing the level of small scale nonlinear clustering. We discuss in detail the impact of GCG clustering on the background results and evolution of linear density perturbations. We also show how the CMB and matter power spectra are affected on nonlinear Chaplygin gas cosmologies. We finally provide constraints from Pantheon, Planck 2018, and Kilo Degree Survey (KiDS)-450. Part of the contents of this chapter are based on the results from Thesis paper 4 (in preparation) [165].

We conclude in chapter 7, by drawing some perspectives on the viability of isentropic UDE scenarios, the role of nonlinearities, and outlook future developments. We finalize by presenting a summary of the main results obtained in this thesis.

The Appendices contain details on the methodology and the data sets used in this work.

Chapter 2

Theoretical framework

This chapter aims to present, on a more technical level, a succinct review of essential principles behind modern cosmology. For more detail we refer the reader to several reference textbooks and lecture notes [166–174]. One should bear in mind that several hypotheses are required in the construction of any well defined cosmological model. While in the following sections the discussion focus on the standard model of cosmology, our work in subsequent chapters relies on the same fundamental assumptions regarding the theory of gravity, large scale symmetry, and the standard matter content in the Universe.

Notation and conventions

Unless otherwise stated, throughout this thesis we work in the natural units $\hbar = c = k_{\rm B} = 1$, where $\hbar$ is the reduced Planck constant, c is the speed of light in the vacuum, and $k_{\rm B}$ is the Boltzmann constant. We follow the Einstein summation convention, with upper and lower repeated indices being summed over. The Greek indices run over the spacetime coordinates and Latin indices run over the spatial coordinates e.g.

$$x^\mu x_\mu \equiv \sum_{\mu=0}^{3} x^\mu x_\mu \,, \qquad x^i x_i \equiv \sum_{i=1}^{3} x^i x_i \,,$$

for $3+1$ spacetime dimensions. We shall also employ a spacelike signature $(-,+,+,+)$ for the spacetime metric $g_{\mu\nu}$.

2.1 General Relativity

In the theory of General Relativity gravity is interpreted as a physical manifestation of spacetime geometry, which is ultimately a consequence of Einstein's insight [175] that there is a "*complete physical equivalence of a gravitational field and a corresponding acceleration of the reference system*"

[1]. This statement became known as the Einstein equivalence principle, and was a keystone in the formulation of the gravitational field equations first published in 1915 [1]. In the same year, Einstein also showed that the theory of General Relativity correctly accounts for the precession in the perihelion of Mercury's orbit [176], which Newtonian gravitational theory was unable to fully explain [177] (as first reported by Le Verrier in 1859 [178]). However, it was only in 1919 that the most celebrated prediction of General Relativity was confirmed by observations, when Eddington and his collaborators measured the deflection of light from distant stars by the Sun [179]. The collected data was in agreement with Einstein calculations. More recent and precise measurements performed in several astrophysical scenarios [180–184] have conferred the results obtained back in the beginning of the 20th century.

Indirect evidence for the existence of gravitational waves had been already found from observations of the first binary pulsar ever discovered by Russell Hulse and Joseph Taylor in 1974 [185]. The measured orbital decay of this binary system provides a striking match with the estimated energy loss due to gravitational radiation predicted by General Relativity [186]. More recently, the Laser-Interferometer Gravitational-Wave Observatory (LIGO) team and Virgo collaboration reported the first direct detection of gravitational waves [113], laying down the foundations of Gravitational-Wave Astronomy. With the subsequent detection of the gravitational wave signal GW170817 and the observation of its electromagnetic counterpart GRB 170817A, the difference between the speed of propagation of gravitational waves and the speed of light was tightly constrained to be between -3×10^{-15} and $+7 \times 10^{-16}$ times the speed of light [141], in perfect agreement with General Relativity.

A direct implication of the Einstein equivalence principle is the gravitational redshift of light, which has also been tested with high precision using photon sources artificially generated e.g. Gravity Probe A [187], or by measuring the shift in the spectral lines of stars [188]. A more elementary formulation of the Einstein equivalence principle, known as the weak equivalence principle, states that all bodies fall with the same acceleration when subjected to the same gravitational field. The results from the MICROSCOPE mission showed that the relative difference in the free-fall accelerations between two test masses is smaller than $\sim 10^{-14}$ [189].

So far, no significant deviations from the predictions of General Relativity have been observed. Although several alternative theories of gravity do exist, in this thesis we shall assume that General Relativity provides an accurate description of the gravitational interaction on cosmological scales. As mentioned before, in General Relativity gravity is a manifestation of spacetime curvature. Mathematically, the spacetime geometry is described by a pseudo-Riemannian manifold $\mathcal{M}$ embedded with a metric tensor $\mathbf{g}$. We shall denote the spacetime coordinates by x^μ and the partial derivative with respect to a coordinate system as $\partial_\mu \equiv \partial/\partial x^\mu$. The Riemann curvature tensor is given by

$$R^\rho{}_{\sigma\mu\nu} = \partial_\mu \Gamma^\rho_{\nu\sigma} - \partial_\nu \Gamma^\rho_{\mu\sigma} + \Gamma^\rho_{\mu\lambda}\Gamma^\lambda_{\nu\sigma} - \Gamma^\rho_{\nu\lambda}\Gamma^\lambda_{\mu\sigma}\,, \tag{2.1}$$

[1] The Collected Papers of Albert Einstein. Volume 2: The Swiss Years: Writings, 1900-1909 (English translation supplement) Page 302

where the components of the Chistoffel connection, better known as the Christoffel symbols, are

$$\Gamma^{\lambda}_{\mu\nu} = \frac{1}{2} g^{\lambda\sigma} \left(\partial_\mu g_{\nu\sigma} + \partial_\nu g_{\sigma\mu} - \partial_\sigma g_{\mu\nu} \right) , \tag{2.2}$$

with $g_{\mu\nu}$ being the components of the metric, and $g^{\mu\nu}$ the inverse metric, where $g^{\mu\alpha} g_{\nu\alpha} = \delta^{\mu}_{\nu}$ is Kronecker's delta. Contracting the first and third index of the Riemann curvature tensor given in Eq. (2.1) one gets the Ricci tensor

$$R_{\mu\nu} = R^{\alpha}{}_{\mu\alpha\nu} = g^{\rho\alpha} R_{\rho\mu\alpha\nu} , \tag{2.3}$$

while the Ricci scalar is obtained from the trace of the Ricci tensor $R = R^{\mu}{}_{\mu} = g^{\mu\nu} R_{\mu\nu}$. The Christoffel connection is metric-compatible, meaning that $\nabla_\alpha g_{\mu\nu} = 0$, where the covariant derivative is defined as

$$\nabla_\alpha \mathcal{T}^{\mu_1 \ldots \mu_p}{}_{\nu_1 \ldots \nu_q} = \partial_\alpha \mathcal{T}^{\mu_1 \ldots \mu_p}{}_{\nu_1 \ldots \nu_q} + \Gamma^{\mu_1}_{\alpha\sigma} \mathcal{T}^{\sigma \ldots \mu_p}{}_{\nu_1 \ldots \nu_q} + \ldots - \Gamma^{\sigma}_{\alpha\nu_1} \mathcal{T}^{\mu_1 \ldots \mu_p}{}_{\sigma \ldots \nu_q} - \ldots \tag{2.4}$$

for a general tensor $\mathcal{T}^{\mu_1 \ldots \mu_p}{}_{\nu_1 \ldots \nu_q}$. Another important concept is that of parallel transport of a tensor $\boldsymbol{\mathcal{T}}$ along a path $x^\mu(\lambda)$ defined by

$$\frac{dx^\alpha}{d\lambda} \nabla_\alpha \mathcal{T}^{\mu_1 \ldots \mu_p}{}_{\nu_1 \ldots \nu_q} = 0 , \tag{2.5}$$

with λ being an affine parameter. If we parallel transport the vector $dx^\mu/d\lambda$ (i.e. the tangent vector to the path) along the curve, one gets the geodesic equation

$$\frac{dx^\alpha}{d\lambda} \left[\partial_\alpha \left(\frac{dx^\mu}{d\lambda} \right) + \Gamma^{\mu}_{\alpha\beta} \frac{dx^\beta}{d\lambda} \right] = 0 \Rightarrow \frac{d^2 x^\mu}{d\lambda^2} + \Gamma^{\mu}_{\alpha\beta} \frac{dx^\alpha}{d\lambda} \frac{dx^\beta}{d\lambda} = 0 . \tag{2.6}$$

Notice that Eq. (2.6) is invariant under the affine reparameterization $\lambda \to a\lambda + b$, where a and b are some constant real numbers.

Einstein field equations encode the interplay between the curvature of spacetime and a source of matter (expressed by the energy-momentum tensor $T_{\mu\nu}$)

$$G_{\mu\nu} = R_{\mu\nu} - \frac{1}{2} g_{\mu\nu} R = 8\pi G T_{\mu\nu} , \tag{2.7}$$

where $G_{\mu\nu}$ is the Einstein tensor. The differential Bianchi identity gives $\nabla_\mu G^{\mu\nu} = 0$ and, therefore, ensures that the total energy-momentum tensor is automatically conserved i.e. $\nabla_\mu T^{\mu\nu} = 0$ regardless of the metric under consideration. The field equations may also be derived from the following action functional

$$\mathcal{S}\left[g_{\mu\nu}, \Phi^i \right] = \mathcal{S}_{\text{E.H.}} + \mathcal{S}_{\text{M}} , \tag{2.8}$$

by considering variations with respect to the metric, where $\Phi^i(x^\mu)$ can be any spacetime dependent

tensor field in $\mathcal{M}$ (here the superscript i is used to label the fields). The first term in Eq. (2.8) is known as the Einstein-Hilbert action,

$$\mathcal{S}_{\text{E.H.}}\left[g_{\mu\nu}\right] = \int d^4x\sqrt{-g}\frac{R}{16\pi G}\,, \tag{2.9}$$

and depends solely on quantities derived from the metric tensor, viz., R and g, where $g = \det\left(g_{\mu\nu}\right)$. The second term is given by

$$\mathcal{S}_{\text{M}}\left[g_{\mu\nu}, \Phi^i\right] = \int d^4x\sqrt{-g}\mathcal{L}_{\text{M}}\left(g_{\mu\nu}, \Phi^i\right)\,, \tag{2.10}$$

and, being a functional of the metric and the matter fields Φ^i, it is usually dubbed as the matter action (in general, $\mathcal{S}_{\text{M}}$ is a function of the matter field derivatives as well i.e. $\mathcal{S}_{\text{M}}\left[g_{\mu\nu}, \Phi^i, \nabla_\mu\Phi^i\right]$). The energy-momentum tensor, appearing on the right side of Eq. (2.7), is given by

$$T_{\mu\nu} = -\frac{2}{\sqrt{-g}}\frac{\delta\left(\sqrt{-g}\mathcal{L}_{\text{M}}\right)}{\delta g^{\mu\nu}} = -2\frac{\delta\mathcal{L}_{\text{M}}}{\delta g^{\mu\nu}} + \mathcal{L}g^{\mu\nu}\,, \tag{2.11}$$

where the variation is taken with respect to the inverse metric (note that $\delta g_{\mu\nu} = -g_{\mu\alpha}g_{\nu\beta}\delta g^{\alpha\beta}$). The equation of motion characterizing the dynamics of a given field Φ^i is simply given by

$$\frac{\delta\mathcal{S}_{\text{M}}}{\delta\Phi^i} = 0\,. \tag{2.12}$$

We shall rely on Eq. (2.11) to compute the energy-momentum tensor in Chap. 4, where we explore possible Lagrangian descriptions of perfect fluids and their connection with scalar field theories.

2.2 Homogeneous cosmology

The Standard Cosmological Model stands upon the assumption that, on very large scales (typically larger than 100 Mpc), the Universe is essentially homogeneous and isotropic at each instant of cosmic time. This postulate, being of crucial importance in contemporary cosmology, is known as the Cosmological Principle. The hypothesis of spatial uniformity can be viewed as a remnant of the Copernican Principle, according to which the Earth does not have a privileged location in the Universe. Isotropy, on the other hand, assert that there is no preferred spatial direction. The two concepts are not completely independent, although in general homogeneity does not imply isotropy, and vice versa. Isotropy around every point in space however implies homogeneity. The observed distributions of radio sources [190], galaxies [191], clusters of galaxies [192], and gamma-ray bursts [193] have been used to test isotropy, finding no significant evidence against statistical isotropy on large scales. Of particular relevance are the CMB measurements, where deviations from isotropy are found to be on the order of 10^{-5} [194]. Hence, given the high level of isotropy inferred from observations and by assuming that the Copernican Principle holds, the Cosmological Principle follows. Although the validity of the Copernican Principle is much harder to probe than isotropy, the assumption of homogeneity on large scales is shown to be compatible with several observations

and consistency tests [195–199] (see also the review [200]). Hence, even if the Cosmological Principle leads to a very idealized model, it seems to be consistent (at first approximation) with the Universe we observe.

2.2.1 Friedmann-Lemaître-Robertson-Walker metric

The investigation of homogeneous and isotropic solutions to the Einstein's equations was pioneered by Friedmann and Lemaître in the 1920's [10–12], and later rediscovered by Howard Robertson and Arthur Walker [201–204].

The most general metric, fulfilling the requirements of the Cosmological Principle, is given by the spherically symmetric Friedmann-Lemaître-Robertson-Walker (FLRW) metric

$$ds^2 = -dt^2 + a^2(t)\, g^{(3)}_{ij} dx^i dx^j \,, \tag{2.13}$$

where t is the physical cosmic time, $a(t)$ is the scale factor, and $g^{(3)}_{ij}$ is a 3-dimensional metric of constant curvature $\mathcal{K}$. Depending on the sign of $\mathcal{K}$, the spatial geometry can be closed (if $\mathcal{K} > 0$), open (if $\mathcal{K} < 0$), or flat (if $\mathcal{K} = 0$). The spatial line element may be written as

$$g^{(3)}_{ij} dx^i dx^j = \frac{dr^2}{1 - \mathcal{K} r^2} + r^2 \left(d\theta^2 + \sin^2\theta d\varphi^2 \right) \,, \tag{2.14}$$

with r, θ and φ being comoving spatial coordinates, which remain constant in time for a comoving observer i.e. a free-falling observer for which the Universe is homogeneous and isotropic.

One may now use Eq. (2.2) to find the non-vanishing connection coefficients for the FLRW metric

$$\Gamma^0_{ij} = a\dot{a} g^{(3)}_{ij} \,, \qquad \Gamma^i_{0j} = \Gamma^i_{j0} = \frac{\dot{a}}{a}\delta^i_j \,, \tag{2.15}$$

$$\Gamma^1_{11} = \frac{\mathcal{K} r}{1 - \mathcal{K} r^2} \,, \qquad \Gamma^1_{22} = -r\left(1 - \mathcal{K} r^2\right) \,, \tag{2.16}$$

$$\Gamma^1_{33} = -r\left(1 - \mathcal{K} r^2\right)\sin^2\theta \,, \qquad \Gamma^2_{33} = -\sin\theta\cos\theta \,, \tag{2.17}$$

$$\Gamma^2_{12} = \Gamma^2_{21} = \Gamma^3_{13} = \Gamma^3_{31} = \frac{1}{r} \,, \qquad \Gamma^3_{23} = \Gamma^3_{32} = \cot\theta \,, \tag{2.18}$$

where an over-dot represents the derivative in order to the cosmic time (i.e. $\dot{x} \equiv dx/dt$). From Eq. (2.1) one gets the components of the Ricci tensor

$$R_{00} = -3\frac{\ddot{a}}{a} \,, \tag{2.19}$$

$$R_{ij} = \left(a\ddot{a} + 2\dot{a}^2 + 2\mathcal{K}\right) g^{(3)}_{ij} \,, \tag{2.20}$$

while the Ricci scalar is given by

$$R = 6\left[\frac{\ddot{a}}{a} + \left(\frac{\dot{a}}{a}\right)^2 + \frac{\mathcal{K}}{a^2}\right] . \tag{2.21}$$

Notice that if the Universe is spatially closed, a coordinate singularity arises for $r = r_{\mathcal{K}} = 1/\sqrt{\mathcal{K}}$. This singularity can be removed with a coordinate transformation

$$d\chi = \frac{dr}{\sqrt{1-\mathcal{K}r^2}} , \tag{2.22}$$

where χ defines a new radial coordinate. Integrating the equation above one finds

$$r = f_{\mathcal{K}}(\chi) = \begin{cases} \frac{1}{\sqrt{\mathcal{K}}}\sin(\chi) , & \mathcal{K} > 0 \\ \chi , & \mathcal{K} = 0 \\ \frac{1}{\sqrt{|\mathcal{K}|}}\sinh(\chi) , & \mathcal{K} < 0 , \end{cases} \tag{2.23}$$

so the FLRW metric may be recasted as follows

$$ds^2 = -dt^2 + a^2 f_{\mathcal{K}}(\chi)^2\left[d\chi^2 + d\theta^2 + \sin^2\theta d\varphi^2\right] . \tag{2.24}$$

In several situations it is useful to work with a conformal time coordinate η

$$d\eta = \frac{dt}{a(t)} , \tag{2.25}$$

giving us a complete comoving coordinate system (η, r, θ, φ), or (η, χ, θ, φ) (if one uses Eq. (2.24)).

An essential observable in cosmology is the redshift associated with the propagation of light in an expanding Universe. As we have seen in Chapter 1, the redshift of spectral lines of distant galaxies was key to Hubble's insight. Given that the trajectory of a light-ray follows a null geodesic (i.e. $ds^2 = 0$), one gets

$$\frac{dt}{d\lambda} = \frac{a(t)}{\sqrt{1-\mathcal{K}r^2}}\frac{dr}{d\lambda} , \tag{2.26}$$

where the affine parameter λ is normalized such that $p^\mu = dx^\mu/d\lambda$ gives the photon 4-momentum. Notice that, due to spatial isotropy, θ and φ may be set to zero without generality being lost. Combining Eq. (2.26) with the component $\mu = 0$ from Eq. (2.6) leads to

$$\frac{d^2t}{d\lambda^2} + \frac{\dot{a}}{a}\left(\frac{dt}{d\lambda}\right)^2 = 0 , \tag{2.27}$$

which has the solution

$$\frac{dt}{d\lambda} = \frac{\omega_0}{a(t)} , \tag{2.28}$$

with ω_0 being an integration constant. Let us now consider a comoving observer i.e. an observer for which $u^\mu = (1, 0, 0, 0)$ — here $u^\mu = dx^\mu/d\tau$ are the components of the 4-velocity, and τ is the proper time. Such observer measures the energy of a photon to be

$$E = -g_{\mu\nu} p^\mu u^\nu = -g_{00} \frac{dx^0}{d\lambda} u^0 = \frac{\omega_0}{a\,(t)}\,. \tag{2.29}$$

Since $\dot{a} > 0$ in an expanding Universe, the energy of a photon decreases with time and the associated wavelength is stretched in proportion to the scale factor. Hence, the energy of a photon emitted from a source at a time $t_{\rm em}$ and observed at a time $t_{\rm obs} > t_{\rm em}$ is changed by a factor of

$$\frac{E\,(t_{\rm em})}{E\,(t_{\rm obs})} = \frac{a\,(t_{\rm obs})}{a\,(t_{\rm em})}\,, \tag{2.30}$$

and the cosmological redshift is then

$$z = \frac{E\,(t_0)}{E\,(t_{\rm obs})} - 1 = \frac{a\,(t_0)}{a\,(t_{\rm em})} - 1\,, \tag{2.31}$$

for a comoving observer making the measurement at the present time t_0. For the remaining of the thesis we shall normalize the scale factor to unity at t_0 (so that $z = 0$ corresponds to the present epoch).

The physical distance, or proper distance, may be defined as the travel time of a photon emitted at a time t and observed at t_0

$$d_{\rm P}\,(t) = -\int_{t_0}^{t} dt = a\,(t) \int_0^r \frac{dr'}{\sqrt{1 - \mathcal{K} r'^2}} = a\,(t)\, f_{\mathcal{K}}^{-1}\,(r) = a\,(t)\, d^{(\rm c)}\,, \tag{2.32}$$

where $d^{(\rm c)}$ is the comoving distance. The associated "recessional velocity" of a comoving object at a distance $d_{\rm P}$ is simply given by

$$v\,(t) = \dot{d_{\rm P}} = H d_{\rm P}\,. \tag{2.33}$$

Considering small values of the redshift ($z \ll 1$), the expansion rate $H \equiv \dot{a}/a$ can be well approximated by its present value H_0

$$v \simeq H_0 d_{\rm P}\,, \tag{2.34}$$

which is precisely the relation that Hubble derived from observations in the 1920's, and thus called the Hubble's law. The quantity H_0 is known as the Hubble parameter, and is often written in terms of a dimensionless parameter h

$$H_0 = 100\, h \text{ km s}^{-1} \text{ Mpc}^{-1}\,. \tag{2.35}$$

2.2.2 Perfect fluids

Physical systems containing a very large number of "free" particles[2] may be effectively approximated by a fluid. The validity of such approximation is usually quantified in terms of the ratio $K_{\rm n} \equiv L_{\rm p}/L_{\rm s} \ll 1$ known as the Knudsen number, where $L_{\rm p}$ is the typical inter-particle separation and $L_{\rm s}$ is the characteristic size of the system. The building blocks of a fluid are the so called fluid elements (also dubbed fluid "particles"). A fluid element is defined as a small volume of the fluid (relatively to the scale $L_{\rm s}$) in order to guarantee homogeneity within the element, but large enough to contain a very large number of particles, such that, in each of these fluid elements, the particles are in thermodynamical equilibrium. Hence, fluids provide a high-level description of matter: only a few continuous macroscopic quantities are required in order to effectively characterize the system. A perfect fluid, defined as one that can be completely specified by a rest-frame energy density ρ, and an isotropic[3] rest-frame pressure p, often provides an adequate framework to model the source of the gravitational field.

The energy-momentum tensor

Having fixed the background geometry to be described by a FLRW metric, Einstein field equations can be solved once the matter content of the Universe is specified in terms of its energy-momentum tensor. Considering a perfect fluid, the energy-momentum tensor may be expressed in a matrix form as

$$T_{\hat{\mu}\hat{\nu}} = T^{\hat{\mu}\hat{\nu}} = \begin{pmatrix} \rho & 0 & 0 & 0 \\ 0 & p & 0 & 0 \\ 0 & 0 & p & 0 \\ 0 & 0 & 0 & p \end{pmatrix} , \tag{2.36}$$

where the "hats" over the indices indicate that the components are computed in the local inertial rest frame of the fluid (i.e. $g_{\hat{\mu}\hat{\nu}} = \eta_{\hat{\mu}\hat{\nu}}$ where $\eta_{\mu\nu} = (-1, 1, 1, 1)$ are the components of the Minkowski metric in cartesian coordinates). In any other frame, the energy-momentum tensor of a perfect fluid is given by

$$T^{\mu\nu} = (\rho + p)\, u^{\mu} u^{\nu} + p g^{\mu\nu} . \tag{2.37}$$

For a comoving observer in a FLRW background at rest with the fluid one has

$$T^{00} = \rho = T_{00} , \tag{2.38}$$

$$T^{ij} = p g^{ij} = \frac{1}{a^2} p g^{ij}_{(3)} . \tag{2.39}$$

[2] Here *free* is meant to indicate that the particles are not part of a rigid structure, such as e.g. a crystal lattice.

[3] By relaxing this assumption one may construct a broader class of perfect fluids, which are characterized by having distinct values for the pressure along different spatial directions and are, therefore, known as anisotropic perfect fluids [205].

As mentioned in Sec. 2.1, the conservation of the total energy-momentum tensor follows from Einstein equations together with the differential Bianchi identity, that demands $\nabla_\mu G^{\mu\nu} = 0$. Taking the covariant derivative of Eq. (2.37), the conservation equations for a perfect fluid are

$$\nabla_\mu T^{\mu\nu} = \partial_\mu T^{\mu\nu} + \Gamma^\mu_{\mu\alpha} T^{\alpha\nu} + \Gamma^\nu_{\mu\alpha} T^{\mu\alpha} \,. \tag{2.40}$$

For the component $\nu = 0$ one gets

$$\nabla_\mu T^{\mu 0} = \partial_0 T^{00} + \Gamma^\mu_{\mu 0} T^{00} + \Gamma^0_{\mu\alpha} T^{\mu\alpha} = \dot{\rho} + 3H\left(\rho + p\right) = 0 \,, \tag{2.41}$$

whereas the equations for the spatial components $\nu = i$

$$\nabla_\mu T^{\mu i} = \partial_j T^{ij} + \Gamma^\mu_{\mu j} T^{ij} + \Gamma^i_{\mu\alpha} T^{\mu\alpha} \Rightarrow \partial_i p = 0 \,, \tag{2.42}$$

are trivially satisfied. On the other hand, the $\nu = 0$ component in Eq. (2.41) tell us how the energy density evolves with time given the expansion rate of the Universe and the pressure of the fluid. This conservation equation is usually written as

$$\dot{\rho} + 3H\rho\left(1 + w\right) = 0 \,, \tag{2.43}$$

where $w \equiv p/\rho$ is the equation of state parameter. In Sec. 2.2.3 we show that Einstein equations provide a further relation between ρ and H. Thus, in order to solve Eq. (2.43) additional information is needed. One possible way to close the system of equations is by providing a relation between the pressure and energy density in the form of a *barotropic* equation of state $p = p\left(\rho\right)$ (or $w = w\left(\rho\right)$).

Thermodynamics

In addition to ρ and p, let us now also consider the proper particle number density $n = N/V$ and the entropy density $\widetilde{s} = \mathcal{S}/V$ of a perfect fluid (these quantities being also defined in the local comoving inertial frame) where N is the number of particles and $\mathcal{S}$ is the entropy within a physical volume V. Assuming that there are no creation or annihilation processes the total number of particles is conserved. The local form of the first law of thermodynamics may be written as

$$d\left(\frac{\rho}{n}\right) + p d\left(\frac{1}{n}\right) = T d\left(\frac{\widetilde{s}}{n}\right) \,, \tag{2.44}$$

where T is the temperature of the fluid. The conservation of the total number of particles can be expressed through the continuity equation for the particle number density

$$\nabla_\alpha j^\alpha = u^\alpha \nabla_\alpha n + n \nabla_\alpha u^\alpha = 0 \,, \tag{2.45}$$

where $j^\alpha = n u^\alpha$ is the particle number current. For a comoving observer one gets

$$u^\alpha \nabla_\alpha n + n\left(\partial_\alpha u^\alpha + \Gamma^\alpha_{\alpha\beta} u^\beta\right) = \dot{n} + 3Hn = 0\,, \tag{2.46}$$

being straightforward to show from Eq. (2.46) that, in an expanding Universe, the particle number density decays as $n \propto a^{-3}$ (N is fixed while the physical volume grows as $V \propto a^3$).

Now let us consider the projection of the covariant derivative of the energy-momentum tensor for a perfect fluid along u_β

$$u_\beta \nabla_\alpha T^{\alpha\beta} = 0 = u_\beta \nabla_\alpha \left[(\rho + p)\, u^\alpha u^\beta + p g^{\alpha\beta}\right] = \tag{2.47}$$

$$= -u^\alpha \nabla_\alpha \rho - (\rho + p)\, \nabla_\alpha u^\alpha = \tag{2.48}$$

$$= -n\left[u^\alpha \nabla_\alpha \left(\frac{\rho}{n}\right) + p u^\alpha \nabla_\alpha \left(\frac{1}{n}\right)\right]\,, \tag{2.49}$$

where we have used the identity $u^\alpha u_\alpha = -1$. Identifying the expression inside the parenthesis in Eq. (2.49) with the l.h.s. in Eq. (2.44) one obtains

$$u^\alpha \nabla_\alpha \left(\frac{\widetilde{s}}{n}\right) = 0\,, \tag{2.50}$$

implying that, for perfect fluids conserving the total number of particles, the entropy per particle $s = \widetilde{s}/n$ is conserved along the fluid lines. Fluids that satisfy Eq. (2.50) are said to be *adiabatic*. In fact, for fluids conserving the number of particles and defined by a barotropic equation of state, the entropy is going to be the same constant throughout the volume of the fluid at all times, i.e.

$$\nabla_\alpha \left(\frac{\widetilde{s}}{n}\right) = 0 \quad \Rightarrow \quad \mathcal{S} = \text{const.} \tag{2.51}$$

which defines an *isentropic* motion (see e.g. [206]). Clearly, if Eq. (2.51) holds then the adiabaticity condition is also satisfied. Although we will not need to work directly with Eq. (2.51), it is worth to make here this distinction between adiabaticity and isentropy.

Notice that the adiabaticity condition simplifies Eq. (2.44) to

$$d\left(\frac{\rho}{n}\right) + p d\left(\frac{1}{n}\right) = 0\,. \tag{2.52}$$

It is a simple matter to show that Eq. (2.43) is recovered from Eq. (2.49) (in combination with Eq. (2.45)). Hence, instead of a barotropic equation of state, one may also define an isentropic perfect fluid from an equation of state of the form $\rho = \rho\,(n)$ and solve Eq. (2.52), giving the pressure in terms of n

$$p(n) = \mu n - \rho\,(n)\,, \tag{2.53}$$

where $\mu = d\rho/dn$ is the chemical potential. Alternatively, if $p = p(n)$ is assumed, then Eq. (2.52) implies that

$$\rho(n) = mn + n\int^{n} \frac{p(n')}{n'^2} dn' \,. \tag{2.54}$$

The integration constant m may be identified as the rest mass of the particles (so as to recover $\rho = nm$ for $p = 0$).

2.2.3 Friedmann equations

Now that we have a suitable mathematical formulation of a geometry complying with the symmetries imposed by the Cosmological Principle, we are in position to determine the dynamical evolution of the Universe (with its matter content being described in terms of a perfect fluid energy-momentum tensor) by solving Einstein equations. Using Eqs. (2.19), (2.20), and (2.21), one finds the components (00) and (ij) of the Einstein tensor to be

$$G_{00} = 3\left(H^2 + \frac{\mathcal{K}}{a^2}\right) , \tag{2.55}$$

and

$$G_{ij} = -\left(2\ddot{a}a + \dot{a}^2 + \mathcal{K}\right) g^{(3)}_{ij} \,, \tag{2.56}$$

with all the other components being identically zero. Combining Eqs. (2.55) and (2.38) one obtains

$$H^2 = \frac{8\pi G}{3}\rho - \frac{\mathcal{K}}{a^2} \,, \tag{2.57}$$

while Eqs. (2.56) and (2.39) give

$$2\frac{\ddot{a}}{a} + H^2 + \frac{\mathcal{K}}{a^2} = -8\pi G p \,. \tag{2.58}$$

Eqs. (2.57) and (2.58) are known as the Friedmann equations. Another important relation can be obtained by eliminating the curvature term by combining Eqs. (2.57) and (2.58)

$$\frac{\ddot{a}}{a} = -\frac{4\pi G}{3}\left(\rho + 3p\right) , \tag{2.59}$$

which is usually known (in a cosmological context) as the Raychaudhuri equation. It is clear from Eq. (2.59) that the condition $w < -1/3$ is required to obtain an accelerated rate of expansion (i.e. $\ddot{a} > 0$). Dividing Eq. (2.59) by $-H^2$ one gets the deceleration parameter

$$q \equiv -\frac{\ddot{a}}{aH^2} = \frac{1}{2}\left(1 + 3w\right) , \tag{2.60}$$

where q is negative (positive) if the cosmic expansion accelerates (decelerates). Also notice that the continuity equation given in Eq. (2.43) can be obtained by first multiplying Eq. (2.57) by a^2, differentiating with respect to time, and then using Eq. (2.58).

So far we have presented the equations in terms of the full energy-momentum tensor. The results can be easily generalized to the case of $N_{\rm f}$ several perfect fluids by taking

$$\rho = \sum_i^{N_{\rm f}} \rho_i \,, \quad p = \sum_i^{N_{\rm f}} p_i \,, \tag{2.61}$$

while the continuity equation holds individually for each fluid

$$\dot{\rho}_i + 3H\left(\rho_i + p_i\right) = 0 \,, \tag{2.62}$$

provided that they interact only through gravity. For a perfect fluid with constant equation of state parameter w_i the above equation can be integrated to give

$$\rho_i = \rho_{i0} a^{-3(1+w_i)} \,. \tag{2.63}$$

A perfect fluid with constant w is sufficient to model the background dynamics of several cosmological components of interest. It covers, for instance, radiation ($w_{\rm r} = 1/3$), pressureless matter ($w_{\rm m} = 0$), and a cosmological constant ($w_\Lambda = -1$). From Eq. (2.63) one finds that the energy density of these components evolve as $\rho_{\rm r} \propto a^{-4}$, $\rho_{\rm m} \propto a^{-3}$, and $\rho_\Lambda \propto$ const., respectively.

It is often useful to work with the fractional contribution from each component to the total energy density. For a given component the dimensionless density parameter is usually defined as

$$\Omega_i = \frac{\rho_i}{\rho_{\rm crit}} \,, \tag{2.64}$$

whereas the reduced density parameter is given by

$$\omega_i = \Omega_i h^2 \,. \tag{2.65}$$

The critical density $\rho_{\rm crit}$ is defined such that $\mathcal{K} = 0$, i.e.

$$\rho_{\rm crit} = \frac{3H^2}{8\pi G} \,. \tag{2.66}$$

As one may check from Eq. (2.57), the Universe is closed (i.e. $\mathcal{K} > 0$) if the total energy density is above the $\rho_{\rm crit}$, and open (i.e. $\mathcal{K} < 0$) if the total energy density is bellow $\rho_{\rm crit}$. With these definitions in place, the first Friedmann equation may be rewritten as

$$\sum_i \Omega_i + \Omega_{\mathcal{K}} = 1 \,, \tag{2.67}$$

where

$$\Omega_{\mathcal{K}} = -\frac{\mathcal{K}}{H^2 a^2}\,. \tag{2.68}$$

2.2.4 The ΛCDM model

The Standard Cosmological model assumes General Relativity and a FLRW metric, while a few free parameters have to be constrained from observations. These include the present fractional densities of the energy and matter content in the Universe Ω_{i0}, the curvature parameter $\Omega_{\mathcal{K}0}$, and the present rate of expansion H_0, which are sufficient to completely determine the background dynamics.

The joint results of the most recent CMB [146] and BAO data [207–209] are able to tightly constrain the curvature term

$$\Omega_{\mathcal{K}0} = 0.0007 \pm 0.0019\,, \tag{2.69}$$

thus suggesting that our Universe is virtually flat. Given such strong observational bound on $\Omega_{\mathcal{K}0}$ the curvature is usually taken to be exactly zero in the ΛCDM model. We assume hereafter $\mathcal{K} = 0$ and, therefore, we shall work with a flat FLRW metric (so we can set a cartesian metric for the spatial part of the metric i.e. $g^{(3)}_{ij} = \delta_{ij}$).

Regarding the content described by the Standard Model of Particle Physics, for most cosmological purposes it is sufficient to consider photons, neutrinos, and baryons. Photons emitted by stars or hot gas represent only a small fraction of the photons in the Universe; most of the photons are, by large, part of the CMB. Their energy density can then be characterized by the CMB monopole temperature, which has been measured with an outstanding precision from a combination of the COBE/FIRAS data [210,211]. Considering the mean value for the temperature, the reduced photon density parameter at the present is found to be

$$\omega_{\gamma 0} = 2.47 \times 10^{-5}\,. \tag{2.70}$$

Neutrinos also behave as relativistic particles provided that their masses are small. Although cosmic neutrinos have not yet been observed the theoretical arguments in favor of their existence are well grounded, based on very well-understood physics [212]. By accounting for the contribution from relativistic neutrinos to the radiation density one gets

$$\omega_{\mathrm{r}0} = 4.17 \times 10^{-5}\,. \tag{2.71}$$

It turns out that the radiation contribution to the total energy density at the present time is extremely small. Hence, in most late-time analysis one can safely ignore this component on the background dynamics.

Some of the non-relativistic matter is found in the form of atomic nuclei and electrons. Following the widespread terminology among the cosmology community, these are referred to as *baryons*[4]. The density of baryons in the Universe may be estimated in several ways, either directly e.g. by measuring the emission or absorption in the electromagnetic spectrum [213], indirectly e.g. via the abundance of light elements from BBN [214], or from CMB anisotropies, with the latest Planck data providing the tightest constraint to date of $\omega_{\rm b0} = 0.00224 \pm 0.0001$ [146]. All these estimates using different techniques agree to a large extent on a baryonic fractional energy density of about

$$\Omega_{\rm b0} \approx 0.05\,, \tag{2.72}$$

showing that baryonic matter accounts for a small fraction ($\sim 5\%$) of the total energy density at the present time.

In the present paradigm the largest proportion of non-relativistic matter is attributed to CDM. The reduced fraction of CDM is well constrained by Planck to be [146]

$$\omega_{\rm cdm0} = 0.120 \pm 0.001\,, \tag{2.73}$$

while the derived total matter density[5] is

$$\Omega_{\rm m0} = 0.315 \pm 0.007\,. \tag{2.74}$$

A Universe containing $\sim 30\%$ of matter is consistent with the values determined e.g. from weak-lensing measurements [150, 151] and the distribution of large scale structures [215].

Within the standard cosmological model, the remaining chunk of the cosmic energy budget (satisfying the closure relation given by Eq. (2.67)) is identified with a cosmological constant

$$\Omega_{\Lambda 0} = 0.6847 \pm 0.0073\,, \tag{2.75}$$

being responsible for the present state of cosmic acceleration.

Multiple independent methods have been used to measure the Hubble constant at different cosmic epochs. With the improvement of the precision obtained by these experiments, a significant tension in the H_0 value started to emerge (see Sec. 1.6.3). For instance, Planck's inferred value (which assumes a flat ΛCDM model)

[4] Though electrons are technically *leptons*, protons and neutrons are so much more massive than electrons that most of the mass accounted by standard particles is indeed found in the form of baryons.

[5] The total matter density fraction includes baryons, CDM, and also the small contribution from one massive neutrino with $m_\nu = 0.06$ eV. The analysis presented in [146] show that the combination of CMB and BAO data tightly constrains the upper bound on the sum of neutrino masses to be $\sum_i m_{\nu\, i} < 12\,{\rm eV}$ at 95% C.L. . Since neutrinos have such a small mass, they behave essentially as relativistic particles for most of the cosmic expansion history. Hence, for simplicity, throughout this thesis we shall treat neutrinos as massless particles.

$$H_{0[\mathrm{CMB}]} = 67.4 \pm 0.5 \text{ km s}^{-1} \text{ Mpc}^{-1} , \tag{2.76}$$

is in tension at a statistical significance of more than 4σ with the value reported in [147]

$$H_{0[\mathrm{SNIa}]} = 73.2 \pm 1.3 \text{ km s}^{-1} \text{ Mpc}^{-1} . \tag{2.77}$$

The latter relies on distance ladder measurements, with the magnitude of supernovae being calibrated through variable Cepheid stars. Currently, the reason for the discrepancy on the value of H_0 obtained by different probes still remains unclear.

2.3 Perturbation theory

Although an homogeneous and isotropic Universe described by a FLRW metric might be an adequate description on sufficiently large scales, on smaller scales our universe is fairly inhomogeneous; cosmic structures in the form of e.g. galaxies, clusters of galaxies, filaments or voids, can have densities significantly different from the average value. One of the first attempts to describe the formation of planets and stars in a static Universe governed by Newtonian gravity was published by James Jeans in 1902, in which he demonstrated that small density perturbations can grow with time in a homogeneous and isotropic self-gravitating fluid via gravitational instability [216]. The evolution of density perturbations in a FLRW expanding Universe was pioneered by Lifshitz in 1946 [217], and provided the basis for further developments regarding the formation of cosmic structures e.g. [218–223] (see the editorial note by Ellis in [224] for a historical perspective). These works used linear perturbations theory by considering small perturbations around an "unperturbed" background. According to the prevailing scenario, primordial density perturbations originated from an inflationary phase in the early Universe seeded the formation of cosmic structures, which were then amplified due to self gravity.

To get the perturbed relativistic equations we must consider perturbations to the FLRW metric

$$g_{\mu\nu}(\eta, \mathbf{x}) = g^{(0)}_{\mu\nu}(\eta) + \delta g_{\mu\nu}(\eta, \mathbf{x}) , \tag{2.78}$$

where $g^{(0)}_{\mu\nu}(\eta)$ stands for the background metric (zero-th order)[6] and $\delta g_{\mu\nu}(\eta, \mathbf{x}) \ll 1$ (in the linear regime) are the components of the perturbed metric tensor, so we may write

$$ds^2 = g_{\mu\nu} dx^\mu dx^\nu = a^2(\eta) \left[-d\eta^2 + \delta_{ij} dx^i dx^j + \delta g_{\mu\nu} dx^\mu dx^\nu \right] . \tag{2.79}$$

The most general linear perturbation around the FLRW metric can be decomposed as follows

$$\delta g_{00} = -2\Psi , \quad \delta g_{0i} = \mathrm{w}_i , \quad \delta g_{ij} = 2\left(\mathrm{h}_{ij} - \Phi \delta_{ij}\right) , \tag{2.80}$$

[6] In general we shall denote zero-th order quantities by an upper or lower script "(0)". For ease of notation, we drop the (0) when it is clear to which value we are referring to (i.e. either to the background or to the total variable).

where the perturbations Ψ and Φ are scalar functions, w_i is a 3-vector, and h_{ij} is a symmetric and traceless ($\delta^{ij}\mathrm{h}_{ij} = 0$) second order tensor. Notice that Φ encodes the trace of δg_{ij} as $\Phi = -\delta^{ij}\delta g_{ij}/6$.

2.3.1 Scalar-vector-tensor decomposition

One may decompose any 3-vector into a longitudinal and transverse parts

$$\mathbf{w} = \mathbf{w}_{||} + \mathbf{w}_{\perp}\,, \tag{2.81}$$

where a longitudinal vector is curl-free (i.e. $\vec{\nabla} \times \mathbf{w}_{||} = 0$) and a transverse vector is divergence-free (i.e. $\vec{\nabla} \cdot \mathbf{w}_{\perp} = 0$). Given that the curl of a gradient is always zero, the longitudinal part can be written as the gradient of a scalar field $\mathbf{w}_{||} = \vec{\nabla}\mathrm{w_s}$, being also known as the irrotational part. On the other hand we can write the transverse (or rotational) part as $\mathbf{w}_{\perp} = \vec{\nabla} \times \mathbf{w}_{\mathrm{v}}$. It is clear that the longitudinal part has one degree of freedom carried by the w_s, and the transverse part two degrees of freedom (the null divergence implies that one of the three components of the vector $\mathbf{w}_{\perp}$ is constrained by the other two). By definition $\mathbf{w}_{||}$ represents a scalar perturbation and $\mathbf{w}_{\perp}$ represents a vector perturbation. Analogously, we can decompose the traceless 2-tensor h_{ij} as

$$\mathbf{h} = \mathbf{h}_{||} + \mathbf{h}_{\perp} + \mathbf{h}_{T}\,, \tag{2.82}$$

where now the divergences $\vec{\nabla} \cdot \mathbf{h}_{||}$ and $\vec{\nabla} \cdot \mathbf{h}_{\perp}$ are longitudinal and transverse, respectively, and $\mathbf{h}_T$ is transverse. Thus, the divergence of $\mathbf{h}_T$ is zero

$$\delta^{jk}\partial_k \mathrm{h}_{ij\,T} = 0\,, \tag{2.83}$$

while the divergence of $\vec{\nabla} \cdot \mathbf{h}_{\perp}$ (sometimes also called the solenoid part) is divergence-free

$$\delta^{il}\delta^{jk}\partial_l\partial_k \mathrm{h}_{ij\,\perp} = 0\,. \tag{2.84}$$

One can then derive $\mathrm{h}_{ij\,\perp}$ from a transverse vector field $\mathbf{h}_{\mathrm{v}}$

$$\mathrm{h}_{ij\,\perp} = \partial_i \mathrm{h}_{j\,\mathrm{v}} + \partial_j \mathrm{h}_{i\,\mathrm{v}}\,. \tag{2.85}$$

Hence $\mathbf{h}_T$ and $\mathbf{h}_{\perp}$ carry two degrees each. The longitudinal part $\vec{\nabla} \cdot \mathbf{h}_{||}$ is (similarly to the vector decomposition case) curl-free, so it can be derived from a scalar function as

$$\mathrm{h}_{ij||} = \left(\partial_i\partial_j - \frac{1}{3}\delta_{ij}\nabla^2\right)\mathrm{h_s}\,, \tag{2.86}$$

and it will have just one degree of freedom. Physically tensor modes represent gravitational waves, while vector modes are associated to rotational velocity perturbations. As for scalar modes, they are related to the density perturbations. It turns out that at first order, scalar, vector, and tensor modes evolve independently of each other. Here we shall focus on the growth of cosmic structures

and, consequently, only scalar perturbations will be taken into account, i.e. we assume that the two other types of perturbations vanish. Therefore, the perturbed line element that shall be considered is given by

$$ds^2 = a^2(\eta)\left\{-(1+2\Psi)\,d\eta^2 + 2\mathrm{w}_{i\,||}d\eta dx^i + \left[(1-2\Phi)\,\delta_{ij} + 2\mathrm{h}_{ij\,||}\right]dx^i dx^j\right\}. \tag{2.87}$$

2.3.2 Perturbed field equations

In order to derive the first-order Einstein equations we decompose the Einstein tensor $G_{\mu\nu}$ and the energy-momentum tensor $T_{\mu\nu}$ into background and perturbed parts

$$G_{\mu\nu} = G^{(0)}_{\mu\nu} + \delta G_{\mu\nu}\,, \quad T_{\mu\nu} = T^{(0)}_{\mu\nu} + \delta T_{\mu\nu}\,. \tag{2.88}$$

which results in the Einstein equations for the background

$$G^{(0)}_{\mu\nu} = 8\pi G T^{(0)}_{\mu\nu}\,, \tag{2.89}$$

and for the perturbations

$$\delta G_{\mu\nu} = 8\pi G \delta T_{\mu\nu}\,. \tag{2.90}$$

The perturbed Einstein tensor is

$$\delta G_{\mu\nu} = \delta R_{\mu\nu} - \frac{1}{2}\left(\delta g_{\mu\nu} R + g_{\mu\nu}\delta R\right) \Rightarrow \delta G^{\mu}{}_{\nu} = \delta g^{\mu\alpha} G_{\alpha\nu} + g^{\mu\alpha}\delta G_{\alpha\nu}\,, \tag{2.91}$$

and going all the way through the perturbed Ricci scalar δR, Ricci tensor $\delta R_{\mu\nu}$ and Christoffel symbols $\delta\Gamma^{\mu}_{\nu\lambda}$ we get everything in terms of the perturbed metric

$$\delta R = \delta g^{\mu\alpha} R_{\alpha\mu} + g^{\mu\alpha}\delta R_{\alpha\mu}\,, \tag{2.92}$$

$$\delta R_{\mu\nu} = \delta\Gamma^{\alpha}_{\mu\nu,\alpha} - \delta\Gamma^{\alpha}_{\mu\alpha,\nu} + \delta\Gamma^{\alpha}_{\mu\nu}\Gamma^{\beta}_{\alpha\beta} + \Gamma^{\alpha}_{\mu\nu}\delta\Gamma^{\beta}_{\alpha\beta} - \delta\Gamma^{\alpha}_{\mu\beta}\Gamma^{\beta}_{\alpha\nu} - \Gamma^{\alpha}_{\mu\beta}\delta\Gamma^{\beta}_{\alpha\nu}\,, \tag{2.93}$$

$$\delta\Gamma^{\mu}_{\nu\lambda} = \frac{1}{2}\delta g^{\mu\alpha}\left(g_{\alpha\nu,\lambda} + g_{\alpha\lambda,\nu} - g_{\nu\lambda,\alpha}\right) + \frac{1}{2}g^{\mu\alpha}\left(\delta g_{\alpha\nu,\lambda} + \delta g_{\alpha\lambda,\nu} - \delta g_{\nu\lambda,\alpha}\right). \tag{2.94}$$

From the condition $g_{\nu\alpha}g^{\alpha\mu} = \delta^{\mu}_{\nu}$ it follows that, at first order (i.e. drooping the quadratic terms of the perturbed quantities)

$$\delta g^{\mu\nu} = -\delta g_{\alpha\beta}\, g^{(0)\alpha\mu} g^{(0)\beta\nu}\,. \tag{2.95}$$

Here we shall assume that the perturbed fluid can also be treated as a perfect fluid, which implies that $\delta T^{ij} = 0$ if $i \neq j$. Working with mixed components for convenience

$$T^{\mu}{}_{\nu} = (\rho + p)\, u^{\mu} u_{\nu} + p \delta^{\mu}_{\nu} \tag{2.96}$$

we have

$$\delta T^{\mu}{}_{\nu} = (\delta\rho + \delta p)\, u^{\mu(0)} u_{\nu(0)} + \left(\rho^{(0)} + p^{(0)}\right)\left(u^{\mu(0)} \delta u_{\nu} + u_{\nu(0)} \delta u^{\mu}\right) + \delta p \delta^{\mu}_{\nu}\,, \tag{2.97}$$

where

$$\rho\,(\eta, \mathbf{x}) = \rho^{(0)}\,(\eta) + \delta\rho\,(\eta, \mathbf{x}) \tag{2.98}$$

$$p\,(\eta, \mathbf{x}) = p^{(0)}\,(\eta) + \delta p\,(\eta, \mathbf{x}) \tag{2.99}$$

$$u^{\mu}\,(\eta, \mathbf{x}) = u^{\mu(0)}\,(\eta) + \delta u^{\mu}\,(\eta, \mathbf{x})\ . \tag{2.100}$$

We now proceed to evaluate the velocity perturbations. The fluid 4-velocity can be written as $u^{\mu} = u^0\left(1, v^i\right)$ where $v_i = v^i = dx^i/d\eta = a dx^i/dt$ is the coordinate 3-velocity, and $u^0 = d\eta/d\tau$. Using Eq. (2.87) one obtains from the normalization condition for the 4-velocity

$$u^0 = \frac{1}{a} \frac{1}{\sqrt{1 - v^2 + 2\left(\Psi - \mathrm{w}_{i\,||} v^i + \Phi v^2 - \mathrm{h}_{ij\,||} v^i v^j\right)}}\,, \tag{2.101}$$

where $v^2 = \delta_{ij} v^i v^j$. Since the metric perturbations are assumed to be small, we may Taylor expand Eq. (2.101) to obtain

$$u^0 = \frac{1}{a\sqrt{1 - v^2}} \left[1 - \frac{\Psi - \mathrm{w}_{i\,||} v^i + \Phi v^2 - \mathrm{h}_{ij\,||} v^i v^j}{1 - v^2}\right]\,. \tag{2.102}$$

Furthermore, if the fluid is non-relativistic the quadratic terms in v can be neglected, which leads leads to

$$u^{\mu} = \left[\frac{1}{a}\left(1 - \Psi\right), \frac{v^i}{a}\right]\,, \tag{2.103}$$

$$u_{\mu} = g_{\mu\nu} u^{\nu} = \left[-a\left(1 + \Psi\right), a\left(v_i + \mathrm{w}_{i\,||}\right)\right]\ . \tag{2.104}$$

The 4-velocity in the background is $u^{\mu(0)} = \left(a^{-1}, 0, 0, 0\right)$ so, from the expansion $u^{\mu} = u^{\mu(0)} + \delta u^{\mu}$ one gets

$$\delta u^{\mu} = \left(-\frac{\Psi}{a}, u^i\right) \quad , \quad \delta u_{\mu} = \left(-a\Psi, u_i\right)\,, \tag{2.105}$$

which results in the following components of the perturbed energy-momentum tensor

$$\begin{aligned} \delta T^0{}_0 &= -\rho^{(0)}\delta \quad , \quad \delta T^i{}_0 = -\rho^{(0)}\left(1+w\right)v^i \\ \delta T^0{}_i &= \rho^{(0)}\left(1+w\right)\left(v_i + \mathrm{w}_{i\,||}\right) \quad , \quad \delta T^i{}_j = \rho^{(0)}\delta c_{\mathrm{s}}^2 \delta^i_j \end{aligned} \tag{2.106}$$

with the density contrast and the sound speed squared being defined as

$$\delta = \delta\left(\eta, \mathbf{x}\right) \equiv \frac{\rho\left(\eta,\mathbf{x}\right) - \rho^{(0)}}{\rho^{(0)}} = \frac{\delta\rho}{\rho^{(0)}}\,, \tag{2.107}$$

$$c_{\mathrm{s}}^2 \equiv \frac{\delta p}{\delta \rho}\,, \tag{2.108}$$

and $w = p^{(0)}/\rho^{(0)}$.

To compute the perturbation equations it is often convenient to decompose the perturbation fields in Fourier modes. For instance, for the density contrast one has

$$\delta\left(\eta,\mathbf{x}\right) = \frac{1}{\left(2\pi\right)^3}\int e^{i\mathbf{k}\cdot\mathbf{x}}\delta_{\mathbf{k}}\left(\eta\right)d^3k\,, \tag{2.109}$$

with the Fourier transform associated to a given comoving wavevector $\mathbf{k}$ (notice that $\mathbf{x}$ are comoving coordinates) being

$$\delta_{\mathbf{k}}\left(\eta\right) = \int e^{-i\mathbf{k}\cdot\mathbf{x}}\delta\left(\eta,\mathbf{x}\right)d^3x\,. \tag{2.110}$$

Operationally, this translates to the following substitutions of the perturbations and its derivatives

$$\delta\left(\eta,\mathbf{x}\right) \to e^{i\mathbf{k}\cdot\mathbf{x}}\delta_{\mathbf{k}}\left(\eta\right)\,, \tag{2.111}$$

$$\vec{\nabla}\delta\left(\eta,\mathbf{x}\right) \to i\mathbf{k}e^{i\mathbf{k}\cdot\mathbf{x}}\delta_{\mathbf{k}}\left(\eta\right)\,, \tag{2.112}$$

$$\nabla_i\nabla^i\delta\left(\eta,\mathbf{x}\right) \to -k^2 e^{i\mathbf{k}\cdot\mathbf{x}}\delta_{\mathbf{k}}\left(\eta\right)\,. \tag{2.113}$$

Since the equations are linear the spatial parts cancel out, and each plane wave obeys the same equations with a different comoving wavenumber. The physical scale λ_{p} of the perturbation associated to a given comoving wavenumber k evolves as $\lambda_{\mathrm{p}} = \left(2\pi/k\right)a$ in the linear regime.

2.3.3 Fixing the gauge

At the background level (described by the metric $g^{(0)}_{\mu\nu}$) comoving coordinates were defined such that observers expanding with the Universe remain at fixed coordinates. However, in the presence of perturbations $\delta g_{\mu\nu}$ we no longer have a preferred coordinate system. This amounts to say that the decomposition of the physical metric between a background plus small perturbations is, in general, not unique. However we constrain our choice of coordinate systems such that, in the limit where the perturbations vanish, the coordinates must reduce to the preferred coordinates in the unperturbed background. Hence, we consider that $g^{(0)}_{\mu\nu}$ is invariant under a general infinitesimal coordinate transformation $x^\mu \to x^\mu - \xi^\mu$ (generated by the vector field ξ^μ such that $\xi^\mu \ll 1$), while $\delta g_{\mu\nu}$ is subject to change. This class of transformations are called *gauge* transformations, and the metric perturbation is changed by

$$\delta g_{\mu\nu} \to \delta g_{\mu\nu} + \nabla_\mu \xi_\nu + \nabla_\nu \xi_\mu \,, \tag{2.114}$$

but the Riemann tensor (and, therefore, the "physics") is unaltered by the transformation. Therefore, the 4 degrees of freedom carried by the vector field ξ^μ do not correspond to any real perturbation. This gauge freedom when dealing with perturbations around a FLRW metric created a great deal of confusion in the past, as pointed out in [225, 226]. The construction of gauge invariant quantities from the four scalar functions Ψ, Φ, $\mathrm{w_s}$ and $\mathrm{h_s}$ is one way to deal with the gauge issue (see e.g. the references [223, 226]). Alternatively, one may specify a coordinate system when defining the metric perturbations (i.e. fix the gauge) by imposing the appropriate conditions on the metric and energy-momentum tensor components. In the following sections we shall introduce two of the most common gauges used in cosmological perturbation theory: the conformal Newtonian gauge (also called longitudinal gauge), and the synchronous gauge. Both of them are implemented in the publicly available `CLASS` code (see Appendix A.1), which we use to numerically solve the background cosmology and the evolution of anisotropies and inhomogeneities in several of the models explored in this thesis.

2.3.4 Conformal Newtonian gauge

This is in fact the most intuitive gauge that we can choose because it provides a direct link between the variables in relativistic perturbations and the Newtonian theory of small perturbations when we take the Newtonian gravity limit. The perturbed metric is obtained making $w_{i\,||} = h_{ij\,||} = 0$ in Eq. (2.87), so

$$ds^2 = a^2(\eta)\left[-(1+2\Psi)\,d\eta^2 + (1-2\Phi)\,\delta_{ij}dx^i dx^j\right] . \tag{2.115}$$

If the expansion of the universe is neglected (i.e. for $a = 1$) the metric describes a weak gravitational field. Here the observers are attached to the points in the unperturbed frame and will detect a velocity field of particles falling into the clumps of matter, measuring a gravitational potential. The metric perturbations Φ and Ψ are known as the Bardeen potentials. The function Φ is also called Newtonian potential since it becomes equal to the Newtonian potential perturbation in

appropriated limit; Ψ is the Newtonian curvature perturbation and determines the curvature of the spatial section at $t = \text{const}$ which are flat in the unperturbed universe.

From Eq. (2.91) we get the components of the perturbed Einstein tensor in Fourier space

$$\delta G^0{}_0 = \frac{2}{a^2}\left[3\mathcal{H}\left(\mathcal{H}\Psi + \Phi^{'}\right) + k^2\Phi\right] , \tag{2.116}$$

$$\delta G^0{}_j = -\frac{2}{a^2} ik_j \left(\Phi' + \mathcal{H}\Psi\right) , \tag{2.117}$$

$$\delta G^i{}_j = \frac{2}{a^2}\left[\left(\mathcal{H}^2 + 2\mathcal{H}^{'}\right)\Psi + \mathcal{H}\Psi^{'} + \Phi^{''} + 2\mathcal{H}\Phi^{'}\right]\delta^i_j + \frac{1}{a^2}\left[-k^2\left(\Psi - \Phi\right)\delta^i_j + \left(\Psi - \Phi\right)k^i k_j\right] , \tag{2.118}$$

where the prime stands for $^{'} = d/d\eta$ and $\mathcal{H} = a^{'}/a$ is the conformal Hubble function.

The perturbed part of the energy-momentum tensor for this gauge follows from Eqs. (2.106), so the components of Eq. (2.90) are given by

$$3\mathcal{H}\left(\mathcal{H}\Psi + \Phi^{'}\right) + k^2\Phi = -4\pi G a^2 \delta\rho, \tag{2.119}$$

$$k^2\left(\Phi^{'} + \mathcal{H}\Psi\right) = 4\pi G a^2 \left(1 + w\right)\rho^{(0)}\theta, \tag{2.120}$$

$$\Psi = \Phi, \tag{2.121}$$

$$\Phi^{''} + 2\mathcal{H}\Phi' + \mathcal{H}\Psi' + \left(\mathcal{H}^2 + \mathcal{H}^{'}\right)\Psi - \frac{k^2}{3}\left(\Psi - \Phi\right) = 4\pi G a^2 c_s^2 \delta\rho\,. \tag{2.122}$$

Here we have introduced the velocity divergence $\theta = \nabla_j v^j = ik_j v^j$. Notice that Eq. (2.121) follows from the fact that $\delta T^i{}_j = 0$ for $i \neq j$, and Eq. (2.122) is obtained by taking the trace of Eq. (2.118) and $\delta T^i{}_j$. Using the continuity equation for the perturbed energy-momentum tensor one gets a set of differential equations for the evolution of the density contrast and the velocity divergence

$$\nabla_\mu \delta T^\mu{}_0 = 0 \Rightarrow \delta_k^{'} + 3\mathcal{H}\left(c_{\rm s}^2 - w\right)\delta_k = -\left(1 + w\right)\left(\theta_k - 3\Phi^{'}\right) , \tag{2.123}$$

$$\nabla_\mu \delta T^\mu{}_j = 0 \Rightarrow \theta_k^{'} + \left[\mathcal{H}\left(1 - 3w\right) + \frac{w^{'}}{1 + w}\right]\theta_k = k^2\left(\frac{c_{\rm s}^2}{1 + w}\delta_k + \Psi\right) , \tag{2.124}$$

with the subscript k for the Fourier mode now being explicit. These equations hold individually for each fluid $T_i^{\mu\nu}$ (minimally coupled) contributing to the total $T_{\mu\nu} = \sum_i T_i^{\mu\nu}$. The system of

equations describing the scalar perturbations is then closed using Eqs. (2.119) and (2.122). We workout the result in the next section, and focus for now in the single fluid case.

Combining Eqs. (2.119), (2.120) and using $\Phi = \Psi$ one obtains the relation

$$k^2\Phi = 4\pi G a^2 \rho \left[\delta_k + 3\mathcal{H}\left(1+w\right)\frac{\theta_k}{k^2}\right] = 4\pi G a^2 \rho \delta_k^* \,, \tag{2.125}$$

where the total-matter density contrast δ_k^* is defined as

$$\delta_k^* \equiv \delta_k + 3\mathcal{H}\left(1+w\right)\frac{\theta_k}{k^2} \,. \tag{2.126}$$

Using Eqs. (2.119) and (2.122) the evolution of Φ is determined by

$$\Phi^{''} + 3\mathcal{H}\left(1+c_{\rm s}^2\right)\Phi^{'} + \left(c_{\rm s}^2 k^2 + 3\mathcal{H}^2 c_{\rm s}^2 + 2\mathcal{H}^{'} + \mathcal{H}^2\right)\Phi = 0 \,. \tag{2.127}$$

On the other hand, one may use Eq. (2.125) and the relation

$$\mathcal{H}^{'} = -\frac{1}{2}\left(1+3w\right)\mathcal{H}^2 \tag{2.128}$$

to write Eq. (2.127) as

$$\delta_k^{*''} + \mathcal{H}\left(1+3c_s^2-6w\right)\delta_k^{*'} - \left[\frac{3}{2}\mathcal{H}^2\left(1-6c_s^2-3w^2+8w\right) - c_s^2 k^2\right]\delta_k^* = 0 \,, \tag{2.129}$$

describing the evolution of $\delta_k^*\left(\eta\right)$.

2.3.5 Synchronous gauge

The synchronous gauge was first introduced by Lifshitz in 1946 [217] and is defined by the conditions $\Psi = w_{i\,||} = 0$, so the perturbed line element is

$$ds^2 = a^2\left(\eta\right)\left\{-d\eta^2 + \left[\left(1-2\Phi\right)\delta_{ij} + 2\mathrm{h}_{ij\,||}\right]dx^i dx^j\right\} \,. \tag{2.130}$$

With this gauge choice the conformal time η coincide with the proper time and observers following geodesics do not change their spacial coordinates (they only move along η-threads), so the coordinates in synchronous gauge are Lagrangian coordinates and the observers are attached to the perturbed particles. This implies that large density perturbations will deform the coordinate lines giving rise to caustic formation (singularities). Since this problem is only noticeable when perturbations grow large enough, the synchronous gauge can be safely used in the linear regime ($\left|\delta\rho/\rho^{(0)}\right| \ll 1$) [227].

We have the components of the perturbed Einstein tensor (from Eq. (2.91)) in the synchronous gauge

$$\delta G^0{}_0 = \frac{1}{a^2}\left[2k^2\left(\Phi - \frac{\mathrm{h_s}}{3}\right) + 6\mathcal{H}\Phi'\right], \tag{2.131}$$

$$\delta G^0{}_j = -\frac{2ik_j}{a^2}\Phi', \tag{2.132}$$

$$\delta G^i{}_j = \frac{1}{a^2}\left[2\Phi'' + k^2\Phi + 4\mathcal{H}\Phi' + \frac{1}{3}\left(\mathrm{h_s}'' + 2\mathcal{H}\mathrm{h_s}' - k^2\mathrm{h_s}\right)\right]\delta^i_j - \tag{2.133}$$

$$-\frac{k^i k_j}{a^2}\left[\Phi - \frac{1}{3}\mathrm{h_s} + \frac{1}{k^2}\left(\mathrm{h_s}'' + 2\mathcal{H}\mathrm{h_s}'\right)\right], \tag{2.134}$$

while components of the perturbed Einstein equation for n minimally coupled perfect fluids read

$$k^2\left(\Phi - \frac{\mathrm{h_s}}{3}\right) + 3\mathcal{H}\Phi' = -4\pi G\sum_i \delta\rho_i\,, \tag{2.135}$$

$$k^2\left(\Phi' - \frac{\mathrm{h_s}'}{3}\right) = 4\pi G a^2\sum_i \rho_i^{(0)}\left(1+w_i\right)\theta_i\,, \tag{2.136}$$

$$\mathrm{h_s}'' + 2\mathcal{H}\mathrm{h_s}' - k^2\left(\Phi - \frac{\mathrm{h_s}}{3}\right) = 0\,, \tag{2.137}$$

and

$$3\Phi'' + 6\mathcal{H}\Phi' + k^2\left(\Phi - \frac{\mathrm{h_s}}{3}\right) = 12\pi G a^2\sum_i \delta p_i\,, \tag{2.138}$$

where the sum on i goes over all n fluid components in the model. The corresponding equations determining the evolution of δ_k (from $\nabla_\mu \delta T^\mu{}_0 = 0$) and θ_k (from $\nabla_\mu \delta T^\mu{}_j = 0$) for each fluid i are given by

$$\delta_k' + 3\mathcal{H}\left(c_\mathrm{s}^2 - w\right)\delta_k + (1+w)\left(\theta_k - 3\Phi_k'\right) = 0\,, \tag{2.139}$$

and

$$\theta_k' + \mathcal{H}\left(1 - 3c_s^2\right)\theta_k - \frac{c_\mathrm{s}^2 k^2}{1+w}\delta_k = 0\,. \tag{2.140}$$

Combining Eqs. (2.135) and (2.138) we determine the evolution of Φ

$$\Phi'' + \mathcal{H}\Phi' - \frac{1}{2}\mathcal{H}^2\sum_i\left(1 + 3c_{\mathrm{s},i}^2\right)\Omega_i\delta_i = 0\,, \tag{2.141}$$

closing the system of equations describing the scalar perturbations.

2.3.6 Statistical description of the density field

Linear perturbation theory is not expected to predict the exact value of the density contrast field at some particular time and location. Hence, we got to rely on a statistical treatment to compare the predictions of the theory with observations. Usually one assumes that the density contrast is a random field with its statistical properties being determined from a distribution function. In this regard, a useful descriptor is the two-point correlation function

$$\xi\left(r\right)=\left\langle \delta\left(\mathbf{x}\right)\delta\left(\mathbf{x}+\mathbf{r}\right)\right\rangle \,, \tag{2.142}$$

where $\mathbf{r}$ is the vector distance and $r=|\mathbf{r}|$. Note that statistical homogeneity forces the correlation function to depend only on $\mathbf{r}$ i.e. that the statistical properties of the field do not change under a spatial translation. Moreover, statistical isotropy ensures that $\xi\left(r\right)$ depends only on the norm of $\mathbf{r}$. The angle brackets in Eq. (2.142) indicate that the average is taken over all realizations of the field, being also known as the ensemble average. In practice, cosmological observations can only measure one realization of the density field (corresponding to the particular realization in our Universe). However, one may assume that sufficiently large and independent volumes have similar statistical properties (i.e. that these regions represent a fair sample of the Universe), so that measurements of the field on these different volumes can be considered as measurements of independent realizations. In other words, the sample average coincides with the ensemble average, an assumption known as the ergodicity hypothesis. Writing the two-point correlation function in Fourier space one has

$$\begin{aligned}
\left\langle \delta_{\mathbf{k}}\delta_{\mathbf{k}'}^{*}\right\rangle &= \left\langle \int d^{3}x\delta\left(\mathbf{x}\right)e^{i\mathbf{k}\cdot\mathbf{x}}\int d^{3}x'\delta\left(\mathbf{x}'\right)e^{-i\mathbf{k}'\cdot\mathbf{x}'}\right\rangle & (2.143)\\
&= \int d^{3}xe^{i\mathbf{k}\cdot\mathbf{x}}\int d^{3}re^{-i\mathbf{k}'\cdot\left(\mathbf{x}+\mathbf{r}\right)}\left\langle \delta\left(\mathbf{x}\right)\delta\left(\mathbf{x}+\mathbf{r}\right)\right\rangle & (2.144)\\
&= \int d^{3}xe^{i\left(\mathbf{k}-\mathbf{k}'\right)\cdot\mathbf{x}}\int d^{3}r\xi\left(r\right)e^{-i\mathbf{k}'\cdot\mathbf{r}} & (2.145)\\
&= \left(2\pi\right)^{3}\delta_{\mathrm{D}}\left(\mathbf{k}-\mathbf{k}'\right)P\left(k\right)\,, & (2.146)
\end{aligned}$$

where

$$\delta_{\mathrm{D}}\left(\mathbf{k}-\mathbf{k}'\right)=\frac{1}{\left(2\pi\right)^{3}}\int d^{3}xe^{i\left(\mathbf{k}-\mathbf{k}'\right)\cdot\mathbf{x}} \tag{2.147}$$

is the Fourier transform of the Dirac's delta and, since the density contrast is a real field, we have used $\delta_{\mathbf{k}}^{*}=\delta_{-\mathbf{k}}$ (the star indicates complex conjugation). The quantity $P\left(k\right)$ depends only on $k=|\mathbf{k}|$, and it is usually called the power spectrum of the field, being defined as the Fourier transform of the correlation function

$$P\left(k\right)=\int d^{3}r\xi\left(r\right)e^{-i\mathbf{k}'\cdot\mathbf{r}}\,. \tag{2.148}$$

Standard inflation models predict a Gaussian distribution for the primordial density field, as well as a power law for the primordial power spectrum $P_i(k) = A_s k^{n_s}$, where n_s is the spectral index and A_s is the amplitude. Notice that, for a linear evolution, the density field preserves the initial statistical distribution, and remains Gaussian at any later time. Thus, the statistics of the linear density contrast field is completely characterized by its correlation function or, equivalently, by its power spectrum. The primordial power spectrum is then modified by the evolution of linear density perturbations as

$$P(k,\eta) = |\delta_k|^2 T^2(k) P_i(k) \,, \tag{2.149}$$

where $T(k)$ is the transfer function, which enable us to process the primordial power spectrum from the radiation era to late times using linear theory. In general, we shall use the Boltzmann code `CLASS` to compute the power spectrum for the models that are discussed in this thesis.

While the shape of the primordial power spectrum can be fixed by Inflation theory, its initial amplitude is not specified and has to be fixed by observations at a certain scale. The usual way to do this normalization is through the variance in the smoothed density field. Let us start by writing the variance of the field

$$\sigma^2 = \left\langle \delta(\mathbf{x})^2 \right\rangle - \langle \delta(\mathbf{x}) \rangle^2 = \frac{1}{(2\pi)^3} \int d^3k P(k) \,, \tag{2.150}$$

where $\langle \delta(\mathbf{x}) \rangle = 0$ by definition (as the density contrast is a random field). One can then define a parameter $\sigma_{\rm R}$ as a weighted average

$$\sigma_R^2 = \frac{1}{(2\pi)^3} \int d^3k P(k) W^2(k,R) = \frac{1}{2\pi^2} \int_0^\infty P(k) W^2(k,R) k^2 dk \,, \tag{2.151}$$

with $W(k,R)$ being a window function. A typical choice is to consider a spherical top-hat filter $W_{\rm hat}(x,R)$ in real space, such that it assigns a constant weight for $x < R$ and a zero weight for $x > R$. The Fourier transform of this filter is given by

$$W_{\rm hat}(k,R) = \int d^3x W_{\rm hat}(x,R) e^{-i\mathbf{k}\cdot\mathbf{x}} = 3\frac{\sin(kR) - kR\cos(kR)}{(kR)^3} \,. \tag{2.152}$$

One can fix the amplitude of the power spectrum from Eq. (2.151) once σ_R is known, the usual choice for the normalization being $R = 8\,h^{-1}\,$Mpc.

Chapter 3

UDE: Perfect fluid models

3.1 Single dark fluid hypothesis

The dark sector can be defined, to a good approximation, as the cosmological content that couples only through gravity with the fields of the standard model of particle physics — despite the experimental efforts to detect signatures of possible interactions via any of the other three fundamental forces, so far its presence has been inferred only gravitationally. Within the standard cosmological model, which assumes General Relativity and the Cosmological Principle, the dark sector is separated into two components: CDM, and a cosmological constant. This is however, a quite circumstantial assumption; historically, CDM was required to account for the observed dynamics of galaxies and clusters of galaxies well before the first evidence for the late accelerated expansion of the Universe. As it turns out, such decomposition into two independent components is not even unique.

To make it more concrete, let us define the energy-momentum tensor associated to the dark sector as

$$T_{\mu\nu}^{(\mathrm{dark})} = \frac{1}{8\pi G} G_{\mu\nu} - T_{\mu\nu}^{(\mathrm{visible})} \,, \tag{3.1}$$

being $T_{\mu\nu}^{(\mathrm{visible})}$ the energy-momentum tensor of the content which can be observed directly (i.e. through the detection of photons). Gravity alone is only sensitive to the total $T_{\mu\nu}^{(\mathrm{dark})}$ and, therefore, can not discriminate the number of individual components that comprise the dark sector. This remark was first made in [228], being further explored in [229–231], and it has become known as the *dark degeneracy* (see also [232–235]). In general this degeneracy could be broken if, for instance, dark matter particles [236] or a dark energy field [237] were directly detected in laboratory experiments. However, as we have mentioned above, up until now no conclusive evidence for a non-minimal coupling between these dark entities and standard model particles has been found [109,238].

Our ignorance of the fundamental nature of $T_{\mu\nu}^{(\mathrm{dark})}$ precludes a definitive answer regarding the number of dark components. Thus, even if dark matter and dark energy manifest differently at

the macroscopic level, there is still the possibility that they may share a common origin. Unified Dark Energy (UDE) models are built upon the hypothesis that the entire dark sector can be characterized by a single fluid or field. The first definite prototype of a UDE model, known as the Chaplygin gas [239], is able to mimic matter and a cosmological constant, depending on the value that its local density takes. Such unification scenarios can be achieved in several ways and were extensively explored in the literature: these include generalizations to the Chaplygin gas equation of state [160–162,240–250], k-essence models [251,252], tachyon fields [253–255], logotropic fluids [163,256], UDE models with a fast transition [257,258], and even a negative mass fluid [259].

In this thesis we shall mainly focus our attention on UDE isentropic perfect fluids, with an equation of state of the form $p = p(\rho)$ or, under suitable conditions (that we shall discuss in more detail in chapter 4), by a real scalar field ϕ whose dynamics is described by a purely kinetical Lagrangian $\mathcal{L}(X)$, where $X = -\nabla^{\mu}\phi\nabla_{\mu}\phi/2$.

3.2 The Chaplygin gas

The Chaplygin gas (CG), pioneered in a cosmological context by Alexander Kamenshchik and collaborators [239], is defined as a perfect fluid obeying the following barotropic equation of state

$$p_{\mathrm{cg}} = -\frac{A}{\rho_{\mathrm{cg}}}\,, \tag{3.2}$$

where A is a positive constant. An interesting generalization of Eq. (3.2), known as the Generalized Chaplygin gas (GCG), was proposed in [240]

$$p_{\mathrm{gcg}} = -\frac{A}{\rho_{\mathrm{gcg}}^{\alpha}}. \tag{3.3}$$

The additional parameter α is usually assumed to lie in the range $0 \leq \alpha \leq 1$. As we shall discuss later, negative values of α lead to instabilities associated with imaginary sound speeds, whereas $\alpha > 1$ would imply a maximum sound speed greater than the speed of light.

It is noticeable from Eq. (3.3) that the GCG approximates the behavior of a pressureless fluid for sufficiently large values of the energy density i.e. $p_{\mathrm{gcg}} \to 0$ as $\rho_{\mathrm{gcg}} \to \infty$. On the other hand, since the pressure is always negative for any $A > 0$ and $\rho_{\mathrm{gcg}} > 0$, the condition for an accelerated expansion (i.e. $q > 0$) can be realized if the energy density is low enough.

3.2.1 Background dynamics

From the continuity equation given in Eq. (2.63), one may determine the evolution of the energy density of the GCG with the scale factor. The differential equation

$$\frac{d\rho_{\mathrm{gcg}}}{da} = -\frac{3}{a}\rho_{\mathrm{gcg}}\left(1 + w_{\mathrm{gcg}}\right) \tag{3.4}$$

admits the analytical solution

$$\rho_{\rm gcg}\left(a\right)=\rho_{\rm gcg0}\left[\overline{A}+\left(1-\overline{A}\right)a^{-3(1+\alpha)}\right]^{\frac{1}{1+\alpha}}\,, \tag{3.5}$$

where $\overline{A}=A/\rho_{\rm gcg0}^{1+\alpha}$. Hence, the equation of state parameter as a function of the scale factor is given by

$$w_{\rm gcg}=-\frac{\overline{A}}{\overline{A}+\left(1-\overline{A}\right)a^{-3(1+\alpha)}}\,, \tag{3.6}$$

and its value at the present is simply $w_{\rm gcg0}=-\overline{A}$. As the Universe expands, the GCG model interpolates from a matter state ($w_{\rm gcg}\sim 0$) at early times

$$\rho_{\rm gcg}\approx\rho_{\rm gcg0}\left(1-\overline{A}\right)^{\frac{1}{1+\alpha}}a^{-3}\quad\text{for}\quad a\ll\left(\frac{\overline{A}}{1-\overline{A}}\right)^{-\frac{1}{3(1+\alpha)}}\,, \tag{3.7}$$

to a dark energy state at later times, asymptotically approaching a cosmological constant at sufficiently late times ($w_{\rm gcg}\sim -1$)

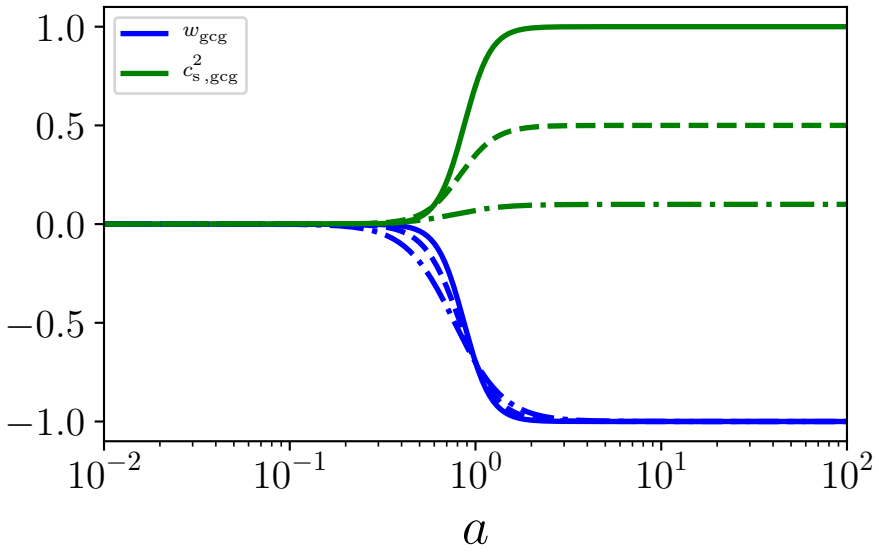

Figure 3.1: The equation of state parameter $w_{\rm gcg}$ (blue lines) and the sound speed squared $c^2_{\rm s,gcg}$ (green lines) as a function of the scale factor a, with $\overline{A}=0.7$. The different line styles correspond to the choices $\alpha=1$ (solid line), $\alpha=0.5$ (dashed line) and $\alpha=0.1$ (dotted-dashed line).

$$\rho_{\rm gcg}\approx\rho_{\rm gcg0}\overline{A}^{\frac{1}{1+\alpha}}\quad\text{for}\quad a\gg\left(\frac{\overline{A}}{1-\overline{A}}\right)^{-\frac{1}{3(1+\alpha)}}\,, \tag{3.8}$$

as depicted in Fig. 3.1 (blue lines). Hence, the value

$$a_{\rm tr}=\left(\frac{\overline{A}}{1-\overline{A}}\right)^{-\frac{1}{3(1+\alpha)}}\,, \tag{3.9}$$

defines the transition scale factor between both regimes (i.e. when $w_{\rm gcg} = -0.5$). The limiting vacuum-like state for $a \to \infty$ means that the GCG energy density has a non-zero minimum value, set by the model parameters A and α.

Considering that the background dynamics is dominated by a GCG fluid, the transition between a decelerating and an accelerating regime occurs when

$$a_{q=0} = \left(\frac{1 - \overline{A}}{2\overline{A}} \right)^{\frac{1}{3(1+\alpha)}} . \tag{3.10}$$

Therefore, the condition for an accelerated expansion at the present time driven by the GCG fluid can only be met if $\overline{A} > 1/3$ (note that, given any $\alpha \geq 0$, the GCG behaves essentially as CDM for $\overline{A} = 0$, and as a cosmological constant for $\overline{A} = 1$). From Fig. 3.1 one may also note that the steepness of the GCG equation of state parameter function $w_{\rm gcg}(a)$ interpolating from $w_{\rm gcg} \sim 0$ to $w_{\rm gcg} \sim -1$ is sensitive to the value of α, the transition being faster for larger values of α. Models that enter an accelerated epoch at earlier times also experience a quicker transition. Eq. (3.10) shows that the scale factor at which the background starts to accelerate is mostly influenced by $\overline{A}$, higher values of $\overline{A}$ corresponding to models with lower $a_{q=0}$.

Another interesting (and convenient) property of the GCG is that of being completely degenerate with the ΛCDM model for $\alpha = 0$. Indeed, it is clear that from Eq. (3.5) and fixing $\alpha = 0$ we recover the same background evolution

$$\rho_{\rm gcg}(a) = \rho_{\rm gcg0} \left[\overline{A} + \left(1 - \overline{A}\right) a^{-3} \right] , \tag{3.11}$$

once we make the following identifications: $\rho_\Lambda = \rho_{\rm gcg0}\overline{A}$ and $\rho_{\rm cdm0} = \rho_{\rm gcg0}\left(1 - \overline{A}\right)$ (in a Universe dominated by the GCG these would simply be $\Omega_\Lambda = \overline{A}$ and $\Omega_{\rm cdm0} = 1 - \overline{A}$). This equivalence between the GCG in the $\alpha = 0$ limit and the ΛCDM model holds not only at the background level, but at any order [260].

3.2.2 SNIa constraints

We use the Pantheon SNIa compilation [261] (see Appendix B.1 for further details) to place constraints on the GCG parameters $\overline{A}$ and α, assuming flat priors in the interval $[0, 1]$ for both parameters. We consider a Universe containing baryons and a GCG fluid, so the Friedmann equation for our model is

$$H^2 = H_0^2 \left\{ \Omega_{\rm b0} a^{-3} + \Omega_{\rm gcg0} \left[\overline{A} + \left(1 - \overline{A}\right) a^{-3(1+\alpha)} \right] \right\} , \tag{3.12}$$

where $H_0 = 67.3\,{\rm km\,s^{-1}\,Mpc^{-1}}$, $\Omega_{\rm b0} = 0.0487$ and $\Omega_{\rm gcg0} = 1 - \Omega_{\rm b0}$ (the radiation component is negligible for the background dynamics at $z \sim 1 - 2$). The absolute magnitude $\mathcal{M}$ is taken as a nuisance parameter in the luminosity distance estimate. Since H_0 is degenerate with $\mathcal{M}$, the specific value of the Hubble constant is irrelevant for the obtained SNIa constraints (the uncertainty on $\mathcal{M}$ is marginalized).

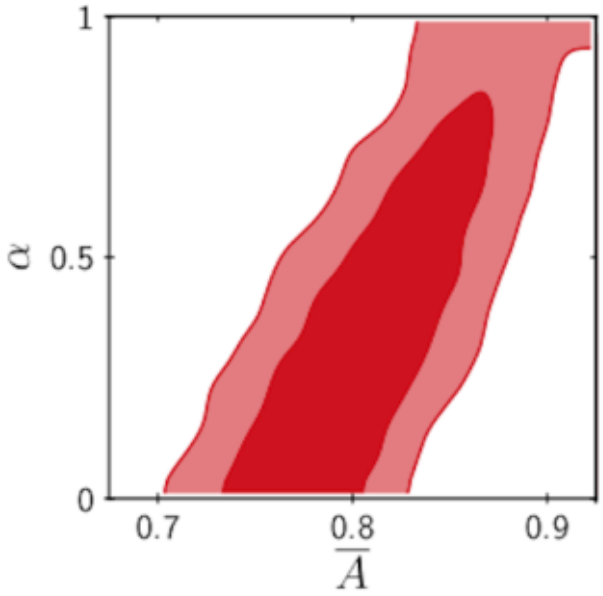

Figure 3.2: Pantheon SNIa data constraints for the GCG parameters $\overline{A}$ and α. Darker and lighter regions correspond to the 1σ and 2σ confidence level, respectively. For the analysis we consider a cosmology with $\Omega_{\rm gcg} + \Omega_{\rm b} = 1$ where $\Omega_{\rm b0} = 0.0487$ (the radiation component can be safely ignored in the analysis).

The 1σ (darker red) and 2σ (lighter red) confidence regions are shown in Fig. 3.2. After marginalizing over α, the parameter $\overline{A}$ is restricted to $0.713 < \overline{A} < 0.845$ at a 95% level; α, on the other hand, is not so well constrained by the data. Since the luminosity distance depends on a double integration of $w_{\rm gcg}(z)$ over some redshift (or scale factor) interval, SNIa measurements are mostly sensitive to an effective $w_{\rm gcg}$ (which strongly depends on $\overline{A}$, see Eq. (3.6)), and not so much to its time variation [262].

The combination $(\overline{A}, \alpha, \mathcal{M})$ for the best-fit has a minimum χ^2 of 1027. Although the original Chaplygin gas model lies outside the 1σ region, a separate run with $\alpha = 1$ gives a similar goodness of fit (considering the number of SNIa data points of $\sim 10^3$ and the fact that it has one free parameter less), with $\chi^2_{\rm min} = 1029$. Regarding the ΛCDM limit of the GCG model (i.e. $\alpha = 0$), one may find the corresponding $\overline{A}$ using Ω_Λ (or $\Omega_{\rm cdm0}$) as mentioned in the previous subsection. Taking the conservative estimate $\Omega_\Lambda \approx 0.7$ for the cosmological constant density, the resulting value $\overline{A} = \Omega_\Lambda / (1 - \Omega_{\rm b0}) \approx 0.74$ is found the be within the derived 1σ limits.

3.2.3 Evolution of linear density perturbations

Due to a smooth transition from a matter state at early times to a present epoch of accelerated expansion, the GCG model is compatible with SNIa data for a wide range of α. In this regard, a GCG equation of state is able to mimic both dark matter and dark energy at the background level. However, if it is to be considered as a viable alternative to CDM, one would expect the GCG to also account for the observed large scale structures in the Universe.

As discussed in Sec. 2.3, a fundamental quantity in linear perturbation theory is the sound speed

(introduced in Eq. (2.108)) which relates the pressure and energy density perturbations. In the case of a barotropic fluid the pressure depends on ρ alone, so one has

$$c_{\rm s}^2 \equiv \frac{\delta p}{\delta \rho} = \frac{dp}{d\rho}\,. \tag{3.13}$$

Taking Eqs. (3.13) and (3.3), one finds that the sound speed squared associated to the GCG model is given by

$$c_{\rm s[gcg]}^2 = \alpha \frac{A}{\rho_{\rm gcg}^{1+\alpha}} = -\alpha w_{\rm gcg}\,. \tag{3.14}$$

If the GCG has a matter like evolution, then $c_{\rm s[gcg]}^2 \sim 0$ irrespectively of the value of α. With the background transition to a dark energy state, $w_{\rm gcg}$ approaches -1, so the sound speed squared is bounded by α. This behavior can be seen in Fig. 3.1, where we plot $c_{\rm s[gcg]}^2$ (green lines) as a function of the scale factor, considering three values of α ($\alpha = 1$, 0.5 and 0.1, corresponding to the solid, dashed and dotted-dashed lines, respectively). For the original CG, the maximum sound speed attained as $w_{\rm gcg} \to -1$ equals the speed of light i.e. $c_{\rm s[gcg]}^2 = 1$. If $\alpha = 0$ (corresponding to the ΛCDM limit) then $c_{\rm s[gcg]}^2 = 0$ at all times, while for $\alpha < 0$ the GCG admits negative values of the sound speed squared.

To study the evolution of linear density perturbations with a comoving wavenumber k in a Universe dominated by a GCG fluid, on scales much smaller than the horizon (i.e. $k \gg aH$) we may use Eq. (2.129)

$$\ddot{\delta}_{\rm gcg} + \left(2 + 3c_{\rm s[gcg]}^2 - 6w_{\rm gcg}\right) H\dot{\delta}_{\rm gcg} - \left[\frac{3}{2}H^2\left(1 - 6c_{\rm s[gcg]}^2 - 3w_{\rm gcg}^2 + 8w_{\rm gcg}\right) - \left(\frac{c_{\rm s[gcg]}k}{a}\right)^2\right]\delta_{\rm gcg} = 0\,. \tag{3.15}$$

Here the derivatives of $\delta_{\rm gcg}$ are taken in order to the cosmic time (note that we consider conformal time in the derivation of Eq. (2.129)). Before analyzing Eq. (3.15) with all generality, let us first briefly examine how the sign of the sound speed affects the evolution of the density fluctuations in the absence of gravity. Neglecting the effect of the cosmic expansion (effectively taking the Minkowski limit $H \to 0$ and fix $a = 1$) Eq. (3.15) reduces to

$$\ddot{\delta}_k + c_{\rm s}^2 k^2 \delta_k = 0\,. \tag{3.16}$$

Substituting the ansatz $\delta_k \propto \exp(\lambda t)$ it is a simple matter to show that δ_k admits an oscillatory solution for $c_{\rm s}^2 > 0$, while if $c_{\rm s}^2 < 0$ the solution is composed by a growing mode $\delta_k \propto \exp(c_{\rm s} k t)$ and a decaying mode $\delta_k \propto \exp(-c_{\rm s} k t)$. The decaying solution quickly becomes irrelevant with respect to the growing one, so it can be safely neglected[1].

Considering now the full equation for the evolution of linear perturbations one finds that Eq. (3.15)

[1] Throughout this thesis we will consistently ignore decaying solutions.

admits a growing solution provided that

$$|c^2_{\mathrm{s[gcg]}}| \lesssim \frac{3}{2}\left(\frac{aH}{k}\right)^2 . \tag{3.17}$$

The non-null sound speed sets a characteristic length defining the stability criteria for the perturbations

$$\lambda_{\mathrm{J}} = |c_{\mathrm{s}}|\sqrt{\frac{\pi}{G\rho}}\,, \tag{3.18}$$

being known as the Jeans length [216]. Therefore, for physical scales $\lambda_{\mathrm{p}} = (2\pi/k)\,a$ larger than $\lambda_{\mathrm{J[gcg]}}$, linear density perturbations can grow via the gravitational instability. In contrast, if $\lambda_{\mathrm{p}} < \lambda_{\mathrm{J[gcg]}}$ and $c_{\mathrm{s[gcg]}} > 0$ the density fluctuations oscillate and inhomogeneities do not grow due to pressure support. On the other hand if $c_{\mathrm{s[gcg]}} < 0$ the GCG density perturbations on physical scales smaller than the Jeans length are exponentially unstable. Note that, since the Jeans length gets smaller for higher energy densities, smaller scales may become gravitationally unstable at earlier times (remember that at the background level $\rho_{\mathrm{gcg}} \to \infty$ as $a \to 0$). Regarding the particular $\alpha = 0$ case, the linear sound speed and the Jeans length are identically zero at all times.

Hence, as the sound speed starts to deviate from zero with the transition to a dark energy state, the condition given in Eq. (3.17) can only be met on ever larger scales. Using Eq. (3.17) one may estimate the upper bound

$$|\alpha| \lesssim 10^{-5}\,, \tag{3.19}$$

where we take $w_{\mathrm{gcg}} = -1$, $H_0 = h/3000\ \mathrm{Mpc}^{-1}$ and $k = 0.1\ h\ \mathrm{Mpc}^{-1}$ (i.e., a comoving scale firmly in the linear regime).

3.2.4 The GCG power spectrum

To compute the linear GCG power spectrum, here we shall consider the fitting form of Bardeen, Bond, Keiser and Szalay (BBKS) transfer function [263]

$$T\,(k) = \frac{\ln\left(1+2.34\frac{k}{\Gamma}\right)}{2.34\frac{k}{\Gamma}}\left[1+3.89\frac{k}{\Gamma}+\left(16.1\frac{k}{\Gamma}\right)^2+\left(5.46\frac{k}{\Gamma}\right)^3+\left(6.71\frac{k}{\Gamma}\right)^4\right]^{-1/4}, \tag{3.20}$$

where k is given in units of $h^{-1}\,\mathrm{Mpc}$ and the coefficient $\Gamma = \Omega_{\mathrm{m0}}h$ is the shape parameter. In this way, one takes into account the stagnation period of the GCG perturbations during the radiation era for scales inside the Hubble radius (due to the Mészáros effect[2]) to process the primordial power spectrum. In order to solve numerically Eq. (3.15) we use the independent variable $y = \ln(a)$

[2]Even if CDM (or, in our case, the GCG) does not couple to photons, the rate of expansion during the radiation era prevents the gravitational collapse. However, this effect is not experienced for perturbations on scales larger than the Hubble radius at the matter radiation equality (only during the matter era they become smaller than the Hubble radius).

instead of t. Then, one may rewrite Eq. (3.15) as

$$\frac{d^2\delta_{\rm gcg}}{dy^2}+\left(2+\zeta-6w_{\rm gcg}+3c^2_{\rm s[gcg]}\right)\frac{d\delta_{\rm gcg}}{dy}-\left[\frac{3}{2}\left(1-6c^2_{\rm s[gcg]}+8w_{\rm gcg}-3w^2_{\rm gcg}\right)-c^2_{\rm s[gcg]}\left(\frac{k}{aH}\right)^2\right]\delta_{\rm gcg}=0\,, \tag{3.21}$$

with $\zeta=-3\left(1+w_{\rm gcg}\right)/2$. Since we consider small values of α, we fix $\overline{A}=1-\Omega_{\rm m0}$ for $\Omega_{\rm m0}=0.315$. Eq. (3.21) is numerically solved for each k from $a=10^{-2}$ up to $a=1$, starting with a set of normalized initial conditions. Combining these solutions at $a=1$ with Eq. (3.20) one gets the linear GCG power spectrum from Eq. (2.149), where we take $n_{\rm s}=0.96$ and the spectra is normalized such that $\sigma_8=0.83$

In Fig. 3.3 we plot the predicted linear GCG power spectra for values of α close to the bound given in Eq. (3.19). Indeed, if $|\alpha|\gtrsim 10^{-5}$ the power spectra on linear scales start to deviate significantly relatively to the ΛCDM result, showing fast oscillations on smaller scales (corresponding to fluctuations on physical scales bellow $\lambda_{\rm J}$). Note that we also show in Fig. 3.3 models with $\alpha=-10^{-4}$ and $\alpha=-10^{-5}$ (solid blue and green lines, respectively), for which $c^2_{\rm s[gcg]}<0$. The GCG is well behaved for small k, giving rise to a ΛCDM-like matter power spectrum on linear scales if $|\alpha|\gtrsim -10^{-5}$. However, in these cases the density fluctuations are exponentially unstable on small scales, and the GCG power spectra blows up, unless if α is close enough to zero.

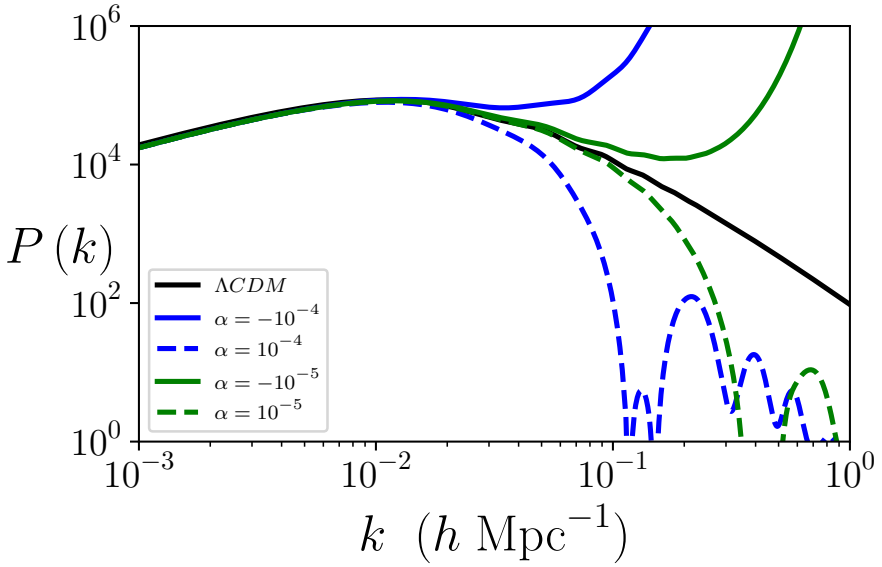

Figure 3.3: The present linear GCG power spectra for $\alpha=0$ (black line), $|\alpha|=10^{-5}$ (green lines) and $|\alpha|=10^{-4}$ (blue lines). The amplitude of the power spectrum is normalized such that all models agree on very large scales. Deviations with respect to the ΛCDM model on linear scales (i.e. $k\lesssim 0.1\ h\ \mathrm{Mpc}^{-1}$) are significant if $|\alpha|\gtrsim 10^{-5}$.

3.2.5 Matter power spectrum constraints: GCG + baryons

By comparing the theoretically predicted GCG matter power spectrum against that observed with the 2dF Galaxy Redshift Survey [264,265], the work [266] strongly constrained the value of α to be

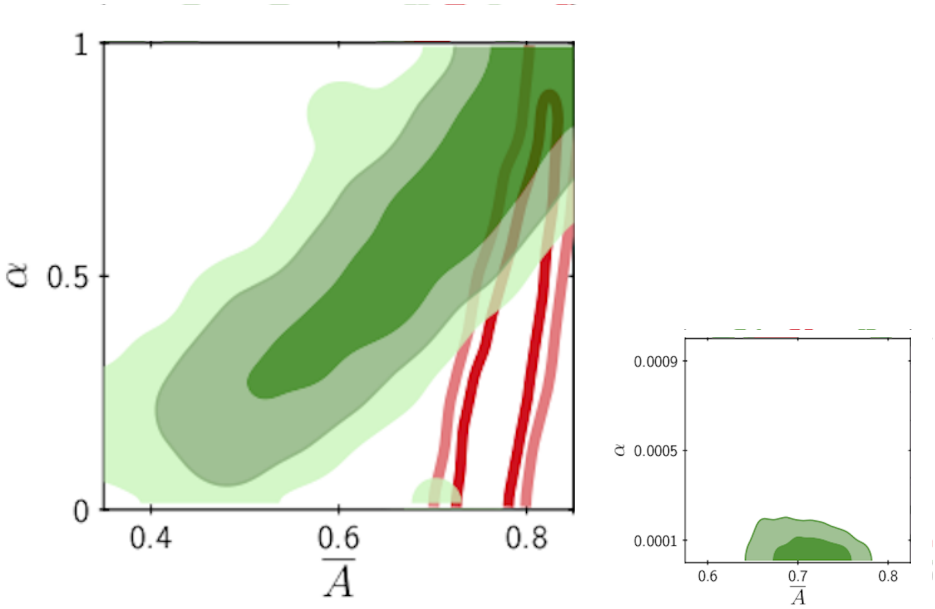

Figure 3.4: Left: GCG observational constraints in the $(\alpha, \overline{A})$ plane (the other free parameters being marginalized). The constraints coming from large scale structure data (SDSS DR7) are shown by the green regions (darker areas correspond to points with an higher likelihood). The SNIa constraints (Pantheon) presented in Sec. 3.2.2 are shown by the red contours. Right: 1σ and 2σ confidence regions for values of α very close to zero that are allowed by the observations (corresponding to the ΛCDM limit).

very close to zero. Taken at face value, such result imply that the GCG model would have to behave essentially as ΛCDM. However, the analysis made in [266] relies on the simplifying assumption of a cosmology in the absence of baryons. By having a very small sound speed, baryons can still keep the growth of inhomogeneities when the density fluctuations of the GCG start to decay. Therefore, the influence of baryons on structure formation should not be ignored. If one considers the contribution of the baryonic density fluctuations to the matter power spectrum, any value of α in the range $[0, 1]$ is consistent with the 2dF Galaxy Redshift Survey data within 3σ, as reported in [160].

Following the same reasoning, we have obtained similar results to [160], though here we use a different (and slightly more recent) matter power spectrum data set from the SDSS DR7 [267] (see Appendix B.2), and the matter power spectrum is obtained from our implementation in `CLASS` (see Appendix A.1). Flat priors for α and $\overline{A}$ have been assumed (between $[0, 1]$); h and A_s (the power spectrum amplitude) are also left free in the analysis, with the priors being $[0.6, 0.8]$ and $\left[10^{-11}, 6 \times 10^{-9}\right]$, respectively. The observational constraints in the $(\alpha, \overline{A})$ parameter space are shown in Fig. 3.4, with the uncertainties on h and A_s being marginalized. Notice that there are two disjoint green regions in the left plot, with the largest one showing that a good fit to the data is possible for wide range of values of α, in particular $\alpha = 1$. The very small region around $\alpha \sim 0$ and $\overline{A} \sim 0.75$ correspond to the ΛCDM limit of the GCG. Due to the lack of resolution of this tiny area on the global constraints, we ran a separate MCMC analysis focusing on small values of α (see right plot in Fig. 3.4). The overlap of the green regions with the SNIa contours show that both the original CG proposal (i.e. $\alpha = 1$) and the ΛCDM give an equally good fit to the data.

However, the large region is only possible for small values of σ_8 and A_s (see Fig. 3.5), which can be ruled out if combined with CMB data. On the other hand, the small region for small values of α (corresponding to the ΛCDM limit) is compatible with all SNIa+WL+CMB probes combined. These conclusions are consistent with the analysis presented in [245].

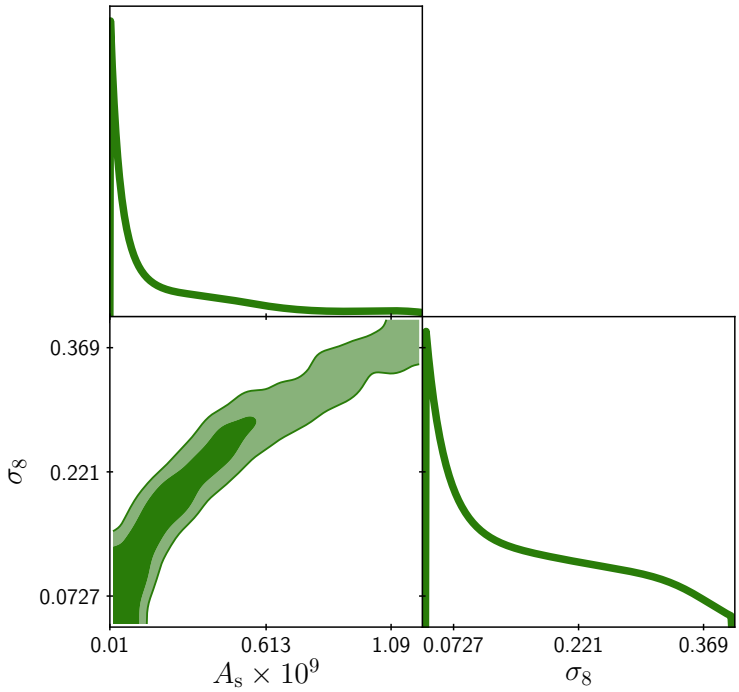

Figure 3.5: GCG observational constraints in the (σ_8, A_s) plane (the other free parameters being marginalized) obtained from large scale structure data (SDSS DR7) corresponding to the large region in Fig. 3.4.

Notwithstanding the obvious importance of considering baryons in the matter power spectrum analysis, CMB constraints are able to impose stringent limits on the GCG model [243, 245, 248, 268, 269] (particularly on large angular scales [246, 252]), forcing α close to zero. Beware that this result only applies as long as linear perturbation theory is a valid approximation for large scales. As we shall discuss in more detail in chapter 6, the usual linear treatment is not enough to characterize all the relevant physics, neglecting the potential effect that inhomogeneities have on the cosmological evolution of the GCG and, in general, on other UDE models. Hence, a more careful analysis may significantly change the results that we have discussed in this section.

3.2.6 Logarithmic limit of the GCG model

So far, when taking the $\alpha \to 0$ limit of the GCG, a finite $A > 0$ was always implicitly assumed. As we have mentioned, in this limit the GCG is completely equivalent to the ΛCDM model. However, a regularization of the limit ($\alpha \to 0\,,\ A \to \infty$) leads to a model with a logarithmic equation of state, as we have shown in Thesis paper 2 [161]. Following the steps of our work, let us start by recalling the equation for the sound speed of the GCG

$$c^2_{\mathrm{s[gcg]}} = \alpha \frac{A}{\rho^{1+\alpha}_{\mathrm{gcg}}} \,. \tag{3.22}$$

Note that, from the definition of the sound speed (i.e. $c^2_{\mathrm{s}} \equiv dp/d\rho$), one we may integrate Eq. (3.22) to obtain the corresponding pressure for $\alpha \neq 0$

$$p_{\mathrm{gcg}} = -\frac{A}{\rho^{\alpha}_{\mathrm{gcg}}} + C \,, \tag{3.23}$$

where C is a real constant which is usually assumed to be equal to zero. Rewriting Eq. (3.23) as

$$p_{\mathrm{gcg}} = -\frac{A}{\rho^{\alpha}_{*}} \left(\frac{\rho_*}{\rho_{\mathrm{gcg}}} \right)^{\alpha} + C \,, \tag{3.24}$$

and expanding around $\alpha = 0$ gives

$$p_{\mathrm{gcg}} = A \left[-1 + \alpha \ln \left(\frac{\rho_{\mathrm{gcg}}}{\rho_*} \right) + \mathcal{O}\left(\alpha^2\right) \right] + C \,. \tag{3.25}$$

Considering the following limit

$$\mathcal{A} = \lim_{\substack{A\to\infty \\ \alpha\to 0}} \alpha A \,, \tag{3.26}$$

such that $\mathcal{A}$ is finite and $C = A$, one obtains a logarithmic equation of state

$$p_{\mathrm{log}} = \mathcal{A} \ln \left(\frac{\rho_{\mathrm{log}}}{\rho_*} \right) \,, \tag{3.27}$$

with the sound speed squared being equal to

$$c^2_{\mathrm{s[log]}} = \frac{\mathcal{A}}{\rho_{\mathrm{log}}} \,. \tag{3.28}$$

This logarithmic limit of the GCG (that we shall refer to as logCG) is one of the simplest extensions of the standard ΛCDM model containing a single extra parameter. By tuning the value of $\mathcal{A}$ and the reference density ρ_*, this model allows for the study small deviations from the ΛCDM model. On the other hand, the ΛCDM model can be obtained by considering the $\mathcal{A} \to 0$, $\rho_* \to \infty$ limit, with finite $\mathcal{A} \ln \rho_*$. In Sec. 4.2.3 we shall derive a Lagrangian formulation for this model in the non-relativistic limit.

3.2.7 The modified CG

As previously discussed, the GCG sound speed has a huge impact on the GCG power spectrum at late times, specially on small scales. Effectively, the sound speed is zero when the GCG behaves firmly as CDM, and only starts to become large as the fluid transitions to a dark energy state (if $\alpha > 0$). Let us now consider the following generalization of the GCG equation of state, known as the modified Chaplygin gas (MCG) [241, 270]

$$p_{\rm mcg} = B\rho_{\rm mcg} - \frac{A}{\rho_{\rm mcg}^{\alpha}}\,. \tag{3.29}$$

Here B is a constant parameter, and for $B = 0$ Eq. (3.29) reduces to the GCG model. Using Eq. (2.63) the background evolution of the energy density in the MCG is

$$\rho_{\rm mcg} = \rho_{\rm mcg0}\left[\tilde{A} + \left(1-\tilde{A}\right)a^{-3(1+B)(1+\alpha)}\right]^{\frac{1}{1+\alpha}}\,, \tag{3.30}$$

with $\tilde{A} = A\rho_{\rm mcg0}^{-(1+\alpha)}/\left(1+B\right)$. Similarly to the GCG, the MCG model tends to a vacuum-like state as $a \to \infty$ (i.e. $w_{\rm mcg} \to -1$) corresponding to an energy density $\rho_{\rm mcg}\left(a\to\infty\right) = \left[A/\left(1+B\right)\right]^{1/(1+\alpha)}$. On the other hand, for small values of the scale factor the energy density scales as $a^{-3(1+B)}$. Therefore, B parametrizes deviations with respect to a pressureless CDM behavior at early times [one has $w_{\rm mcg}\left(a\to 0\right) = B$].

The MCG sound speed squared is obtained from Eq. (3.13)

$$c_{\rm s[mcg]}^2 \equiv \frac{dp}{d\rho} = B + \alpha\frac{A}{\rho_{\rm mcg}^{1+\alpha}}\,. \tag{3.31}$$

Notice that, for $B \geq 0$ then $c_{\rm s[mcg]} \to \sqrt{B}$ in the $\rho_{\rm mcg} \to \infty$ limit. Thus, if the MCG is taken as a UDE model, the extra parameter $B \neq 0$ accounts for a non-zero sound speed associated to the effective DM component i.e. in the high density regime. Furthermore, assuming that the MCG model plays the role of DM on galactic scales, it is possible to find an upper limit on the value B from the observed rotational velocity of galaxies [162].

Measurements of the orbital velocity of stars and hot gas in galaxies strongly support the existence of large amounts of DM (see discussion in Secs. 1.4 and 1.6.1). Considering a spherically symmetric distribution of matter with radius r (where $r = 0$ at the center), in the Newtonian limit the radial orbital velocity profile $v\left(r\right)$ is given by

$$v^2\left(r\right) = \frac{GM\left(r\right)}{r} = \frac{4\pi}{3}G\rho\left(r\right)r^2\,, \tag{3.32}$$

where $M\left(r\right)$ is the mass enclosed by a sphere of radius r, and $\rho\left(r\right) = 3M\left(r\right)/\left(4\pi r^3\right)$ is the correspondent average density. At sufficiently large distances from the center, the rotational velocity curves of spiral galaxies are typically flattened [271–273]. Considering these outskirt regions to be at a distance $r_{\rm f}$ from the galactic center, we may write

$$G\rho\left(r_{\rm f}\right) = \frac{3}{4\pi}\frac{v_{\rm f}^2}{r_{\rm f}^2}\,, \tag{3.33}$$

for the flat part of the rotation curves, where $v\left(r_{\rm f}\right) = v_{\rm f} \sim$ const. The positive value $c_{\rm s[mcg]}^2 \to B$ attained for large enough energy densities implies a Jeans length larger than zero, which determines the stability criteria of MCG DM halos. Using Eqs. (3.18) and (3.33) one obtains

$$\frac{\lambda_{\mathrm{J[DM]}}}{r_{\mathrm{f}}} = \sqrt{\frac{4}{3}\pi}\frac{c_{\mathrm{s[DM]}}}{v_{\mathrm{f}}}\,. \tag{3.34}$$

Since collapse may only occur on scales smaller than r_{f} if $\lambda_{\mathrm{J[DM]}} < r_{\mathrm{f}}$, we have

$$c_{\mathrm{s[DM]}} < \sqrt{\frac{3}{4}}\frac{v_{\mathrm{f}}}{\pi}\,. \tag{3.35}$$

In turn, this implies the following inequality

$$B < c^2_{\mathrm{s[DM]}} < \frac{3}{4}\left(\frac{v_{\mathrm{f}}}{\pi}\right)^2\,. \tag{3.36}$$

The values for v_{f} derived from the observations of rotation curves in spiral galaxies are of the order of $v_{\mathrm{f}} \sim 10^{-3}$ (typically in the range $v_{\mathrm{f}} \sim 100 - 300$ km s^{-1} [271–273]). Hence, from Eq. (3.36) we get a conservative estimate for an upper limit on the value of B allowed by the data

$$B < 10^{-8}\,. \tag{3.37}$$

This restriction is consistent with those obtained by other authors using a wide variety of data to constrain the MCG model, including BAO, CMB and matter power spectrum observations [274–281] (see [250] for a more recent analysis). The constraints on the parameter B presented in these works are, however, not as stringent as the one given in Eq. (3.37) (as further explained in [162]).

3.3 The logotropic model

Fluids defined by a logarithmic equation of state (also known as logotropes) were first considered as a phenomenological approach to the analysis of the gravitational collapse of molecular clouds [282,283]. More recently, Chavanis proposed a cosmological model based on a logotropic equation of state, as a way to achieve a unification of dark matter and dark energy from a single perfect fluid [256,284]. Remarkably, it was claimed that the logotropic model could predict several observational results that the ΛCDM model fails to explain in a satisfactory way, while having the same number of free parameters. Thenceforth, the logotropic model raised considerable attention, being tested against observations [285,286] and further extended by other authors in [287–290] using the so-called Anton-Schmidt's equation of state [291] (originally introduced to describe the pressure of crystalline solids which deform under isotropic stress). However, these works fail to critically assess the viability of the logotropic model as a single dark fluid. Following closely the analysis presented in Thesis paper 1 [163], in this section we shall present the main features of the logotropic fluid, and discuss in more detail implications of this UDE model on the cosmological dynamics, structure formation, as well as on the stability of DM halos.

3.3.1 Logotropic equation of state

The logotropic fluid has an equation of state of the form [256,284]

$$p\left(n\right)=A_{\mathrm{lgt}}\ln\left(\frac{n}{n_{*}}\right)\,, \tag{3.38}$$

where n is the particle number density of the fluid, and A_{lgt} and $n_{*}>0$ are constant parameters of the model. Owing to the properties of the logarithmic function, the parameter n_{*} sets the condition for vanishing pressure of the logotropic fluid i.e. $p=0$ if $n=n_{*}$. Inserting the logotropic equation of state given by Eq. (3.38) into Eq. (2.54) one obtains the energy density ρ as a function of n (see top panel in Fig. 3.6)

$$\rho\left(n\right)=mn+n\int^{n}\frac{p\left(n'\right)}{n'^{2}}dn'=n-A_{\mathrm{lgt}}\ln\left(\frac{n}{n_{*}}\right)-A_{\mathrm{lgt}}\,, \tag{3.39}$$

where in the last term we set $m=1$. Taking the derivative of Eq. (3.39) one finds that the minimum energy density

$$\rho_{(\mathrm{min})}=-A_{\mathrm{lgt}}\ln\left(\frac{A_{\mathrm{lgt}}}{n_{*}}\right) \tag{3.40}$$

is attained for $n=A_{\mathrm{lgt}}$. Hence, to satisfy the condition $\rho\geq 0$ for any given $n>0$, the parameter A_{lgt} is bounded to $0\leq A_{\mathrm{lgt}}\leq n_{*}$ (which we shall assume henceforth). Considering the particular case $A_{\mathrm{lgt}}=0$, and assuming that n_{*} is fixed to a finite value, Eq. (3.38) is zero independently of the value of n, and the energy density is simply $\rho\left(n\right)=n$. Also notice that Eq. (3.40) has the well defined limit

$$\lim_{A_{\mathrm{lgt}}\to 0}\rho_{(\mathrm{min})}=0\,. \tag{3.41}$$

Despite being originally defined by an equation of state of the form $p=p\left(n\right)$, it is interesting to note that the logotropic model admits an explicit barotropic formulation $p=p\left(\rho\right)$, as we have shown in [163]. Combining Eqs. (3.38) and (3.39), and after some algebraic manipulation, we get

$$\left(-\frac{p+\rho}{A_{\mathrm{lgt}}}-1\right)\exp\left(-\frac{p+\rho}{A_{\mathrm{lgt}}}-1\right)=f\left(\rho\right)\,, \tag{3.42}$$

where

$$f\left(\rho\right)=-\frac{n_{*}}{A_{\mathrm{lgt}}}\exp\left(-\frac{\rho}{A_{\mathrm{lgt}}}-1\right)\,. \tag{3.43}$$

Eq. (3.42) may be solved using the so-called Lambert W function [292], provided that $f\left(\rho\right)\geq -e^{-1}$ for any value of the energy density. This function has a minimum $f\left(\rho_{(\mathrm{min})}\right)=-e^{-1}$ [with $\rho_{(\mathrm{min})}$ being given by Eq. (3.40)] so the condition $f\left(\rho\right)\geq -e^{-1}$ is always satisfied. Thus, the barotropic equation of state for the logotropic model is given by

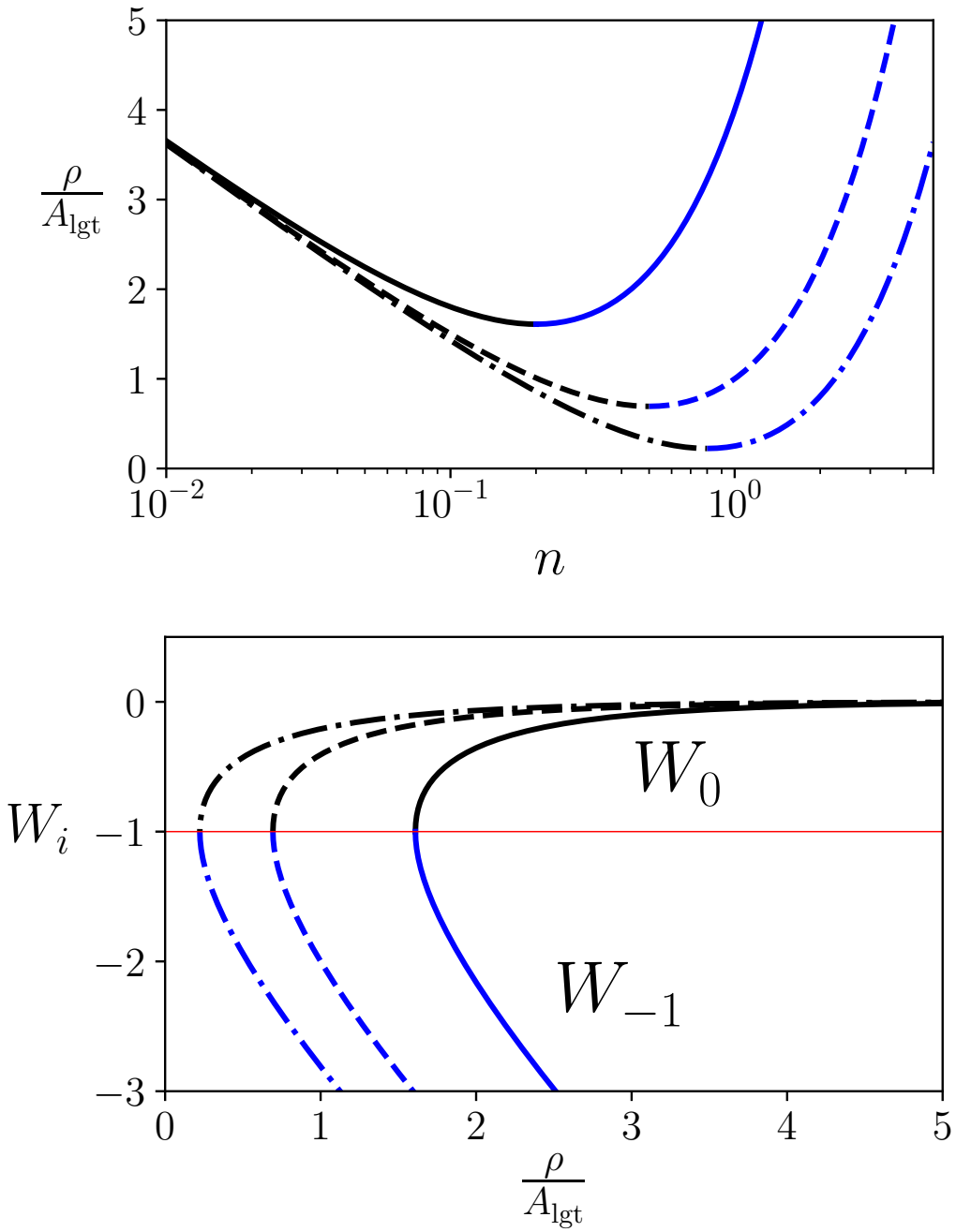

Figure 3.6: Top panel: Ratio between the energy density of the logotropic fluid and $A_{\rm lgt}$ as a function of the number density, with n_* being fixed to unity and $A_{\rm lgt} = 0.2$ (solid line), $A_{\rm lgt} = 0.5$ (dashed line) and $A_{\rm lgt} = 0.8$ (dotted-dashed line). Blue and black lines correspond to $d\rho/dn > 0$ and $d\rho/dn < 0$, respectively. Bottom panel: Plot of the two real branches of the Lambert W function $W_0\left(f\left(\rho\right)\right) > -1$ and $W_{-1}\left(f\left(\rho\right)\right) < -1$. The color and line styles match the ones of the top panel.

$$-\frac{p+\rho}{A_{\rm lgt}}-1=W_i\left[f\left(\rho\right)\right]\Leftrightarrow \tag{3.44}$$

$$\Leftrightarrow p\left(\rho\right)=-A_{\rm lgt}W_i\left[f\left(\rho\right)\right]-\rho-A_{\rm lgt}\,, \tag{3.45}$$

where W_i is the Lambert W function, and the subscript $i=0\,,-1$ refers to the two real branches of this multivalued function, with $W_0\left(-e^{-1}\right)=W_{-1}\left(-e^{-1}\right)=-1$. Notice that there is a clear physical interpretation of these two real branches, as one may see in Fig. 3.6 (bottom panel): the branch W_{-1} corresponds to a standard evolution of the energy density (i.e. $d\rho/dn>0$), and W_0 to a phantom regime (i.e. $d\rho/dn<0$).

3.3.2 Logotropic cosmologies

We will now explore the logotropic fluid as a UDE model. For that purpose, we shall consider a Universe filled solely by a dark fluid described by a logotropic equation of state. The background evolution of the energy density in a FLRW Universe may be found as usual i.e. by plugging Eq. (3.45) into the continuity equation (given by Eq. (2.63)) and solving the resultant differential equation. However, observe that, due to the conservation of the number of particles, the number particle density scales as $n\propto a^{-3}$. From Eq. (3.39) one immediately gets

$$\rho\left(a\right)=n_0a^{-3}-A_{\rm lgt}\ln\left(\frac{n_0a^{-3}}{n_*}\right)-A_{\rm lgt}\,. \tag{3.46}$$

Notice that the first term on the r.h.s. dilutes in the same way as matter as the Universe expands, so we may identify $n_0=\rho_{\rm m0}$. At the present time, i.e. for $a=1$, Eq. (3.46) provides the following relation

$$n_*=\Omega_{\rm m0}\rho_0\exp\left(1+\frac{1}{B_{\rm lgt}}\right)\,, \tag{3.47}$$

where

$$B_{\rm lgt}=\frac{A_{\rm lgt}}{\rho_0\left(1-\Omega_{\rm m0}\right)}\geq 0\,. \tag{3.48}$$

Using Eq. (3.47) one may rewrite Eq. (3.49) as

$$\rho\left(a\right)=\rho_0\left[\Omega_{\rm m0}a^{-3}+\left(1-\Omega_{\rm m0}\right)\left(1+3B_{\rm lgt}\ln a\right)\right]\,, \tag{3.49}$$

while the pressure of the logotropic fluid is given by

$$p\left(a\right)=-\rho_0\left(1-\Omega_{\rm m0}\right)\left(1+B_{\rm lgt}+3B_{\rm lgt}\ln a\right)\,. \tag{3.50}$$

From the two free parameters $A_{\rm lgt}$ and n_* that we started with in Eq. (3.38), the dimensionless quantity $B_{\rm lgt}$ remains as the only extra free parameter inherent to the logotropic model. Deviations

with respect to the ΛCDM are found for logotropic cosmologies considering values of $B_{\rm lgt}$ larger than zero. Observe that both models are completely equivalent for $B_{\rm lgt} = 0$: the limit $B_{\rm lgt} \to 0$ implies both $A_{\rm lgt} \to 0$ and $n_* \to \infty$ [from Eqs. (3.47) and (3.48)], with the pressure of the logotropic fluid being, in this case, a negative constant

$$p\left(B_{\rm lgt} = 0\right) = -\rho_0 \left(1 - \Omega_{\rm m0}\right) . \tag{3.51}$$

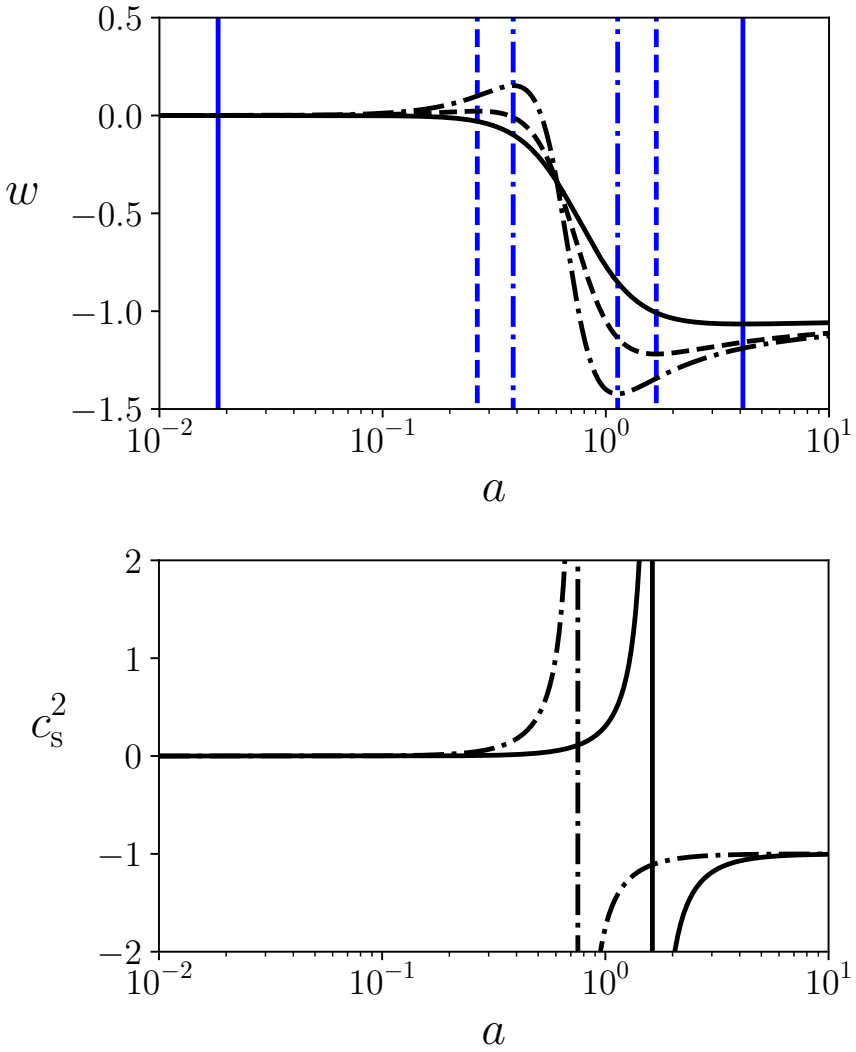

Figure 3.7: The matter density parameter is fixed to $\Omega_{\rm m0} = 0.3$ in both panels. Top panel: Evolution of the equation of state parameter as a function of the scale factor (black lines) while the blue vertical lines denote the value of the scale factor when w has a maximum or a minimum. The solid, dashed, and dotted-dashed lines correspond to $B_{\rm lgt} = 0.1$, 0.5 and 1, respectively. Bottom panel: Evolution of the sound speed squared as a function of the scale factor. For illustration purposes, we just plot $c_{\rm s}^2$ for the values $B_{\rm lgt} = 0.1$ and 1 (solid and dotted dashed lines, respectively).

From Eqs. (3.49) and (3.50) one obtains the equation of state parameter as a function of the scale factor

$$w = -\frac{(1-\Omega_{\rm m0})\,(1+B_{\rm lgt}+3B_{\rm lgt}\ln a)}{\Omega_{\rm m0}a^{-3}+(1-\Omega_{\rm m0})\,(1+3B_{\rm lgt}\ln a)}\,. \tag{3.52}$$

Similarly to the GCG, the logotropic dark fluid mimics dark matter at sufficiently early times, and asymptotically approaches a cosmological constant state as $a \to \infty$ [Eq. (3.52) has the limiting cases $w\,(a\to 0)=0$ and $w\,(a\to\infty)=-1$]. However, the intermediary behavior is in general not as smooth (see left plot in Fig. 3.7). Before the transition to a DE state the equation of state parameter is a positive and growing function, reaching a maximum before becoming negative for $a > a_{(p=0)}$, where

$$a_{(p=0)} = \exp\left(-\frac{1+B_{\rm lgt}}{3B_{\rm lgt}}\right)\,. \tag{3.53}$$

As w decreases, it passes -1 for

$$a_{(w=-1)} = \sqrt[3]{\frac{\Omega_{\rm m0}}{B_{\rm lgt}\,(1-\Omega_{\rm m0})}}\,, \tag{3.54}$$

and reaches a minimum before converging asymptotically to -1. The extrema of w occur at

$$a_{\rm extrema} = \sqrt[3]{-\frac{\Omega_{\rm m0}}{B_{\rm lgt}\,(1-\Omega_{\rm m0})}W_i\left[-\frac{B_{\rm lgt}\,(1-\Omega_{\rm m0})}{\Omega_{\rm m0}}\exp\left(-2-\frac{1}{B_{\rm lgt}}\right)\right]}\,, \tag{3.55}$$

with the branches $i=0$ and $i=-1$ giving the value of the scale factor when w is maximum and minimum, respectively (see blue vertical lines in Fig. 3.7).

Therefore, the DM-DE interpolation in the logotropic model strongly depends on $B_{\rm lgt}$, with higher values resulting on a steeper transition and larger absolute values for the extrema of w. Consequently, the background evolution deviates significantly with respect to the ΛCDM model, unless $B_{\rm lgt}$ is sufficiently small. As mentioned in the previous subsection, $A_{\rm lgt} < n_*$ is required for consistency with $\rho > 0$ at all times. Using Eqs. (3.47) and (3.48) one gets

$$B_{\rm lgt} < \left[W_0\left(\frac{1-\Omega_{\rm m0}}{\Omega_{\rm m0}e^{-1}}\right)\right]^{-1} \lesssim 2\,, \tag{3.56}$$

where we take the reference value $\Omega_{\rm m0}=0.3$. If the upper limit is considered, notice that both extrema for w would occur for the same value of the scale factor (from Eq. (3.55)).

3.3.3 Constraint on $B_{\rm lgt}$ from the growth of cosmic structures

From the usual definition for the sound speed (i.e. $c_{\rm s}^2 \equiv dp/d\rho$), and taking into account that for any branch $dW\,(x)\,/dx = x^{-1}W\,(x)\,/\,(1+W\,(x))$ (except for $x=0$ and $x=-e^{-1}$) one obtains from Eq. (3.45)

$$c_{\rm s}^2 = -\frac{1}{1+W_i\,[f\,(\rho)]}\,. \tag{3.57}$$

The logotropic sound speed is positive in the W_{-1} branch, negative in the W_0 branch, and diverges when $f\left(\rho_{(\min)}\right) = -e^{-1}$. From Eqs. (3.47) and (3.49), and using the identity $W_i\left(xe^x\right) = x$ (valid for both branches) we may write the sound speed as a function of the scale factor

$$c_{\rm s}^2 = \left(\frac{\Omega_{\rm m0}}{B_{\rm lgt}\left(1-\Omega_{\rm m0}\right)}a^{-3} - 1\right)^{-1} . \tag{3.58}$$

Unless $B_{\rm lgt}$ is exactly zero (in which case $c_{\rm s} = 0$ at all times), the sound speed diverges at $a_{(w=-1)}$, being positive for $a < a_{(w=-1)}$, and negative for $a > a_{(w=-1)}$ (see right plot in Fig. 3.7). In models with $B_{\rm lgt} < \Omega_{\rm m0}/\left(1-\Omega_{\rm m0}\right)$ the sound speed diverges only for $a > 1$, so the logotropic fluid can be taken as an effective model up to the present time without facing any discontinuity on the evolution of the sound speed.

In the following discussion we consider a Universe dominated by a logotropic fluid at sufficiently early times, such that it still firmly evolves as DM (i.e. $w \sim 0$). Under this assumption, the sound speed is well approximated by

$$c_{\rm s}^2 \sim \frac{B_{\rm lgt}\left(1-\Omega_{\rm m0}\right)}{\Omega_{\rm m0}}a^3 , \tag{3.59}$$

and $\rho \sim n = \rho_{\rm m0}a^{-3}$ (so the sound speed is always positive in this regime). Due to a non-zero sound speed for $B_{\rm lgt} > 0$, the growth of linear density perturbations can only occur on scales larger than the comoving Jeans length (on smaller scales pressure gradients give rise to acoustic oscillations, as we have discussed in Sec. 3.2.3). Using Eq. (3.59), and taking into account that $\rho_{\rm m0} = 3H_0^2\,\Omega_{\rm m0}/(8\pi G)$, the comoving Jeans length $\lambda_J^c = \lambda_J/a$ (see Eq. (3.18)) is given by

$$\lambda_J^c = \frac{\pi}{\Omega_{\rm m0}H_0\left(1+z\right)^2}\sqrt{\frac{8}{3}B_{\rm lgt}\left(1-\Omega_{\rm m0}\right)} . \tag{3.60}$$

One may estimate an upper limit on $B_{\rm lgt}$ by requiring that the linear growth of cosmic structures is not significantly affected with respect to the standard matter era evolution on comoving scales larger than $R = 8h^{-1}\,$Mpc. Thus, the condition $\lambda_J^c < R$ implies

$$B_{\rm lgt} < \frac{3}{8\pi^2}\frac{\left(RH_0\Omega_{\rm m0}\right)^2}{1-\Omega_{\rm m0}}\left(1+z\right)^4 . \tag{3.61}$$

Taking $z = 1$ and $H_0 = h/3000\,{\rm Mpc}^{-1}$ in Eq. (3.61), together with $\Omega_{\rm m0} = 0.3$ and $R = 8h^{-1}\,$Mpc, we get [163]

$$B_{\rm lgt} \lesssim 6\times 10^{-7} . \tag{3.62}$$

This upper limit on $B_{\rm lgt}$ is more than three orders of magnitude smaller than the value $B_{\rm lgt} = 3.53\times 10^{-3}$ considered in [256, 284, 285], which was shown to provide a good fit to SNIa, BAO, and CMB data (see also [286]). We shall now discuss the motivation behind this particular choice for the value of $B_{\rm lgt}$.

3.3.4 The role of the Planck density

The logotropic model, defined in Eq. (3.52), has two fundamental parameters, $A_{\rm lgt}$ and n_*. The dimensionless parameter $B_{\rm lgt}$ is obtained combining $A_{\rm lgt}$, the present value of the energy density ρ_0, and the matter density parameter $\Omega_{\rm m0}$ (see Eq. (3.48)). The reference particle number density n_*, given in Eq. (3.47), depends on ρ_0, $\Omega_{\rm m0}$, and $B_{\rm lgt}$.

Though it is a priori a free parameter of the model, n_* has been identified with the Planck density $\rho_{\rm pl}$ in [256, 284]. Assuming the values for the cosmological $\Omega_{\rm m0} = 0.3$ and $h = 0.67$, one may fix the parameter $B_{\rm lgt}$ using Eq. (3.47)

$$B_{\rm lgt} = B_{\rm pl} = \left(\ln\left(\frac{\rho_{\rm pl}}{\Omega_{\rm m0}\rho_0}\right) - 1\right)^{-1} = 3.53 \times 10^{-3}\,, \tag{3.63}$$

where $\rho_{\rm pl}/\rho_0 \sim 2.74 \times 10^{122}\, h^{-2}$. In this case, the logotropic model has the same number of free parameters as the ΛCDM. However, given the analysis from the previous subsection, it is clear that such large $B_{\rm lgt}$ would significantly affect the growth of linear perturbations on scales much larger than $R = 8h^{-1}\,$Mpc. Indeed, for $B_{\rm lgt} = 3.53 \times 10^{-3}$, the linear density perturbations in the logotropic dark fluid at $z = 1$ would be able to grow only on scales $\gtrsim 600\, h^{-1}\,$Mpc, in clear contradiction with observations.

Due to the logarithmic dependence in Eq. (3.63), $B_{\rm lgt}$ is rather insensitive to the exact values of n_*, ρ_0 and $\Omega_{\rm m0}$. In contrast, small changes on $B_{\rm lgt}$ may led to very large differences on the value of n_*, specially when $B_{\rm lgt} \ll 1$. Considering the constraint $B < 6 \times 10^{-7}$ and using Eq. (3.47) one has

$$\frac{n_*}{\rho_{\rm pl}} = \exp\left(\frac{1}{B_{\rm lgt}} - \frac{1}{B_{\rm pl}}\right) > 10^{7\times 10^5}\,, \tag{3.64}$$

resulting on a value of n_* which is many orders of magnitude larger than the Planck density [163]. Such a large value of the fundamental density of the logotropic fluid model may be hard to justify at a more fundamental level.

3.3.5 Logotropic DM halos

Let us now consider that DM halos are described by a logotropic equation of state as given in Eq. (3.52). The structure of a spherically symmetric configuration of a perfect fluid in gravitational equilibrium is completely determined by the Tolman–Oppenheimer–Volkoff equation [293, 294]. In the non-relativistic limit[3] (where $n \sim \rho$, $c_s^2 \ll 1$, and $|w| = |p/\rho| \ll 1$) it reduces to the classical hydrostatic equilibrium equation

$$\frac{1}{\rho}\frac{dp}{dr} = -\frac{GM\,(r)}{r^2}\,, \tag{3.65}$$

[3] Notice that in the non-relativistic regime the logotropic equation of state is degenerate with the logCG defined in Sec. 3.2.6

with $M(r)$ being the mass inside a sphere of radius r, and $\rho(r) = 3M(r)/\left(4\pi r^3\right)$ being the average density. Thus, for a logotropic sphere one has

$$\frac{1}{\rho}\frac{dp}{dr} = \frac{A_{\rm lgt}}{\rho^2}\frac{d\rho}{dr} = -\frac{GM(r)}{r^2}\,, \tag{3.66}$$

that may be rewritten as

$$\frac{1}{r^2}\frac{d}{dr}\left(\frac{r^2}{\rho^2}\frac{d\rho}{dr}\right) = -\frac{4\pi G}{A_{\rm lgt}}\rho\,, \tag{3.67}$$

taking into account that $dM/dr = 4\pi r^2 G\rho$. One may easily check that $\rho_{\rm lgt} \propto r^{-1}$ is a solution of Eq. (3.67). Therefore, the surface density of the logotropic sphere is a constant

$$\rho_{\rm lgt} r \propto \sqrt{\frac{A_{\rm lgt}}{G}} = \sqrt{\frac{B_{\rm lgt}\rho_0\left(1-\Omega_{\rm m0}\right)}{G}}\,. \tag{3.68}$$

Observations do seem to suggest that the central surface density of galaxy DM halos is nearly constant and independent of galaxy luminosity [295] (see [296] for a different perspective). Using the value $B_{\rm pl} = 3.53\times10^{-3}$ (corresponding to the identification $n_* = \rho_{\rm pl}$), it was shown in [256,284] that the estimated value of the surface density of logotropic DM halos is consistent with the one inferred from observations. However, if the logotropic fluid is to be considered as a UDE model, the upper limit $B = 6\times10^{-7}$ derived in Sec. 3.3.3 would result on a value almost two orders of magnitude lower. The same also applies to the claim that the logotropic equation of state with $n_* = \rho_{\rm pl}$ would also explain the observed Tully-Fisher relation and the mass of dwarf galaxies, since both of these depend strongly on the surface density of the DM halos.

In order to derive the stability criteria of a logotropic sphere, we shall consider a homologous perturbation [297] i.e. we assume that the halo is initially in hydrostatic equilibrium and then expand or contract the radius $r = r_{(0)} + \delta r$, where $r_{(0)}$ is the radius of the unperturbed configuration, and δr is a small perturbation. We employ the same notation for the pressure and density perturbations, which also change in response to the change in the radius (assuming that $|\delta p/p_{(0)}| \ll 1$ and $|\delta\rho/\rho_{(0)}| \ll 1$). The equation of motion

$$\ddot{r} = -\frac{1}{\rho}\frac{dp}{dr} - \frac{GM(r)}{r^2} \tag{3.69}$$

reduces to the classical hydrostatic equilibrium equation for $\ddot{r} = 0$. Notice that one may further rewrite Eq. (3.69) as

$$\ddot{r}dM = -\frac{GM}{r^2}dM - 4\pi r^2 dp\,, \tag{3.70}$$

using the relation $dM/dr = 4\pi r^2\rho$. Thus, the equation for the unperturbed configuration can be written as

$$\frac{GM}{r_{(0)}^2}dM + 4\pi r_{(0)}^2 dp_{(0)} = 0\,, \tag{3.71}$$

while the perturbed configuration satisfies

$$dM\ddot{r} = -\frac{GM}{r^2}dM - 4\pi r^2 dp\,. \tag{3.72}$$

The substitution of $p = p_{(0)} + \delta p$ and $r = r_{(0)} + \delta r$ in Eq. (3.72) gives

$$dM\frac{d^2}{dt^2}\left(r_{(0)} + \delta r\right) = -\frac{GM}{\left(r_{(0)} + \delta r\right)^2}dM - 4\pi\left(r_{(0)}^2 + \delta r\right)^2 d\left(p_{(0)} + \delta p\right)\,. \tag{3.73}$$

Keeping only linear terms, one obtains

$$dM\ddot{\delta r} = 2\frac{GM}{r_{(0)}^2}\delta r dM - 4\pi\left(2\frac{\delta r}{r_{(0)}} + \frac{\delta p}{p_{(0)}}\right) r_{(0)} dp_{(0)} = 0\,. \tag{3.74}$$

Now we must find how the pressure responds to a small change in the radius of the sphere. From the logotropic equation of state one may relate δp and $\delta\rho$ as

$$p_{(0)}\left(1 + \frac{\delta p}{p_{(0)}}\right) = A_{\rm lgt}\ln\left[\frac{1}{n_*}\rho_{(0)}\left(1 + \frac{\delta\rho}{\rho_{(0)}}\right)\right] \approx p_{(0)} + A_{\rm lgt}\frac{\delta\rho}{\rho_{(0)}}\,, \tag{3.75}$$

where the last term is found by Taylor expanding the logarithm $\ln\left(1 + \delta\rho/\rho_{(0)}\right) \approx \delta\rho/\rho_{(0)}$. Hence, we find

$$\delta p = A_{\rm lgt}\frac{\delta\rho}{\rho_{(0)}}\,. \tag{3.76}$$

In a homologous expansion or contraction, r and ρ vary, while leaving the shell mass dM unchanged

$$dM = 4\pi\left[r_{(0)}\left(1 + \frac{\delta r}{r_{(0)}}\right)\right]^2 \rho_{(0)}\left(1 + \frac{\delta\rho}{\rho_{(0)}}\right) dr_{(0)}\left(1 + \frac{\delta r}{r_{(0)}}\right) \approx \tag{3.77}$$

$$\approx 4\pi r_{(0)}^2 d\rho_{(0)}\left(1 + 3\frac{\delta r}{r_{(0)}} + \frac{\delta\rho}{\rho_0}\right) \tag{3.78}$$

so one has

$$\frac{\delta\rho}{\rho_{(0)}} = -3\frac{\delta r}{r_{(0)}}\,. \tag{3.79}$$

Combining Eqs. (3.74), (3.76) and (3.79) one finally obtains

$$\ddot{\delta r} = -\frac{GM}{r_{(0)}^3}\left[\frac{3}{\ln\left(\frac{\rho_{(0)}}{n_*}\right)} - 4\right]\delta r\,. \tag{3.80}$$

Given the solution $\delta r \propto \exp(i\omega t)$ for this second order differential equation, one finds that the logotropic halo is stable provided that

$$\omega^2 = -\frac{GM}{r_{(0)}^3}\left[\frac{3}{\ln\left(\frac{\rho_{(0)}}{n_*}\right)} - 4\right] > 0\,, \tag{3.81}$$

which implies that

$$\rho_{(0)} > n_* \exp\left(\frac{3}{4}\right) \sim 2n_*\,. \tag{3.82}$$

Therefore, if $n_* = \rho_{\rm pl}$ the condition given in Eq. (3.82) could only be met for unrealistic large values of $\rho_{(0)}$.

Chapter 4

UDE: scalar field models

Scalar fields are ubiquitous in cosmology, being central to the primordial inflation paradigm [31,33, 34,298–300], and considered as potential candidates to explain the current accelerated expansion of the Universe [135,301,302] or even CDM [303–305]. In the literature one may also find scalar fields being evoked to describe, in a unified way, both primordial inflation and DE [306], while in the works [307–309] it is shown that a single scalar field can account for CDM and both (early and late) periods of acceleration. Indeed, the discovery of a Higgs-like particle in 2012 [310,311] (so far, the only fundamental scalar field for which we have strong experimental evidence) reinforces the idea that scalar fields play a fundamental role in physics.

We have so far considered a fluid description of UDE models, in which the dynamics is fully characterized given an equation of state $p = p(\rho)$ or, equivalently, by $p = p(n)$. On the other hand, it is well known that a minimally coupled scalar field in General Relativity admits a perfect fluid description [312]. Therefore, if one starts by modeling the energy content of the Universe as a collection of perfect fluids, an equivalent description (although contingent, as we explain later) in terms of a collection of scalar fields is also possible. In this chapter we shall explore in more detail this duality, focusing on scalar field theories that are appropriate to describe isentropic perfect fluids.

4.1 Action functionals for perfect fluids

4.1.1 Schutz-Sorkin action

The derivation of the equations of motion of a perfect fluid from an action functional has been studied by several authors [313–318]. We shall start by considering the following action

$$\mathcal{S} = \int d^4x \sqrt{-g}\, \mathcal{L}(g_{\alpha\beta}, j^\alpha, \phi)\,, \tag{4.1}$$

where the Lagrangian is given by

$$\mathcal{L} = F\left(|\mathbf{j}|\right) + j^{\alpha}\nabla_{\alpha}\phi\,, \tag{4.2}$$

with j^{α} being the components of a timelike vector field $\mathbf{j}$, ϕ is a scalar field, and F is a function of $|\mathbf{j}|$, where

$$|\mathbf{j}| = \sqrt{-j^{\alpha}j_{\alpha}} = \sqrt{-g_{\alpha\beta}j^{\alpha}j^{\beta}}\,. \tag{4.3}$$

Varying the action with respect to the dynamical fields j^{α} and ϕ (see Eq. (2.12)) leads to the following equations of motion

$$\frac{\delta\mathcal{S}}{\delta j^{\alpha}} = 0 = -\frac{1}{|\mathbf{j}|}\frac{dF}{d|\mathbf{j}|}j_{\alpha} + \nabla_{\alpha}\phi\,, \tag{4.4}$$

$$\frac{\delta\mathcal{S}}{\delta\phi} = 0 = \nabla_{\alpha}j^{\alpha}\,. \tag{4.5}$$

From the definition of the energy-momentum tensor given in Eq. (2.11) one obtains[1]

$$T^{\alpha\beta} = -\frac{dF}{d|\mathbf{j}|}\frac{j^{\alpha}j^{\beta}}{|\mathbf{j}|} + \left(F - |\mathbf{j}|\frac{dF}{d|\mathbf{j}|}\right)g^{\alpha\beta}\,, \tag{4.6}$$

where we have also used Eq. (4.4). Let us retrieve the expression for the energy-momentum tensor of a perfect fluid

$$T^{\alpha\beta} = (\rho + p)\,u^{\alpha}u^{\beta} + pg^{\alpha\beta}\,. \tag{4.7}$$

Eq. (4.7) is obtained from Eq. (4.6) once the following identifications are made:

$$n = |\mathbf{j}|\,, \tag{4.8}$$

$$\rho\left(n\right) = -F\,, \tag{4.9}$$

$$p\left(n\right) = F - n\frac{dF}{dn}\,, \tag{4.10}$$

$$u^{\alpha} = \frac{j^{\alpha}}{n}\,, \tag{4.11}$$

Notice that combining Eqs. (4.9) and (4.10) one obtains the relationship presented in Eq. (2.53) (with the chemical potential being given by $\mu = d\rho/dn$)

$$p + \rho = n\mu\,, \tag{4.12}$$

[1]Notice that in Eq. (2.11) the energy-momentum tensor was defined in terms of the variation with respect to the inverse metric (so the energy-momentum tensor was given in its covariant form i.e. with lower indices). In the present case one has $T^{\alpha\beta} = \frac{2}{\sqrt{-g}}\frac{\delta\left(\sqrt{-g}\mathcal{L}\right)}{\delta g_{\alpha\beta}} = 2\frac{\delta\mathcal{L}}{\delta g_{\alpha\beta}} + \mathcal{L}g^{\alpha\beta}$.

which follows from the 1st law of thermodynamics. Hence, Eqs. (4.4), (4.8), and (4.11) now define the 4-velocity of the fluid as

$$u^\alpha = -\frac{\nabla^\alpha \phi}{\mu}\,, \tag{4.13}$$

associated with an irrotational flow, meaning that the spatial components of u^α are curl-free in the local comoving inertial frame (also referred to as potential flow, since in this case the 4-velocity of the fluid is fully determined by the gradient of a scalar function). The normalization condition $u^\alpha u_\alpha = -1$ implies that

$$\mu^2 = 2X\,, \tag{4.14}$$

where

$$X \equiv -\frac{1}{2}\nabla^\alpha \phi \nabla_\alpha \phi > 0\,, \tag{4.15}$$

thus requiring the quantity $\nabla_\alpha \phi$ to be timelike. The equation of motion (4.5) guarantees that the fluid conserves the number of particles.

The Lagrangian we considered in Eq. (4.2) is a particular case of the following model (see e.g. [318])

$$\mathcal{S}\left[g_{\alpha\beta},\, j^\alpha,\, \phi,\, \theta,\, s,\, A^a,\, B_a\right] = \int d^4x\sqrt{-g}\left\{-\rho\left(n,s\right) + j^\alpha\left(\nabla_\alpha\phi + s\nabla_\alpha\theta + B_a\nabla_\alpha A^a\right)\right\}\,, \tag{4.16}$$

being usually known as the Schutz-Sorkin action. This more general Lagrangian, often considered in the literature to describe a perfect fluid [319–327], considers s, θ, B_a and A^a as dynamical variables (in addition to $g_{\alpha\beta}$, n and ϕ). Here $\rho\left(n,s\right)$ is the energy density of the fluid as usual, though in this case it is a function of both the number density n and entropy per particle s. From Eq. (4.16) one has the additional equations of motion

$$\frac{\delta\mathcal{S}}{\delta s} = 0 = -\frac{\partial\rho}{\partial s} + j^\alpha\nabla_\alpha\theta\,, \tag{4.17}$$

$$\frac{\delta\mathcal{S}}{\delta\theta} = 0 = \nabla_\alpha\left(sj^\alpha\right)\,, \tag{4.18}$$

$$\frac{\delta\mathcal{S}}{\delta A^a} = 0 = j^\alpha\nabla_\alpha A^a\,, \tag{4.19}$$

$$\frac{\delta\mathcal{S}}{B_a} = 0 = \nabla_\alpha\left(j^\alpha B_a\right)\,, \tag{4.20}$$

whereas

$$\frac{\delta S}{\delta j^\alpha} = 0 = \frac{\partial\rho}{\partial n}u_\alpha + \nabla_\alpha\phi + s\nabla_\alpha\theta + B_a\nabla_\alpha A^a\,, \tag{4.21}$$

replaces our Eq. (4.4) (note that Eq. (4.5) remains unchanged). Here, the scalar field θ works as a Lagrange multiplier, ensuring that the entropy exchange constraint in Eq. (4.18) is satisfied. In combination with the particle number conservation equation [i.e., Eq. (4.5)] it implies that $j^\alpha \nabla_\alpha s = 0$, which defines an adiabatic flow [328]. The Lagrange multipliers B_a (where $a = 1, 2, 3$) restrict the fluid 4-velocity to be directed along the flow lines of constant A^a [Eq. (4.19)], where A^a are the Lagrangian coordinates of the fluid.

Thus, from the Schutz-Sorkin action defined in Eq. (4.16), some of the most important dynamical and thermodynamical relations characterizing a perfect fluid undergoing an adiabatic flow can be elegantly derived from the equations of motion. Nonetheless, the model defined in Eq. (4.2) will be sufficient for our discussion of particle conserving isentropic irrotational perfect fluids and their connection with pure k-essence scalar field models, as we shall discuss next.

4.1.2 Pure k-essence

It is a simple matter to show that, using the equation of motion (4.4) and the relations (4.8 - 4.10), the Lagrangian given in Eq. (4.2) can be written on-shell (i.e. the scalar field satisfies the equation of motion) as

$$\mathcal{L}_{\text{on-shell}} = -\rho + n\frac{d\rho}{dn} = p\,. \tag{4.22}$$

Let us assume the chemical potential $\mu(n)$ to be a strictly monotonic function of n (such that there is a one-to-one relation between μ and n)[2]. Then, Eq. (4.12) may be written as

$$p(\mu) = \mu n - \rho\,, \tag{4.23}$$

where $p(\mu)$ is the Legendre transform of $\rho(n)$, with the conjugate variables being related through

$$n = \frac{dp}{d\mu}\,, \quad \mu = \frac{d\rho}{dn}\,. \tag{4.24}$$

Having the relation given in Eq. (4.14), the pressure can be written as a function of X, so that the Lagrangian from Eq. (4.22) reduces to that of a pure k-essence model

$$\mathcal{L}(X) = p(X)\,. \tag{4.25}$$

Using Eq. (4.14) we find $\mu = \pm\sqrt{2X}$, so one can express the number density as

$$n(X) = \frac{dX}{d\mu}p_{,X} = \pm\sqrt{2X}p_{,X}\,. \tag{4.26}$$

[2]This guarantees that the Legendre transform is single valued and has continuous first derivatives [329]. Such assumption may be relaxed in order to allow for a scalar field description of a more broad class of isentropic perfect fluids. Note, however, that the expressions given in this section also hold in this more general case.

where a comma denotes a partial derivative (e.g., $p_{,X} \equiv dp/dX$). The condition $n\,(X) > 0$ implies that one has $p_{,X} > 0$ or $p_{,X} < 0$, if $\mu > 0$ or $\mu < 0$, respectively. The equation of motion of the scalar field may be found by varying Eq. (4.22) with respect to ϕ

$$\nabla_\alpha \left(\mathcal{L}_{,X} \nabla^\alpha \phi\right) = 0\,. \tag{4.27}$$

Notice that Eq. (4.27) provides the equivalent in the scalar field theory of the particle number conservation, given by Eq. (4.5). From Eq. (2.11) one finds the energy-momentum tensor of a model given by Eq. (4.25) to be

$$T^{\alpha\beta} = \mathcal{L}_{,X} \nabla^\alpha \phi \nabla^\beta \phi + \mathcal{L} g^{\alpha\beta}\,. \tag{4.28}$$

Therefore, with the identification $u_\alpha = -\nabla_\alpha \phi / \sqrt{2X}$, in combination with

$$\rho = 2X\mathcal{L}_{,X} - \mathcal{L}\,, \tag{4.29}$$

a pure k-essence Lagrangian may be used to describe an irrotational perfect fluid with conserved particle number and constant entropy per particle, provided that $X > 0$ [330–332]. Considering Eqs. (4.25) and (4.29) one finds the sound speed squared to be given by

$$c_{\rm s}^2 = \frac{\delta p}{\delta \rho} = \frac{\mathcal{L}_{,X}\,\delta X}{\left(\mathcal{L}_{,X} + 2X\mathcal{L}_{,XX}\right)\delta X} = \frac{p_{,X}}{\rho_{,X}}\,. \tag{4.30}$$

4.1.3 The case $\mathcal{L}_{\rm on-shell} = -\rho$

Surface terms may be added to an action without changing the equations of motion. Hence, even if the resultant action appears to be different, it still describes the same physics. Let us take the action in Eq. (4.1) and consider the following transformation

$$\mathcal{L} \to \mathcal{L} - \nabla_\alpha (\phi j^\alpha)\,. \tag{4.31}$$

and, since we are adding a surface term, the equations of motion given in Eqs. (4.4) and (4.5) are insensitive to this transformation. The resulting Lagrangian is given by

$$\begin{aligned} \mathcal{L} &= F(n) + j^\alpha \nabla_\alpha \phi - \nabla_\alpha (\phi j^\alpha) \\ &= F(n) - \phi \nabla_\alpha j^\alpha\,. \end{aligned} \tag{4.32}$$

Varying the matter action with respect to the metric components one obtains

$$\begin{aligned}\delta\mathcal{S} &= \int d^4x \frac{\delta\left(\sqrt{-g}\mathcal{L}\right)}{\delta g_{\alpha\beta}}\delta g_{\alpha\beta} \\ &= \frac{1}{2}\int d^4x\sqrt{-g}\,T^{\alpha\beta}\delta g_{\alpha\beta}\,,\end{aligned} \tag{4.33}$$

where

$$\begin{aligned}\delta\left(\sqrt{-g}\mathcal{L}\right) &= \sqrt{-g}\delta\mathcal{L} + \mathcal{L}\delta\sqrt{-g} \\ &= \sqrt{-g}\delta\mathcal{L} + \frac{\mathcal{L}}{2}\sqrt{-g}g^{\alpha\beta}\delta g_{\alpha\beta}\,,\end{aligned} \tag{4.34}$$

with

$$\delta\mathcal{L} = -\frac{1}{2}\frac{dF}{d|\mathbf{j}|}\frac{j^\alpha j^\beta}{|\mathbf{j}|}\delta g_{\alpha\beta} - \phi\delta(\nabla_\nu j^\nu)\,, \tag{4.35}$$

and

$$\begin{aligned}\phi\delta\left(\nabla_\nu j^\nu\right) &= \phi\delta\left(\frac{\partial_\nu\left(\sqrt{-g}j^\nu\right)}{\sqrt{-g}}\right) \\ &= -\frac{1}{2}g^{\alpha\beta}\delta g_{\alpha\beta}\nabla_\nu\left(\phi j^\nu\right) \\ &+ \frac{1}{2}\nabla_\nu\left(\phi j^\nu g^{\alpha\beta}\delta g_{\alpha\beta}\right)\,.\end{aligned} \tag{4.36}$$

Discarding the last term in Eq. (4.36) — this term gives rise to a vanishing surface term in Eq. (4.33) (since $\delta g_{\alpha\beta} = 0$ on the boundary) — and using Eqs. (4.4) and (4.5) it is simple to show that the energy-momentum tensor associated with the transformed Lagrangian defined in (4.32) is still given by Eq. (4.6). However, in this case the on-shell Lagrangian is equal to

$$\mathcal{L}_{\rm on-shell} = F = -\rho\,. \tag{4.37}$$

Using this result, in combination with Eq. (2.54), it is possible to write the on-shell Lagrangian as

$$\mathcal{L}_{\rm on-shell} = -mn - n\int^n \frac{p\left(n'\right)}{n'^2}dn' \tag{4.38}$$

(see also [333] for an alternative derivation of this result).

Other on-shell Lagrangians may be considered to describe the dynamics of a perfect fluid by adding surface terms to Eq. (4.16). However note that, although these different models are degenerate when considering minimally coupled matter fields, this degeneracy is generally broken in the presence of nonminimal coupling either to gravity [334–338] or to other fields [138, 339–346]. This issue is discussed in more detail in Thesis paper 3 [164].

4.2 Scalar field description of isentropic perfect fluids: specific models

4.2.1 Generalized Chaplygin gas

The original CG was first given in terms of a quintessence Lagrangian in the seminal paper [239]. However, in this derivation the scalar field was taken to be a function of time alone, meaning that the result relies on the assumption of perfect spatial homogeneity. Moreover, it is clear that Lagrangians with a canonical kinetic term cannot do the job: quintessence models have $c_{\mathrm{s}}^2 = 1$ irrespectively of the potential [347,348], while in the CG the sound speed strongly depends on the value of the energy density. Relaxing the assumption of homogeneity, it was shown in [240,349] that the CG and its generalization admit a scalar field theory description in terms of a purely kinetical Lagrangian (see also [232]).

As seen in Sec. 4.1.2, in pure k-essence models the Lagrangian is identified with the pressure of the fluid i.e. $\mathcal{L}(X) = p(X)$. From the relation given in Eq. (4.29) and using the GCG equation of state $p_{\mathrm{gcg}} = -A\rho_{\mathrm{gcg}}^{-\alpha}$ one obtains

$$p_{\mathrm{gcg}} = -A\left(2Xp_{\mathrm{gcg},X} - p_{\mathrm{gcg}}\right)^{-\alpha} \Rightarrow 2Xp_{\mathrm{gcg},X} = p_{\mathrm{gcg}} + \left(-\frac{p_{\mathrm{gcg}}}{A}\right)^{-\frac{1}{\alpha}} . \tag{4.39}$$

Up to an integration constant, the solution for the above equation is given by

$$p_{\mathrm{gcg}}(X) = \mathcal{L}_{\mathrm{gcg}}(X) = -A^{\frac{1}{1+\alpha}}\sqrt{\left(1-(2X)^{\frac{1+\alpha}{2\alpha}}\right)^{\frac{2\alpha}{1+\alpha}}}, \tag{4.40}$$

such that $0 < 2X < 1$, to ensure that p_{gcg} is a non-null real value. This restriction immediately satisfies the condition $X > 0$, which is needed in order for Eq. (4.40) to describe the GCG defined as an isentropic perfect fluid. From Eq. (4.29) one finds the GCG energy density

$$\rho_{\mathrm{gcg}} = A^{\frac{1}{1+\alpha}}\left(1-(2X)^{\frac{1+\alpha}{2\alpha}}\right)^{\frac{-1}{1+\alpha}} , \tag{4.41}$$

and the equation of state parameter

$$w_{\mathrm{gcg}} = -\left(1-(2X)^{\frac{1+\alpha}{2\alpha}}\right) , \tag{4.42}$$

while the sound speed squared is simply $c_{\mathrm{s[gcg]}}^2 = -\alpha w_{\mathrm{gcg}}$.

4.2.2 Logotropic model

In [284] it was shown that a logotropic equation of state (see Sec. 3.3) arises from a complex scalar field with a self-interacting potential. Being the logotropic model defined as an isentropic perfect fluid, a pure k-essence Lagrangian may also be obtained. The derivation is straightforward, though, to our knowledge, it has not been presented in the literature. For the sake of completeness we shall present it here.

Going back to the results presented in Sec. 3.3, let us rewrite Eq. (3.42) as

$$\rho = n_* \exp\left(\frac{p}{A_{\rm lgt}}\right) - p - A_{\rm lgt}\,. \tag{4.43}$$

Using Eq. (4.29) one gets

$$2Xp_{,X} = n_* \exp\left(\frac{p}{A_{\rm lgt}}\right) - A_{\rm lgt}\,, \tag{4.44}$$

with the solution

$$p\,(X) = \mathcal{L}\,(X) = -A_{\rm lgt} \ln\left(\frac{n_* + C\sqrt{X}}{A_{\rm lgt}}\right)\,, \tag{4.45}$$

where C is an integration constant. Hence, substituting Eq. (4.45) back in Eq. (4.43) one obtains the energy density as a function of X

$$\rho = A_{\rm lgt} \ln\left(\frac{n_* + C\sqrt{X}}{A_{\rm lgt}}\right) - A_{\rm lgt}\frac{C\sqrt{X}}{C\sqrt{X} + n_*}\,. \tag{4.46}$$

It is straightforward to check that by substituting

$$C\sqrt{X} = n_*\left(\frac{a^3}{\rho_0 \Omega_{\rm m0}} - 1\right) \tag{4.47}$$

into Eqs. (4.46) and (4.45), one recovers the correct equations for the evolution of $p\,(a)$ and $\rho\,(a)$ [given in Eqs. (3.49) and (3.50)].

4.2.3 Logarithmic CG

The Lagrangian $\mathcal{L}\,(X)$ for the logCG model (see Sec. 3.2.6) could in principle be found in the same way as shown in Secs. 4.2.1 and 4.2.2. Considering the logCG equation of state given in Eq. (3.27) one obtains the following relation between X and $p_{\rm log}$

$$\frac{dX}{X} = 2\frac{dp_{\rm log}}{p_{\rm log} + \rho_* e^{p_{\rm log}/\mathcal{A}}} \tag{4.48}$$

or, equivalently,

$$\ln\left(\frac{X}{X_*}\right) = 2\int_{p_*}^{p_{\rm log}} \frac{dp'}{p' + \rho_* e^{p'/\mathcal{A}}} \tag{4.49}$$

where X_* is an arbitrary integration constant. Unfortunately, the right hand side of Eq. (4.49) does not have a simple analytical solution. Nevertheless, in the following we shall obtain an analytical form of the Lagrangian valid in the non-relativistic regime, following our work [161].

Let us start by briefly review some aspects of the canonical theory for perfect fluids (see e.g. [350]). In classical fluid dynamics, the Hamiltonian of an irrotational perfect fluid is given by

$$H\left(\rho,\vartheta,t\right)=\int dx^{3}\mathcal{H}=\int dx^{3}\left(\frac{1}{2}\rho\,\vartheta_{,i}\vartheta^{,i}+V\left(\rho\right)\right)\,, \tag{4.50}$$

and $\mathcal{H}\left(\rho,\vartheta,x^{i},t\right)$ is equal to

$$\mathcal{H}\left(\rho,\vartheta,x^{i},t\right)=\dot{\rho}\,\vartheta-\mathcal{L}\left(\rho,\rho_{,i},\dot{\rho},x^{i},t\right)\,, \tag{4.51}$$

with the comma denoting the partial derivative with respect to one of the coordinates (e.g. $\vartheta_{,i}\equiv\partial\vartheta/\partial x^{i}$). Here $V\left(\rho\right)$ is some potential, ϑ a scalar field, and ρ is the density, as usual. Comparing Eqs. (4.50) and (4.51) the Lagrangian reads

$$\mathcal{L}=\dot{\rho}\vartheta-\frac{1}{2}\rho\,\vartheta_{,i}\vartheta^{,i}-V\left(\rho\right)\,, \tag{4.52}$$

with

$$\vartheta=\frac{\partial\mathcal{L}}{\partial\dot{\rho}}\,, \tag{4.53}$$

and, since ρ and ϑ are canonically conjugate we have

$$\dot{\vartheta}=\frac{\partial\mathcal{L}}{\partial\rho}=-\frac{1}{2}\vartheta_{,i}\vartheta^{,i}-\frac{dV}{d\rho}\,. \tag{4.54}$$

Assuming an irrotational flow (i.e. that the 3-velocity is written as the gradient of a scalar $v_{i}=\vartheta_{,i}$) the gradient of Eq. (4.54) may be identified with Euler's equation, provided that

$$\frac{d^{2}V}{d\rho^{2}}=\frac{1}{\rho}\frac{dp}{d\rho}\Leftrightarrow p=\rho\frac{dV}{d\rho}-V\,. \tag{4.55}$$

Specifying for the case of the logCG equation of state, Eqs. (3.27) and (4.55) imply that

$$\begin{aligned}V &= -\mathcal{A}\left[1+\ln\left(\frac{\rho_{\log}}{\rho_{*}}\right)\right]+D\rho_{\log} &(4.56)\\ &= -\mathcal{A}\left[1+\ln\left(\frac{\rho_{\log}}{\rho_{*}}\right)\right]\,, &(4.57)\end{aligned}$$

where D is an arbitrary integration constant which is taken to be zero. Using Eq. (4.54) one finds

$$\rho_{\log}=\mathcal{A}\left(\dot{\vartheta}+\frac{1}{2}\vartheta_{,i}\vartheta^{,i}\right)^{-1}\,. \tag{4.58}$$

One may now eliminate $\rho_{\log}$ from Eq. (4.52) to obtain a Lagrangian describing a perfect fluid with

a logCG equation of state in the non-relativistic regime

$$\mathcal{L}_{\mathrm{NR[log]}} = \mathcal{A}\left[\ln\left(\frac{\mathcal{A}}{\rho_*}\right) - \ln\left(\dot{\vartheta} + \frac{1}{2}\vartheta_{,i}\theta^{,i}\right)\right] . \tag{4.59}$$

Interestingly, Eq. (4.59) may also be obtained by considering the non-relativistic Lagrangian of the GCG [351]

$$\mathcal{L}_{\mathrm{NR[gcg]}} = -A^{\frac{1}{1+\alpha}}\left(\frac{1+\alpha}{\alpha}\right)^{\frac{\alpha}{1+\alpha}}\sqrt{\left(\dot{\vartheta} + \frac{1}{2}\vartheta_{,i}\vartheta^{,i}\right)^{\frac{2\alpha}{1+\alpha}}} + A\,, \tag{4.60}$$

which coincides with the Lagrangian proposed in [352] for the CG when $\alpha = 1$. Compared with the expression given in [351], Eq. (4.60) has an additional constant term A. Naturally, one may always add a constant term to the Lagrangian without affecting the dynamics of ϑ.

Performing a Puiseux series expansion of Eq. (4.60) around $\alpha = 0$ and keeping up to first order terms in α one obtains

$$\mathcal{L}_{\mathrm{NR[gcg]}} = \alpha A\left[\ln\left(\alpha\frac{A}{\rho_*}\right) - \ln\left(\dot{\vartheta} + \frac{1}{2}\vartheta_{,i}\vartheta^{,i}\right)\right] + \mathcal{O}\left(\alpha^2\right) . \tag{4.61}$$

In Sec. 3.2.6 we have introduced the logCG equation of state as a regularization of the limit $\alpha \to 0$ and $A \to \infty$ of the GCG model with finite $\mathcal{A} = \alpha A$. By the same token, one finds that the Lagrangian given in Eq. (4.61) is equal to that given in Eq. (4.59).

A similar approach to the one presented in this section was followed in [290], showing that the Lagrangian (4.59) is also recovered for the logotropic model (the logotropic model being a sub-class of the more general Anton-Schmidt fluids). This was to be expected, since the logCG and the logotropic model are degenerate in the non-relativistic limit.

4.3 One-parameter extension to the GCG model

The formalism introduced in the previous section shows how one may describe an isentropic perfect fluid using a scalar field theory whose dynamics is determined by a pure k-essence Lagrangian — the scalar field description of the GCG model is a well known example. In [161] we have considered an extension of Eq. (4.40) so as to accommodate different Lagrangians proposed in the literature to describe the GCG. The proposed Lagrangian is given by

$$\mathcal{L}_{\mathrm{ext}}\left(X\right) = -\rho_{\Lambda(\mathrm{eff})}\sqrt{\left(1 - \left(2X\right)^{\beta}\right)^{\frac{2\alpha}{1+\alpha}}}\,, \tag{4.62}$$

where $\alpha \geq 0$, $\beta > 0$ and $\rho_{\Lambda(\mathrm{eff})} > 0$ are model parameters. This model provides a simple extension to the GCG Lagrangian given in Eq. (4.40), the latter being recovered if $\beta = (1+\alpha)/(2\alpha)$ and $\rho_{\Lambda(\mathrm{eff})} = A^{\frac{1}{1+\alpha}}$. Eq. (4.62) is also general enough to include the Lagrangian proposed in [351], which corresponds to the choice $\beta = 1$. Using Eq. (4.29), the energy density can be computed

$$\rho_{\text{ext}} = \rho_{\Lambda(\text{eff})} \left[1 + (2X)^{\beta} \left(\beta \frac{2\alpha}{1+\alpha} - 1\right)\right] \left(1 - (2X)^{\beta}\right)^{-\frac{1}{1+\alpha}} , \tag{4.63}$$

being always positive for $\rho_{\Lambda(\text{eff})} > 0$, $\beta > 0$ and $\alpha \geq 0$. The corresponding equation of state parameter reads

$$w_{\text{ext}} = -\frac{1 - (2X)^{\beta}}{1 + (2X)^{\beta} \left(\beta \frac{2\alpha}{1+\alpha} - 1\right)} , \tag{4.64}$$

and is bounded between -1 and 0 ($-1 \leq w_{\text{ext}} \leq 0$). Using Eq. (4.30) the sound speed squared is given by

$$c^2_{\text{s[ext]}} = \alpha \frac{1 - (2X)^{\beta}}{1 + \left(1 + \alpha - \alpha (2X)^{\beta}\right) \left(\beta \frac{2\alpha}{1+\alpha} - 1\right)} , \tag{4.65}$$

with $c^2_{\text{s[ext]}} > 0$ at all times if $\beta > 1/2$. Given that, for $\beta > 1/2$, $c_s^2(X)$ is a monotonically decreasing function of X, the maximum sound speed

$$c^2_{\text{s[ext]}}(X = 0) = \frac{1}{2\beta - 1} , \tag{4.66}$$

is attained for $X = 0$. On the other hand, the requirement that $c^2_{\text{s[ext]}} \leq 1$ at all times is satisfied if $\beta \geq 1$. Hence, the conditions of classical stability and subluminal sound speed are satisfied by this class of models if $\beta \geq 1$.

Rewriting Eq. (4.63) as

$$\rho_{\text{ext}} = \rho_{\Lambda(\text{eff})} \left\{1 + \left[1 - \left(-\frac{p_{\text{ext}}}{\rho_{\Lambda(\text{eff})}}\right)^{\frac{1+\alpha}{\alpha}}\right] \left[\beta \frac{2\alpha}{1+\alpha} - 1\right]\right\} \left(-\frac{p_{\text{ext}}}{\rho_{\Lambda(\text{eff})}}\right)^{-\frac{1}{\alpha}} , \tag{4.67}$$

it is clear that only the particular choice $\beta = (1+\alpha)/2\alpha$ leads to the standard GCG equation of state (see Eq. (3.3)) with $A = \rho_{\Lambda(\text{eff})}^{1+\alpha}$, $w_{\text{ext}} = -A\rho_{\text{ext}}^{1+\alpha}$, and $c^2_{\text{s[ext]}} = -\alpha w_{\text{ext}}$, independently of the value of ρ_{ext}.

In Fig. 4.1 we plot the equation of state parameter w_{ext} (top plot) and the sound speed squared $c^2_{\text{s[ext]}}$ (bottom plot) as a function of the proper density ρ_{ext} for different values of β [$(\beta = (1+\alpha)/2\alpha$, solid line), ($\beta = 0.5$, dotted-dashed line), and ($\beta = 2$, dotted line)], while keeping α fixed to unity. The value of w_{ext} interpolates from $w_{\text{ext}} = 0$ ($\rho_{\text{ext}} \gg \rho_{\Lambda(\text{eff})}$) to $w_{\text{ext}} = -1$ ($\rho_{\text{ext}} = \rho_{\Lambda(\text{eff})}$) for any value of β (this is also true for any other value of $\alpha > 0$). For the represented values of β the sound speed $c_{\text{s[ext]}}$ is always a decreasing positive function of ρ_{ext}, with $c_{\text{s[ext]}} \to 0$ for $\rho_{\text{ext}}/\rho_{\Lambda(\text{eff})} \to \infty$ and $c_{\text{s[ext]}} \to (2\beta - 1)^{-1/2}$, for $\rho_{\text{ext}}/\rho_{\Lambda(\text{eff})} \to 1$ (note that this is true for any $\beta \geq 0.5$, and that if $\beta = 0.5$ then $c_{\text{s[ext]}} \to \infty$ for $\rho_{\text{ext}}/\rho_{\Lambda(\text{eff})} \to 1$).

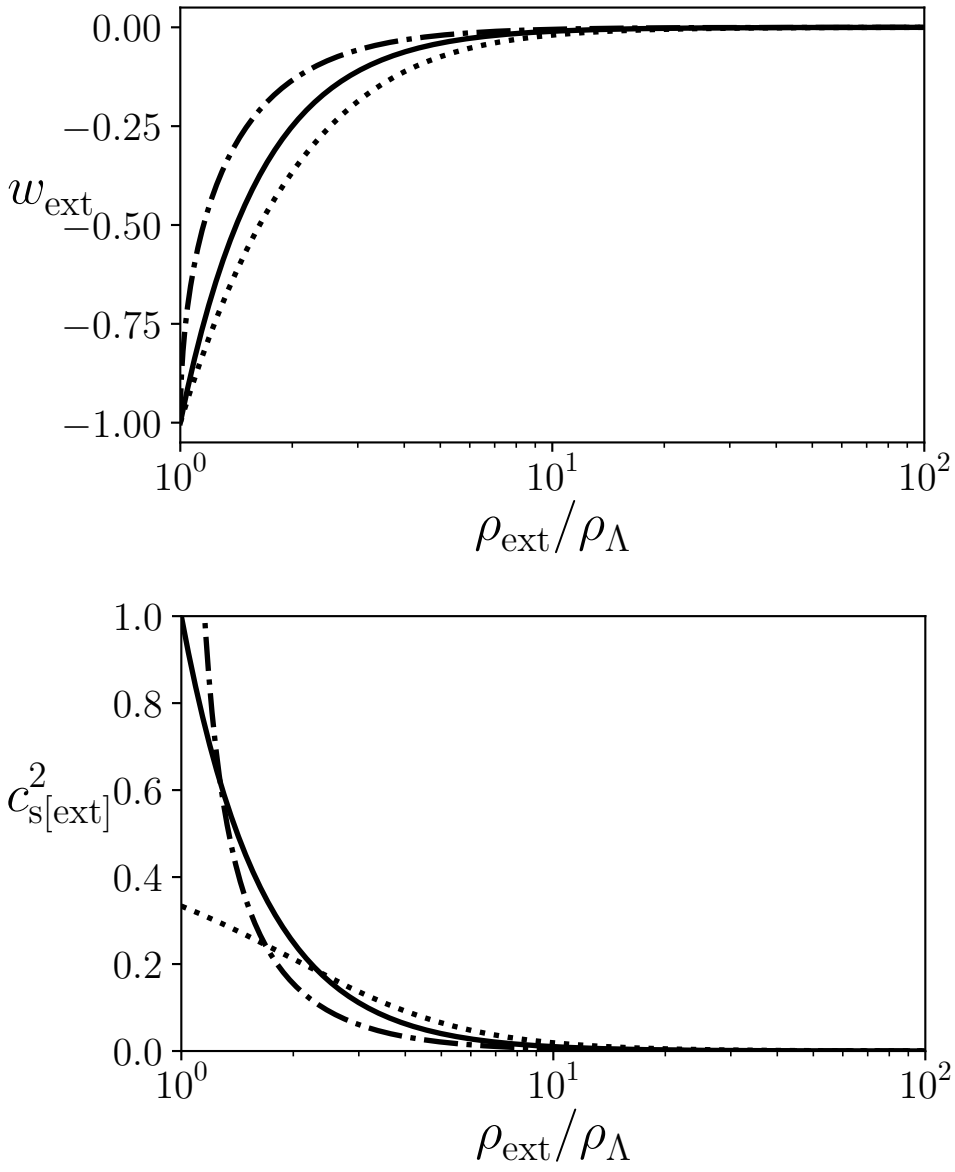

Figure 4.1: The equation of state parameter $w_{\rm ext}$ (top plot) and the sound speed squared $c^2_{\rm s[ext]}$ (bottom plot) as a function of $\rho_{\rm ext}$ for the GCG model ($\beta = (1+\alpha)/2\alpha$, solid line), $\beta = 0.5$ (dotted-dashed line), and $\beta = 2$ (dotted line). Here, α has been fixed to unity.

4.3.1 Non-relativistic limit

In the following we will show that the GCG equation of state is always recovered in the non-relativistic regime, independently of the value of β. Consider the (high-density) non-relativistic regime of Eq. (4.62) with $2X \sim 1$ and $\mathcal{L}_{\mathrm{NR[ext]}} = p_{\mathrm{ext}} \approx 0$. One can define a small parameter $\varepsilon = 1 - 2X \approx 0$ and Taylor expand at first order

$$(1-\varepsilon)^{\beta} \approx 1 - \varepsilon\beta\,. \tag{4.68}$$

Hence, considering the expansion above one obtains from Eq. (4.62)

$$\mathcal{L}_{\mathrm{NR[ext]}} = -\rho_{\Lambda(\mathrm{eff})}\beta^{\frac{\alpha}{1+\alpha}}\sqrt{(1-2X)^{\frac{2\alpha}{1+\alpha}}}\,, \tag{4.69}$$

which coincides with the Lagrangian considered in [351] to describe the generalized Chaplygin gas (and, consequently, also coincides with the non-relativistic CG Lagrangian in [352] when $\alpha = 1$).

The relation between p_{ext} and ρ_{ext} given in Eq. (4.67) may be written as

$$\frac{\rho_{\mathrm{ext}}}{\rho_{\Lambda(\mathrm{eff})}} = \left(-\frac{p_{\mathrm{ext}}}{\rho_{\Lambda(\mathrm{eff})}}\right)\left(\frac{2\alpha}{1+\alpha} - 1\right) + \beta\frac{2\alpha}{1+\alpha}\left(-\frac{p_{\mathrm{ext}}}{\rho_{\Lambda(\mathrm{eff})}}\right)^{-\frac{1}{\alpha}}\,. \tag{4.70}$$

Notice that the first term on the right hand side of Eq. (4.70) is negligible in the non relativistic regime (since $p_{\mathrm{ext}} \approx 0$), thus leading to the standard GCG equation of state $p_{\mathrm{gcg}} = -A\rho_{\mathrm{gcg}}^{-\alpha}$ with

$$A = \rho_{\Lambda(\mathrm{eff})}^{1+\alpha}\left(\frac{2\alpha}{1+\alpha}\beta\right)^{\alpha}\,. \tag{4.71}$$

Therefore, the GCG equation of state is recovered in the non-relativistic regime for any $\beta > 0$, meaning that the construction of a non-relativistic GCG Lagrangian is, in this sense, not unique. The model we have defined in Eq. (4.62) encompasses an extended family of models that reduce to the GCG in the non-relativistic limit.

Coming full circle, the non-relativistic Lagrangian description of the GCG proposed in [351] may be obtained from Eq. (4.69) considering the identification $\phi = -t + \vartheta$ (where $v_i = \vartheta_{,i}$ for an irrotational flow, as in Sec. 4.2.3)

$$\mathcal{L}_{\mathrm{NR[ext]}}|_{\phi\to t-\vartheta} = -\rho_{\Lambda(\mathrm{eff})}\beta^{\frac{\alpha}{1+\alpha}}\sqrt{\left[1 - 2\left(\frac{\dot{\vartheta}^2}{2} - \dot{\vartheta} + \frac{1}{2} - \frac{\vartheta^{,i}\vartheta_{,i}}{2}\right)\right]^{\frac{2\alpha}{1+\alpha}}}\,, \tag{4.72}$$

Keeping only linear terms on $\dot{\vartheta}$ and using Eq. (4.71) one gets

$$\mathcal{L}_{\mathrm{NR[ext]}}|_{\phi\to t-\vartheta} \sim -\rho_{\Lambda(\mathrm{eff})}\,(2\beta)^{\frac{\alpha}{1+\alpha}}\sqrt{\left(\dot{\vartheta}+\frac{1}{2}\vartheta_{,i}\vartheta^{,i}\right)^{\frac{2\alpha}{1+\alpha}}} \tag{4.73}$$

$$= -A^{\frac{1}{1+\alpha}}\left(\frac{1+\alpha}{\alpha}\right)^{\frac{\alpha}{1+\alpha}}\sqrt{\left(\dot{\vartheta}+\frac{1}{2}\vartheta_{,i}\vartheta^{,i}\right)^{\frac{2\alpha}{1+\alpha}}}\,, \tag{4.74}$$

cf. Eq. (4.60).

4.3.2 Background cosmology

In this subsection we focus on the background evolution of the extended CG scalar field model defined by Eq. (4.62), and restrict the discussion to $\beta \geq 1$ in order to avoid superluminal sound speeds. The evolution of the scalar field is determined by the equation of motion (4.27) which, at the background level, is a function of time alone i.e. $\phi = \phi\,(t)$. For a generic Lagrangian $\mathcal{L} = \mathcal{L}\,(X)$, Eq. (4.27) may be written as

$$\nabla_\mu\left(\mathcal{L}_{,X}\nabla^\mu\right) = \mathcal{L}_{,XX}\nabla_\mu X\nabla^\mu\phi + \mathcal{L}_{,X}\Box\phi\,, \tag{4.75}$$

where $\Box \equiv g^{\mu\nu}\nabla_\mu\nabla_\nu$ is the d'Alembert operator

$$\Box\phi = g^{\mu\nu}\nabla_\mu\left(\partial_\nu\phi\right) = g^{\mu\nu}\left[\partial_\mu\left(\partial_\nu\phi\right) - \Gamma^\gamma_{\mu\nu}\partial_\gamma\phi\right]\,, \tag{4.76}$$

and the covariant derivative of X is given by

$$\nabla_\mu X = -\frac{1}{2}g^{\alpha\beta}\nabla_\mu\left(\nabla_\alpha\phi\nabla_\beta\phi\right) \tag{4.77}$$

$$= -g^{\alpha\beta}\nabla_\alpha\phi\nabla_\mu\left(\nabla_\beta\phi\right) \tag{4.78}$$

$$= -g^{\alpha\beta}\partial_\alpha\phi\left[\partial_\mu\left(\partial_\beta\phi\right) - \Gamma^\gamma_{\mu\beta}\partial_\gamma\phi\right]\,, \tag{4.79}$$

where we now explicitly write that $\nabla_\mu\phi = \partial_\mu\phi$. Using the Christoffel symbols computed in Eqs. (2.15)-(2.18) for a flat FLRW metric one gets the following equation of motion determining the background dynamics of ϕ

$$\ddot{\phi} + 3H\dot{\phi}\frac{\mathcal{L}_{,X}}{\mathcal{L}_{,X}+\dot{\phi}^2\mathcal{L}_{,XX}} = 0\,, \tag{4.80}$$

or, alternatively

$$\dot{X} + 6HXc_{\mathrm{s}}^2 = 0\,, \tag{4.81}$$

with the sound speed squared being given by Eq. (4.30). Changing the independent variable from t to a, Eq. (4.81) can be integrated exactly for an arbitrary $\mathcal{L}\,(X)$ [251, 270]

$$X\mathcal{L}_{,X}^{2} \propto a^{-6}\,. \tag{4.82}$$

Hence, one can now take Eq. (4.62) and determine the evolution of $X\left(a\right)$ for the extended CG model

$$\frac{\left(1-\left(2X\right)^{\beta}\right)^{-\frac{2}{1+\alpha}}}{\left(2X\right)^{1-2\beta}} = \frac{\left(1-\left(2X_{0}\right)^{\beta}\right)^{-\frac{2}{1+\alpha}}}{\left(2X_{0}\right)^{1-2\beta}}a^{-6}\,, \tag{4.83}$$

where X_0 is fixed using Eq. (4.63)

$$\frac{\rho_{\mathrm{ext0}}}{\rho_{\Lambda(\mathrm{eff})}} = \left[1+\left(2X_{0}\right)^{\beta}\left(\beta\frac{2\alpha}{1+\alpha}-1\right)\right]\left(1-\left(2X_{0}\right)^{\beta}\right)^{-\frac{1}{1+\alpha}}\,. \tag{4.84}$$

Observe that, in general, X and X_0 cannot be found explicitly from Eqs. (4.83) and (4.84). A notable exception is the GCG i.e. for $\beta = \left(1+\alpha\right)/2\alpha$ we have

$$\left(2X\right)^{-\frac{1+\alpha}{2\alpha}} - 1 = \left[\left(2X_{0}\right)^{-\frac{1+\alpha}{2\alpha}} - 1\right]a^{3(1+\alpha)}\,, \tag{4.85}$$

and

$$1-\left(2X_{0}\right)^{\frac{1+\alpha}{2\alpha}} = \left(\frac{\rho_{\Lambda(\mathrm{eff})}}{\rho_{\mathrm{gcg0}}}\right)^{(1+\alpha)} = \overline{A}\,. \tag{4.86}$$

For the extended CG model superluminal sound speeds can be avoided at all times if $\beta \geq 1$ for any $\alpha > 0$ (remember that in the case of the GCG this condition can only be fulfilled if $\alpha \leq 1$). Considering models with $\alpha \gg 1$ (formally we take $\alpha \to \infty$) we may write Eq. (4.83) as

$$X \approx X_{0}a^{-\frac{6}{2\beta-1}}\,, \tag{4.87}$$

leading to

$$\rho_{\mathrm{ext}} \approx \rho_{\Lambda(\mathrm{eff})} + \left(\rho_{\mathrm{ext0}} - \rho_{\Lambda(\mathrm{eff})}\right)a^{-\frac{6\beta}{2\beta-1}} = \rho_{\mathrm{ext0}}\left[\frac{\Omega_{\Lambda(\mathrm{eff})}}{\Omega_{\mathrm{ext0}}} + \left(1-\frac{\Omega_{\Lambda(\mathrm{eff})}}{\Omega_{\mathrm{ext0}}}\right)a^{-\frac{6\beta}{2\beta-1}}\right]\,. \tag{4.88}$$

Thus, in the limit of large values of α, $\rho_{\mathrm{ext}} \propto a^{-\frac{6\beta}{2\beta-1}}$ at early times, reaching a minimum energy density $\rho_{\mathrm{ext}} \to \rho_{\Lambda(\mathrm{eff})}$ as $a \to \infty$. For $\beta = 1$ the model can be interpreted as the sum of a stiff fluid (i.e. a fluid with equation of state parameter $w = 1$) and a cosmological constant. On the other hand, the ΛCDM model is found in the limit $\beta \to \infty$, with the present CDM density fraction being $\Omega_{\mathrm{cdm0}} = \left(1-\Omega_{\Lambda(\mathrm{eff})}/\Omega_{\mathrm{ext0}}\right)$. Actually, the extended CG model reduces to ΛCDM in the limit $\beta \to \infty$ independently of the value of α: from Eq. (4.66), the maximum sound speed attained is solely regulated by β, and one has $c_{\mathrm{s[ext]}}^{2} \to 0$ as $\beta \to \infty$.

For arbitrary values of $\alpha > 0$ and $\beta \geq 1$, Eqs. (4.83) and (4.84) have to be solved numerically. We have implemented a root finding algorithm using Ridder's method [353] in `CLASS` (see Appendix A.1) to find X_0 (given the value of $\rho_{\rm ext0}$ and the model parameters α, β and $\rho_{\Lambda({\rm eff})}$) and $X\,(a)$, which is then used to compute the evolution of $\rho_{\rm ext}\,(a)$.

4.3.3 SNIa constraints

We constrain the parameters of the extended CG (taken as a UDE model) against the SNIa Pantheon data [261] (see Appendix B.1) considering a cosmology with $\Omega_{\rm ext} + \Omega_{\rm b} = 1$. Given the required lower bounds $\alpha > 0$, $\beta \geq 1$ and $\rho_{\Lambda({\rm eff})} > 0$ we choose to work with the quantities $e^{-\alpha}$, $1/\beta$ and $\rho_{\Lambda({\rm eff})}/\rho_0$ to compose our parameter space. In this way, flat priors can be assumed in the open interval $]0,1[$ for $e^{-\alpha}$ and $1/\beta$, while the remaining cosmological parameters are fixed to the standard values (namely $H_0 = 67.3\,{\rm km\,s^{-1}\,Mpc^{-1}}$ and $\Omega_{\rm b0} = 0.0487$). The 2-dimensional contours and the marginalized likelihoods for all three parameters are shown in Fig. 4.2.

The results can be understood in terms of the correspondent values of $w_{\rm ext0}$, which are found from the relation

$$\frac{\rho_{\Lambda({\rm eff})}}{\rho_{\rm ext0}} = -w_{\rm ext0} F_0^{\frac{\alpha}{1+\alpha}}\,, \tag{4.89}$$

where

$$F_0 = 1 - \frac{(1+w_{\rm ext0})\,(1+\alpha)}{2\alpha\beta w_{\rm ext0}}\,, \tag{4.90}$$

obtained from Eqs. (4.64) and (4.84). The solutions of Eq. (4.89) as a function of $e^{-\alpha}$ and $1/\beta$ are presented in Fig. 4.3 for $\rho_{\Lambda({\rm eff})} = 0.67\rho_0$ (black lines) and $\rho_{\Lambda({\rm eff})} = 0.86\rho_0$ (red lines) where, for each case, we show three curves along which $w_{\rm ext0}$ has a constant value. Comparing the pairs of neighboring red and black lines (covering similar regions of the parameter space), one notes that models with higher $\rho_{\Lambda({\rm eff})}/\rho_0$ have lower $w_{\rm ext0}$ (i.e. these models get closer to $w_{\rm ext0} = -1$). Overall, larger values of β also correspond to a lower value of $w_{\rm ext0}$ if α is sufficiently large (in this region the value of $w_{\rm ext0}$ is mostly insensitive to α). Hence, one may have the same value for $w_{\rm ext0}$ by increasing (decreasing) $\rho_{\Lambda({\rm eff})}/\rho_0$ while decreasing (increasing) β. The 2-dimensional constraints from the panel $\left(\rho_{\Lambda({\rm eff})}/\rho_0, 1/\beta\right)$ in Fig. 4.2 show this degeneracy between both parameters. On the other hand, for $\alpha \lesssim 1$ small changes on α can lead to very different values of $w_{\rm ext0}$. These variations can, however, be compensated by changes on β and $\rho_{\Lambda({\rm eff})}$, in order to have a $w_{\rm ext0}$ consistent with the observations; notice the enlargement of the likelihood regions as $e^{-\alpha} \to 1$ (i.e. as $\alpha \to 0$) in the panels $\left(\rho_{\Lambda({\rm eff})}/\rho_0, e^{-\alpha}\right)$ and $(1/\beta, e^{-\alpha})$.

The results show that the parameter $\rho_{\Lambda({\rm eff})}$ is constrained to the region between $\sim 0.67\rho_0$ and $\sim 0.86\rho_0$ at 95% C.L., with a mean value of $\sim 0.77\rho_0$. All values $\alpha > 0$ and $\beta \geq 1$ are consistent with the SNIa data at the 95% level, with the maximum likelihood for $e^{-\alpha}$ and $1/\beta$ being found for $\alpha \to 0$ and $\beta \to \infty$, respectively. The best-fit has the same minimum χ^2 that was obtained in the GCG SNIa analysis presented in Sec. 3.2.2, i.e. $\chi^2_{\rm min} = 1027$. This point of the parameter space

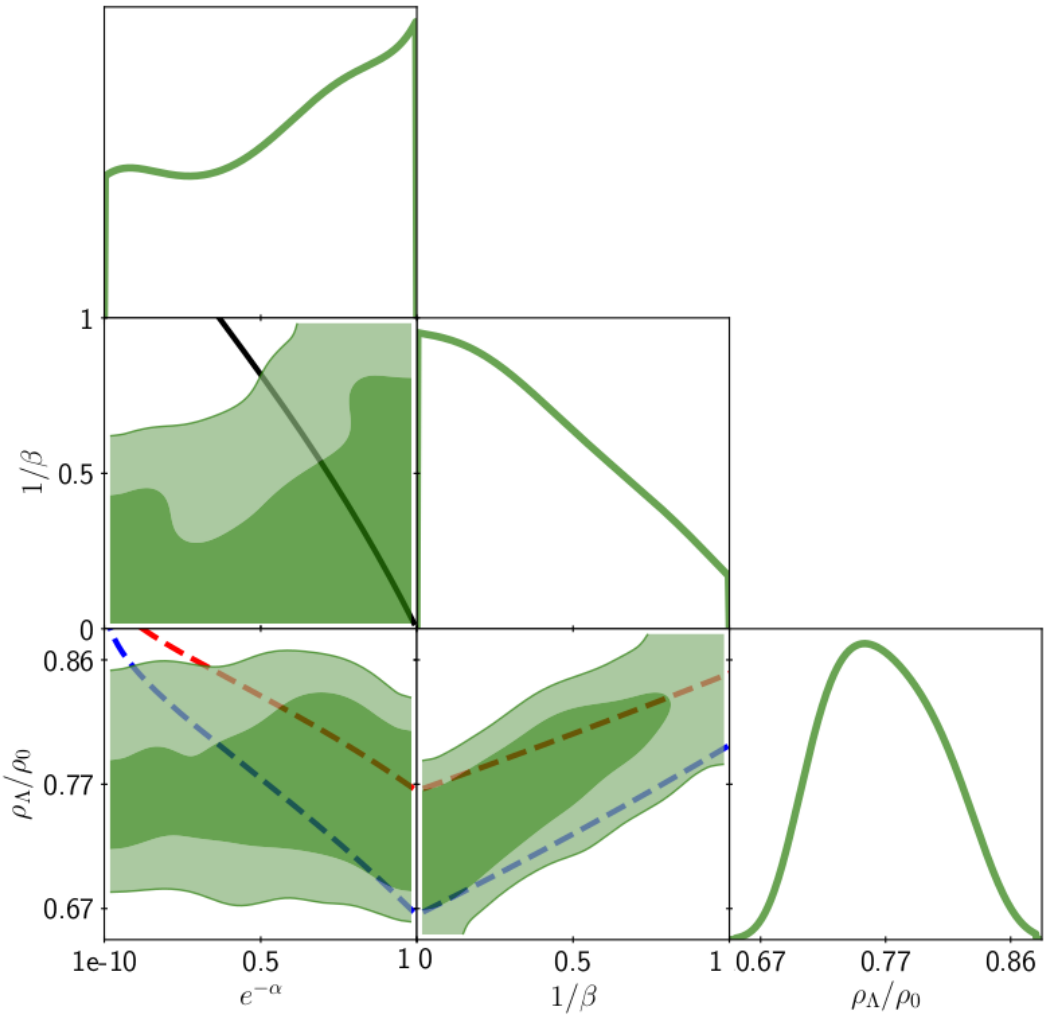

Figure 4.2: SNIa constraints on the parameters $\rho_{\Lambda(\text{eff})}/\rho_0$, $e^{-\alpha}$ and β using the Pantheon data set, where darker and lighter regions correspond to the 68% and 95% confidence level, respectively. The top plots in each column show the 1-dimensional likelihood, marginalized over the remaining parameters. The black line shown in the panel $(1/\beta,\, e^{-\alpha})$ satisfies the relation $\beta = (1+\alpha)/2\alpha$, thus corresponding to the GCG model. The dashed-lines represent GCG models with $\overline{A} = 0.7$ (blue lines) and $\overline{A} = 0.8$ (red lines) as given by Eq. (4.86).

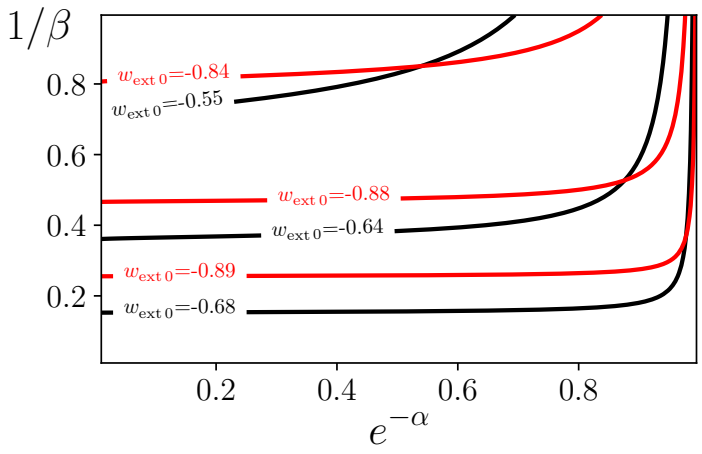

Figure 4.3: Lines of constant $w_{\rm ext0}$ as a function of $e^{-\alpha}$ and $1/\beta$. We choose to plot the lines for the values $\rho_{\Lambda({\rm eff})} = 0.67\rho_0$ (black lines) and $\rho_{\Lambda({\rm eff})} = 0.86\rho_0$ (red lines), which correspond approximately to the lower and upper limit of the 95% C.L. interval estimated from the SNIa constraints (see Fig. 4.2).

has $w_{\rm ext0} \sim -0.75$, corresponding to an effective equation of state parameter of $w_0 = \Omega_{\rm ext0} w_{\rm ext0} \sim -0.72$ (which is consistent with the mean value from the Table 5. in [261] for the ΛCDM model).

4.3.4 Structure formation

In the extended CG model the maximum sound speed, attained as $a \to \infty$, depends only on β. Since $c_{\rm s[ext]}\,(a)$ is a monotonically increasing function, the Jeans length may be taken to be arbitrarily small if β is large enough. Hence, density perturbations can grow on sufficiently large scales independently of the value of α, even when $w_{\rm ext0} \sim -1$, as long as β is sufficiently large. Combining Eqs. (4.65), (4.84) and (4.89), one finds the present sound speed to be given by

$$c^2_{\rm s[ext]0} = \alpha \frac{1}{F_0 + (F_0 + \alpha)\left(\beta \frac{2\alpha}{1+\alpha} - 1\right)}\,. \tag{4.91}$$

Deep in the matter era, linear perturbations can grow provided that $c^2_{\rm s[ext]} \lesssim (3/2)a^2H^2/k^2$ [*cf.* Eq. (3.17)]. Taking $F_0 = 1$, $H_0 = h/3000\,{\rm Mpc}^{-1}$ and $\alpha = 1$, one estimates that $\beta \gtrsim 10^5$ is required for the growth of linear density perturbations on scales larger than $k = 0.1\ h\ {\rm Mpc}^{-1}$.

We compute the matter power spectrum using our implementation of the extended CG on the `CLASS` code (see A.1), assuming a Universe containing the standard content (i.e. relativistic species and baryons) and an extended CG component with $\alpha = 1$. The usual cosmological parameters take their standard values, with the exception of the amplitude of the power spectrum, which is normalized such that all models have the same power on very large scales. The density of the extended CG fulfills the relation $\Omega_{\rm ext} + \Omega_{\rm r} + \Omega_{\rm b} = 1$ for a flat FLRW metric, and $\rho_{\Lambda({\rm eff})}$ is fixed such that $w_0 \sim -0.7$. The results plotted in Fig. 4.4 show that an agreement with the ΛCDM result on linear scales is attained for an extended CG model with $\beta = 5 \times 10^5$. Large oscillations of the matter spectrum would rule out completely smaller values of β, as shown in the figure for

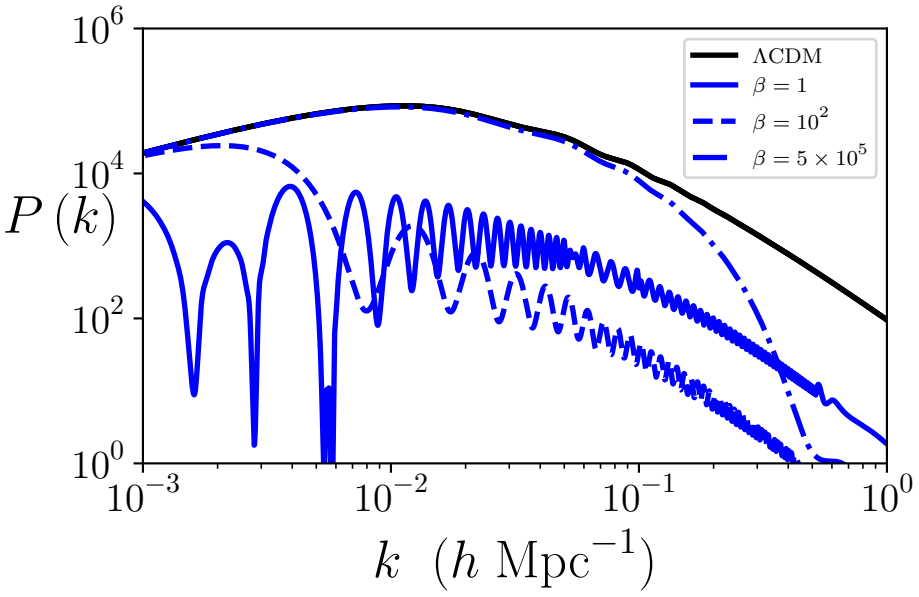

Figure 4.4: The linear matter power spectra at the present epoch for the extended CG + baryons (blue lines) normalized to the ΛCDM model (black line) amplitude on large scales, for different choices of β (see legend) and $\alpha = 1$. The parameter $\rho_{\Lambda(\mathrm{eff})}$ is fixed such that $w_0 \sim -0.7$. For increasingly larger values of β the spectra gets closer to the ΛCDM prediction, with the oscillations appearing on ever smaller scales.

$\beta = 1$ (corresponding in this case to the original CG model, i.e. $\alpha = 1$) and $\beta = 10^2$. Notice that, since in this analysis α has been fixed to unity, all these models have a CG equation of state in the non-relativistic limit, as we have shown in Sec. 4.3.1.

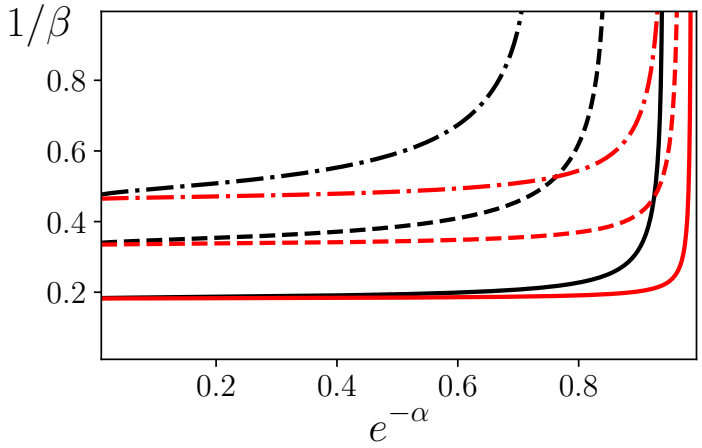

Figure 4.5: Contour lines of constant $c^2_{\mathrm{s[ext]}0} = 0.1$ (solid lines), 0.2 (dashed lines), and 0.3 (dotted-dashed lines), as a function of $e^{-\alpha}$ and $1/\beta$. The black and red lines correspond to the fixed values of $w_{\mathrm{ext}0} = -0.7$ and $w_{\mathrm{ext}0} = -0.8$, respectively.

While models with $\beta \to \infty$ are assured to have $c_{\mathrm{s[ext]}} \to 0$ at all times, one can also have arbitrarily small sound speeds at the present time for small β (i.e. models with a large maximum $c_{\mathrm{s[ext]}}$), provided that α is close enough to zero. This relation between α and β is clear in Fig. 4.5, where

we plot lines of constant $c^2_{\mathrm{s[ext]0}}$ (from Eq. (4.91)) as a function of $e^{-\alpha}$ and $1/\beta$, for the values $w_{\mathrm{ext0}} = -0.7$ (black lines) and $w_{\mathrm{ext0}} = -0.8$ (red lines).

Chapter 5

Mapping DE models into Unified Dark Energy

As we have seen so far, the main feature of UDE models is that of mimicking DE and CDM with a single underlying perfect fluid or scalar field. In this section we follow Sec. IV of the published Thesis paper 4. [164], where we show how a DE scalar field model can be mapped into a UDE model, with both Lagrangians having the same value on-shell.

5.1 Mapping pure k-essence models: trivial case

Before moving to the specificities of this mapping, let us start by considering the following construction of a UDE Lagrangian

$$\mathcal{L}_{\rm ude} = \mathcal{L}_{\rm de} + \mathcal{L}_{\rm cdm}\,. \tag{5.1}$$

Assuming that $\mathcal{L}_{\rm de} \equiv \mathcal{L}_{\rm de}\,(X)$ is an arbitrary pure kinetic DE Lagrangian and that $\mathcal{L}_{\rm cdm}$ is a Lagrangian describing CDM, one has that the ratio between $\mathcal{L}_{\rm cdm}$ and $\mathcal{L}_{\rm de}$ vanishes on-shell (or is extremely small), so that the contribution of $\mathcal{L}_{\rm cdm}$ to the total pressure can be neglected. Therefore, the UDE Lagrangian $\mathcal{L}_{\rm ude}$ describes a fluid with proper pressure $p_{\rm ude} = \mathcal{L}_{\rm ude(on-shell)} = \mathcal{L}_{\rm de(on-shell)} = p_{\rm de}$ and energy density

$$\rho_{\rm ude} = \rho_{\rm de} + \rho_{\rm cdm}\,, \tag{5.2}$$

where $\rho_{\rm de} = 2X\mathcal{L}_{{\rm de},X} - \mathcal{L}_{\rm de}$. Hence, the new Lagrangian may be regarded as a UDE model provided that, at late times, $w_{\rm de} = p_{\rm de}/\rho_{\rm de} \sim -1$ or, equivalently, $\rho_{\rm de} = \mathcal{L}_{\rm de(on-shell)}/w_{\rm de} \sim -\mathcal{L}_{\rm de(on-shell)}$. Now one has to define a suitable Lagrangian to describe CDM.

5.1.1 CDM via a Lagrange multiplier

A possible choice for $\mathcal{L}_{\rm cdm}$, discussed in [303, 354], would be to consider a canonical Quintessence field constrained by a Lagrange multiplier λ

$$\mathcal{L}_{\rm cdm} = \lambda \left(X - V \left(\phi \right) \right) . \tag{5.3}$$

The equation of motion

$$\frac{\delta \mathcal{L}_{\rm cdm}}{\delta \lambda} = 0 \rightarrow X - V \left(\phi \right) = 0 \, , \tag{5.4}$$

ensures that the constraint $X = V(\phi)$ is always satisfied on-shell, thus implying that $\mathcal{L}_{\rm cdm(on-shell)} = 0$ or, equivalently, from Eq. (5.1), that $p_{\rm ude} = \mathcal{L}_{\rm ude(on-shell)} = \mathcal{L}_{\rm de(on-shell)} = p_{\rm de}$. The CDM energy density is given by Eq. (4.29) as usual

$$\rho_{\rm cdm} = 2X\mathcal{L}_{\rm cdm,\mathcal{X}} - \mathcal{L}_{\rm cdm} = \lambda \left(X + V \left(\phi \right) \right) = 2\lambda X \, , \tag{5.5}$$

while the 4-velocity can be written as

$$u^{\alpha} = - \frac{\nabla^{\alpha} \phi}{\sqrt{2X}} = - \frac{\nabla^{\alpha} \phi}{\sqrt{2V \left(\phi \right)}} \, , \tag{5.6}$$

so that the constraint $X = V \left(\phi \right)$ gives

$$- \frac{1}{2} \nabla^{\alpha} \phi \nabla_{\alpha} \phi = V \left(\phi \right) \Leftrightarrow u^{\alpha} \nabla_{\alpha} \phi = \sqrt{2V \left(\phi \right)} \, . \tag{5.7}$$

Regarding the dynamics of the Lagrange multiplier λ, its evolution is such as to ensure that the energy-momentum tensor of the UDE fluid

$$T^{\alpha \beta}_{\rm cdm} = \lambda \nabla^{\alpha} \phi \nabla^{\beta} \phi \, , \tag{5.8}$$

is covariantly conserved. In order to stay in the realm of irrotational perfect fluid models with conserved particle number and constant entropy per particle, we want the Lagrangian to depend solely on the kinetic term. Notice that for the particular case with $V(\phi) = V_0 = \text{const}$ one would get $X = V_0 = \text{const}$, thus implying that $p_{\rm ude} = \mathcal{L}_{\rm de(on-shell)}$ would be a constant [since we are assuming that $\mathcal{L}_{\rm de} = \mathcal{L}_{\rm de} \left(X \right)$]. Hence, such UDE model would be totally equivalent to ΛCDM [232, 233, 260].

5.1.2 CDM via pure k-essence

An alternative would be to consider a class of purely kinetic Lagrangians given by

$$\mathcal{L} \left(X \right) = p \left(X \right) = A X^{\gamma} \, , \tag{5.9}$$

where A and γ are positive real constants, and the energy density is

$$\rho = 2X\mathcal{L}_{,X} - \mathcal{L} = (2\gamma - 1)\, AX^{\gamma}\,, \tag{5.10}$$

For this class of models the equation of state parameter is a constant determined by γ

$$w \equiv \frac{p}{\rho} = \frac{1}{2\gamma - 1}\,. \tag{5.11}$$

Since we have $w \to 0$ for $\gamma \to \infty$, in this limit the scalar field mimicks pressureless dust. Thus, another possible choice for $\mathcal{L}_{\rm cdm}$ would be

$$\mathcal{L}_{\rm cdm}\,(X) = \lim_{\gamma\to\infty} A(\gamma)X^{\gamma}\,. \tag{5.12}$$

The function $A(\gamma)$ is chosen in such a way that $p_{\rm cdm}$ vanishes at every space time point in this limit. On the other hand, the CDM density

$$\rho_{\rm cdm} = \lim_{\gamma\to\infty} (2\gamma - 1)\, A(\gamma)X^{\gamma} \tag{5.13}$$

is essentially unrestricted. Note that by choosing $A(\gamma)$ such that the function $C(\gamma) = (2\gamma - 1)A(\gamma)$ tends to a constant C_∞ in the $\gamma \to \infty$ limit, X must be equal to unity in this limit. However, the density may take any value in this limit since 1^∞ is indeterminate. The equation of motion of the scalar field

$$\begin{aligned}\left(\mathcal{L}_{,X}g^{\alpha\beta} + \mathcal{L}_{,XX}\nabla^{\alpha}\phi\nabla^{\beta}\phi\right)\nabla_{\alpha}\nabla_{\beta}\phi = \\ = \left(g^{\alpha\beta} + \frac{\gamma - 1}{X}\nabla^{\alpha}\phi\nabla^{\beta}\phi\right)\nabla_{\alpha}\nabla_{\beta}\phi = 0\end{aligned} \tag{5.14}$$

reduces to

$$\nabla^{\alpha}\phi\nabla^{\beta}\phi\nabla_{\alpha}\nabla_{\beta}\phi = -\nabla^{\alpha}\phi\nabla_{\alpha}X = 0\,, \tag{5.15}$$

for $\gamma \to \infty$, thus implying that the equation of motion preserves the condition $X = 1$ in this limit. Furthermore, the condition $X > 0$ is always satisfied, so this model describes the dynamics of a perfect fluid. Notice that this UDE model would have $p_{\rm ude} = \mathcal{L}_{\rm de(on-shell)}\,(X = 1) = \text{const}$ and, therefore, would again be totally equivalent to ΛCDM.

5.2 Mapping pure k-essence models: general case

5.2.1 Mapping the Lagrangian

Let us consider an isentropic perfect fluid with proper pressure and density $p = p(\mu)$, $\rho = \rho(\mu)$ (with $\mu = \mu(n)$), and 4-velocity $\mathbf{u}$ at each spacetime point. The transformation

$$\widetilde{\rho} = \rho + mn\,, \tag{5.16}$$

$$\widetilde{\mu} = \mu + m\,, \tag{5.17}$$

at every point with the 4-velocity unchanged leads to a different perfect fluid, but leaves the proper pressure unaltered, so that $\widetilde{p}\,(\widetilde{\mu}) = p\,(\mu)$ (here, $m > 0$ is a constant) — i.e. the transformations given in Eqs. (5.16) and (5.17) leave Eq. (4.23) invariant. Note that, if the original fluid represented a constant density with $p = -\rho = \text{const}$ (a cosmological constant), then this transformation would simply add a pressureless dust-like component to the original dark energy fluid.

Starting with a perfect fluid described by a purely kinetic Lagrangian $\mathcal{L}(X) = p(X)$ with $\mu^2 = 2X$, let us write the Lagrangian of the new fluid as $\widetilde{\mathcal{L}}(\widetilde{X}) = \mathcal{L}(X)$ and its 4-velocity as $\widetilde{u}^\alpha = -\nabla^\alpha\widetilde{\phi}/\sqrt{2\widetilde{X}}$, where $\widetilde{X} = -\nabla_\alpha\widetilde{\phi}\nabla^\alpha\widetilde{\phi}/2$ and $\widetilde{\mu}^2 = 2\widetilde{X}$. Hence, Eq. (5.17) is just $\sqrt{2\widetilde{X}} = \sqrt{2X} + m$, and we get the following relation between the kinetic terms X and $\widetilde{X}$:

$$\widetilde{X} = X + m\sqrt{2X} + \frac{m^2}{2}\,. \tag{5.18}$$

Applying the previous transformations, the energy-momentum tensor of the new fluid may be written as [*cf.* Eq. (4.28)]

$$\begin{aligned}
\widetilde{T}^{\alpha\beta} &= (\widetilde{\rho} + \widetilde{p})\,\widetilde{u}^\alpha\widetilde{u}^\beta + \widetilde{p}g^{\alpha\beta} \\
&= 2\widetilde{X}\widetilde{\mathcal{L}}_{,\widetilde{X}}\widetilde{u}^\alpha\widetilde{u}^\beta + \widetilde{\mathcal{L}}g^{\alpha\beta} = \widetilde{\mathcal{L}}_{,\widetilde{X}}\nabla^\alpha\widetilde{\phi}\nabla^\beta\widetilde{\phi} + \widetilde{\mathcal{L}}g^{\alpha\beta} \\
&= \sqrt{2X}\left(\sqrt{2X} + m\right)\mathcal{L}_{,X}u^\alpha u^\beta + \mathcal{L}g^{\alpha\beta}\,, \\
&= T^{\alpha\beta} + T_m^{\alpha\beta}\,,
\end{aligned} \tag{5.19}$$

where $T^{\alpha\beta}$ is the energy-momentum tensor of the original fluid. For the additional dustlike component one has (remember that $n = \sqrt{2X}\mathcal{L}_{,X}$)

$$T_m^{\alpha\beta} = \rho_\mathrm{m}u^\alpha u^\beta\,, \qquad \rho_\mathrm{m} = mn = m\sqrt{2X}\mathcal{L}_{,X}\,, \tag{5.20}$$

where we have used Eq. (5.18) and the relations

$$X_{,\widetilde{X}} = \left(\widetilde{X}_{,X}\right)^{-1} = \frac{\sqrt{2X}}{\sqrt{2X} + m}\,, \tag{5.21}$$

$$u^\alpha = -\frac{\nabla^\alpha\phi}{\sqrt{2X}} = -\frac{\nabla^\alpha\widetilde{\phi}}{\sqrt{2\widetilde{X}}} = \widetilde{u}^\alpha\,. \tag{5.22}$$

Thus, Eq. (5.22) is equivalent to

$$\nabla^\alpha \widetilde{\phi} = \frac{\sqrt{2X}+m}{\sqrt{2X}} \nabla^\alpha \phi \,. \tag{5.23}$$

However, given a scalar field ϕ it may not always be possible to find another scalar field $\widetilde{\phi}$ which satisfies this equation. Nevertheless, in a perfectly homogeneous and isotropic FLRW Universe, ϕ and X are functions of cosmic time alone, making it always possible to define a scalar field $\widetilde{\phi}$ fulfilling Eq. (5.23). Given that the dark energy field is expected to be nearly homogeneous this will turn out to be the most relevant case, which will be further explored later. Also, having defined $\widetilde{\mathcal{L}}(\widetilde{X})$ it is possible to explore the full consequences of the model, taking into account cosmological perturbations.

The energy momentum tensor is covariantly conserved or equivalently, $\nabla_\alpha \widetilde{T}^{\alpha\beta} = 0$. With all generality, this implies that

$$\nabla_\alpha T^{\alpha\beta} = Q^\beta \,, \tag{5.24}$$
$$\nabla_\alpha T_m^{\alpha\beta} = -Q^\beta \,, \tag{5.25}$$

where Q^β is the coupling between the two components. Contracting the equation $\nabla_\alpha \widetilde{T}^{\alpha\beta} = 0$ with $\widetilde{u}_\beta$, one obtains the continuity equation

$$\widetilde{u}^\alpha \nabla_\alpha \widetilde{\rho} + (\widetilde{\rho} + \widetilde{p}) \nabla_\alpha \widetilde{u}^\alpha = 0 \,, \tag{5.26}$$

which is equivalent to the equation of conservation of the particle number $\nabla_\alpha \left(\widetilde{\mathcal{L}}_{,\widetilde{X}} \sqrt{2\widetilde{X}} \widetilde{u}^\alpha \right) = 0$ [see Eq. (4.27)]. Given the relations from Eqs. (5.18) and (5.21) one may check that

$$n = \sqrt{2X}\mathcal{L}_{,X} = \left(\sqrt{2\widetilde{X}} - m \right) X_{\widetilde{X}} \widetilde{\mathcal{L}}_{,\widetilde{X}} = \sqrt{2\widetilde{X}} \widetilde{\mathcal{L}}_{,\widetilde{X}} = \widetilde{n} \,. \tag{5.27}$$

Using Eq. (5.22),the particle number conservation equation may also be written as

$$\nabla_\alpha \left(\widetilde{\mathcal{L}}_{,\widetilde{X}} \sqrt{2\widetilde{X}} \widetilde{u}^\alpha \right) = \nabla_\alpha \left(\mathcal{L}_{,X} \sqrt{2X} u^\alpha \right) = 0 \,. \tag{5.28}$$

Taking this into account, it is simple to show that

$$\begin{aligned} u_\beta Q^\beta &= u_\beta \nabla_\alpha T^{\alpha\beta} = \\ &= -u^\alpha \nabla_\alpha \left(2X\mathcal{L}_{,X} \right) - u^\alpha \nabla_\alpha \mathcal{L} - 2X\mathcal{L}_{,X} \nabla_\alpha u^\alpha = \\ &= -\frac{1}{\sqrt{2X}} \nabla_\alpha \left(\mathcal{L}_{,X} \sqrt{2X} u^\alpha \right) = 0 \,. \end{aligned} \tag{5.29}$$

The contraction of $\nabla_\alpha \widetilde{T}^{\alpha\beta} = 0$ with $h^\nu_\beta = \delta^\nu_\beta + u^\nu u_\beta$ results in

$$\left(g^{\nu\alpha}+\widetilde{u}^{\nu}\widetilde{u}^{\alpha}\right)\nabla_{\alpha}\widetilde{p}=-\left(\widetilde{\rho}+\widetilde{p}\right)\widetilde{a}^{\nu}\,, \tag{5.30}$$

with $\widetilde{a}^{\alpha}=\widetilde{u}^{\beta}\nabla_{\beta}\widetilde{u}^{\alpha}=a^{\alpha}$ being the components of the 4-acceleration (notice that $\widetilde{u}_{\alpha}\widetilde{a}^{\alpha}=0$). From the contraction of h^{ν}_{β} with Eq. (5.25) one finds that

$$\rho_{\rm m}a^{\nu}=-h^{\nu}_{\beta}Q^{\beta}\,. \tag{5.31}$$

In a perfectly homogeneous and isotropic FLRW background $u^0=1$ and $a^{\nu}=0$. Hence, Eq. (5.31) in combination with the condition $Q^{\beta}u_{\beta}=0$, implies that $Q^{\nu}=0$. In this case, the energy-momentum tensors of the matter and dark energy components are separately conserved.

5.2.2 Equation-of-state and the sound speed

Having determined the Lagrangian and energy density of the the transformed fluid in terms of the original scalar field, we may now write the equation of state of the transformed fluid as

$$\widetilde{w}\equiv\frac{\widetilde{p}}{\widetilde{\rho}}=\frac{\mathcal{L}\left(X\right)}{\sqrt{2X}\mathcal{L}_{,X}\left(\sqrt{2X}+m\right)}\,, \tag{5.32}$$

and the sound speed squared as

$$\widetilde{c}_{\rm s}^{2}=\frac{\widetilde{p}_{,\widetilde{X}}}{\widetilde{\rho}_{,\widetilde{X}}}=\frac{\sqrt{2X}}{\sqrt{2X}+m}\frac{\mathcal{L}_{X}}{2X\mathcal{L}_{,X}+\mathcal{L}}=\frac{\sqrt{2X}}{\sqrt{2X}+m}c_{\rm s}^{2}\,, \tag{5.33}$$

where $c_{\rm s}^{2}$ is the sound speed of the original fluid [*cf.* Eq. (4.30)].

Considering a FLRW metric, we have shown in Sec. 4.3.2 that the equation of motion for a scalar field described by a pure k-essence Lagrangian has the general solution

$$X\mathcal{L}_{,X}^{2}\propto a^{-6}\propto(1+z)^{6}\,. \tag{5.34}$$

Therefore, we may write $n=\sqrt{2X}\mathcal{L}_{,X}=n_0(1+z)^3$, where $n_0\equiv n(z=0)$. This means that $\rho_{\rm m}=mn=mn_0(1+z)^3$ as expected for the matter component, irrespective of the original pure k-essence model. Thus, from Eq. (5.32), the equation of state parameter of the transformed fluid is given by

$$\widetilde{w}=\frac{p}{\rho+mn}=\frac{w}{1+mn_0(1+z)^3/\rho}\,, \tag{5.35}$$

where $w\equiv p/\rho$ is the equation of state parameter of the original fluid. On the other hand, the sound speed of the transformed fluid given in Eq. (5.33) is equal to

$$\widetilde{c}_{\rm s}^{2}=\frac{\widetilde{p}_{,z}}{\widetilde{\rho}_{,z}}=\frac{c_{\rm s}^{2}}{1+mn_{,z}/\rho_{,z}}=\frac{c_{\rm s}^{2}}{1+3mn_0(1+z)^2/\rho_{,z}}\,. \tag{5.36}$$

Hence, given m and n_0, the evolution of the sound speed squared of the transformed fluid $\widetilde{c}_{\rm s}^2$ with the redshift is completely determined by the evolution of the sound speed squared $c_{\rm s}^2$ and of the density of the original model. It is straightforward to show that, for $|\rho_{,z}/n_{,z}| \ll m$ (or, equivalently, $m \gg \sqrt{2X}$), one has $\widetilde{c}_{\rm s}^2 \ll c_{\rm s}^2$.

5.2.3 Scalar field linear perturbations

Given a scalar field model defined by a Lagrangian $\mathcal{L}(X)$, its description in term of an isentropic perfect fluid is possible (provided that $X > 0$) also at the linear level. In this subsection we shall briefly consider the linear evolution of the field perturbations and show that the map $\sqrt{2\widetilde{X}} = \sqrt{2X} + m$ leads to the expected sound speed of the UDE model.

Let us write $\phi = \phi_{(0)} + \delta\phi$, so that $\phi_{(0)}$ refers to the purely time dependent background value of ϕ and $\delta\phi$ denotes the fluctuation of ϕ with respect to the background value (we shall use the same notation in the case of the other variables). At first order in $\delta\phi$, the energy-momentum tensor defined in Eq. (5.19) may be written as

$$\widetilde{T}^{\alpha}_{\beta} = \widetilde{T}^{\alpha}_{\beta(0)} + \delta\widetilde{T}^{\alpha}_{\beta}\,, \tag{5.37}$$

where $\widetilde{T}^{0}_{0(0)} = -\widetilde{\rho}_{(0)}$, $\widetilde{T}^{i}_{j(0)} = \widetilde{p}_{(0)}\,\delta^i_j$, and

$$\begin{aligned}
\delta\widetilde{T}^{0}_{0} &= -\delta\widetilde{\rho} = -\left(\mathcal{L}_{,X(0)} + 2X_{(0)}\mathcal{L}_{,XX(0)}\right) \\
&\times \left(1 + \frac{m}{\sqrt{2X_{(0)}}}\right)\delta X\,, && (5.38)\\
\delta\widetilde{T}^{0}_{i} &= a^{-2}\mathcal{L}_{,X(0)}\left(\phi^{'}_{(0)} + m\right)\phi^{'}_{(0)}\delta u_i\,, && (5.39)\\
\delta\widetilde{T}^{i}_{0} &= -a^{-4}\mathcal{L}_{,X(0)}\left(\phi^{'}_{(0)} + m\right)\phi^{'}_{(0)}\delta u_i\,, && (5.40)\\
\delta\widetilde{T}^{i}_{j} &= \delta\widetilde{p}\,\delta^i_j = \mathcal{L}_{,X(0)}\delta^i_j\delta X\,. && (5.41)
\end{aligned}$$

Here $\delta u_i = a^2\delta u^i$, and it has been taken into account that, up to first order in $\delta\phi$, the perturbation to the kinetic term X is given by

$$\delta X = 2X_{(0)}\left(\frac{\delta\phi^{'}}{\phi^{'}_{(0)}} - \Phi\right)\,. \tag{5.42}$$

Given the energy-momentum tensor defined by Eqs. (5.37)-(5.41), and the perturbed Einstein equations in the Newtonian gauge i.e. Eqs. (2.119) and (2.122) one obtains

$$3\mathcal{H}\left(\mathcal{H}\Phi + \Phi^{'}\right) + k^2\Phi = 4\pi G a^2\left(\mathcal{L}_{,X(0)} + 2X_{(0)}\mathcal{L}_{,XX(0)}\right) \times \left(1 + \frac{m}{\sqrt{2X_{(0)}}}\right)\delta X\,, \tag{5.43}$$

and

$$\Phi^{''} + 3\mathcal{H}\Phi' + \left(\mathcal{H}^2 + \mathcal{H}^{'}\right)\Phi = 4\pi G a^2 \mathcal{L}_{,X(0)}\delta X\,, \tag{5.44}$$

resulting in the usual evolution of the gravitational potential

$$\Phi^{''} + 3\mathcal{H}\left(1+\widetilde{c}_{\rm s}^2\right)\Phi^{'} + \left(\widetilde{c}_{\rm s}^2 k^2 + 3\mathcal{H}^2\widetilde{c}_{\rm s}^2 + 2\mathcal{H}^{'} + \mathcal{H}^2\right)\Phi = 0\,, \tag{5.45}$$

with $\widetilde{c}_{\rm s}^2$ being given by Eq. (5.33).

5.3 Mapping specific input DE models into UDE

In this subsection we shall assume that the original Lagrangian $\mathcal{L}(X)$ describes a dark energy fluid with equation of state parameter at the present being $w_0 = w_{\rm de0} \sim -1$, so that the transformed Lagrangian $\widetilde{\mathcal{L}}(\widetilde{X})$ defines a UDE fluid with equation of state parameter $\widetilde{w} = w_{\rm ude}$ (in the following, we shall use the subscripts "de" and "ude", respectively, when referring to dark energy and UDE). Thus, we write Eqs. (5.35) and (5.36) as

$$w_{\rm ude}(z) = \frac{w_{\rm de}(z)}{1 + mn_0(1+z)^3/\rho_{\rm de}(z)}\,, \tag{5.46}$$

$$c^2_{\rm s(ude)} = \frac{p_{\rm ude,z}}{\rho_{\rm ude,z}} = \left(1 + 3\frac{mn_0\,(1+z)^2}{\rho_{\rm de,z}}\right)^{-1} c^2_{\rm s(de)}\,, \tag{5.47}$$

respectively. Notice that, as long as the sound speed squared $c^2_{\rm s(de)}$ of the input dark energy fluid is positive, the same is verified in the case of the resulting UDE fluid, thus ensuring that no pathological instabilities occur (at a nonlinear level it is guaranteed *a priori* by the fact that the behavior of UDE is similar to that of CDM in the high density regime). If $\rho_{\rm de,z} > -3mn_0\,(1+z)^2$ then $c^2_{\rm s(de)} > 0$ is required in order to guarantee that $c^2_{\rm s(ude)} > 0$. On the other hand, if $\rho_{\rm de,z} < -3mn_0\,(1+z)^2 < 0$ the condition $c^2_{\rm s(ude)} > 0$ would be satisfied if, and only if, $c^2_{\rm s(de)} < 0$. Here we shall not explore the latter case.

5.3.1 Input DE model: $w_{\rm de} = \text{const}$

It is instructive to start by examining a dark energy model with constant $w_{\rm de} \sim -1$ (here, we shall consider a non-phantom dark energy model with $w_{\rm de} > -1$) defined by the Lagrangian

$$\mathcal{L}(X) = CX^{\frac{1+w_{\rm de}}{2w_{\rm de}}}\,, \tag{5.48}$$

where $C < 0$ is a constant (notice that a constant $w_{\rm de}$ implies that $c^2_{\rm s(de)} = w_{\rm de}$). One can use Eq. (5.18) to obtain the Lagrangian

$$\widetilde{\mathcal{L}}(\widetilde{X}) = C\left(\sqrt{\widetilde{X}} - \frac{m}{\sqrt{2}}\right)^{\frac{1+w_{\rm de}}{w_{\rm de}}} \tag{5.49}$$

describing a UDE model with proper energy density

$$\begin{aligned}\rho_{\rm ude}(\widetilde{X}) &= 2\widetilde{X}\widetilde{\mathcal{L}}_{,\widetilde{X}} - \widetilde{\mathcal{L}} = C\left(\frac{\sqrt{\widetilde{X}}}{w_{\rm de}} + \frac{m}{\sqrt{2}}\right) \\ &\times \left(\sqrt{\widetilde{X}} - \frac{m}{\sqrt{2}}\right)^{\frac{1}{w_{\rm de}}}\end{aligned} \tag{5.50}$$

and proper pressure $p_{\rm ude}(\widetilde{X}) = \widetilde{\mathcal{L}}(\widetilde{X}) = \mathcal{L}(X)$. Notice that $\rho_{\rm ude} \to \infty$ for $\widetilde{X} \to m^2/2$ (dark matter limit, with $p_{\rm ude} \to 0$), and that

$$\rho_{\rm ude} \sim \frac{C}{w_{\rm de}} X^{\frac{w_{\rm de}+1}{w_{\rm de}}} \to 0 \tag{5.51}$$

in the $\widetilde{X} \to \infty$ limit (dark energy limit, satisfying $p_{\rm ude} \sim w_{\rm de}\rho_{\rm ude} \sim -\rho_{\rm ude}$). Since $\widetilde{X} \in]m^2/2, +\infty[$ the perfect fluid correspondence is always verified. However, the sound speed squared of the UDE fluid

$$c^2_{\rm s(ude)} = \frac{p_{{\rm ude},\widetilde{X}}}{\rho_{{\rm ude},\widetilde{X}}} = w_{\rm ude}\left(1 - \frac{m}{\sqrt{2\widetilde{X}}}\right), \tag{5.52}$$

is negative for $\widetilde{X} \in]m^2/2, +\infty[$. Although, this may appear to constitute a no-go condition for this model, that may not be the case. Indeed, for $w_{\rm de}$ sufficiently close to -1, the negative sound speed would only become significant in extremely underdense regions (note that $\widetilde{c}_s^2 \to 0$ when $\widetilde{X}^2 \to m^2/2$). In any case, UDE models with a negative sound speed may be avoided by starting with a non-phantom dark energy model satisfying the condition $c^2_{\rm s(de)} > 0$.

5.3.2 Input DE model: GCG

Let us consider the case of the GCG Lagrangian discussed in Sec. 4.2.1

$$\mathcal{L}(X) = -A^{\frac{1}{1+\alpha}}\left(1 - (2X)^{\frac{1+\alpha}{2\alpha}}\right)^{\frac{\alpha}{1+\alpha}}, \tag{5.53}$$

where $0 < \alpha < 1$ and $A > 0$ are constants (in the following we shall also assume that variables with dimensions of mass are measured in some arbitrary mass unit $m_{\rm unit}$). Although throughout this thesis we have assumed the GCG as a UDE model, here we shall take it as our input dark energy model. The corresponding equation of state parameter and sound speed squared are given, respectively, by

$$w_{\rm de} = -\frac{A}{\rho_{\rm de}^{1+\alpha}} \qquad c^2_{\rm s(de)} = -\alpha w_{\rm de}\,, \tag{5.54}$$

with $-1 < w_{\rm de} < 0$ and $0 < c_s^2 < 1$ (assuming that $\rho > A^{\frac{1}{1+\alpha}}$) [*cf.* sec. 3.2]. In this case, using Eq. (5.18) one gets

$$\widetilde{\mathcal{L}}(\widetilde{X}) = -A^{\frac{1}{1+\alpha}}\xi(\widetilde{X})^{\frac{\alpha}{1+\alpha}}\,, \tag{5.55}$$

with

$$\xi(\widetilde{X}) = 1 - \left(\sqrt{2\widetilde{X}} - m\right)^{\frac{1+\alpha}{\alpha}}\,, \tag{5.56}$$

describing a UDE model with proper pressure $p_{\rm ude}(\widetilde{X}) = \widetilde{\mathcal{L}}(\widetilde{X})$ and proper energy density

$$\rho_{\rm ude}(\widetilde{X}) = 2\widetilde{X}\widetilde{\mathcal{L}}_{,\widetilde{X}} - \widetilde{\mathcal{L}} = \rho_{\rm m}(\widetilde{X}) + \rho_{\rm de}(\widetilde{X})\,, \tag{5.57}$$

$$\rho_{\rm de}(\widetilde{X}) = A^{\frac{1}{1+\alpha}}\xi(\widetilde{X})^{-\frac{1}{1+\alpha}}\,, \tag{5.58}$$

$$\rho_{\rm m}(\widetilde{X}) = mn = m\left(\sqrt{2\widetilde{X}} - m\right)^{\frac{1}{\alpha}}\rho_{\rm de}\,. \tag{5.59}$$

At late times one has $\widetilde{X} \to m^2/2$, thus implying that both $\rho_{\rm ude}$ and $-p_{\rm ude}$ approach the constant value $A^{1/(1+\alpha)}$ (notice that $\rho_{\rm m} \to 0$ and $\xi \to 1$ in this limit). On the other hand, at early times $\widetilde{X}$ approaches $(m+1/2)^2/2$. As a result, the energy density becomes large and $\rho_{\rm m}$ is roughly proportional to $\rho_{\rm de}$ — this behavior is explained by the fact that the Chaplygin gas behaves as CDM for densities much greater than $A^{1/(1+\alpha)}$. Notice that for m sufficiently large it is always possible to ensure that $\rho_{\rm ude} \sim \rho_{\rm m}$ at early times. As previously discussed, the positive sound speed squared of the input generalized Chaplygin model implies that $c^2_{\rm s(ude)} > 0$, thus guaranteeing that the resulting UDE model is free from pathological instabilities associated with an imaginary sound speed.

5.3.3 Restrictions on isentropic UDE models

Let us now consider the Chevallier-Polarski-Linder (CPL) parametrization of the equation of state of the original dark fluid [355]

$$w_{\rm de}(z) = w_0 + \Delta w\frac{z}{1+z}\,, \tag{5.60}$$

where $w_0 \equiv w_{\rm de}(z=0)$, $w_\infty \equiv w_{\rm de}(z=\infty)$ and $\Delta w \equiv w_\infty - w_0$. Solving the continuity equation, the energy density of the original dark energy fluid is given by

$$d\rho_{\rm de}/dz - 3\rho_{\rm de}\left(1 + w_{\rm de}(z)\right)/\left(1+z\right) = 0 \Longrightarrow \rho_{\rm de} \propto (1+z)^{3(1+w_\infty)}\, e^{3\Delta w/(1+z)}\,, \tag{5.61}$$

so corresponding energy density of the UDE fluid is equal to

$$\rho_{\rm ude} = \rho_{\rm ude0}\left[(1+z)^{3(1+w_\infty)}\, e^{3\Delta w/(1+z)} + \mathcal{Q}\,(1+z)^3\right] , \tag{5.62}$$

where $\mathcal{Q} \equiv mn_0/\rho_{\rm ude0}$. Using Eq. (5.47) the sound speed squared is

$$c^2_{\rm s(ude)} = \frac{(1+w_\infty)\, w_{\rm de}(z) + (1-3w_{\rm de}(z))\,\frac{\Delta w}{3(1+z)}}{1+w_{\rm de}(z) + \mathcal{Q}(1+z)^{-3w_\infty} e^{-3\Delta w/(1+z)}} , \tag{5.63}$$

which simplifies to

$$c^2_{\rm s(ude)0} = \frac{\Delta w + 3w_0\,(1+w_0)}{3(1+w_0+\mathcal{Q}e^{-3\Delta w})} , \tag{5.64}$$

the present time. If one assumes that the original fluid is a dark energy fluid with w_0 sufficiently close to -1 one finds

$$c^2_{\rm s(ude)0} = \frac{w_\infty+1}{3\mathcal{Q}} e^{3(w_\infty+1)} . \tag{5.65}$$

In order for the transformed fluid to play a UDE role $\mathcal{Q} \sim \Omega_{\rm cdm0}/\Omega_{\rm de0} \sim 3/7$, where we assume $\Omega_{\rm cdm0} \sim 0.3$ and $\Omega_{\rm de0} \sim 0.7$ for the fractional CDM and dark energy densities inferred from the observations. This in turn implies that $c^2_{\rm s(ude)0} \sim (w_\infty+1)e^{3(w_\infty+1)}$. Therefore, large sound speeds at recent times would be unavoidable, unless $|w_\infty+1| \ll 1$. One can estimate how small this value has to be in order to not affect significantly the standard growth of perturbation on linear scales by imposing that $c_{\rm s(ude)0} \lesssim 10^{-3}$ (this upper limit being consistent with the values found in chapter 3).

Hence the variation of w is limited to $|1+w_\infty| \lesssim 10^{-6}$, meaning that the original fluid has to follow very closely the behavior of a cosmological constant. More generally, Eq. (5.63) implies that large sound speeds at low redshifts can be avoided only if both $|w_\infty+1|$ and $|w_0+1|$ are extremely small. Such stringent constraints at the linear level regarding a non-null sound speed are, as we have seen so far, typical for isentropic UDE models. The key factor behind this result is the fact that the adiabatic sound speed in isentropic perfect fluids is necessarily tied up to the background evolution. However, it turns out that a traditional approach to perturbation theory is, in general, not sufficient to account for all the relevant physics in UDE scenarios. In fact, it has been shown that the clustering on nonlinear scales can have a potential impact on the large scale evolution in UDE cosmologies [356, 357]. Moreover, taking into account nonlinear effects may render these models (ruled out in a linear analysis) consistent with cosmological observations, as we shall discuss in more detail in the following chapter.

Chapter 6

The role of nonlinearities in UDE models

So far our approach to the formation of structures in UDE models was based on the standard approach to cosmological perturbations, as presented in Sec. 2.3: provided some initial conditions set by Inflation, the growth of structures on sufficiently large scales is determined by the evolution of small perturbations around an homogeneous and isotropic background. This perturbative treatment comes to aid due to our inability to solve Einstein equations completely with all generality. Although our Universe may be well approximated by a FLRW metric $g_{\mu\nu}^{(\mathrm{FLRW})}$ on large scales, on smaller scales it is highly inhomogeneous, having hierarchical structures like e.g. stars, galaxies, and clusters of galaxies, that formed at later times. Hence, a FLRW metric does not account for these nonlinear small scale structures, and the "lumpiness" of the real Universe is simply averaged. Due to the highly nonlinear nature of General Relativity, this raises an important question for cosmology: can the smaller structures influence the dynamics of the Universe on larger scales?

6.1 Backreaction in cosmology

The impact of non-linearities present on smaller scales on the average expansion of the Universe is known as backreaction. This effect was first recognized by Schirokov and Fisher in 1963 [358], but remained virtually unnoticed until Ellis brought back the issue with a more detailed discussion in his 1987 paper [359]. Partially due to the resounding phenomenological success of the standard cosmological model over the last years to fit the available observational data, the backreaction problem did not become a main concern for the cosmology community. The basics of the problem can be understood as follows. Let us assume that a realistic description of the Universe can be given in terms of a metric $g_{\mu\nu}$ and an energy-momentum tensor $T_{\mu\nu}$. Then, operationally, the background cosmology could be obtained by applying a "suitable smoothing procedure" to Einstein's equations

$$G_{\mu\nu}^{(\mathrm{smooth})} = 8\pi G T_{\mu\nu}^{(\mathrm{smooth})} \,, \tag{6.1}$$

where the Einstein tensor $G_{\mu\nu}^{(\mathrm{smooth})}$ and the energy-momentum tensor $T_{\mu\nu}^{(\mathrm{smooth})}$ are a coarse-grained representation of the real (and lumpy) Universe. In contrast, the standard way to build the background is to first consider a FLRW metric and then compute the components of the Einstein tensor $G_{\mu\nu}^{(\mathrm{FLRW})}$. However, note that, since Einstein's equations are highly nonlinear, in general these operations do not commute, i.e. $G_{\mu\nu}^{(\mathrm{smooth})} \neq G_{\mu\nu}^{(\mathrm{FLRW})}$. Thus, the equations for the background dynamics display an extra term

$$G_{\mu\nu}^{(\mathrm{FLRW})} = 8\pi G T_{\mu\nu}^{(\mathrm{smooth})} + B_{\mu\nu}\,, \tag{6.2}$$

where $B_{\mu\nu} = G_{\mu\nu}^{(\mathrm{FLRW})} - G_{\mu\nu}^{(\mathrm{smooth})}$ is an effective matter source, representing the backreaction from the small scales (which were averaged out by the averaging process) to the evolution of the homogeneous and isotropic FLRW metric. The issue of finding the best-fit background FLRW model which does not ignore the lumpy details of the real Universe is referred to as the *fitting problem* [359].

However, the averaging procedure in General Relativity is far from trivial, and while several approaches to the problem may be found on the literature, none is still completely satisfactory (see e.g. [360, 361] and references therein). Regarding the magnitude of the backreaction effect and its relevance on standard cosmologies it is still subject to controversy [362–364]: the claims go from the speculation that such corrections could explain the current accelerated expansion of the Universe (without the need of a dark energy component), to the suggestion that backreaction is completely negligible — a survey of cosmologist's opinions working in the field of inhomogeneous cosmology may be found in [365] (see also [366, 367] and references therein). Meanwhile, improved computing power along with significant progress in the techniques to solve numerically Einstein's equations in generic spacetimes [368] is paving the way to more realistic simulations of fully relativistic cosmologies without the need to assume a background geometry. Efforts in that direction have been made in several independent papers, both with full relativistic cosmological simulations and relativistic N-body methods [369–373] (see [374] for a comparison and consistency check between different codes). The authors, focusing on matter-dominated cosmologies, conclude that backreaction has a small impact on the background dynamics.

In light of these results, it seems reasonable to doubt that backreaction alone can explain the mystery behind the dark sector. Nevertheless, even if one adopts a more conservative point of view regarding the magnitude of this effect, the need to correctly account for the impact of backreaction is growing relevantly as observations get more and more precise. Moreover, with the standard ΛCDM model currently facing significant tensions given the incompatible constraints between different data sets, some authors have further suggested that backreaction corrections may be sufficient to explain these discrepancies (see e.g. [375, 376]).

6.2 Impact of nonlinearities in UDE

While the previous subsection refers to the *gravitational* backreaction (resulting from the left hand side of Einstein's equations, broadly speaking), one still needs to address the problem of averaging

the energy-momentum tensor. The background dynamics depends on the averaged matter source $\langle T_{\mu\nu}\rangle$, with the matter content being defined by a local energy-momentum tensor $T_{\mu\nu}$ at every point of spacetime. For instance, in the case of CDM, its local energy-momentum tensor may be regarded as the energy-momentum tensor of a collection of discrete particles [358]. The averaging process of point particles is well defined in kinetic theory, enabling a smooth and continuous description of CDM, so that $\left\langle T_{\mu\nu}^{(\mathrm{CDM})}\right\rangle = \rho^{(\mathrm{CDM})}u_\mu u_\nu$ for a perfect fluid modeling dust [361]. Recalling that barotropic perfect fluids can be fully specified by a local equation of state $p = \rho(\rho)$, one often identifies the background equation of state with the local one, i.e. that $\langle p(\rho)\rangle = p(\langle\rho\rangle)$. Notice however that this relation does not hold in general, with the exception of $p \propto \rho$ models (from now on the angle brackets $\langle\rangle$ stand for a spatial average, which we shall define forward in this subsection). Indeed, assuming a perturbative decomposition of the local pressure and energy density [232]

$$p = \langle p\rangle + \delta p + ... \tag{6.3}$$

$$\rho = \langle\rho\rangle + \delta\rho + ... \tag{6.4}$$

it is clear that the average quantities differ from the local ones, except if the perturbations are very small. For concreteness, let us take the GCG equation of state (see Eq. (3.3))

$$\langle p_{\mathrm{gcg}}\rangle = -A\left\langle\rho_{\mathrm{gcg}}^{-\alpha}\right\rangle \neq p_{\mathrm{gcg}}\left(\langle\rho_{\mathrm{gcg}}\rangle\right) = -A\langle\rho_{\mathrm{gcg}}\rangle^{-\alpha}\ . \tag{6.5}$$

Of course, if perturbations are small ($\delta_{\mathrm{gcg}} = \delta\rho_{\mathrm{gcg}}/\langle\rho_{\mathrm{gcg}}\rangle \ll 1$) the left and right hand side of Eq. (6.5) will be similar

$$\langle p_{\mathrm{gcg}}\rangle = -A\left\langle\rho_{\mathrm{gcg}}^{-\alpha}\right\rangle \simeq -A\left\langle\ \langle\rho_{\mathrm{gcg}}\rangle^{-\alpha}(1+\delta_{\mathrm{gcg}})^{-\alpha}\right\rangle \tag{6.6}$$

$$\simeq -A\langle\rho_{\mathrm{gcg}}\rangle^{-\alpha}\left\langle(1+\delta_{\mathrm{gcg}})^{-\alpha}\right\rangle \simeq -A\langle\rho_{\mathrm{gcg}}\rangle^{-\alpha}\langle 1-\alpha\delta\rangle \simeq -A\langle\rho_{\mathrm{gcg}}\rangle^{-\alpha}\ , \tag{6.7}$$

where the term $(1+\delta_{\mathrm{gcg}})^{-\alpha}$ was Taylor expanded. However, if density perturbations are large (as one expects in regions where the perturbations become nonlinear) the values of the local and average quantities may differ significantly. Hence, if the role of CDM and DE is played by a single fluid with a barotropic equation of state, the background evolution of a UDE fluid might be susceptible to nonlinear inhomogeneities; accounting for nonlinear effects in the background may then be crucial when confronting the model predictions with cosmological data, as noted e.g. in [356]. This subtlety is not unique to UDE paradigms, and indeed similar remarks have been made in other contexts (see for instance [377–381]).

One may further illustrate this point as follows (see [382]). The average of a scalar quantity $\Upsilon(t,\mathbf{x})$ over a spatial domain $\mathcal{D}$ of volume $V_{\mathcal{D}}$ may be defined as

$$\langle \Upsilon(t,\mathbf{x})\rangle = \frac{1}{V_{\mathcal{D}}}\int_{\mathcal{D}} d^3x\sqrt{g^{(3)}}\Upsilon(t,\mathbf{x}) \,, \tag{6.8}$$

where $g^{(3)}$ is the determinant of the spatial 3-metric and $V_{\mathcal{D}} = \int_{\mathcal{D}} d^3x\sqrt{g^{(3)}}$. Now let us consider a spherical domain of radius R filled with a GCG fluid. If the distribution of $\rho_{\rm gcg}$ inside the sphere is homogeneous, then the average energy density is simply $\langle\rho_{\rm gcg}\rangle = \rho_{\rm gcg}$, while the average pressure is given by $\langle p_{\rm gcg}\rangle = -A\rho_{\rm gcg}^{-\alpha}$. However, if one deviates from this homogeneous case, the result will in general be different. For concreteness, let us consider a non homogeneous radial distribution of the GCG energy density inside the sphere, such that

$$\begin{cases} \rho_1 = \mathcal{N}\langle\rho_{\rm gcg}\rangle \,, & r < R_1 \\ \rho_2 = \rho_{\rm min} \,, & R_1 < r < R \end{cases}$$

where $\mathcal{N} > 1$ (so that the core region has an energy density larger than the average) is some constant. The outer region has $\rho_{\rm min}$ i.e. the minimum energy density attained by the GCG, so that $p(R_1 < r < R) = p_{\rm min} = -\rho_{\rm min}$. Since the energy $E = \langle\rho_{\rm gcg}\rangle V_{\mathcal{D}}$ in the sphere is the same regardless the configuration, one can write a relation between $\mathcal{N}$ and the radius R_1 of the collapsed core

$$E = \rho_1 V_1 + \rho_2(V_{\mathcal{D}} - V_1) \Longrightarrow \mathcal{N} = \left(\frac{R}{R_1}\right)^3 + \left[1 - \left(\frac{R}{R_1}\right)^3\right]\frac{\rho_{\rm min}}{\langle\rho_{\rm gcg}\rangle} \,. \tag{6.9}$$

On the other hand, the average pressure is given by

$$\langle p_{\rm gcg}\rangle = \frac{1}{V_{\mathcal{D}}}\int_{\mathcal{D}} d^3x\sqrt{g^{(3)}}p_{\rm gcg} \tag{6.10}$$

$$= -\frac{4\pi A}{V_{\mathcal{D}}}\int_0^{R_1}\rho_1^{-\alpha}r^2dr - \frac{4\pi}{V_{\mathcal{D}}}\int_{R_1}^{R}\rho_{\rm min}r^2dr \tag{6.11}$$

$$= -A\left(\frac{R_1}{R}\right)^3(\mathcal{N}\langle\rho_{\rm gcg}\rangle)^{-\alpha} - \left[1 - \left(\frac{R_1}{R}\right)^3\right]\rho_{\rm min} \,. \tag{6.12}$$

In the limit of small R_1/R (or large $\mathcal{N}$) one has $\langle p_{\rm gcg}\rangle = -\rho_{\rm min}$, so the average pressure of the GCG fluid will be significantly larger (in modulus) than the average pressure that one obtains from the homogeneous configuration i.e. $\langle p_{\rm gcg}\rangle = -A\langle\rho_{\rm gcg}\rangle^{-\alpha}$. Hence, as nonlinear collapse occurs (even if only on small scales) it can change the background pressure of the GCG in a considerable way, and therefore it might influence the dynamics of the Universe on large scales.

In the remaining of this chapter we shall quantify the impact of small scale nonlinearities by considering an ansatz to parametrize the level of small scale clustering.

6.3 The nonlinear Chaplygin gas model

As we have just discussed, in UDE scenarios nonlinearities have, in general, a potential impact on the evolution of the average Universe — the inhomogeneous configuration from the previous section considering a GCG equation of state illustrates that effect. The study of the nonlinear collapse in GCG-dominated cosmologies presented in [254, 383–385] shows that initially small perturbations can give rise to rise to GCG clumps[1]. Fully relativistic simulations properly taking into account the impact of spatial pressure gradients (which, by construction, are absent in top-hat spherical collapse approximations) would be necessary in order to draw more definite conclusions regarding the details of the formation and evolution of GCG small scale nonlinear structures; to our knowledge such analysis is still lacking in the literature. We shall however assume that clustering can occur at sufficiently high redshifts and on small enough scales, creating stable GCG clumps. In such high density objects the transition from a DM-like to a DE-like stage never occurs.

By adopting a Press-Schechter approach [67] to estimate the abundance of collapsed objects, it has been argued in [254, 383] that the fraction of GCG found in clumps is far too small to affect in a significant way the linear results. However, this conclusion relies heavily on the validity of a standard shape for the primordial power spectrum on all scales. This is a very strong assumption given the current constraints: Planck [146] finds no evidence for significant deviations from a nearly invariant power law spectrum for wavenumbers in the range $0.008\ \mathrm{Mpc}^{-1} \lesssim k \lesssim 0.1\ \mathrm{Mpc}^{-1}$, but for larger k the shape of the power spectrum predicted by inflationary models have not yet been probed by observations[2]. Therefore, a nonstandard form of the primordial power spectrum cannot be ruled out on smaller scales. This loophole is found frequently in the context of e.g. small-scale clumps of DM (see [388] for a review) and PBH's formation scenarios. The abundance and clustering of PBH's is very sensitive to the value of the amplitude of the primordial power spectrum [389, 390] as well as to the statistical distribution of density fluctuations at early times [391, 392]. Modifications to the primordial power spectrum can then lead to an increase of the number of PBH's in the Universe. We expect similar arguments to hold for the GCG model as well, meaning that the enhancement or suppression of nonlinear clustering can be justified by relaxing the assumption of a standard spectrum on small scales, while also being consistent with the present observational constraints.

6.3.1 Small scale clustering parametrization

An attempt to quantify the impact of the backreaction of small scale non-linearities on UDE models has been made in [393], using the GCG as a representative example. Following this work, we assume that the distribution of the GCG component in a large comoving volume V is composed of collapsed and underdense regions. Collapsed regions occupy a very small volume $V_{\mathrm{coll}} \ll V$ and have a density ρ_{coll} much higher than the average GCG density $\langle \rho_{\mathrm{gcg}} \rangle$. More precisely, we assume $\rho_{\mathrm{coll}}^{\alpha} \gg A$ such that the pressure associated to the collapsed regions $p_{\mathrm{coll}} = -A/\rho_{\mathrm{coll}}^{\alpha}$ is negligible. Underdense

[1] In the literature very small bounded structures of DM are usually referred to as clumps, micro-halos, or mini-halos. This terminology is handy to establish a distinction between DM clumps as smaller analogs of the larger DM halos that are expected to exist at the scale of galaxies and clusters of galaxies.

[2] Future CMB experiments, such as the Primordial Inflation eXplorer (PIXIE) [386], might be able to constrain the primordial power spectrum for $50\ \mathrm{Mpc}^{-1} \lesssim k \lesssim 10^4\ \mathrm{Mpc}^{-1}$ [387].

regions, on the other hand, comprise most of the volume, i.e. $V_{\rm und} \sim V$. The energy of the total GCG in a large comoving volume V is simply given by

$$E = \langle \rho_{\rm gcg} \rangle \, V \, . \tag{6.13}$$

One useful way to quantify the level of small scale clustering is by considering the average fraction of E which is incorporated into collapsed objects (with energy $E_{\rm coll} = \rho_{\rm coll} V_{\rm coll}$)

$$\epsilon \, (a) = \frac{E_{\rm coll} \, (a)}{E \, (a)} \, , \tag{6.14}$$

where we write explicitly that $\epsilon \, (a)$ is in general an evolving quantity. The contribution of collapsed regions to the average GCG energy density in the large comoving volume is the average value of $\rho_{\rm coll}$

$$\rho_+ = \langle \rho_{\rm coll} \rangle = \frac{E_{\rm coll}}{V} = \epsilon \, \langle \rho_{\rm gcg} \rangle \, , \tag{6.15}$$

whereas its pressure contribution is negligible, i.e. $p_+ = \langle p_{\rm coll} \rangle \sim 0$. Therefore, this allows us to consider ρ_+ as the energy density of an effective CDM component (or '+' component for short). In the same way, one may also write the contribution from the underdense regions (with energy $E_{\rm und} = E - E_{\rm coll}$) to the average GCG energy density as

$$\rho_- = \langle \rho_{\rm und} \rangle = \frac{E_{\rm und}}{V} = \frac{E - E_{\rm coll}}{V} = (1 - \epsilon) \, \langle \rho_{\rm gcg} \rangle \, . \tag{6.16}$$

The contribution to the average GCG pressure comes solely from the underdense regions, i.e.

$$p_- = \langle p_{\rm und} \rangle = \langle p_{\rm gcg} \rangle = -\frac{A}{\rho_-^{\alpha}} \tag{6.17}$$

Therefore, the equation of state parameter of the average GCG reads

$$\langle w_{\rm gcg} \rangle \equiv \frac{\langle p_{\rm gcg} \rangle}{\langle \rho_{\rm gcg} \rangle} = \frac{p_-}{\langle \rho_{\rm gcg} \rangle} = (1 - \epsilon) \, w_- \, , \tag{6.18}$$

where we have used Eq. (6.16) in the last equality and that $w_- = p_-/\rho_-$, which represents the equation of state parameter of an effective dark energy component (or '−' component for short). For the remaining of this section we drop the angle brackets, so that e.g. the quantity $\rho_{\rm gcg}$ shall stand for the average GCG energy density.

The simplest assumption regarding the level of small scale nonlinear clustering of the GCG is to consider that the total energy $E_{\rm coll}$ incorporated into collapsed objects is a constant. In more realistic parametrizations, $E_{\rm coll}$ could be allowed to vary, and presumably, increase with time. However, assuming that $E_{\rm coll} = {\rm const}$ provides a reasonable first approximation.

6.3.2 Background evolution

With the equation of state parameter for the average GCG being defined in Eq. (6.18), we can use the continuity equation [*cf.* Eq. (2.43)] to obtain

$$\dot{\rho} + 3H\rho\,(1+w) = 0 \longrightarrow \dot{\rho}_{\rm gcg} + 3H\rho_{\rm gcg}\,(1+w_{\rm gcg}) = 0\,. \tag{6.19}$$

Notice that from Eq. (6.18) one has $w_{\rm gcg} = (1-\epsilon)\,w_-$, while from Eqs. (6.16) and (6.17) the equation of state parameter of the '$-$' component can be written as $w_- = -A/\left[(1-\epsilon)\,\rho_{\rm gcg}\right]^{1+\alpha}$. Hence, Eq. (6.19) gives

$$\dot{\rho}_{\rm gcg} + 3H\rho_{\rm gcg}\left[1 - \frac{A}{(1-\epsilon)^{\alpha}\,\rho_{\rm gcg}^{1+\alpha}}\right] = 0\,. \tag{6.20}$$

Changing the integration variable, and taking into account that $V = V_0 a^3$ and $\epsilon = E_{\rm coll}/\left(\rho_{\rm gcg} V\right)$ [from the combination of Eqs. (6.13) and (6.14)] results in the following continuity equation

$$\frac{d\rho_{\rm gcg}}{da} = -3\frac{\rho_{\rm gcg}}{a}\left[1 - A\left(1 - \frac{E_{\rm coll}}{\rho_{\rm gcg} V_0 a^3}\right)^{-\alpha}\rho_{\rm gcg}^{-(1+\alpha)}\right]\,. \tag{6.21}$$

The evolution of $\rho_{\rm gcg}$ with the scale factor is found by solving Eq. (6.21) once $E_{\rm coll}$ is specified. One can write $E_{\rm coll}$ in terms of present quantities i.e. $E_{\rm coll} = \epsilon_0 \rho_{\rm gcg0} V_0$. Solving Eq. (6.21) one obtains

$$\rho_{\rm gcg} = \rho_+ + \rho_-\,, \tag{6.22}$$

where

$$\rho_+ = \rho_{+0} a^{-3}\,, \tag{6.23}$$

$$\rho_- = \rho_{-0}\left[\overline{A}_{\rm eff} + \left(1 - \overline{A}_{\rm eff}\right) a^{-3(1+\alpha)}\right]^{\frac{1}{1+\alpha}}\,, \tag{6.24}$$

and

$$\overline{A}_{\rm eff} = \frac{A}{\rho_{-0}^{1+\alpha}} = \frac{\overline{A}}{(1-\epsilon_0)^{1+\alpha}}\,. \tag{6.25}$$

The first term in Eq. (6.22), corresponding to the energy density of the '$+$' component, evolves as CDM; the second term, corresponding to the '$-$' component, evolves like the original GCG model as if the parameters were α and $\overline{A}_{\rm eff}$ (which in turn depends on the original parameters as given in Eq. (6.25), where $\overline{A} = A/\rho_{\rm gcg0}^{1+\alpha}$). Therefore, with this parametrization of the small scale clustering, the evolution of $\rho_{\rm gcg}$ is equivalent to a decomposition into a CDM and a GCG component interacting only through gravity. In addition, nonlinear clustering affects the background evolution of the '$-$' component through $\overline{A}_{\rm eff}$ (if $\epsilon_0 \neq 0$).

If the condition

$$a \ll \left(\frac{1-\overline{A}_{\rm eff}}{\overline{A}_{\rm eff}}\right)^{\frac{1}{3(1+\alpha)}} \tag{6.26}$$

holds, Eq. (6.22) simplifies to

$$\rho_{\rm gcg} \sim \rho_{+0}a^{-3} + \rho_{-0}\left(1-\overline{A}_{\rm eff}\right)^{\frac{1}{1+\alpha}} a^{-3} = \rho_{\rm gcg0}\left[\epsilon_0 + (1-\epsilon_0)\left(1-\overline{A}_{\rm eff}\right)^{\frac{1}{1+\alpha}}\right] a^{-3}\,, \tag{6.27}$$

meaning that the energy density is proportional to a^{-3} for both components and, as a result, the average GCG fluid mimics pressureless matter. This also shows that Eq. (6.26) defines the scale factor of transition

$$a_{\rm tr} = \left(\frac{1-\overline{A}_{\rm eff}}{\overline{A}_{\rm eff}}\right)^{\frac{1}{3(1+\alpha)}}\,, \tag{6.28}$$

[cf. Eq. (3.9))]. Considering a value a_i satisfying the condition in Eq. (6.26), then $E\left(a_i\right) = \rho_{\rm gcg}\left(a_i\right) V_0 a_i^3$ is constant. Therefore, the level of small scale clustering fraction tends to a constant value at sufficiently early times

$$\epsilon\left(a_i\right) = \epsilon_i = \frac{E_{\rm coll}}{E\left(a_i\right)} = \frac{\epsilon_0\rho_{\rm gcg0}}{\rho_{\rm gcg}\left(a_i\right)} a_i^{-3}\,. \tag{6.29}$$

Using Eq. (6.27), one finds the following relation

$$\epsilon_i = \left(1 + \frac{1-\epsilon_0}{\epsilon_0}\left(1-\overline{A}_{\rm eff}\right)^{\frac{1}{1+\alpha}}\right)^{-1}\,, \tag{6.30}$$

so that ϵ_i is completely determined given ϵ_0, α, and $\overline{A}_{\rm eff}$.

Let us consider a flat Universe containing the GCG fluid, baryons, and relativistic particles. The corresponding Friedmann equation is

$$H^2 = \frac{8\pi G}{3}\rho = \frac{8\pi G}{3}\left(\rho_{\rm gcg} + \rho_{\rm b} + \rho_{\rm r}\right)\,. \tag{6.31}$$

For this discussion we fix $\alpha = 1$, $H_0 = 67.5$ km s^{-1} Mpc^{-1}, $\Omega_{\rm b0} \sim 0.05$ and $\Omega_{\rm r0} \sim 10^{-5}$, such that $\Omega_{\rm gcg0} \sim 0.95$. The density parameters for the '+' and '−' components as functions of redshift are given by

$$\Omega_+\left(z\right) = \frac{\rho_+}{\rho} = \left(1 + \frac{\Omega_{\rm b0} + \Omega_{\rm r0}\left(1+z\right) + \Omega_{-0}\sqrt{1-\overline{A}_{\rm eff} + \overline{A}_{\rm eff}\left(1+z\right)^{-6}}}{\Omega_{+0}}\right)^{-1}\,, \tag{6.32}$$

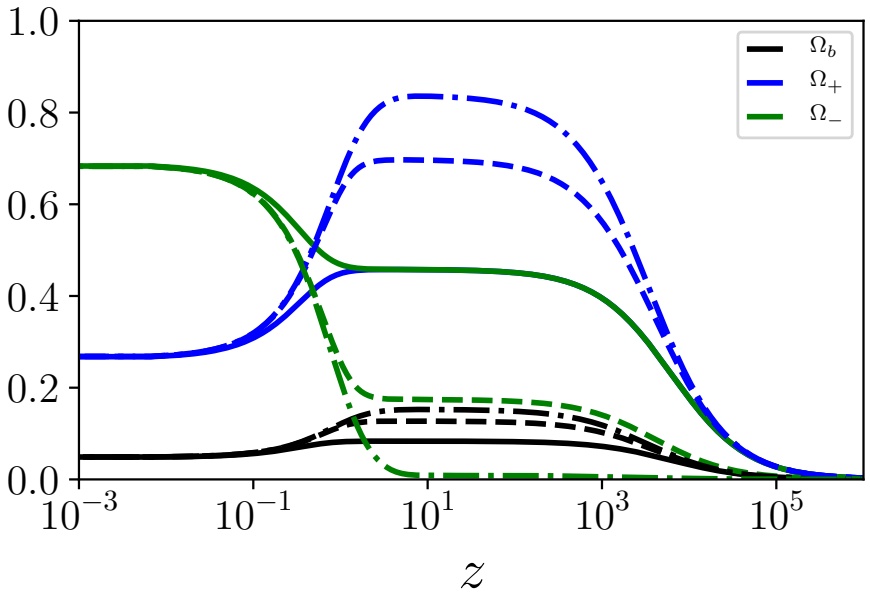

Figure 6.1: Evolution of the baryon (black lines), '+' component (blue lines), and '−' component (green lines), density parameters. We take three values for the initial collapsed GCG fraction $\epsilon_i = 0.5\,, 0.8\,, 0.99$ (solid, dashed and dotted-dashed lines, respectively).

and

$$\Omega_{-}\left(z\right) = \frac{\rho_{-}}{\rho} = \left(1 + \frac{\Omega_{+0} + \Omega_{\rm b0} + \Omega_{\rm r0}\left(1+z\right)}{\Omega_{-0}\sqrt{1 - \overline{A}_{\rm eff} + \overline{A}_{\rm eff}\left(1+z\right)^{-6}}}\right)^{-1}\,, \tag{6.33}$$

respectively. The evolution for the baryonic density parameter is similar to the right hand side of Eq. (6.32) (just swap Ω_{+0} and $\Omega_{\rm b0}$). The present level of small nonlinear clustering fraction is given by $\epsilon_0 = \Omega_{+0}/\Omega_{\rm gcg0}$, with $\Omega_{+0} \sim 0.26$, while the present density fraction of the '−' component is fixed by $\Omega_{-0} = \Omega_{\rm gcg0} - \Omega_{+0}$.

From Eq. (6.30) one finds

$$\overline{A}_{\rm eff} = 1 - \left(\frac{\Omega_{+0}}{\Omega_{-0}}\frac{1-\epsilon_i}{\epsilon_i}\right)^2\,. \tag{6.34}$$

Fig. 6.1 shows that, for $\epsilon_i = 0.5$ (solid line), the '−' and '+' components contribute in the same proportion to the background expansion (i.e. $\Omega_+ = \Omega_-$) until the end of the matter era. The term proportional to $(1+z)^{-6}$ in Eqs. (6.32) and (6.33) is negligible at high redshifts and from Eq. (6.34) one has $1 - \overline{A}_{\rm eff} = (\Omega_{+0}/\Omega_{-0})^2$. For larger values of ϵ_i (dashed and dotted-dashed lines for $\epsilon_i = 0.8$ and 0.99, respectively), Ω_- starts to deviate from zero at smaller redshifts (note that $1 - \overline{A}_{\rm eff} \to 0$ as $\epsilon_i \to 1$): the '+' component dominates the dynamics during the matter era, while the '−' component only becomes relevant to the background evolution at late times.

The evolution for the effective equation of state parameter of the '−' component is given by

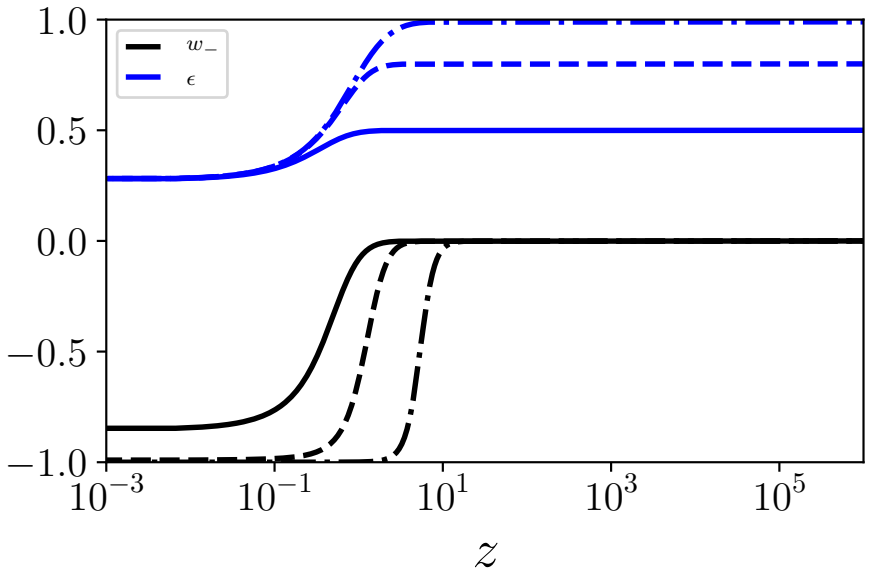

Figure 6.2: Evolution of the equation of state parameter for the '−' component (black lines) and the small scale clustering fraction of the GCG (blue lines) as a function of redshift. We take three values for the initial collapsed GCG fraction $\epsilon_i = 0.5\,, 0.8\,, 0.99$ (solid, dashed and dotted-dashed lines, respectively), and fix $\alpha = 1$.

$$w_- = \frac{p_-}{\rho_-} = -\frac{A}{\rho_{-0}^{1+\alpha}\left[\overline{A}_{\rm eff} + \left(1-\overline{A}_{\rm eff}\right) a^{-3(1+\alpha)}\right]} = -\frac{\overline{A}_{\rm eff}}{\overline{A}_{\rm eff} + \left(1-\overline{A}_{\rm eff}\right) a^{-3(1+\alpha)}}\,, \tag{6.35}$$

with its present value being $w_{-0} = -\overline{A}_{\rm eff}$. In Fig. 6.2 (black lines) we plot $w_-\,(z)$ (black lines) for three different values of ϵ_i. The value of w_- interpolates from $w_- = 0$ at earlier times to $w_- \sim -1$ at later times. At the transition redshift $z_{\rm tr} = 1/a_{\rm tr} - 1$ [see Eq. (6.28)], $w_- = -0.5$.

As ϵ_i increases, the transition to a dark energy state in the '−' component occurs at higher redshifts. The level of nonlinear small scale clustering as a function of the redshift is given by

$$\epsilon\,(z) = \frac{\rho_+}{\rho_{\rm gcg}} = \left(1 + \frac{\Omega_{-0}}{\Omega_{+0}}\sqrt{1 - \overline{A}_{\rm eff} + \overline{A}_{\rm eff}\,(1+z)^{-6}}\right)^{-1}\,. \tag{6.36}$$

As shown in Fig. 6.2, at early times the value of ϵ is approximately constant and close to its initial value. Ignoring the term proportional to $(1+z)^{-6}$ in Eq. (6.36), and using the relation in Eq. (6.34), one obtains $\epsilon\,(z \gg z_{\rm tr}) = \epsilon_i$.

6.3.3 Evolution of perturbations

In this subsection we analyze the evolution of linear density perturbations in the GCG model taking into account the parametrization of small scale nonlinear clustering discussed in the previous subsections. We have modified the `CLASS` code (see Appendix A.1) in order to solve the full Boltzmann equations considering a Universe containing radiation and baryons and the GCG fluid. The full perturbation equations are then used to compute the CMB and matter power spectra

discussed in Secs. 6.3.4 and 6.3.5, as well as to derive the observational constraints in Sec. 6.4. Although all the results follow from the numerical solutions given by our implementation in `CLASS`, we present here the perturbation equations in the synchronous gauge (the same gauge used to obtain the numerical solutions) in order to derive a few analytical results of interest, under appropriate simplifications. Such analysis also provides a consistency check of the numerical results.

Since we shall mainly focus on the evolution of linear perturbations from the epoch of matter domination up to the present time, the contribution from relativistic particles may be safely ignored. In this regime one may also take the baryonic content to be a pressureless perfect fluid interacting with the GCG fluid only through gravity. According to the parametrization presented in the previous section, the '+' component behaves as standard CDM (i.e. it has negligible pressure and negligible sound speed). On the other hand, the sound speed associated to the effective dark energy component is

$$c^2_{\mathrm{s},-} = -\alpha w_- \,. \tag{6.37}$$

One may further simplify the system of equations and include the baryonic density contrast contribution δ_b on δ_+ and consider the total matter density parameter $\Omega_\mathrm{m} = \Omega_+ + \Omega_\mathrm{b}$, where $\Omega_+ = \epsilon\Omega_\mathrm{gcg}$. Note that $\theta_\mathrm{m} = \nabla_i v^i_\mathrm{m} = 0$ at all times, so one may use the matter component to fix the synchronous coordinates. Setting $w_\mathrm{m} = c^2_{\mathrm{s,m}} = \theta_\mathrm{m} = 0$ in Eq. (2.139) one obtains $\delta^{'}_\mathrm{m} = 3\Phi^{'}$. Using this result, Eq. (2.141) gives

$$\delta^{''}_\mathrm{m} + \mathcal{H}\delta^{'}_\mathrm{m} - \frac{3}{2}\left[\Omega_\mathrm{m}\delta_\mathrm{m} + (1 - 3\alpha w_-)\,\Omega_-\delta_-\right] = 0\,, \tag{6.38}$$

while the equations for the perturbations δ_- and θ_- [from Eqs. (2.139) and (2.140)] read

$$\delta^{'}_- + (1 + w_-)\left[\theta_- - \delta^{'}_\mathrm{m}\right] - 3w_-\,(1 + \alpha)\,\delta_- = 0\,, \tag{6.39}$$

$$\theta^{'}_- + \mathcal{H}\,(1 + 3\alpha w_-)\,\theta_- + \frac{\alpha w_- k^2}{1 + w_-}\delta_- = 0\,. \tag{6.40}$$

For convenience, we shall rewrite this system of equations as

$$\begin{cases} \ddot{\delta}_\mathrm{m} + (2 + \xi)\,\dot{\delta}_\mathrm{m} - \dfrac{3}{2}\left[\Omega_\mathrm{m}\delta_\mathrm{m} + (1 - 3\alpha w_-)\,\Omega_-\delta_-\right] = 0 & (6.41) \\ \dot{\delta}_- + (1 + w_-)\left[\dfrac{\theta_-}{\mathcal{H}} - \dot{\delta}_\mathrm{m}\right] - 3w_-\,(1 + \alpha)\,\delta_- = 0 & (6.42) \\ \dot{\theta}_- + (1 + 3\alpha w_-)\,\theta_- + \dfrac{\alpha w_- k^2}{\mathcal{H}\,(1 + w_-)}\delta_- = 0 & (6.43) \end{cases}$$

where, exceptionally, we have $\dot{} \equiv d/d\ln a$ and $\xi = \dot{H}/H$.

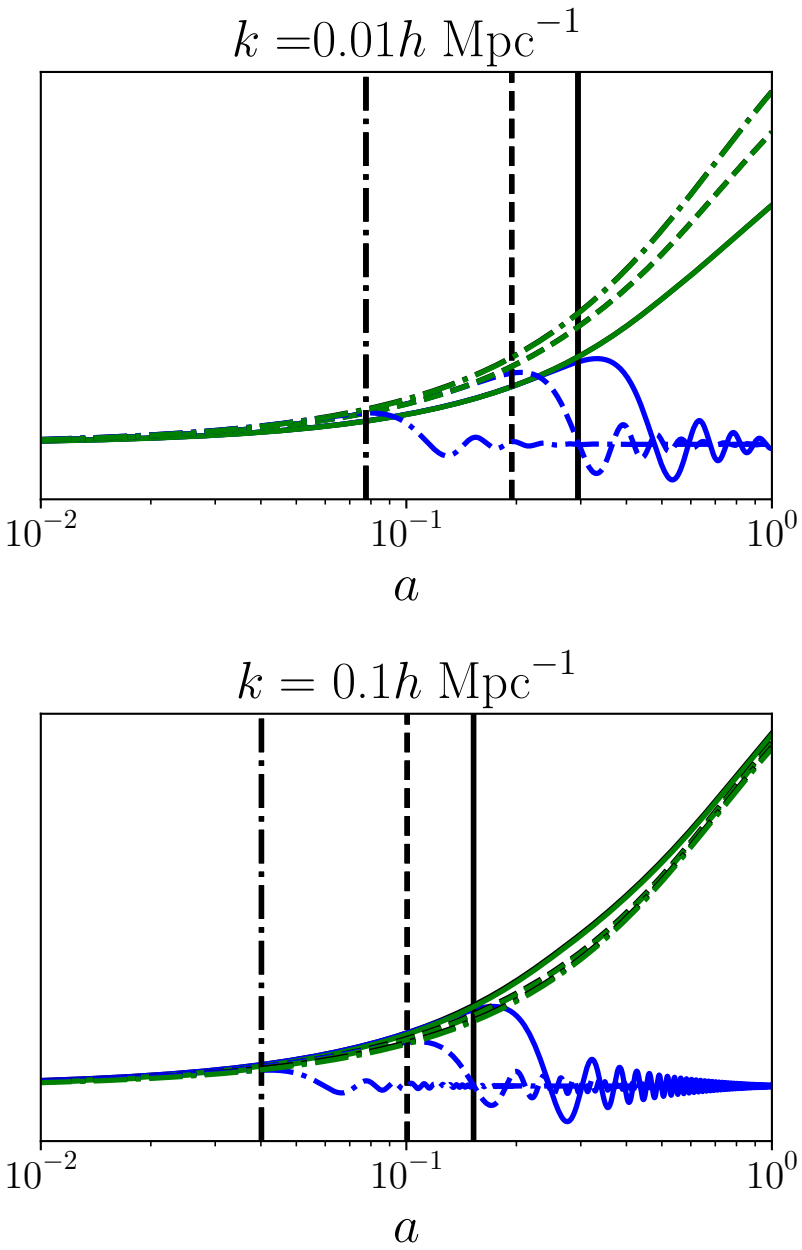

Figure 6.3: Evolution of the density perturbations with the scale factor on the scales $k = 0.01\ h\,\mathrm{Mpc}^{-1}$ (top plot) and $k = 0.1\ h\,\mathrm{Mpc}^{-1}$ (bottom plot) for the '+' component (green lines) and '−' component (blue lines). We fix the cosmological parameters as in Fig. 6.1 with the initial collapsed fraction being $\epsilon_i = 0.5$ (solid lines), $\epsilon_i = 0.8$ (dashed lines) and $\epsilon_i = 0.99$ (dotted-dashed lines). The vertical lines denote the value of the scale factor when the fluctuations of the effective dark energy component stop growing (with the corresponding line style for each ϵ_i).

In Fig. 6.3 we plot the evolution of the density perturbations for the '+' and '−' components as a function of the scale factor. We take $\epsilon_i = 0.5, 0.8$ and 0.99, for the scales $k = 0.01\ h\,\mathrm{Mpc}^{-1}$ and $k = 0.1\ h\,\mathrm{Mpc}^{-1}$, where h is the usual reduced Hubble parameter, and $\alpha = 1$. The present collapsed fraction is fixed to $\epsilon_0 = 0.277$ and $\overline{A}$ is found from Eq. (6.30). At early times, the perturbations of the '+' and '−' components evolve in a similar manner for all models, on scales larger than the

sound horizon (i.e. for $k \ll \mathcal{H}/c_{s,-}$). In the matter era one has $H \propto a^{-3/2}$, so $\xi = -3/2$. Thus, we may write Eq. (6.41) as

$$\ddot{\delta}_{\rm m} + \frac{1}{2}\dot{\delta}_{\rm m} - \frac{3}{2}\delta_{\rm m} = 0\,, \tag{6.44}$$

recovering the standard result for the CDM perturbations: a growing mode $\delta_{\rm m} \propto a$ and a decaying mode $\delta_{\rm m} \propto a^{-3/2}$. All components evolve as matter, so $w_- \sim 0$, and Eqs. (6.42) and (6.43) can be combined to give $\dot{\delta}_- = \dot{\delta}_{\rm m}$.

If $\alpha > 0$, $w_- < 0$ for $a > a_{\rm tr}$, and the '$-$' component has a non-null sound speed which prevents the growth of δ_- on scales smaller than the sound horizon (i.e. for $k \gg \mathcal{H}/c_{\rm s,-}$ the density perturbations start to oscillate and decay). The damped oscillatory behavior of δ_- happens approximately when $kc_{\rm s,-}/\mathcal{H} \sim 1$. Taking into account that $H \sim H_0 a^{-3/2}$ in the matter dominated era, and using Eq. (6.37), we may estimate that the fluctuations of the effective dark energy component stop growing at the scale factor

$$a_k \sim \left(\frac{k}{H_0}\right)^{-\frac{2}{4+3\alpha}} \alpha^{-\frac{1}{4+3\alpha}} a_{\rm tr}^{\frac{3(1+\alpha)}{4+3\alpha}}\,, \tag{6.45}$$

where

$$a_{\rm tr} = \left[\left(\frac{1-\epsilon_0}{1-\epsilon_i}\frac{\epsilon_i}{\epsilon_0}\right)^{1+\alpha} - 1\right]^{-\frac{1}{3(1+\alpha)}}\,, \tag{6.46}$$

being obtained from Eqs. (6.28) and (6.30) (see vertical lines in Fig. 6.3). Comparing the upper and lower plots in Fig. 6.3 we note that for higher k, δ_- stops growing at earlier times. Higher values of ϵ_i (the vertical lines are plotted from right to left for increasing values of ϵ_i) also have a similar effect, since $a_{\rm tr}$ decreases as ϵ_i increases, leading to an earlier increase of the critical scale in the '$-$' component, preventing further collapse (notice that for $\epsilon_i \to 1$, corresponding to a ΛCDM limit, the density fluctuations of the '$-$' component become negligible at all scales). If the transition to a dark energy state in the '$-$' component happens while the background is still dominated by the matter components, then Eq. (6.41) gives

$$\ddot{\delta}_{\rm m} + \frac{1}{2}\dot{\delta}_{\rm m} - \frac{3}{2}\Omega_{\rm m}\delta_{\rm m} = 0\,, \tag{6.47}$$

taking $\delta_- \sim 0$. During the matter era one can assume $\Omega_{\rm m} \sim$ const, so Eq. (6.47) has the growing solution $\delta_{\rm m} \propto a^{\lambda}$ where

$$\lambda = \frac{1}{4}\left(-1 + \sqrt{1 + 24\Omega_{\rm m}}\right)\,. \tag{6.48}$$

In this case, the contribution of the '$-$' component is also subdominant (i.e. $\Omega_- = 1 - \Omega_{\rm m} \ll 1$), so we may expand the radical to obtain

$$\lambda \sim 1 - \frac{3}{5}\Omega_{-}\,, \tag{6.49}$$

showing that, on scales smaller than the sound horizon, density perturbations grow at a slower pace when compared to the standard case (i.e. $\lambda = 1$).

6.3.4 CMB power spectra

The CMB power spectra computed by `CLASS` is shown in Fig. 6.4. The blue line shows the ΛCDM model with the standard values for the cosmological parameters being considered (see Sec. A.1). The Nonlinear GCG CMB power spectra predictions (with $\alpha = 1$) are plotted in black lines, for three values of the initial collapsed fraction: $\epsilon_i = 0.5$ (solid lines), $\epsilon_i = 0.8$ (dashed lines) and $\epsilon_i = 0.99$ (dotted-dashed lines). The GCG changes the CMB temperature spectrum with respect to the ΛCDM prediction mainly for two reasons: a different the expansion history resulting on a shift in the location of the peaks, and a different decay of the gravitational potential at late times, affecting the CMB anisotropies for low-multipoles due to the late integrated Sachs-Wolfe (ISW) effect [394]. For this discussion we fix ϵ_0 such that the angular scale of the sound horizon at the last scattering surface

$$\ell_A = \pi \frac{d_A^{(\mathrm{c})}(z_*)}{r_*}\,, \tag{6.50}$$

is the same for the different choices of ϵ_i (we take $\ell_A \sim 300$). Here $d_A^{(\mathrm{c})}$ is the comoving angular diameter distance, defined in a flat Universe as

$$d_A^{(\mathrm{c})}(z) = \int_0^z \frac{dz'}{H(z')}\,, \tag{6.51}$$

and r_* is the comoving size of the sound horizon of the coupled baryon-photon system at z_*

$$r_* = r_{\mathrm{s}}(z_*) = \frac{1}{\sqrt{3}} \int_{z_*}^{\infty} \frac{dz}{H(z)\sqrt{1 + (3/4)\,\rho_{\mathrm{b}}/\rho_\gamma}}\,, \tag{6.52}$$

where z_* is the redshift at the photon decoupling epoch.

With this requirement, we get lower values for the present total matter density parameter for lower ϵ_i ($\Omega_{\mathrm{m0}} \approx 0.21$ and $\Omega_{\mathrm{m0}} \approx 0.29$ for $\epsilon_i = 0.5$ and $\epsilon_i = 0.8$, respectively). The increase of Ω_{-} for models with lower ϵ_i is compensated by having a higher a_{tr} [see Eq. (6.46)], so the transition to a dark energy state in the '$-$' component happens at later times. The primordial amplitude A_s at the pivot scale $k_{\mathrm{P}} = 0.05\ \mathrm{Mpc}^{-1}$ is also adjusted to match the ΛCDM CMB peak amplitude. Hence, on small angular scales ($\ell \gtrsim 200$) all models follow the ΛCDM result, thus being consistent with CMB observations. Note that the model with $\epsilon_i = 0.99$ perfectly overlaps the blue line (i.e. the ΛCDM model) on all scales. On the other hand, models with values of ϵ_i not sufficiently close to 1, produce a strong signal on large angular scales, due to the late ISW effect.

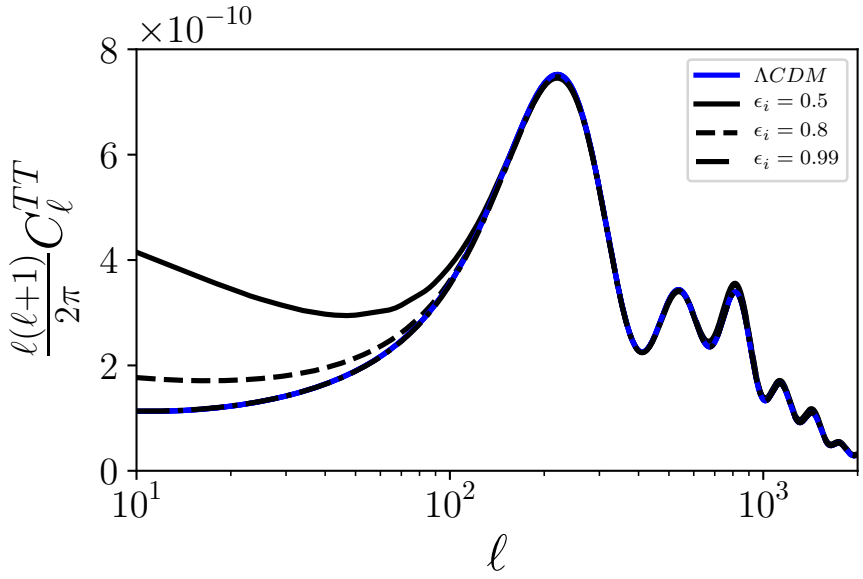

Figure 6.4: CMB power spectrum for cosmologies with a similar characteristic angle for the location of peaks on the CMB power spectrum ($\ell_{\rm A} \sim 300$). The result for the ΛCDM model considering the standard values (see Sec. A.1) is shown by the blue line. The black lines correspond to the CMB power spectrum predicted by the Nonlinear Chaplygin gas model with $\alpha = 1$, for three choices of the initial collapsed fraction: $\epsilon_i = 0.5$ (solid lines), $\epsilon_i = 0.8$ (dashed lines) and $\epsilon_i = 0.99$ (dotted-dashed lines).

6.3.5 Matter power spectra

In our implementation, the matter power spectrum incorporates the contribution from density fluctuations of the effective CDM component (δ_+) and baryons ($\delta_{\rm b}$). We also consider nonlinear corrections to the power spectrum using the Halofit model, as these corrections are needed for the weak lensing constraints presented in the following section (see [395, 396] for details). This fitting formula for the nonlinear matter power spectrum is calibrated from CDM N-body simulations, which is perfectly consistent with our assumptions regarding the collapse properties of the GCG (the GCG clusters very early, effectively behaving as CDM particles for most of the cosmic expansion history). Fig. 6.5 shows the matter power spectra for the ΛCDM model (blue line) and the Nonlinear CG models (black lines) with the same choice of parameters as given in the previous section, i.e. $\ell_A \sim 300$ for all models. Notice that the typical oscillations of the GCG matter power spectrum due to a large sound speed are absent. The pressure perturbations are carried by the '$-$' component, and its density perturbations become negligible with the transition to a dark energy state (see Sec. 6.3.3). On large scales all models agree with the ΛCDM result, while on smaller scales the variation of ϵ_i leads to slight changes in the amplitude of the matter power spectrum.

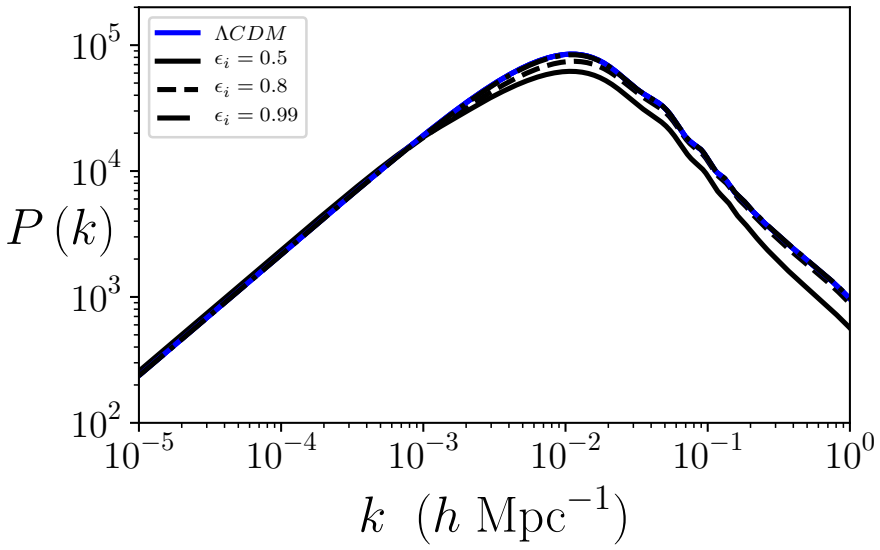

Figure 6.5: Matter power spectra for the same choice of parameters as in Sec. 6.3.4, including nonlinear corrections from the Halofit model. The blue line shows the ΛCDM result.

6.4 Observational constraints on nonlinear Chaplygin gas cosmologies

Here we present the observational constraints on the Nonlinear GCG model parameters using a likelihood analysis. We have performed the parameter estimation with the publicly available Monte Carlo code `Montepython` [397, 398], with the Python implementation `PyMultiNest` [399] of the nested sampling algorithm `Multinest` [400] to sample the parameter space. To guarantee that the chains are well converged, we verify that the Gelman-Rubin criterium [401] is satisfied (see Appendix A). For the data sets we take the Pantheon SNIa compilation [261], KiDS weak lensing [148, 402], and Planck 2018 CMB measurements [146] (see Appendix B).

The parameters defining the Nonlinear GCG model $\{\alpha\,,\,\epsilon_0\,,\,\epsilon_i\}$ are constrained against each data set and their combination. The cosmological parameters considered in the analysis are given in Table 6.2: the the physical baryonic density $\Omega_{\mathrm{b}0}h^2$, $\ln 10^{10}A_s$ (A_s is the amplitude of the scalar primordial power spectrum), the spectral index of scalar primordial power spectrum n_s, the present Hubble parameter H_0, and the optical depth τ_{reio}.

6.4.1 SNIa

We start by studying background constraints, using SNIa Pantheon data (see Appendix B.1). In order to be readily compared with the results obtained in [393], in this analysis we fix the parameters $\Omega_{\mathrm{b}0} = 0.0487$ and $H_0 = 67.3$ km s^{-1} Mpc^{-1} (a relativistic component is also taken into account by `CLASS`, but in this discussion we can safely ignore its contribution to the background). We also consider a fixed baryonic fractional density deep in the matter era of $\Omega_{\mathrm{b}i} = 0.155$ (corresponding to the ΛCDM value $\Omega_{\mathrm{b}i} = \Omega_{\mathrm{b}0}/\Omega_{\mathrm{m}0}$ for $\Omega_{\mathrm{m}0} = 0.315$). With this restriction, cosmologies dominated by the baryonic component during the matter era are avoided in the analysis. Otherwise, since

SNIa constraints are only sensitive to $H(z)$, large degeneracies would appear in the results.

Thus, using Eqs. (6.27) and (6.30) one obtains

$$\Omega_{\mathrm{b}i} = \frac{\Omega_{\mathbf{b}0}}{\Omega_{\mathbf{b}0} + \Omega_{\mathrm{gcg}0}\left[\epsilon_0 + (1-\epsilon_0)\left(1 - A_{\mathrm{eff}}\right)^{1/(1+\alpha)}\right]} = \frac{\Omega_{\mathbf{b}0}}{\Omega_{\mathbf{b}0} + \Omega_{\mathrm{gcg}0}\epsilon_0/\epsilon_i}\,, \tag{6.53}$$

which fixes the present collapsed fraction to

$$\epsilon_0 = \frac{\Omega_{\mathrm{b}0}}{\Omega_{\mathrm{gcg}0}}\frac{1-\Omega_{\mathrm{b}i}}{\Omega_{\mathrm{b}i}}\epsilon_i\,. \tag{6.54}$$

In this case the GCG model has only two independent parameters, that we take to be ϵ_i and α, while $\overline{A}$ and ϵ_0 are derived parameters, given by Eqs. (6.25), (6.30) and (6.54).

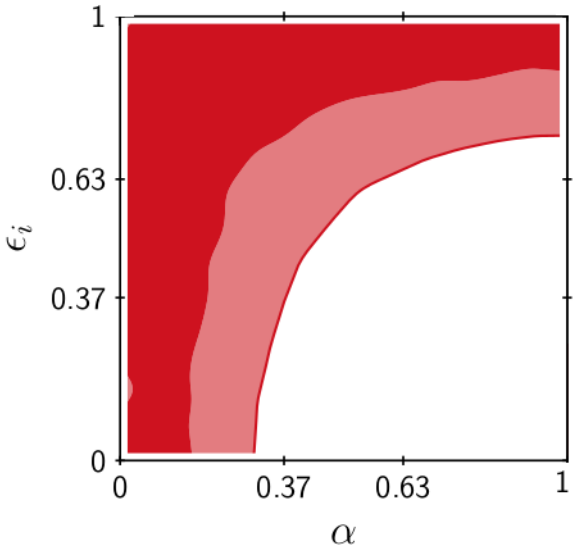

Figure 6.6: Observational constraints on the GCG parameters ϵ_i and α from the Pantheon SNIa compilation. Darker and lighter regions correspond to the 1σ and 2σ confidence level, respectively. In this analysis we assume $\Omega_{\mathrm{b}0} = 0.0487$, $\Omega_{\mathrm{m}0} = 0.315$, $H_0 = 67.3$ km s^{-1} Mpc^{-1}, and a fixed baryonic fractional density deep in the matter era of $\Omega_{\mathrm{b}i} = 0.155$

We perform a nested sampling analysis of a 3-dimensional parameter space. Besides the 2 GCG independent model parameters, we only include the absolute magnitude M as nuisance parameter. The result, marginalized over M, is shown in Fig. 6.6. Comparing the results from [393] with Fig. 6.6 we get slightly tighter constraints on the 1σ and 2σ regions (the Pantheon compilation being roughly twice the size of the Union 2.1 SNIa data set [403] and with data points at higher redshifts). All values of α in the interval $[0,1]$ are consistent with the SNIa observations at 1σ, provided that the value of ϵ_i is high enough. For models with lower values of ϵ_i this is no longer the case, and models with α closer to 1 are disfavored. Notice that, with the value of $\Omega_{\mathrm{b}i}$ being considered in this analysis, Eq. (6.54) limits the present collapsed fraction to the maximum value $\epsilon_0 = 0.279$ (obtained when $\epsilon_i \to 1$). The present value of the GCG equation of state parameter w_0 is constrained by this analysis to $w_0 = -0.75^{+0.03}_{-0.01}$. From Eqs. (6.18), (6.29), and (6.54), one may

write w_0 as

$$\begin{aligned} w_0 &= \left(\frac{\Omega_{\rm b0}\,(1-\Omega_{\rm bi})}{\Omega_{\rm bi}\,(1-\Omega_{\rm b0})}\epsilon_i - 1\right) + \left(\frac{1-\epsilon_i}{\frac{\Omega_{\rm bi}(1-\Omega_{\rm b0})}{\Omega_{\rm b0}(1-\Omega_{\rm bi})} - \epsilon_i}\right)^{1+\alpha} \\ &= (0.279\,\epsilon_i - 1) + \left(\frac{1-\epsilon_i}{\frac{1}{0.279} - \epsilon_i}\right)^{1+\alpha} . \end{aligned} \tag{6.55}$$

Taking $\epsilon_i = 0$

$$w_0|_{\epsilon_i=0} = -1 + 0.279^{1+\alpha}\,, \tag{6.56}$$

we get $w_0|_{\epsilon_i=0} = -0.721$ for $\alpha = 0$, which lies in the 1σ uncertainty interval. The absolute value of $w_0|_{\epsilon_i=0}$ gets larger as $\alpha \to 1$, reaching $w_0|_{\epsilon_i=0} \approx -0.92$ for $\alpha = 1$, which is already ruled out at more than 2σ. The lower 2σ bound obtained in the analysis $w_0 > -0.8$ constrains $\alpha \lesssim 0.26$ when $\epsilon_i = 0$. On the other hand, in the $\epsilon_i \to 1$ limit the second term on the r.h.s. of Eq. (6.55) becomes negligible. Therefore, one recovers

$$w_0|_{\epsilon_i=1} = -0.721\,, \tag{6.57}$$

being consistent at 1σ with the data irrespectively of the value of α.

Table 6.1: Parameters and corresponding flat priors used for the SNIa likelihood analysis in Sec. 6.4.1.

Type	Parameters	Prior
Model	α	$[0,\ 1]$
	ϵ_i	$[0,\ 1]$
	ϵ_0	Derived
	w_{-0}	Derived
	w_0	Derived
Cosmological	$\Omega_{\rm b0}$	0.0487
	h	0.673
Pantheon	$\mathcal{M}$	$[-20,\ -18]$

On the other hand, CMB data is able to impose tight constraints on the baryonic density fraction. Hence, when SNIa data is combined with Planck data (see Sec. 6.4.5), the baryon/GCG degeneracy "problem" from background constraints is irrelevant, and we no longer need to impose $\Omega_{\rm bi} = 0.155$ to reduce the number of free parameters. Therefore, for the analyses in the following sections, we consider instead the parameters and correspondent priors given in Table 6.2.

6.4.2 Weak lensing

For the analysis with weak lensing we use KiDS-450 data (see Appendix B.4). We use 3 tomographic bins ($z_1 \in [0.10, 0.30]$, $z_2 \in [0.30, 0.60]$ and $z_3 \in [0.60, 0.90]$). The uncertainties of the measured convergence power spectra on these 3 redshift bins (3 auto power spectra and 3 cross-spectra

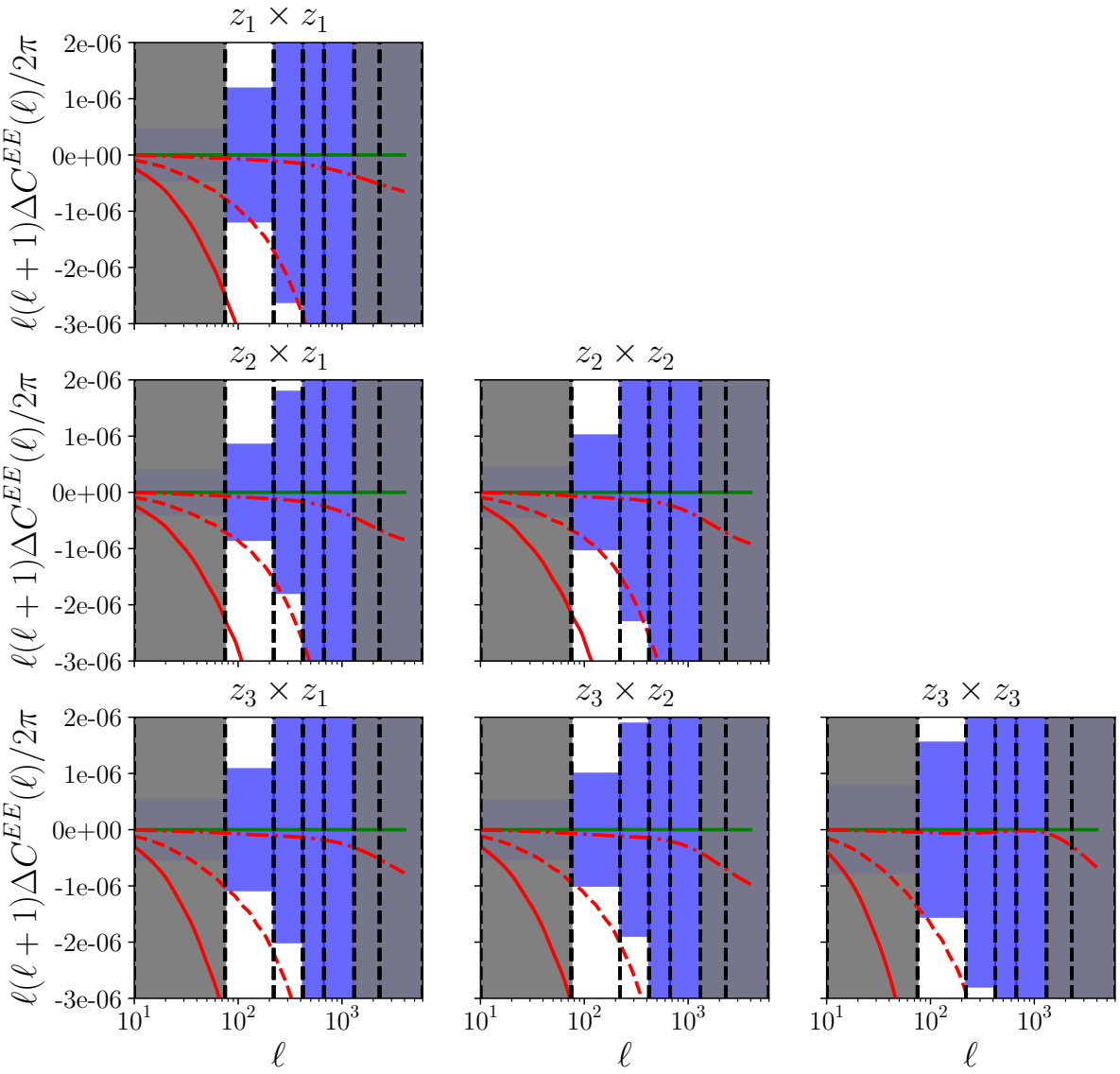

Figure 6.7: Diference of the convergence power spectrum for the Nonlinear GCG (red lines) with respect to the ΛCDM model considering $\epsilon_i = 0.5$ (solid line), $\epsilon_i = 0.8$ (dashed line) and $\epsilon_i = 0.99$ (dotted-dashed line). All models have $\alpha = 1$ and $\ell_A \sim 300$ (see Sec. 6.3.4). The auto-correlations are shown on the diagonal panels and the unique cross-correlations between the redshift bins are presented in the off-diagonal plots. The dashed vertical lines delimit the band powers, with the shadow regions in grey being excluded from the KiDS-450 analysis. The blue regions show the 1σ errors for each band derived from the analytical covariance matrix.

between pairs of bins) are shown in Fig. 6.7 for multipoles in the range $76 \leq \ell \leq 1310$; the first, second to last, and last band powers are not considered in the analysis (shaded in grey). This choice for the redshift bins and multipole range correspond to the ones used in the KiDS data [148]. The auto power spectra are shown on the diagonal panels and the cross-spectra are presented in the off-diagonal plots. We also plot the difference between the Nonlinear GCG and the ΛCDM model in the predicted convergence power spectrum, i.e. $\Delta C^{EE}(\ell) = C^{EE}_{\Lambda\mathrm{CDM}}(\ell) - C^{EE}_{\mathrm{gcg}}(\ell)$, for different values of ϵ_i. This allows us to have a hint on the potential of KIDS-450 data to discriminate between our GCG model and ΛCDM. The behavior of $\Delta C^{EE}(\ell)$ is similar for all power spectra. Here $\alpha = 1$ and ϵ_0 is fixed such that all models have $\ell_A \sim 300$ (see Sec. 6.3.4). The deviation of the $\epsilon_i = 0.99$ model from ΛCDM starts to manifest on the small scales of the data, but the error bars are too large to allow to distinguish the models. Models with $\epsilon_i < 0.8$ start deviating at least by 1σ from ΛCDM. Since the deviations are small (less than 2σ), degeneracies with other parameters will most likely prevent these data to strongly constrain ϵ_i.

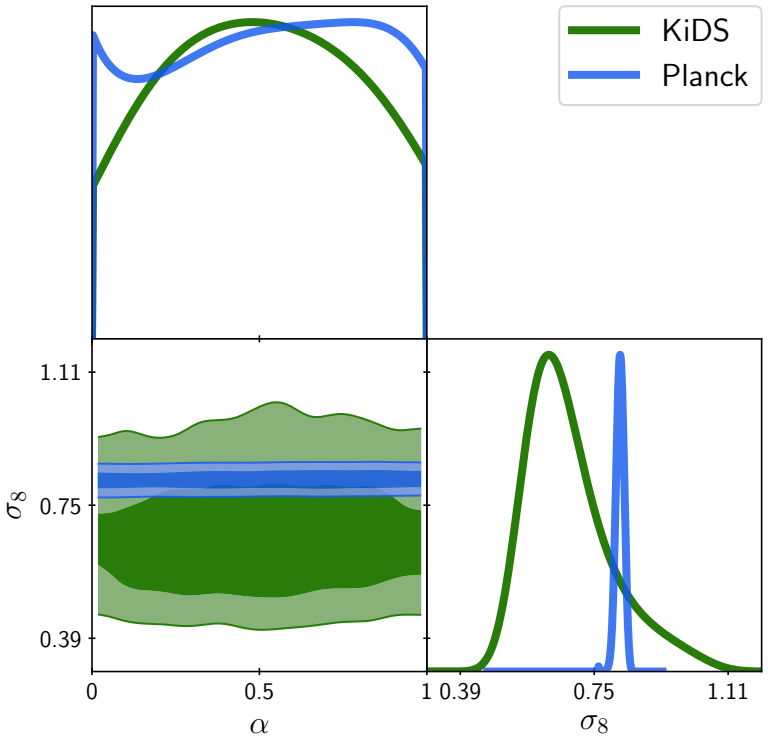

Figure 6.8: Comparison of the constraints from KiDS (green contours) and Planck (cyan contours) in the σ_8, α plane. Nonlinear GCG models with values over all the range of α are allowed by CMB and the joint analysis CMB+WL.

Let us move then to the full WL analysis. We perform a nested sampling analysis of a 14-dimensional parameter space. The parameters used are: 3 GCG model parameters (α, ϵ_i, ϵ_0), 5 standard cosmological parameters, and 6 WL nuisance parameters (see Appendix B.4). The list of parameters and the corresponding limits of flat priors used in the analysis are given in Table 6.2. The constraints for the GCG models parameters, marginalized over all nuisance and standard cosmology parameters are shown in the Fig. 6.9 (green contours). The model parameters are only mildly constrained; only

ϵ_0 and w_0 are constrained at 2σ in the prior interval, with the constraints on ϵ_0 being comparable with the ones presented in [148] for the present matter density parameter.

Note that like in the galaxy survey data analysis of chapter 3 (using SDSS galaxy clustering data), we also find that galaxy survey data (in this case WL) basically does not limit α, all values between 0 and 1 being allowed. However, in that analysis (where the clustering of the GCG model is driven by the baryons), the wide range of α was allowed only for models with low σ_8 values. When combining with CMB data, only a small region close to $\alpha = 0$ remained viable (corresponding to higher σ_8 values compatible with CMB constraints) reducing to the ΛCDM limit. Here on the contrary, for a model where the clustering is driven by the nonlinear GCG clumps, the wide range of α found is more robust, not being restricted to low σ_8 amplitudes. The corresponding Planck and KiDS constraints on the $(\sigma_8\,, \alpha)$ plane (when marginalizing over all other parameters) is shown in Fig. 6.8.

Table 6.2: Priors used for the likelihood analysis with KiDS-450 (green contours in Fig. 6.9), Planck 2018 (blue contours in Fig. 6.9) and for the combined analysis Pantheon + KiDS-450 + Planck 2018 (results given in Table 6.5).

Type	Parameters	Prior
Model	α	[0, 1]
	ϵ_i	[0.5, 0.9999]
	ϵ_0	[0, 0.4999]
	w_0	Derived
	w_{0-}	Derived
Cosmological	$\Omega_{\rm b0}h^2$	[0.019, 0.026]
	$ln10^{10}A_s$	[1.7, 5.0]
	n_s	[0.7, 1.3]
	H_0	[60.0, 80.0]
	$\tau_{\rm reio}$	[0.01, 0.15]
	σ_8	Derived
Pantheon	$\mathcal{M}$	[−20, −18]
Planck	$A_{\rm planck}$	[90, 110]
KiDS	$m_{\rm corr}$	[−0.03368, 0.00632]
	$A_{\rm noise}\,(z_1)$	[−0.1, 0.1]
	$A_{\rm noise}\,(z_2)$	[−0.1, 0.1]
	$A_{\rm noise}\,(z_3)$	[−0.1, 0.1]
	$A_{\rm bary}$	[0, 10]
	$A_{\rm IA}$	[−6, 6]

6.4.3 CMB

For the analysis with CMB we use Planck 2018 data (see Appendix B.3). We use the combination of the high-ℓ TT likelihood at multipoles $\ell \geq 30$ (`Plik_lite`) and the low-ℓ ($\ell = 2$ to $\ell = 29$) temperature (`Commander`) and polarization (`SimAll`) likelihoods [404]. We perform a nested sampling analysis of a 9-dimensional parameter space. Besides the 3 GCG model parameters and the 5 standard cosmological parameters, we only include one CMB nuisance parameter $A_{\rm planck}$. The

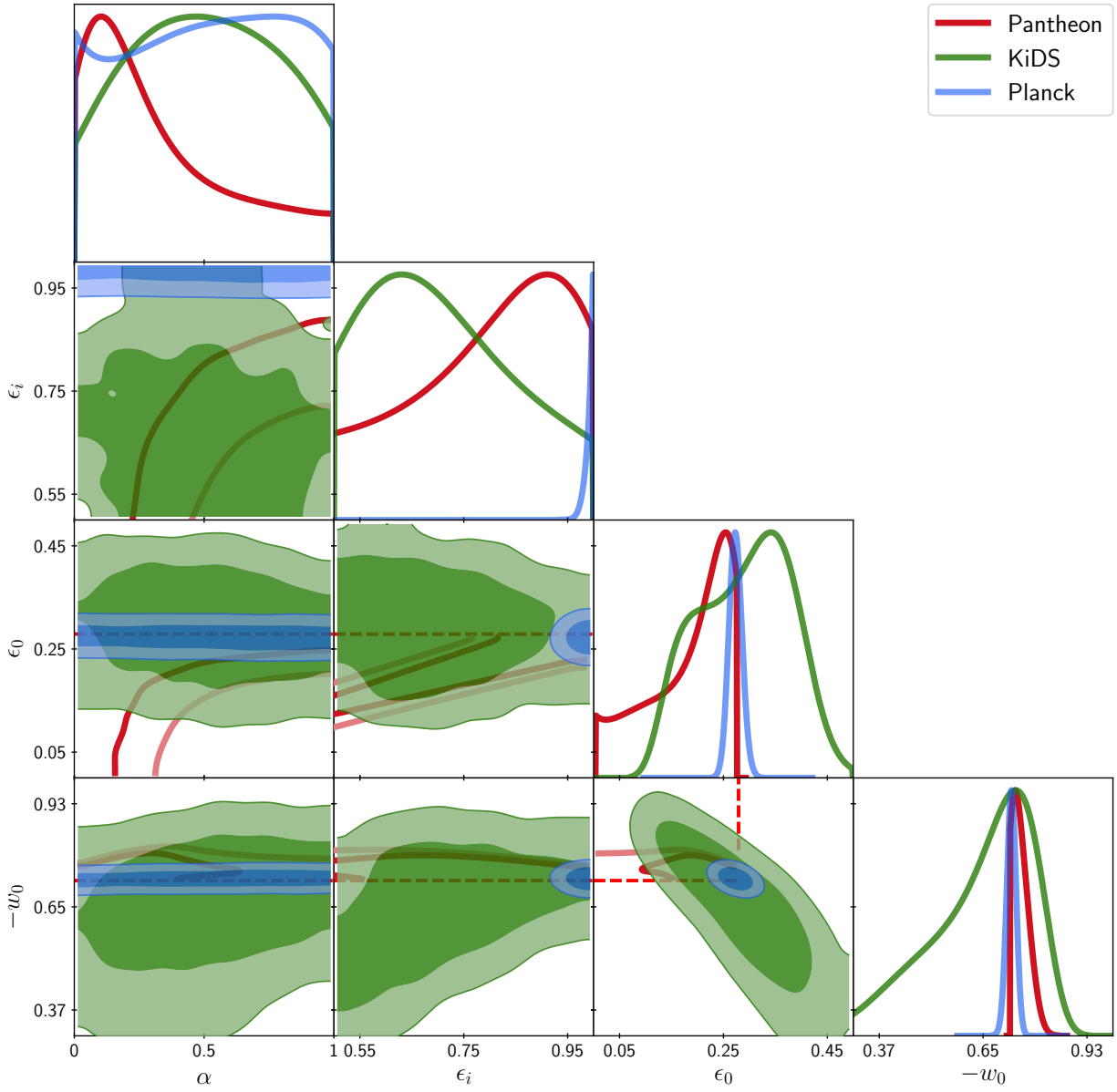

Figure 6.9: One and two dimensional posterior distribution showing the 1σ (darker regions) and 2σ (lighter regions) constraints for the Nonlinear Chaplygin gas model parameters obtained from KiDS weak lensing (green contours) and Planck 2018 CMB measurements (cyan contours) (check Table 6.2 for the assumed priors). The open contours in red refer to the constraints with Pantheon SNIa data (see Sec. 6.4.1 for details on the analysis). The dashed red lines indicate the upper bounds on the values of ϵ_0 and w_0 resulting from the priors assumed in Table 6.1.

Table 6.3: Results from the likelihood analysis with KiDS-450 data. We show the best-fit and mean values for the nonlinear GCG model and cosmological parameters, with the correspondent 1 and 2σ deviations. Notice that α is unconstrained in the $[0\,,1]$ interval by the data. The minimum χ^2 given by the best-fit values is $\chi^2_{\rm min} = 49$.

Parameters	Best-Fit	Mean$\pm\sigma$	-2σ	$+2\sigma$
ϵ_0	0.44	$0.29^{+0.10}_{-0.09}$	0.12	0.45
$-w_0$	0.34	$0.63^{+0.17}_{-0.11}$	0.34	0.89
$-w_{-0}$	0.61	$0.89^{+0.11}_{-0.02}$	0.60	0.99
σ_8	0.55	$0.68^{+0.08}_{-0.15}$	0.47	0.96
$\Omega_{\rm m0}$	0.470	$0.323^{+0.098}_{-0.084}$	0.159	0.477
S_8	0.704	$0.724^{+0.067}_{-0.075}$	0.581	0.863

list of parameters and the corresponding limits of flat priors used in the analysis are given in Table 6.2. The constraints for the GCG models parameters, marginalized over all nuisance and standard cosmology parameters are shown in Fig. 6.9 (cyan contours).

Table 6.4: Results from likelihood analysis with Planck 2018 data. We show the best-fit and mean values for the nonlinear GCG model and cosmological parameters, with the correspondent 1 and 2σ deviations. The parameters ϵ_i and w_{0-} are tightly constrained to $\epsilon_i \gtrsim 0.97$ and $w_{-0} \lesssim -0.99$ at 2σ, while α is unconstrained in the $[0\,,1]$ interval. The minimum χ^2 given by the best-fit values is $\chi^2_{\rm min} = 623$.

Parameters	Best-Fit	Mean$\pm\sigma$	-2σ	$+2\sigma$
ϵ_0	0.267	0.273 ± 0.015	0.244	0.303
$-w_0$	0.733	0.726 ± 0.015	0.697	0.755
$\Omega_{\rm m0}$	0.302	0.308 ± 0.015	0.278	0.338
$\omega_b \times 10^2$	2.223	$2.211^{+0.027}_{-0.028}$	2.156	2.264
$ln10^{10}A_s$	3.045	3.041 ± 0.018	3.005	3.077
n_s	0.968	0.963 ± 0.007	0.949	0.977
H_0 [km/s/Mpc]	68.3	67.8 ± 1.1	65.7	70.0
$\tau_{\rm reio}$	0.057	0.052 ± 0.008	0.036	0.069
σ_8	0.821	0.819 ± 0.015	0.794	0.849
S_8	0.87	0.87 ± 0.03	0.81	0.93

Fig. 6.9 shows a very strong constraint on ϵ_i, being highly restricted to assume values close to 1. Due to Planck high precision data of the CMB temperature spectrum at multipoles $\ell > 30$, GCG models are tightly constrained to a combination of parameters giving similar ℓ_A. As we have shown in Sec. 6.3.4, varying the value of ϵ_i (while keeping ℓ_A fixed) changes the spectrum on large scales, where the Planck error bars are larger. Yet, models with $\epsilon_i < 0.8$ start deviating significantly from ΛCDM already at $\ell \sim 60 - 70$. Hence, we get a lower limit $\epsilon_i \gtrsim 0.968$ at 2σ from CMB data alone. Constraints on the parameters ϵ_0 and w_0 are also improved in comparison to the results from KiDS. However, α remains unconstrained for values inside the prior interval $[0, 1]$. This is an interesting result: nonlinear GCG models with values over all the range of α are allowed by CMB and the joint analysis CMB+WL, overcoming the shortcomings pointed out by [266] on the one side, and the problem of the low clustering amplitude introduced by the baryon-driven clustering solution on

the other side.

6.4.4 CMB vs WL Tensions

The projection of cosmological constraints in the σ_8 versus $\Omega_{\rm m0}$ plane from KiDS and Planck data is shown in Fig. 6.10. Notice that the well known disagreement between CMB and cosmic shear measurements is still present for the nonlinear GCG model at $\sim 1.7\sigma$, with $\sigma_8 = 0.68^{+0.08}_{-0.15}$ and $\sigma_8 = 0.82 \pm 0.02$ for the marginalized constraints from KiDS and Planck, respectively. Slightly larger values for the present matter density are favored by KiDS ($\Omega_{\rm m0} = 0.32^{+0.10}_{-0.08}$) when compared to Planck ($\Omega_{\rm m0} = 0.31 \pm 0.02$) but their values are perfectly consistent at 1σ. In the literature the tension between CMB and weak lensing is often quantified using the combination $S_8 = \sigma_8 \sqrt{\Omega_{\rm m0}/0.3}$. Our analysis give $S_8 = 0.72^{+0.07}_{-0.08}$ for KiDS and $S_8 = 0.87 \pm 0.03$ for Planck, which are in tension at the $\sim 2\sigma$ level. This value is slightly lower than the reported $\sim 2.3\sigma$ discrepancy between KiDS-450 [148] and CMB Planck data for the standard ΛCDM model.

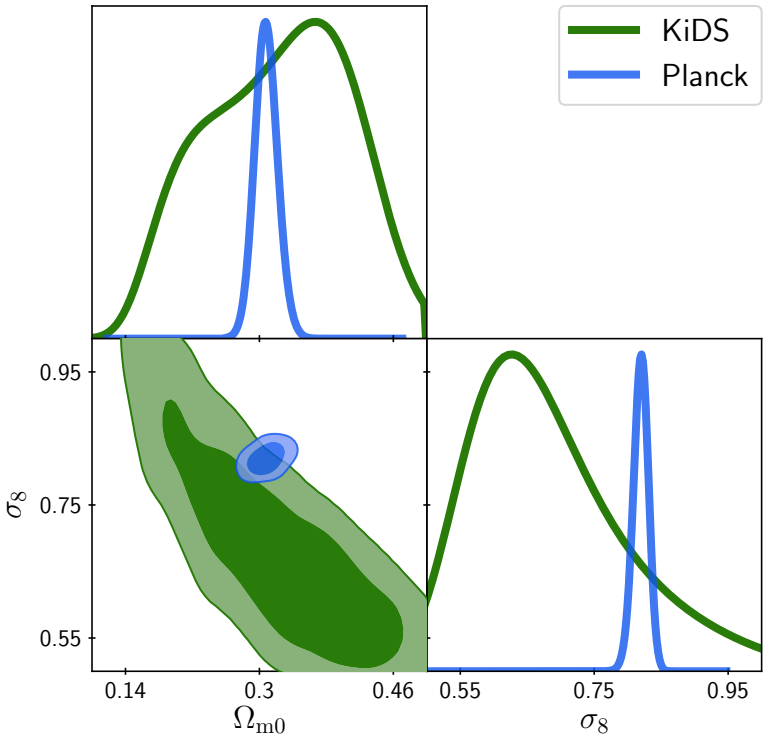

Figure 6.10: Comparison of the constraints from KiDS (green contours) and Planck (cyan contours) in the σ_8, $\Omega_{\rm m0}$ plane (where $\Omega_{\rm m0} = \Omega_{\rm b0} + \Omega_{+0}$).

6.4.5 Joint SNIa+WL+CMB analysis

We perform a combined likelihood analysis with Pantheon + KiDS-450 + Planck 2018. Here, for the CMB data, we take the temperature only likelihoods i.e. high-ℓ TT likelihood at multipoles $\ell \geq 30$ (`Plik_lite`) and the low-ℓ ($\ell = 2$ to $\ell = 29$) `Commander` likelihood. The full set of parameters used and their priors are given in Table 6.2. The results are shown in Table 6.5. The combined analysis imposes stringent limits to the present and initial collapsed fraction of the GCG, which are

Table 6.5: Results for the combined likelihood analysis Pantheon + KiDS-450 + Planck 2018. We show the best-fit and mean values for the nonlinear GCG model and cosmological parameters, with the correspondent 1 and 2σ deviations. The parameters ϵ_i and w_{0-} are tightly constrained to $\epsilon_i \gtrsim 0.96$ and $w_{-0} \lesssim -0.99$ at 2σ, while α is unconstrained in the $[0\,,1]$ interval. The minimum χ^2 given by the best-fit values is $\chi^2_{\rm min} = 1310$.

Parameters	Best-Fit	Mean $\pm$ 1σ	-2σ	$+2\sigma$
ϵ_0	0.253	$0.250^{+0.015}_{-0.014}$	0.219	0.278
$\overline{A}$	0.652	$0.654^{+0.068}_{-0.059}$	0.552	0.758
w_0	-0.747	-0.749 ± 0.014	-0.776	-0.723
$\Omega_{\rm b0}h^2 \times 10^2$	2.25	2.24 ± 0.04	2.17	2.31
$\ln\left(10^{10}A_{\rm s}\right)$	3.12	$3.12^{+0.06}_{-0.05}$	3.03	3.22
$n_{\rm s}$	0.976	0.973 ± 0.010	0.956	0.990
H_0 [km/s/Mpc]	69.5	$69.6^{+1.2}_{-1.3}$	67.3	72.1
$\tau_{\rm reio} \times 10^2$	9.38	$9.77^{+3.10}_{-2.40}$	4.89	14.47
σ_8	0.845	0.840 ± 0.026	0.792	0.889

driven by the Planck constraints. Their mean values and 1σ deviations are $\epsilon_0 = 0.2499^{+0.015}_{-0.014}$ and $\epsilon_i = 0.9855^{+0.014}_{-0.0088}$. The value of the dark energy equation of state parameter w_{0-} is also tightly constrained to values close to -1, thus following closely the behavior of a cosmological constant at the present. In contrast, the parameter α is essentially unconstrained by the combined data in the interval $[0, 1]$. The best-fit values are shown in Table 6.5, and are in general close to the mean values of the posterior distribution. It is a model with ϵ_i close to 1, $\epsilon_0 = 0.253$, $w_0 = -0.747$ and $w_{-0} \sim -1$. The mean density parameters of the '+' and '$-$' components are $\Omega_{+0} = 0.241$ and $\Omega_{-0} = 0.712$, respectively.

The χ^2 of the best-fit model is $\chi^2_{\rm min} = 1310$. As a consistency check, we have also verified that the ΛCDM model provides a similar goodness of fit to the data.

Chapter 7

Conclusions and Outlook

In this thesis we have explored the possibility of accounting for the phenomenology associated to the cosmological dark sector (conventionally assumed to be constituted by CDM and a cosmological constant) using a single fluid. In particular, we focused on a class of UDE models described by isentropic perfect fluids. We found that, when a traditional approach to perturbation theory is assumed, observations restrict isentropic UDE models to behave very closely to ΛCDM. The key factor behind this result is the fact that the adiabatic sound speed in isentropic perfect fluids is necessarily tied up to the background evolution. A sound speed significantly different from zero typically arises in isentropic UDE, when the transition from a dark matter state to a dark energy state occurs. This introduces a characteristic length determining the stability of linear perturbations which, if not sufficiently small, affects in a crucial way the standard growth of cosmic structures on linear scales. Therefore, the sound speed has to be very close to zero in order to be consistent with large scale structure observations; in these models, the background evolution is necessarily ΛCDM-like.

Notice that this result, by itself, does not refute the single dark fluid hypothesis in general, or invalidate isentropic UDE models in particular. As we have discussed, the ΛCDM model also admits a single fluid interpretation in terms of an isentropic perfect fluid with zero sound speed (remember that the dark sector, so far, has only been inferred gravitationally, and gravity alone does not discriminate the number of dark components). Furthermore, with an equation of state being given just by a negative and constant pressure, the ΛCDM may be regarded as the simplest UDE model one can concoct. On the other hand, the strong restrictions on isentropic UDE from linear analysis could discourage the pursue of further models or parametrizations; in the literature, a common way out to avoid large sound speeds in UDE models is to give up entirely on isentropic perfect fluids, and consider e.g. non adiabatic contributions to the sound speed [405, 406]. It turns out that a proper analysis of UDE scenarios is much more complex to deal with than what could be initially expected, and one does not need to go beyond the isentropic perfect fluid assumption to find far more richer phenomenology.

We have argued in this thesis that potential backreaction effects cannot, in general, be ignored in

the context of UDE. As the behavior of both dark matter and dark energy arise from the same single fluid, the local equation of state has to reproduce both phenomena. Hence, the background dynamics is prone to be affected by inhomogeneities (even if present only on small scales), as the values of the local and large scale average quantities can be completely different. A standard approach to perturbations can be safely used on linear scales in the case that dark matter and dark energy are independent i.e. when the equations of state of both components do not depend on one another. As a result, the nonlinear collapse of CDM on small scales (occurring mainly during the matter era) does not influence the dynamics of the dark energy component, which in the case of the standard model is given by a constant Λ everywhere. Note that this insusceptibility of the background dynamics to small scale inhomogeneities is also consistent with the single fluid interpretation of ΛCDM — the equation of state of the total fluid is simply determined by a constant pressure everywhere, irrespectively of the level of clustering. However, this is not the case if more general UDE models are considered.

Taking into account the formation of nonlinear structures in these models may become crucial even for background analyses. To study the impact of small scale nonlinear clustering we have restricted our attention to the GCG, taken as a representative model of isentropic UDE. As we have noted, previous studies suggest that level of nonlinear clustering is expected to not be significant if a standard scale-invariant primordial power spectrum is assumed. However, the amplitude and shape of the power spectrum on small scales is poorly constrained by observations, and deviations with respect to the simple power law on these scales cannot be dismissed. Hence, it is relevant to study the impact of such deviations on the efficiency of nonlinear clustering in the GCG. In turn, the exact details on the formation and evolution of small scale nonlinearities are expected to be model dependent. Therefore, even if nonlinear clustering is likely to affect any isentropic UDE model in a critical way, the degree to which backreaction effects are important need to be assessed for a each particular case. Of course, this includes all the other isentropic UDE models that we have studied in this thesis.

Ultimately, the problem of backreaction in isentropic UDE cosmologies should be addressed by solving the full Einstein equations. Tackling this problem with all generality is, by all means, inconceivable in the foreseeable future. However, as we have mentioned, fully relativistic simulations have been used to compute the evolution of inhomogeneous distributions of matter and measure departures with respect to the background and linear predictions of FLRW cosmologies. Particularly, in [369] it was computed for the first time the exact behavior of geometric backreaction as defined by Buchert's averaging formalism [407]. It should be underlined that most discussions in the literature are often centered on the problem of backreaction by geometrical averaging, as this is the relevant case in the ΛCDM model scenario. In this context, simulations have also consistently shown that backreaction effects are negligible given the current precision of cosmological observations. Interestingly, Buchert extended his formalism to the perfect fluid case in [377] (see also [408]), and mentions the backreaction effect arising from the non-trivial averaging of the perfect fluid energy-momentum tensor (that we have discussed in Sec. 6.2). We are not aware of any numerical analyses focusing on this more general case, which may be pertinent to clarify the

importance of the impact of nonlinearities in the background evolution and clustering properties of isentropic UDE models.

One should bear in mind that throughout this thesis (and in our discussion above) we have considered that the cosmological dark sector is well described by an isentropic perfect fluid on all scales. In general, the working assumption of a perfect fluid is expected to break on sufficiently small scales [409] — the specific scale at which this happens might have implications for the backreaction problem in UDE. On the other hand, the scalar field theories studied in chapters 4 and 5 to describe isentropic UDE models, also incorporate a regime for which the dynamics of the scalar field is not the one of an isentropic perfect fluid. Therefore, if one considers that the dark sector is fundamentally accounted by a scalar field (whose dynamics is characterized by one of the Lagrangians considered in those chapters), an isentropic perfect fluid can still provide a valid effective description of the scalar field dynamics, except when nonlinearities start to become important (more specifically, when the spatial gradients dominate over the time variations of the scalar field). Further work has yet to be done to determine the susceptibility of these scalar field UDE models to backreaction effects.

Summary

Let's now summarize the main results of our work.

In chapter 3 we discussed the problem of dark degeneracy, motivating a phenomenological approach to model the dark sector by a single fluid. We then presented the GCG in Sec. 3.2 as an archetypal example of isentropic UDE, studying the main cosmological properties at the background level and evolution of linear density perturbations. SNIa observations are shown to constrain $0.713 < \overline{A} < 0.845$ at a 95% level; α, on the other hand, is not well constrained in the $[0\,,\,1]$ prior interval. On the other hand, the GCG power spectrum shows a significant deviation with respect to the ΛCDM-like spectrum on linear scales unless $|\alpha| \lesssim 10^{-5}$. Although this tight restriction can be evaded if baryons are also considered in the analysis of matter power spectrum constraints, a simultaneous fit to the combination of SNIa, CMB, and matter power spectrum observations can only be obtained for α close to zero. In this case, the GCG is forced to behave very similarly to ΛCDM, as both models are completely equivalent in the limit $\alpha \to 0$ and finite $\overline{A}$. We have demonstrated in Sec. 3.2.6 that it is possible to find a logarithmic limit of the GCG, i.e. a perfect fluid with an equation of state $p\,(\rho) \propto \ln\,(\rho)$, dubbed logarithmic Chaplygin gas (logCG), by a regularization of the limit $\left(\alpha \to 0\,,\,\overline{A} \to \infty\right)$. In Sec. 3.2.7 we then briefly discussed the case of the modified Chaplygin gas, as an extension to the GCG model which incorporates an effective dark matter component with a non-zero sound speed regulated by a new parameter B. We showed that the rotational velocity of galaxies can be used to constrain the value of B and derived a conservative upper limit $B < 10^{-8}$, which provides the best constraint to date. In Sec. 3.3 we studied the recently proposed logotropic fluid as UDE, originally given in terms of an equation of state $p\,(n) \propto \ln\,(n)$. We show that this model may alternatively be defined by a barotropic equation of state $p = p\,(\rho)$ via the Lambert W function. The two real branches of this function are found to have a clear physical interpretation: the principal branch W_0 corresponds to a phantom regime and the branch W_{-1} to

a standard evolution of the energy density. Logotropic cosmologies are degenerate with ΛCDM for the logotropic parameter $B_{\rm lgt} = 0$. We determined an upper limit $B_{\rm lgt} \lesssim 6 \times 10^{-7}$ by requiring that the linear growth of cosmic structures is not significantly affected with respect to the standard matter evolution. This result rules out the identification of the logotropic reference number density with the Planck density previously suggested in the literature. Moreover, we have also shown that logotropic dark matter halos are unstable under homologous perturbations unless its present energy density is unrealistically large. We concluded that these results preclude the logotropic dark fluid of providing a solution to the small scale problems of the ΛCDM model.

In chapter 4 we investigated the appropriateness of scalar field theories to describe the dynamics of perfect fluids. The required formalism was reviewed in Sec. 4.1.1. Focusing on a particular case of the Schutz-Sorkin action, we showed in Sec. 4.1.2 that the equation of motion of a minimally coupled scalar field determined by purely kinetic Lagrangians are adequate to describe the dynamics of isentropic perfect fluids, provided that $X > 0$. In Sec. 4.2 we provided examples of Lagrangians describing some of the isentropic UDE models discussed in chapter 3: the GCG, the logotropic fluid, and the logCG. To our knowledge, a pure k-essence Lagrangian representation of the logotropic model has not been presented before. In Sec. 4.3 we motivated a one-parameter extension to the GCG Lagrangian, showing that the GCG model is recovered in the non-relativistic limit independently of the value of the new parameter β. We studied the background evolution of this extended family of GCG models, with an explicit solution for the evolution of the energy density being obtained in the limit $\alpha \to \infty$. Taking the extended GCG as a UDE model, the parameters α and β exhibit a large degeneracy on the SNIa constraints. We then showed that, for $\alpha = 1$, large oscillations in the predicted linear matter power spectrum can be avoided on linear scales if $\beta \gtrsim 10^5$.

In close connection with the results derived in Sec. 4.1.1, we presented in chapter 5 a mapping between pure kinetic dark energy and UDE models, established by an appropriate relation between their kinetic terms. This allows for the explicit determination of a UDE Lagrangian when a dark energy model is given as input. Assuming a CPL parametrization of the equation of state for the input dark energy model, we showed that large sound speeds at late times are unavoidable unless $|1 + w_\infty| \lesssim 10^{-6}$, where $w_\infty = w_{\rm de}\,(z = \infty)$. As a result, the input dark energy model has to follow very closely the behavior of a cosmological constant.

We argued in chapter 6 that the traditional approach to perturbation theory is, in general, not sufficient to account for all the relevant physics in UDE scenarios. In Sec 6.1 we briefly reviewed the problem of cosmological backreaction. The averaging problem in isentropic UDE models is then presented in Sec. 6.2. In Sec. 6.3 we studied the impact of nonlinearities in GCG cosmologies. Given that nonlinear clustering of the GCG fluid is expected to occur at sufficiently high redshifts and on small enough scales, these high density regions are assumed to virialize and decouple from the expansion, effectively behaving as a dark matter component. We also considered that the fraction of GCG in high density regions is constant at high redshifts, which is then taken as a free parameter in an ansatz parametrizing the level of small scale nonlinear clustering. The GCG not contained in collapsed regions is assumed to be distributed in underdense regions, associated to an effective

dark energy component. Thus, we have shown in Sec. 6.3.2 that the background dynamics can be interpreted as a cosmology having CDM minimally coupled with a GCG component. From the analysis of the evolution of perturbations in Sec. 6.3.3, the density perturbations of the effective CDM component are shown to be able to grow on all scales even for models with $\alpha = 1$. We determined observational constraints using SNIa, CMB, and weak lensing data in Sec. 6.4. When the effect of nonlinear small scale clustering is taken into account, the results reveal that all values of $\alpha \in [0\,,\,1]$ are consistent with the observations, provided that initial fraction of GCG in collapsed regions is sufficiently close to 1.

Appendices

Appendix A

Methodology

A.1 Implementation in CLASS

The Cosmic Linear Solving System (CLASS) code[1] is a publicly available cosmological perturbation code written in C (programming language), that implements the full set of Einstein-Boltzmann equations [410–413]. The implementation of the physical equations is structured in a few modules, that compute:

1. background.c - background evolution;
2. thermodynamics.c - thermal history;
3. perturbations.c - perturbation equations for all cosmic components;
4. primordial.c - primordial power spectra;
5. nonlinear.c - linear and non-linear power spectra;
6. transfer.c - transfer functions;
7. spectra.c - linear and non-linear harmonic power spectra;
8. lensing.c - lensed temperature and polarization anisotropy power spectra;

The set of cosmological parameters are given as input in the module input.c and the results are written by the module output.c. If the value of a cosmological parameter is not explicitly given as input, the version of CLASS being used assumes, by default, the following values

[1] In this thesis we work with the version 2.9. released on 21/01/2020.

$$h = 0.67556\,, \tag{A.1}$$
$$\omega_{\rm r0} = 4.18371 \times 10^{-5}\,, \tag{A.2}$$
$$\omega_{\rm b0} = 0.022032\,, \tag{A.3}$$
$$\omega_{\rm cdm0} = 0.12038\,, \tag{A.4}$$
$$A_{\rm s} = 2.215 \times 10^{-9}\,, \tag{A.5}$$
$$n_{\rm s} = 0.9619\,, \tag{A.6}$$
$$\tau_{\rm reio} = 0.0925\,, \tag{A.7}$$

among other quantities (these ones are sufficient for our analyses). Regarding the implementation of the isentropic UDE models studied in this thesis, the necessary physics can be included by a modification of the modules background.c and perturbations.c. The new fluids are introduced as new components at the background level. For the GCG model, the evolution of the energy density with the scale factor is known [cf. Eqs. (3.5) and (6.22)] and can be easily implemented. On the other hand, for the extended GCG the energy density cannot be written explicitly as a function of the kinetic term [cf. Eqs. (4.83) and (4.84)]. Hence, for each time integration step, a root-finding algorithm is employed; due to the simplicity of implementation and robustness, we chose to use the Ridder's method. In the perturbation module perturbations.c, one has to implement the differential equations governing the evolution of linear perturbations (as discussed in Sec. 2.3), with the calculations being performed by default in the synchronous gauge. The procedure ends up being similar to other perfect fluid models already implemented in `CLASS`. Moreovoer, as we do not make any additional assumptions beyond the standard cosmological model besides treating the dark sector as a single fluid, the remaining modules do not need further modifications.

A.2 Cosmological parameters estimation

A.2.1 Statistical inference

To derive the observational constrains presented in this thesis we have implicitly used the theory of statistical inference i.e. we were inferring the properties of the underlying distribution of probability for the cosmological parameters given the observational data. This approach is known as Bayesian inference. Let us consider a model $M\left(p\right)$ that, given a set of k free model parameters $p = \{p_1\,,\, p_2\,,\, ...\,,\, p_k\}$, is able to predict some observable quantity $\psi_M = \psi\left(p\right)$. The probability of p delivering the right result when confronted with a set d of n observations of the quantity i.e. $d = \{\psi_1\,,\, \psi_2\,,\, ...\,,\, \psi_n\}$ (as measured by a certain experiment) is written as $P\left(p|d\right)$. This is known as the *posterior* probability of p given d. Now, the rule for the conditional probabilities gives

$$P\left(p \cap d\right) = P\left(p|d\right) P\left(d\right) = P\left(d|p\right) P\left(p\right)\,, \tag{A.8}$$

where $P(p \cap d)$ is the joint probability of the model to equal a certain p and the probability of the data to equal a certain d. Using Eq. (A.8) one can write the posterior probability as

$$P(p|d) = \frac{P(p)}{P(d)} P(d|p) \ , \tag{A.9}$$

this equation being known as the Bayes' theorem. The denominator $P(d)$ is known as the *evidence*, and plays the role of a constant normalization for the posterior probability. The probability $P(p)$ is called the *prior* probability of p. For each parameter p_i, the prior is often considered to be *flat* in a given interval (assuming a constant value inside that interval and zero outside) in a more conservative approach; if the value of the parameter has been inferred from another cosmological experiment one can also assume a Gaussian distribution i.e. we "expect" the parameter to have a certain mean value and a certain standard deviation.

The term $P(d|p)$ is the probability of getting the data d given the model parameters, and is usually known as the *likelihood*. Considering that observations measure a signal plus some noise given by a Gaussian distribution, one may write the likelihood for a single data point as

$$P(\psi_i|p) \propto \exp\left(-\frac{(\psi_i - \psi(p))^2}{2\sigma_i^2}\right) , \tag{A.10}$$

where σ_i^2 is the variance i.e. the observational error on the measurement of ψ_i. If the measurements of all data points are assumed to be independent then

$$P(d|p) = \prod_i P(\psi_i|p) \propto \exp\left(-\sum_i \frac{(\psi_i - \psi(p))^2}{2\sigma_i^2}\right) . \tag{A.11}$$

However, this is not always the case, and errors from different measurements may be correlated. In general, the likelihood function is written as

$$P(d|p) = L(p) = \frac{1}{(2\pi)^n \sqrt{\det(C)}} \exp\left(-\frac{\chi^2}{2}\right) , \tag{A.12}$$

where C is called the covariance matrix and

$$\chi^2 = [d - \psi(p)]\, C^{-1} [d - \psi(p)]^t \ . \tag{A.13}$$

Here t denotes the transpose. Of course, if $C_{ij} = 0$ for $i \neq j$ then one recovers Eq. (A.11).

A.2.2 Markov chain Monte Carlo methods

Now, we want to find the posterior distribution of the k dimensional space of the free model parameters. Furthermore, cosmological data sets often have several nuisance parameters (specific for each data set) that further increase the dimensions of the search space. Thus, computing the likelihood for a grid of parameters with high enough resolution quickly becomes intractable.

To explore the parameter space and extract the values of the cosmological parameters that are most likely against the several data sets, we use the Markov chain Monte Carlo (MCMC) code `MontePython` [397, 398].

Monte Carlo methods rely on random samples of points of the parameter space to represent the underlying distribution function. A Markov chain is a stochastic model defined by a sequence of random events, in which the probability of the nth element is only determined by the $(n-1)$th element. Given an initial point in the parameter space, the MCMC jumps to another point and computes the likelihood correspondent to that combination of parameters. If the likelihood in that point is higher than in the previous one, the MCMC accepts that new point and proceeds from there. If the likelihood is lower than in the previous one, an algorithm is used to decide if the chain accepts the new step or not. `MontePython` includes several methods to do the sampling which might be more or less efficient, that might depend on several factors e.g. the models being tested, the assumed priors, or the data sets. Taking these factors into account, in this thesis we have used the Metropolis-Hastings and Nested sampling [400] algorithms.

As the sampling progresses, the algorithm produces a chain of points in the parameter space. In `MontePython` the burn-in phase of each chain is defined, by default, as all the first points in the chains until an effective χ^2 value smaller than $\chi^2_{\rm min} + 6$ is reached for the first time. The points from the burn-in phase are then discarded. When the chain is converged, the density of the points reflects the underlying probability distribution. To check if the chains are well converged one can verify e.g. if there is an high acceptance rate of the proposed steps and if different chains starting from different points converge to the same distribution. Another useful convergence diagnostics is the Gelman-Rubin criteria [401]. Consider J chains running in parallel with length L and sampling set

$$x^{(j)} = \left\{ x_1^{(j)} \, , \, x_2^{(j)} \, , \, ... \, , \, x_L^{(j)} \right\} \, , \tag{A.14}$$

for each chain j. The chain and grand mean are given by

$$\overline{x}^{(j)} = \frac{1}{L} \sum_{t=1}^{L} x_t^{(j)} \, , \tag{A.15}$$

$$\overline{x} = \frac{1}{J} \sum_{j=1}^{J} \overline{x}^{(j)} \, , \tag{A.16}$$

respectively. The variance between chains is

$$B = \frac{L}{J} \sum_{j=1}^{J} \left(\overline{x}^{(j)} - \overline{x} \right)^2 \, , \tag{A.17}$$

and for the variance within the chains weighted for all J chains one has

$$W = \frac{1}{J}\sum_{j=1}^{J}\frac{1}{L-1}\sum_{t=1}^{L}\left(x_t^{(j)} - \overline{x}^{(j)}\right)^2 . \tag{A.18}$$

The Gelman-Rubin statistic

$$R = \frac{1}{LW}\left[(L-1)\,W + B\right] , \tag{A.19}$$

condenses the uncertainty on the final probability distribution introduced by the MCMC sampling by checking if the different chains are providing similar results. This ratio approaches 1 for large L and small B. Typically, one must ensure that $R - 1 < 0.01$.

A.2.3 Contour plots

The parameter space has, in general, a large number of dimensions. To obtain the 1 and 2-dimensional contour plots presented in this thesis, one has to *marginalize* the likelihood over the extra parameters. Analytically one has

$$L\left(p_1\right) = \int L\left(p\right) dp_2 \ldots dp_k \,, \tag{A.20}$$

for the 1-dimensional case and

$$L\left(p_1\,,\,p_2\right) = \int L\left(p\right) dp_3 \ldots dp_k \,, \tag{A.21}$$

for the 2-dimensional case. Notice that, if nuisance parameters are also considered in the analysis, they are marginalized over in a similar fashion. To produce the contour plots we use the `MontePython` plotting tools, where the marginalization is automatically made over the other parameters. Here the number of points in the higher dimensional parameter space are added over along the dimensions of marginalized parameters and then normalized over the total number of points in the chain.

The contours on the plots showing the 1σ and 2σ confidence levels are computed by finding and enclosing the highest 68% and 95% density values of the sampled parameter space, respectively. They approximately correspond to iso-contours of $\Delta\chi^2$

$$\Delta\chi^2 = \chi^2 - \chi^2_{\rm min} \,. \tag{A.22}$$

The values of $\Delta\chi^2$ corresponding to 1σ, 2σ and 3σ deviations depend on the number of parameters being fitted. For one parameter one has $\Delta\chi^2 = (1\,,\,4\,,\,9)$ and for two parameters $\Delta\chi^2 = (2.30\,,\,6.18\,,\,11.83)$. For illustration, in the case of the 2-dimensional contours, regions that satisfy the condition $\Delta\chi^2 < 2.30$ are within the 68% confidence level, while regions for which $2.30 < \Delta\chi^2 < 6.18$ are within the 95% confidence level.

Appendix B

Data sets

B.1 Pantheon sample (SNIa)

Due to their extreme intrinsic luminosity, supernova explosions can be detected at relatively high redshifts ($z \sim 1$). In particular, supernova type Ia (SNIa) are known to have an almost constant absolute magnitude M at the peak of their brightness. Hence, if the redshift of a given SNIa is measured, its distance can then be inferred. This makes them interesting events to probe the late time cosmic expansion history. An important concept is the luminosity distance d_L which, assuming a flat Universe, is given by

$$d_L(z) = (1+z)\int_0^z \frac{dz'}{H(z')}\,, \tag{B.1}$$

being determined for a given cosmological model by `CLASS`. The difference between the apparent and absolute magnitude $\mu = m - M$ is known as the distance modulus. For our analyses we use the Pantheon SNIa data set [414] and the correspondent likelihood code in `MontePython`. In [414] they consider the following distance estimator

$$\mu = m_{\rm B} - M + \alpha x_1 - \beta c + \Delta_{\rm M} + \Delta_{\rm B}\,, \tag{B.2}$$

where $m_{\rm B}$ corresponds to the log of the overall flux normalization (the observed peak magnitude of the supernova), x_1 is the light-curve shape parameter (with a coefficient α), c is the supernova color at maximum brightness (with a coefficient β), and $\Delta_{\rm M}$ and $\Delta_{\rm B}$ are distance corrections. Their analysis determines a global calibration solution to combine 13 different supernova samples to form the Pantheon SNIa compilation. Hence, for each SNIa, the code computes

$$\mu_{\rm obs} = m_{\rm obs} - M\,, \tag{B.3}$$

where $m_{\rm obs}$ is the apparent magnitude given by the data set and M is taken as a nuisance parameter. The additional nuisance parameters from Eq. (B.2) are used to standardize the supernovae, such

that a common M parameter can be used to all, since in reality they do not all have the same absolute magnitude.

To find the distance modulus predicted by the cosmological model, the luminosity distance is first determined given the observed SNIa redshift i.e. $d_L(z_{\rm obs})$. Then, using the relation

$$\mu_{\rm model} = 5\log_{10}\left(\frac{d_L}{10\,{\rm pc}}\right), \tag{B.4}$$

one obtains the theoretical value for the distance modulus. This step is repeated for all SNIa, and the χ^2 of the model fit for each point of the parameter space is computed as given in Eq. (A.13), using the data covariance matrix.

B.2 SDSS DR7 (matter power spectrum)

The shape of the power spectrum of density fluctuations is used for the constraints presented in Sec. 3.2.5. Here we follow the work [267], where they present the halo power spectrum reconstructed from the density field derived from a sample of Luminous Red Galaxies from the seventh data release of the Sloan Digital Sky Survey (SDSS DR7). Depending on their position, galaxies are attributed to a DM halo, while neighboring galaxies are consider to occupy the same halo. Having the reconstructed halo density field traced by the galaxies, the overdensity field is obtained by comparing the result with unclustered simulations. The power spectrum $P_{h\,[\rm obs]}(k)$ is then calculated from the overdensity field.

The likelihood code converts the linear matter power spectrum $P_{[\rm model]}(k)$ computed by `CLASS` to a $P_{h\,[\rm model]}(k)$ that can be compared with the inferred halo power spectrum. For this transformation they take into account three effects: the damping of the BAO, the impact of non-linear structure formation in the broad shape of the power spectrum, and the galaxy bias. Although in this process several nuisance parameters calibrated from ΛCDM simulations are introduced, in our analysis we kept them fixed to the standard values. The obtained theoretical halo power spectrum is then processed by a window function, here denoted as $P^{\rm W}_{h\,[\rm model]}(k)$.

To partially correct for the discrepancy between the comoving distance in the fiducial model (assumed to assign positions to the galaxies) and the model to be tested a scale parameter is introduced

$$a_{scl}(z) = \frac{d_V(z)}{d_V^{\rm fid}(z)}, \tag{B.5}$$

where

$$d_V = \left[(1+z)^2\, d_A(z)^2\, \frac{z}{H(z)}\right]^{1/3}, \tag{B.6}$$

with the angular diameter distance being given by

$$d_A(z) = \frac{1}{1+z}\int_0^z \frac{dz'}{H(z')}\,. \tag{B.7}$$

In practice, the theoretical halo power spectrum for the central wavenumbers of the observed bandpowers k_i are scaled as $P^{\rm W}_{h\,[\rm model]}(k_i) \to P^{\rm W}_{h\,[\rm model]}(k_i/a_{scl})$. This quantity is suitable to compare with $P_{h\,[\rm obs]}(k_i)$ and the likelihood can then be computed.

B.3 Planck 2018 (CMB)

The CMB is the oldest radiation we can observe (with its photons being originated from the last scattering surface) and understanding its physics provides an important probe of the early Universe. While the CMB temperature across the sky is highly isotropic, anisotropies have been accurately measured by several missions. In this work we focus on the latest one, and adopt the Planck 2018 CMB data [146, 194] to constrain the cosmological parameters.

CMB observations measure the temperature fluctuations projected in the 2-dimensional spherical surface sky. To confront the model predictions with the data, the temperature anisotropies along the direction given by the unit vector $\hat{n}$ are usually decomposed in a spherical harmonic basis

$$\frac{\delta T}{T} \equiv \Theta(\hat{\mathbf{n}}) = \sum_{\ell=0}^{\infty}\sum_{m=-\ell}^{\ell} a_{\ell m} Y_{\ell m}(\hat{\mathbf{n}})\,, \tag{B.8}$$

where $Y_{\ell m}(\hat{\mathbf{n}})$ are the spherical harmonic functions. The multipole ℓ corresponds to a given angular scale θ in the sky, which is approximately given by $\theta = \pi/\ell$. The case $\ell = 0$ represents the average value of T over the whole sky (i.e. the monopole term). For $\ell = 1$ one has $\theta = \pi$ (corresponding to the dipole term) for which our own motion across the galaxy provides the main contribution to the signal.

When a Gaussian distribution of the coefficients $a_{\ell m}$ is assumed, the ensemble average

$$C_\ell \equiv < |a_{\ell m}|^2 > \tag{B.9}$$

completely characterizes the power spectrum of the temperature field (the mean for the anisotropies is zero by definition). Also notice that the result depends only on ℓ due to statistical isotropy. The temperature correlation function (CMB TT) is then given by

$$< \Theta(\hat{\mathbf{n}})\,\Theta(\hat{\mathbf{n}}') > = \sum_{\ell=0}^{\infty} \frac{2\ell+1}{4\pi} C_\ell P_\ell(\hat{\mathbf{n}}, \hat{\mathbf{n}}')\,, \tag{B.10}$$

where P_ℓ are the Legendre polynomials.

`CLASS` solves numerically the Einstein and Boltzmann equations for the various components to obtain the CMB spectrum for a given cosmological model. The likelihood is computed from the C library `click`, that contains the codes to compute different approximations for the Planck likeli-

hood. The input for the compute function is a $N = N_{\rm cl} + N_{\rm nuisance}$ vector containing the theoretical power spectra in the appropriate range of ℓ's (filling the first $N_{\rm cl}$ entries of the vector) followed by the nuisance parameters (filling the last $N_{\rm nuisance}$ entries). For the analysis we have used two files to compute the CMB TT likelihood: the low-ℓ TT - `Commander` file (in the range $\ell = 2 - 29$), and the high-ℓ TT - `Plik` file (in the range $\ell = 30 - 2508$). These files admit the Planck absolute calibration $A_{\rm planck}$ as the only nuisance parameter. A Python wrapper is also provided so that the functions can be called from the `MontePython` code, where the sampling of the parameter space is done.

B.4 KiDS-450 (weak lensing)

Weak gravitational lensing is the phenomenon of differential deflection of the light emitted from distant galaxies (the sources) as they pass through intervening large scale structures (the lenses). This deflection produces shear and convergence effects in the observed images of distant galaxies. The resulting correlations of galaxy shapes can be measured in galaxy surveys, and can be used to constrain the matter power spectrum of the lenses. In our case, the lenses are the GCG inhomogeneous fluid, whose matter power spectrum we compute with `CLASS`. The convergence power spectra they induce on galaxy shapes is the result of a line-of-sight integration from source to observer, being function of the redshift of the source galaxies and the evolution of the GCG matter power spectrum over redshift. The theoretical prediction of the convergence power spectrum per redshift-bin correlation is given by

$$C_{\mu\nu}^{EE}(\ell) = \int_0^{\chi_H} d\chi \frac{q_\mu(\chi)\, q_\nu(\chi)}{f_K^2(\chi)} P_\delta\left(k = \frac{\ell + 0.5}{f_K(\chi)}; \chi\right), \tag{B.11}$$

where χ is the comoving radial distance, χ_H is the comoving distance to the horizon, and $f_{\mathcal{K}}(\chi)$ is the comoving angular distance [cf. Eq. (2.23)]. $P_\delta(k;\chi)$ is the power spectrum computed by `CLASS`. The weight functions

$$q_\mu(\chi) = \frac{3\Omega_{\rm m0} H_0^2}{2c^2} \frac{f_K(\chi)}{a(\chi)} \int_\chi^{\chi_H} d\chi' n_\mu(\chi') \frac{f_K(\chi' - \chi)}{f_K(\chi')}, \tag{B.12}$$

measure the lensing efficiency in each tomographic bin μ. The source redshift distribution is given by $n_\mu(\chi)\, d\chi = n'(z)_\mu\, dz$ with $\int d\chi n_\mu(\chi) = 1$.

The data power spectra is obtained by applying a quadratic estimator to the galaxy shapes data, and the data is binned in 3 tomographic redshift bins (we refer to the original paper [148] for further details on the KiDS-450 data analysis). The process introduces various nuisance parameters that we have considered in our analysis (see Table 6.2). The nuisance parameters account for the multiplicative bias correction $m_{\rm corr}$ (the observed shear is generally a biased estimator of the true shear) and model excess-noise power in each redshift auto-correlation power spectrum with the free amplitude $A_{\rm noise}(z_i)$ (for each redshift bin $i = 1, 2, 3$). Furthermore, astrophysical systematics are also included. Baryon feedback modifies the matter distribution on small scales and is taken into

account using the fitting formula from [415], with $A_{\rm bary}$ being treated as a general free amplitude. Another important astrophysical systematic are Intrinsic Alignments, which take into account correlation contributions to the total lensing power spectrum besides the cosmological convergence power spectrum. These effects are modeled using a nonlinear modification of the tidal alignment model of intrinsic alignments [416–418], where $A_{\rm IA}$ is a free dimensionless amplitude. The theoretical convergence power spectrum is then modified according to these systematics, resulting in the effective convergence power spectrum to be directly compared with the data to evaluate the likelihood of the GCG parameters. For this, the data covariance matrix is also provided in the likelihood code

Bibliography

[1] Albert Einstein. The Field Equations of Gravitation. *Sitzungsber. Preuss. Akad. Wiss. Berlin (Math. Phys.)*, 1915:844–847, 1915.

[2] W. de Sitter. Einstein's theory of gravitation and its astronomical consequences, First Paper. *Mon. Not. Roy. Astron. Soc.*, 76:699–728, 1916.

[3] W. de Sitter. Einstein's theory of gravitation and its astronomical consequences, Second Paper. *Mon. Not. Roy. Astron. Soc.*, 77:155–184, 1916.

[4] W. de Sitter. Einstein's theory of gravitation and its astronomical consequences, Third Paper. *Mon. Not. Roy. Astron. Soc.*, 78:3–28, 1917.

[5] Albert Einstein. Cosmological Considerations in the General Theory of Relativity. *Sitzungsber. Preuss. Akad. Wiss. Berlin (Math. Phys.)*, 1917:142–152, 1917.

[6] Edwin Hubble. A relation between distance and radial velocity among extra-galactic nebulae. *Proc. Nat. Acad. Sci.*, 15:168–173, 1929.

[7] Henrietta S. Leavitt. 1777 variables in the Magellanic Clouds. *Annals of Harvard College Observatory*, 60:87–108.3, January 1908.

[8] Henrietta S. Leavitt and Edward C. Pickering. Periods of 25 Variable Stars in the Small Magellanic Cloud. *Harvard College Observatory Circular*, 173:1–3, March 1912.

[9] V. M. Slipher. Radial velocity observations of spiral nebulae. *The Observatory*, 40:304–306, August 1917.

[10] A. Friedmann. Über die Krümmung des Raumes. *Zeitschrift fur Physik*, 10:377–386, January 1922.

[11] A. Friedmann. Über die Möglichkeit einer Welt mit konstanter negativer Krümmung des Raumes. *Zeitschrift fur Physik*, 21(1):326–332, December 1924.

[12] Georges Lemaitre. A Homogeneous Universe of Constant Mass and Growing Radius Accounting for the Radial Velocity of Extragalactic Nebulae. *Gen. Rel. Grav.*, 45(8):1635–1646, 2013.

[13] A.S. Eddington. On the Instability of Einstein's Spherical World. *Mon. Not. Roy. Astron. Soc.*, 90:668–678, 1930.

[14] Abbé G. Lemaître. Contributions to a British Association Discussion on the Evolution of the Universe. *Nature*, 128(3234):704–706, October 1931.

[15] G. Gamow. Expanding universe and the origin of elements. *Phys. Rev.*, 70:572–573, Oct 1946.

[16] G. Gamow. The origin of elements and the separation of galaxies. *Phys. Rev.*, 74:505–506, Aug 1948.

[17] R. A. Alpher, R. Herman, and G. A. Gamow. Thermonuclear reactions in the expanding universe. *Phys. Rev.*, 74:1198–1199, Nov 1948.

[18] Ralph A. Alpher and Robert C. Herman. On the relative abundance of the elements. *Phys. Rev.*, 74:1737–1742, Dec 1948.

[19] R. A. Alpher, H. Bethe, and G. Gamow. The origin of chemical elements. *Phys. Rev.*, 73:803–804, Apr 1948.

[20] G. Gamow. The Evolution of the Universe. *Nature*, 162(4122):680–682, October 1948.

[21] A. A. Penzias and R. W. Wilson. A Measurement of Excess Antenna Temperature at 4080 Mc/s. *APJ*, 142:419–421, July 1965.

[22] R. H. Dicke, P. J. E. Peebles, P. G. Roll, and D. T. Wilkinson. Cosmic Black-Body Radiation. *APJ*, 142:414–419, July 1965.

[23] E.A. Milne. *Relativity, Gravitation and World-structure*. International series of monographs on physics. Clarendon Press, 1935.

[24] H. Bondi and T. Gold. The Steady-State Theory of the Expanding Universe. *MNRAS*, 108:252, January 1948.

[25] F. Hoyle. A New Model for the Expanding Universe. *MNRAS*, 108:372, January 1948.

[26] W. Rindler. Visual horizons in world models. *MNRAS*, 116:662, January 1956.

[27] John D. Barrow and Robert J. Scherrer. Constraining Density Fluctuations with Big Bang Nucleosynthesis in the Era of Precision Cosmology. *Phys. Rev. D*, 98(4):043534, 2018.

[28] J.H. Oort. Distribution of galaxies and the density in the universe. In *11ème Conseil de Physique de l'Institut International de Physique Solvay: La structure et l'évolution de l'univers : rapports et discussions*, pages 163–184, 1958.

[29] A. Sandage. The redshift-distance relation. II. The Hubble diagram and its scatter for first-ranked cluster galaxies: A formal value for q_0. *APJ*, 178:1–24, November 1972.

[30] R.H. Dicke and P.J.E. Peebles. The big bang cosmology: Enigmas and nostrums. 1979.

[31] Alan H. Guth. Inflationary universe: A possible solution to the horizon and flatness problems. *Phys. Rev. D*, 23:347–356, Jan 1981.

[32] Ya.B. Zeldovich and M.Yu. Khlopov. On the Concentration of Relic Magnetic Monopoles in the Universe. *Phys. Lett. B*, 79:239–241, 1978.

[33] A. D. Linde. A new inflationary universe scenario: A possible solution of the horizon, flatness, homogeneity, isotropy and primordial monopole problems. *Physics Letters B*, 108(6):389–393, February 1982.

[34] A. A. Starobinsky. Dynamics of phase transition in the new inflationary universe scenario and generation of perturbations. *Physics Letters B*, 117(3-4):175–178, November 1982.

[35] Andreas Albrecht and Paul J. Steinhardt. Cosmology for grand unified theories with radiatively induced symmetry breaking. *Phys. Rev. Lett.*, 48:1220–1223, Apr 1982.

[36] V. F. Mukhanov and G. V. Chibisov. Quantum fluctuations and a nonsingular universe. *Soviet Journal of Experimental and Theoretical Physics Letters*, 33:532, May 1981.

[37] Jerome Martin. The Observational Status of Cosmic Inflation after Planck. *Astrophys. Space Sci. Proc.*, 45:41–134, 2016.

[38] K. Thomson and W. Thomson. *Baltimore Lectures on Molecular Dynamics and the Wave Theory of Light*. Cambridge Library Collection - Physical Sciences. Cambridge University Press, 2010.

[39] H. Poincare. The Milky Way and the Theory of Gases. *Popular Astronomy*, 14:475–488, October 1906.

[40] F. Zwicky. Die Rotverschiebung von extragalaktischen Nebeln. *Helvetica Physica Acta*, 6:110–127, January 1933.

[41] Edwin Hubble and Milton L. Humason. The Velocity-Distance Relation among Extra-Galactic Nebulae. *APJ*, 74:43, July 1931.

[42] Sinclair Smith. The Mass of the Virgo Cluster. *APJ*, 83:23, January 1936.

[43] Erik Holmberg. On the Clustering Tendencies among the Nebulae. *Astrophysical Journal*, 92:200, September 1940.

[44] M. Schwarzschild. Mass distribution and mass-luminosity ratio in galaxies. *Astronomical Journal*, 59:273, September 1954.

[45] J. Neyman, T. Page, and E. Scott. CONFERENCE on the Instability of Systems of Galaxies (Santa Barbara, California, August 1O-12, 1961): Summary of the conference. *Astronomical Journal*, 66:633, December 1961.

[46] K. Lundmark. Über die Bestimmung der Entfernungen, Dimensionen, Massen und Dichtigkeit fur die nächstgelegenen anagalacktischen Sternsysteme. *Meddelanden fran Lunds Astronomiska Observatorium Serie I*, 125:1–13, January 1930.

[47] Horace W. Babcock. The rotation of the Andromeda Nebula. *Lick Observatory Bulletin*, 498:41–51, January 1939.

[48] W. Kent Ford. Electronic image intensification. *Annual Review of Astronomy and Astrophysics*, 6(1):1–12, 1968.

[49] Vera C. Rubin and Jr. Ford, W. Kent. Rotation of the Andromeda Nebula from a Spectroscopic Survey of Emission Regions. *APJ*, 159:379, February 1970.

[50] K. C. Freeman. On the Disks of Spiral and S0 Galaxies. *APJ*, 160:811, June 1970.

[51] D. H. Rogstad and G. S. Shostak. Gross Properties of Five Scd Galaxies as Determined from 21-CENTIMETER Observations. *APJ*, 176:315, September 1972.

[52] M. S. Roberts and A. H. Rots. Comparison of Rotation Curves of Different Galaxy Types. *AAP*, 26:483–485, August 1973.

[53] M. S. Roberts. The Rotation Curve of Galaxies. In Avram Hayli, editor, *Dynamics of the Solar Systems*, volume 69, page 331, January 1975.

[54] Jaan Einasto, Ants Kaasik, and Enn Saar. Dynamic evidence on massive coronas of galaxies. *Nature*, 250(5464):309–310, July 1974.

[55] J. P. Ostriker, P. J. E. Peebles, and A. Yahil. The Size and Mass of Galaxies, and the Mass of the Universe. *Astrophysical Journal*, 193:L1, October 1974.

[56] S. M. Faber and J. S. Gallagher. Masses and mass-to-light ratios of galaxies. *Annual review of astronomy and astrophysics*, 17:135–187, January 1979.

[57] Hubert Reeves, Jean Audouze, William A. Fowler, and David N. Schramm. On the Origin of Light Elements. *APJ*, 179:909–930, February 1973.

[58] P. J. E. Peebles. Large-scale background temperature and mass fluctuations due to scale-invariant primeval perturbations. *Astrophysical Journal*, 263:L1–L5, December 1982.

[59] Juan M. Uson and D. Wilkinson. Improved limits on small-scale anisotropy in cosmic microwave background. *Nature*, 312:427–429, 1984.

[60] J. E. Gunn, B. W. Lee, I. Lerche, D. N. Schramm, and G. Steigman. Some astrophysical consequences of the existence of a heavy stable neutral lepton. *APJ*, 223:1015–1031, August 1978.

[61] A.G. Doroshkevich, Y.B. Zeldovich, R.A. Sunyaev, and M. Khlopov. Astrophysical implications of the neutrino rest mass. III. Nonlinear growth of perturbations and the missing mass. *Sov. Astron. Lett.*, 6:257–259, 1980.

[62] Heinz Pagels and Joel R. Primack. Supersymmetry, cosmology, and new physics at teraelectronvolt energies. *Phys. Rev. Lett.*, 48:223–226, Jan 1982.

[63] R. D. Peccei and Helen R. Quinn. CP conservation in the presence of pseudoparticles. *Phys. Rev. Lett.*, 38:1440–1443, Jun 1977.

[64] F. Wilczek. Problem of strong p and t invariance in the presence of instantons. *Phys. Rev. Lett.*, 40:279–282, Jan 1978.

[65] Steven Weinberg. A new light boson? *Phys. Rev. Lett.*, 40:223–226, Jan 1978.

[66] Michael Dine, Willy Fischler, and Mark Srednicki. A simple solution to the strong CP problem with a harmless axion. *Physics Letters B*, 104(3):199–202, August 1981.

[67] William H. Press and Paul Schechter. Formation of Galaxies and Clusters of Galaxies by Self-Similar Gravitational Condensation. *Astrophysical Journal*, 187:425–438, February 1974.

[68] S. J. Aarseth, III Gott, J. R., and E. L. Turner. N-body simulations of galaxy clustering. I. Initial conditions and galaxy collapse times. *Astrophysical Journal*, 228:664–683, March 1979.

[69] J. Centrella and A. L. Melott. Three-dimensional simulation of large-scale structure in the universe. *Nature*, 305:196–198, September 1983.

[70] A. A. Klypin and S. F. Shandarin. Three-dimensional numerical model of the formation of large-scale structure in the Universe. *MNRAS*, 204:891–907, September 1983.

[71] M. Davis, J. Huchra, D. W. Latham, and J. Tonry. A survey of galaxy redshifts. II. The large scale space distribution. *APJ*, 253:423–445, February 1982.

[72] M. Davis, G. Efstathiou, C. S. Frenk, and S. D. M. White. The evolution of large-scale structure in a universe dominated by cold dark matter. *APJ*, 292:371–394, May 1985.

[73] S. J. Maddox, G. Efstathiou, W. J. Sutherland, and J. Loveday. Galaxy correlations on large scales. *MNRAS*, 242:43, January 1990.

[74] Simon D. M. White, Julio F. Navarro, August E. Evrard, and Carlos S. Frenk. The baryon content of galaxy clusters: a challenge to cosmological orthodoxy. *Nature*, 366(6454):429–433, December 1993.

[75] Pierre Demarque, Constantine P. Deliyannis, and Ata Sarajedini. *Ages of Globular Clusters*, pages 111–129. Springer Netherlands, Dordrecht, 1991.

[76] Brian Chaboyer, Pierre Demarque, Peter J. Kernan, and Lawrence M. Krauss. A Lower Limit on the Age of the Universe. *Science*, 271(5251):957–961, February 1996.

[77] Marc Kamionkowski and David N. Spergel. Large-Angle Cosmic Microwave Background Anisotropies in an Open Universe. *APJ*, 432:7, September 1994.

[78] V. Petrosian, E. Salpeter, and P. Szekeres. Quasi-Stellar Objects in Universes with Non-Zero Cosmological Constant. *APJ*, 147:1222–1226, March 1967.

[79] J. Shklovsky. On the Nature of "standard" Absorption Spectrum of the Quasi-Stellar Objects. *Astrophysical Journal*, 150:L1, October 1967.

[80] N. Kardashev. LEMAÎTRE'S Universe and Observations. *Astrophysical Journal*, 150:L135, December 1967.

[81] Y.B. Zeldovich. Cosmological Constant and Elementary Particles. *JETP Lett.*, 6:316, 1967.

[82] H.B.G. Casimir. On the Attraction Between Two Perfectly Conducting Plates. *Indag. Math.*, 10:261–263, 1948.

[83] M. J. Sparnaay. Attractive Forces between Flat Plates. *Nature*, 180(4581):334–335, August 1957.

[84] S. K. Lamoreaux. Demonstration of the Casimir Force in the 0.6 to 6 μm Range. *Phys. Rev. Lett*, 78(1):5–8, January 1997.

[85] Steven Weinberg. The cosmological constant problem. *Rev. Mod. Phys.*, 61:1–23, Jan 1989.

[86] G. Efstathiou, W. J. Sutherland, and S. J. Maddox. The cosmological constant and cold dark matter. *Nature*, 348(6303):705–707, December 1990.

[87] Lev A. Kofman, Nickolay Y. Gnedin, and Neta A. Bahcall. Cosmological Constant, COBE Cosmic Microwave Background Anisotropy, and Large-Scale Clustering. *APJ*, 413:1, August 1993.

[88] Yuzuru Yoshii and Bruce A. Peterson. Interpretation of the Faint Galaxy Number Counts in the K Band. *APJ*, 444:15, May 1995.

[89] J. P. Ostriker and Paul J. Steinhardt. The observational case for a low-density Universe with a non-zero cosmological constant. *Nature*, 377(6550):600–602, October 1995.

[90] Stacy S. McGaugh. Cosmological constant. *Nature*, 381(6582):483, June 1996.

[91] Adam G. Riess, Alexei V. Filippenko, Peter Challis, Alejandro Clocchiatti, Alan Diercks, Peter M. Garnavich, Ron L. Gilliland, Craig J. Hogan, Saurabh Jha, Robert P. Kirshner, B. Leibundgut, M. M. Phillips, David Reiss, Brian P. Schmidt, Robert A. Schommer, R. Chris Smith, J. Spyromilio, Christopher Stubbs, Nicholas B. Suntzeff, and John Tonry. Observational Evidence from Supernovae for an Accelerating Universe and a Cosmological Constant. *Astronomical Journal*, 116(3):1009–1038, Sep 1998.

[92] S. Perlmutter, G. Aldering, G. Goldhaber, R. A. Knop, P. Nugent, P. G. Castro, S. Deustua, S. Fabbro, A. Goobar, D. E. Groom, I. M. Hook, A. G. Kim, M. Y. Kim, J. C. Lee, N. J. Nunes, R. Pain, C. R. Pennypacker, R. Quimby, C. Lidman, R. S. Ellis, M. Irwin, R. G. McMahon, P. Ruiz-Lapuente, N. Walton, B. Schaefer, B. J. Boyle, A. V. Filippenko, T. Matheson,

A. S. Fruchter, N. Panagia, H. J. M. Newberg, W. J. Couch, and The Supernova Cosmology Project. Measurements of Ω and Λ from 42 High-Redshift Supernovae. *APJ*, 517(2):565–586, Jun 1999.

[93] Anthony N. Aguirre. Dust vs. cosmic acceleration. *Astrophys. J. Lett.*, 512:L19, 1999.

[94] Persis S. Drell, Thomas J. Loredo, and Ira Wasserman. Type Ia supernovae, evolution, and the cosmological constant. *Astrophys. J.*, 530:593, 2000.

[95] Marie-Noelle Celerier. Do we really see a cosmological constant in the supernovae data? *Astron. Astrophys.*, 353:63–71, 2000.

[96] Kenji Tomita. Distances and lensing in cosmological void models. *Astrophys. J.*, 529:38, 2000.

[97] P. de Bernardis et al. A Flat universe from high resolution maps of the cosmic microwave background radiation. *Nature*, 404:955–959, 2000.

[98] John Kovac, E. M. Leitch, C Pryke, J. E. Carlstrom, N. W. Halverson, and W. L. Holzapfel. Detection of polarization in the cosmic microwave background using DASI. *Nature*, 420:772–787, 2002.

[99] Shaun Cole et al. The 2dF Galaxy Redshift Survey: Power-spectrum analysis of the final dataset and cosmological implications. *Mon. Not. Roy. Astron. Soc.*, 362:505–534, 2005.

[100] D. N. Spergel et al. First year Wilkinson Microwave Anisotropy Probe (WMAP) observations: Determination of cosmological parameters. *Astrophys. J. Suppl.*, 148:175–194, 2003.

[101] D. N. Spergel et al. Wilkinson Microwave Anisotropy Probe (WMAP) three year results: implications for cosmology. *Astrophys. J. Suppl.*, 170:377, 2007.

[102] E. Komatsu, K. M. Smith, J. Dunkley, C. L. Bennett, B. Gold, G. Hinshaw, N. Jarosik, D. Larson, M. R. Nolta, L. Page, D. N. Spergel, M. Halpern, R. S. Hill, A. Kogut, M. Limon, S. S. Meyer, N. Odegard, G. S. Tucker, J. L. Weiland, E. Wollack, and E. L. Wright. Seven-year Wilkinson Microwave Anisotropy Probe (WMAP) Observations: Cosmological Interpretation. *Astrophys. J. Suppl.*, 192(2):18, February 2011.

[103] C. L. Bennett, D. Larson, J. L. Weiland, N. Jarosik, G. Hinshaw, N. Odegard, K. M. Smith, R. S. Hill, B. Gold, M. Halpern, E. Komatsu, M. R. Nolta, L. Page, D. N. Spergel, E. Wollack, J. Dunkley, A. Kogut, M. Limon, S. S. Meyer, G. S. Tucker, and E. L. Wright. Nine-year Wilkinson Microwave Anisotropy Probe (WMAP) Observations: Final Maps and Results. *Astrophys. J. Suppl.*, 208(2):20, October 2013.

[104] Gary Steigman and Michael S. Turner. Cosmological Constraints on the Properties of Weakly Interacting Massive Particles. *Nucl. Phys. B*, 253:375–386, 1985.

[105] Gerard Jungman, Marc Kamionkowski, and Kim Griest. Supersymmetric dark matter. *Phys. Rept.*, 267:195–373, 1996.

[106] Gianfranco Bertone, Dan Hooper, and Joseph Silk. Particle dark matter: Evidence, candidates and constraints. *Phys. Rept.*, 405:279–390, 2005.

[107] D. S. Akerib et al. First results from the LUX dark matter experiment at the Sanford Underground Research Facility. *Phys. Rev. Lett.*, 112:091303, 2014.

[108] E. Aprile et al. Search for WIMP Inelastic Scattering off Xenon Nuclei with XENON100. *Phys. Rev. D*, 96(2):022008, 2017.

[109] Jianglai Liu, Xun Chen, and Xiangdong Ji. Current status of direct dark matter detection experiments. *Nature Phys.*, 13(3):212–216, 2017.

[110] B. J. Carr and S. W. Hawking. Black holes in the early Universe. *MNRAS*, 168:399–416, August 1974.

[111] G. F. Chapline. Cosmological effects of primordial black holes. *Nature*, 253(5489):251–252, January 1975.

[112] Bernard Carr and Florian Kuhnel. Primordial Black Holes as Dark Matter: Recent Developments. *Ann. Rev. Nucl. Part. Sci.*, 70:355–394, 2020.

[113] B.P. Abbott et al. Observation of Gravitational Waves from a Binary Black Hole Merger. *Phys. Rev. Lett.*, 116(6):061102, 2016.

[114] Scott Burles and David Tytler. The Deuterium Abundance toward Q1937-1009. *APJ*, 499(2):699–712, May 1998.

[115] Scott Burles and David Tytler. The Deuterium Abundance toward QSO 1009+2956. *APJ*, 507(2):732–744, November 1998.

[116] M. Milgrom. A modification of the Newtonian dynamics as a possible alternative to the hidden mass hypothesis. *APJ*, 270:365–370, July 1983.

[117] J. W. Moffat. Scalar-tensor-vector gravity theory. *JCAP*, 03:004, 2006.

[118] J. R. Brownstein and J. W. Moffat. Galaxy rotation curves without non-baryonic dark matter. *Astrophys. J.*, 636:721–741, 2006.

[119] J. R. Brownstein and J. W. Moffat. The Bullet Cluster 1E0657-558 evidence shows Modified Gravity in the absence of Dark Matter. *Mon. Not. Roy. Astron. Soc.*, 382:29–47, 2007.

[120] Douglas Clowe, Marusa Bradac, Anthony H. Gonzalez, Maxim Markevitch, Scott W. Randall, Christine Jones, and Dennis Zaritsky. A direct empirical proof of the existence of dark matter. *Astrophys. J. Lett.*, 648:L109–L113, 2006.

[121] Marusa Bradac, Douglas Clowe, Anthony H. Gonzalez, Phil Marshall, William Forman, Christine Jones, Maxim Markevitch, Scott Randall, Tim Schrabback, and Dennis Zaritsky. Strong and weak lensing united. 3. Measuring the mass distribution of the merging galaxy cluster 1E0657-56. *Astrophys. J.*, 652:937–947, 2006.

[122] Pieter van Dokkum, Shany Danieli, Yotam Cohen, Allison Merritt, Aaron J. Romanowsky, Roberto Abraham, Jean Brodie, Charlie Conroy, Deborah Lokhorst, Lamiya Mowla, Ewan O'Sullivan, and Jielai Zhang. A galaxy lacking dark matter. *Nature*, 555(7698):629–632, March 2018.

[123] Pieter van Dokkum, Shany Danieli, Roberto Abraham, Charlie Conroy, and Aaron J. Romanowsky. A Second Galaxy Missing Dark Matter in the NGC 1052 Group. *The Astrophysical Journal Letters*, 874(1):L5, March 2019.

[124] Qi Guo, Huijie Hu, Zheng Zheng, Shihong Liao, Wei Du, Shude Mao, Linhua Jiang, Jing Wang, Yingjie Peng, Liang Gao, Jie Wang, and Hong Wu. Further evidence for a population of dark-matter-deficient dwarf galaxies. *Nature Astronomy*, 4:246–251, January 2020.

[125] Andrea V. Macciò, Daniel Huterer Prats, Keri L. Dixon, Tobias Buck, Stefan Waterval, Nikhil Arora, Stéphane Courteau, and Xi Kang. Creating a galaxy lacking dark matter in a dark matter-dominated universe. *MNRAS*, 501(1):693–700, February 2021.

[126] R. A. Jackson, S. Kaviraj, G. Martin, J. E. G. Devriendt, A. Slyz, J. Silk, Y. Dubois, S. K. Yi, C. Pichon, M. Volonteri, H. Choi, T. Kimm, K. Kraljic, and S. Peirani. Dark matter-deficient dwarf galaxies form via tidal stripping of dark matter in interactions with massive companions. *MNRAS*, 502(2):1785–1796, April 2021.

[127] B. Famaey, S. McGaugh, and M. Milgrom. MOND and the dynamics of NGC 1052−DF2. *Mon. Not. Roy. Astron. Soc.*, 480(1):473–476, 2018.

[128] Kris Pardo and David N. Spergel. What is the price of abandoning dark matter? Cosmological constraints on alternative gravity theories. *Phys. Rev. Lett.*, 125(21):211101, 2020.

[129] S. W. Hawking. The Cosmological Constant Is Probably Zero. *Phys. Lett. B*, 134:403, 1984.

[130] Jerome Martin. Everything You Always Wanted To Know About The Cosmological Constant Problem (But Were Afraid To Ask). *Comptes Rendus Physique*, 13:566–665, 2012.

[131] Antonio Padilla. Lectures on the Cosmological Constant Problem. 2 2015.

[132] R. R. Caldwell, Rahul Dave, and Paul J. Steinhardt. Cosmological imprint of an energy component with general equation of state. *Phys. Rev. Lett.*, 80:1582–1585, 1998.

[133] Li-Min Wang, R. R. Caldwell, J. P. Ostriker, and Paul J. Steinhardt. Cosmic concordance and quintessence. *Astrophys. J.*, 530:17–35, 2000.

[134] Paul J. Steinhardt, Li-Min Wang, and Ivaylo Zlatev. Cosmological tracking solutions. *Phys. Rev. D*, 59:123504, 1999.

[135] Edmund J. Copeland, M. Sami, and Shinji Tsujikawa. Dynamics of Dark Energy. *International Journal of Modern Physics D*, 15(11):1753–1935, Jan 2006.

[136] Kazuya Koyama. Cosmological Tests of Modified Gravity. *Rept. Prog. Phys.*, 79(4):046902, 2016.

[137] Martin Kunz and Domenico Sapone. Dark Energy versus Modified Gravity. *Phys. Rev. Lett.*, 98:121301, 2007.

[138] Luca Amendola. Coupled quintessence. *Phys. Rev. D*, 62(4):043511, August 2000.

[139] Austin Joyce, Lucas Lombriser, and Fabian Schmidt. Dark Energy Versus Modified Gravity. *Ann. Rev. Nucl. Part. Sci.*, 66:95–122, 2016.

[140] Justin Khoury and Amanda Weltman. Chameleon fields: Awaiting surprises for tests of gravity in space. *Phys. Rev. Lett.*, 93:171104, 2004.

[141] B.P. Abbott et al. Gravitational Waves and Gamma-rays from a Binary Neutron Star Merger: GW170817 and GRB 170817A. *Astrophys. J. Lett.*, 848(2):L13, 2017.

[142] Paolo Creminelli and Filippo Vernizzi. Dark Energy after GW170817 and GRB170817A. *Phys. Rev. Lett.*, 119(25):251302, 2017.

[143] Jose María Ezquiaga and Miguel Zumalacárregui. Dark Energy After GW170817: Dead Ends and the Road Ahead. *Phys. Rev. Lett.*, 119(25):251304, 2017.

[144] Eleonora Di Valentino, Olga Mena, Supriya Pan, Luca Visinelli, Weiqiang Yang, Alessandro Melchiorri, David F. Mota, Adam G. Riess, and Joseph Silk. In the Realm of the Hubble tension − a Review of Solutions. 3 2021.

[145] Marian Douspis, Laura Salvati, and Nabila Aghanim. On the Tension between Large Scale Structures and Cosmic Microwave Background. *PoS*, EDSU2018:037, 2018.

[146] N. Aghanim et al. Planck 2018 results. VI. Cosmological parameters. *Astron. Astrophys.*, 641:A6, 2020.

[147] Adam G. Riess, Stefano Casertano, Wenlong Yuan, J. Bradley Bowers, Lucas Macri, Joel C. Zinn, and Dan Scolnic. Cosmic Distances Calibrated to 1% Precision with Gaia EDR3 Parallaxes and Hubble Space Telescope Photometry of 75 Milky Way Cepheids Confirm Tension with ΛCDM. *Astrophys. J. Lett.*, 908(1):L6, 2021.

[148] F. Köhlinger et al. KiDS-450: The tomographic weak lensing power spectrum and constraints on cosmological parameters. *Mon. Not. Roy. Astron. Soc.*, 471(4):4412–4435, 2017.

[149] T. M. C. Abbott et al. Dark Energy Survey year 1 results: Cosmological constraints from galaxy clustering and weak lensing. *Phys. Rev. D*, 98(4):043526, 2018.

[150] Marika Asgari et al. KiDS-1000 Cosmology: Cosmic shear constraints and comparison between two point statistics. *Astron. Astrophys.*, 645:A104, 2021.

[151] Catherine Heymans et al. KiDS-1000 Cosmology: Multi-probe weak gravitational lensing and spectroscopic galaxy clustering constraints. *Astron. Astrophys.*, 646:A140, 2021.

[152] George Efstathiou. H0 Revisited. *Mon. Not. Roy. Astron. Soc.*, 440(2):1138–1152, 2014.

[153] G. E. Addison, Y. Huang, D. J. Watts, C. L. Bennett, M. Halpern, G. Hinshaw, and J. L. Weiland. Quantifying discordance in the 2015 Planck CMB spectrum. *Astrophys. J.*, 818(2):132, 2016.

[154] Shahab Joudaki et al. CFHTLenS revisited: assessing concordance with Planck including astrophysical systematics. *Mon. Not. Roy. Astron. Soc.*, 465(2):2033–2052, 2017.

[155] N. Aghanim et al. Planck intermediate results. LI. Features in the cosmic microwave background temperature power spectrum and shifts in cosmological parameters. *Astron. Astrophys.*, 607:A95, 2017.

[156] Tom Shanks, Lucy Hogarth, and Nigel Metcalfe. Gaia Cepheid parallaxes and 'Local Hole' relieve H_0 tension. *Mon. Not. Roy. Astron. Soc.*, 484(1):L64–L68, 2019.

[157] Adam G. Riess, Stefano Casertano, D'Arcy Kenworthy, Dan Scolnic, and Lucas Macri. Seven Problems with the Claims Related to the Hubble Tension in arXiv:1810.02595. 10 2018.

[158] John Soltis, Arya Farahi, Dragan Huterer, and C. Michael Liberato. Percent-Level Test of Isotropic Expansion Using Type Ia Supernovae. *Phys. Rev. Lett.*, 122(9):091301, 2019.

[159] Thomas S. Kuhn. *The structure of scientific revolutions*. University of Chicago Press, Chicago, 1970.

[160] L. M. Beça, P. P. Avelino, J. P. de Carvalho, and C. J. Martins. Role of baryons in unified dark matter models. *Phys. Rev. D*, 67(10):101301, May 2003.

[161] V. M. C. Ferreira and P. P. Avelino. Extended family of generalized Chaplygin gas models. *Phys. Rev. D*, 98(4):043515, Aug 2018.

[162] P. P. Avelino and V. M. C. Ferreira. Constraints on the dark matter sound speed from galactic scales: the cases of the Modified and Extended Chaplygin Gas. *Phys. Rev. D*, 91(8):083508, 2015.

[163] V. M. C. Ferreira and P. P. Avelino. New limit on logotropic unified dark energy models. *Physics Letters B*, 770:213–216, Jul 2017.

[164] V. M. C. Ferreira, P. P. Avelino, and R. P. L. Azevedo. Lagrangian description of cosmic fluids: Mapping dark energy into unified dark energy. *Phys. Rev. D*, 102(6):063525, 2020.

[165] V. M. C. Ferreira, I. Tereno, Castelão D., Alberto Rozas-Fernandez, and P. P. Avelino. *in preparation*.

[166] Steven Weinberg. *Gravitation and Cosmology: Principles and Applications of the General Theory of Relativity*. John Wiley and Sons, New York, 1972.

[167] Robert M. Wald. *General Relativity*. Chicago Univ. Pr., Chicago, USA, 1984.

[168] Phillip James Edwin Peebles. *Principles of physical cosmology*. Princeton University Press, 1993.

[169] John A. Peacock. *Cosmological Physics*. 1999.

[170] Scott Dodelson. *Modern Cosmology*. Academic Press, Amsterdam, 2003.

[171] Sean M. Carroll. *Spacetime and Geometry*. Cambridge University Press, 7 2019.

[172] Luca Amendola and Shinji Tsujikawa. *Dark Energy: Theory and Observations*. 2010.

[173] Luciano Rezzolla and Olindo Zanotti. *Relativistic Hydrodynamics*. 2013.

[174] Oliver F. Piattella. *Lecture Notes in Cosmology*. UNITEXT for Physics. Springer, Cham, 2018.

[175] Albert Einstein. Über das Relativitätsprinzip und die aus demselben gezogenen Folgerungen. *Jahrbuch der Radioaktivität und Elektronik*, 4:411–462, January 1908.

[176] Albert Einstein. Explanation of the Perihelion Motion of Mercury from the General Theory of Relativity. *Sitzungsber. Preuss. Akad. Wiss. Berlin (Math. Phys.)*, 1915:831–839, 1915.

[177] E. Freundlich. Über die Erklärung der Anomalien im Planeten-System durch die Gravitationswirkung interplanetarer Massen. *Astronomische Nachrichten*, 201(3):49, June 1915.

[178] Urbain J. Le Verrier. Theorie du mouvement de Mercure. *Annales de l'Observatoire de Paris*, 5:1, January 1859.

[179] F. W. Dyson, A. S. Eddington, and C. Davidson. A Determination of the Deflection of Light by the Sun's Gravitational Field, from Observations Made at the Total Eclipse of May 29, 1919. *Philosophical Transactions of the Royal Society of London Series A*, 220:291–333, January 1920.

[180] B. Bertotti, L. Iess, and P. Tortora. A test of general relativity using radio links with the Cassini spacecraft. *Nature*, 425:374–376, 2003.

[181] S.S. Shapiro, J.L. Davis, D.E. Lebach, and J.S. Gregory. Measurement of the Solar Gravitational Deflection of Radio Waves using Geodetic Very-Long-Baseline Interferometry Data, 1979-1999. *Phys. Rev. Lett.*, 92:121101, 2004.

[182] Ryan S. Park, William M. Folkner, Alexander S. Konopliv, James G. Williams, David E. Smith, and Maria T. Zuber. Precession of mercury's perihelion from ranging to theMESSENGERSpacecraft. *The Astronomical Journal*, 153(3):121, feb 2017.

[183] Kazunori Akiyama et al. First M87 Event Horizon Telescope Results. I. The Shadow of the Supermassive Black Hole. *Astrophys. J.*, 875(1):L1, 2019.

[184] R. Abuter et al. Detection of the Schwarzschild precession in the orbit of the star S2 near the Galactic centre massive black hole. *Astron. Astrophys.*, 636:L5, 2020.

[185] R. A. Hulse and J. H. Taylor. Discovery of a pulsar in a binary system. *Astrophysical Journal*, 195:L51–L53, January 1975.

[186] J. H. Taylor and J. M. Weisberg. A new test of general relativity - Gravitational radiation and the binary pulsar PSR 1913+16. *Astrophysical Journal*, 253:908–920, February 1982.

[187] R. F. C. Vessot, M. W. Levine, E. M. Mattison, E. L. Blomberg, T. E. Hoffman, G. U. Nystrom, B. F. Farrel, R. Decher, P. B. Eby, C. R. Baugher, J. W. Watts, D. L. Teuber, and F. D. Wills. Test of relativistic gravitation with a space-borne hydrogen maser. *Phys. Rev. Lett.*, 45:2081–2084, Dec 1980.

[188] J.I. González Hernández et al. The solar gravitational redshift from HARPS-LFC Moon spectra. A test of the General Theory of Relativity. 9 2020.

[189] Pierre Touboul et al. MICROSCOPE Mission: First Results of a Space Test of the Equivalence Principle. *Phys. Rev. Lett.*, 119(23):231101, 2017.

[190] Chris Blake and Jasper Wall. Detection of the velocity dipole in the radio galaxies of the nrao vla sky survey. *Nature*, 416:150–152, 2002.

[191] C. Marinoni, J. Bel, and A. Buzzi. The scale of cosmic isotropy. *JCAP*, 2012(10):036, October 2012.

[192] C.A.P. Bengaly, A. Bernui, J.S. Alcaniz, and I.S. Ferreira. Probing cosmological isotropy with Planck Sunyaev–Zeldovich galaxy clusters. *Mon. Not. Roy. Astron. Soc.*, 466(3):2799–2804, 2017.

[193] Uendert Andrade, Carlos A.P. Bengaly, Jailson S. Alcaniz, and Salvatore Capozziello. Revisiting the statistical isotropy of GRB sky distribution. *Mon. Not. Roy. Astron. Soc.*, 490(4):4481–4488, 2019.

[194] Y. Akrami et al. Planck 2018 results. VII. Isotropy and Statistics of the CMB. *Astron. Astrophys.*, 641:A7, 2020.

[195] R. R. Caldwell and A. Stebbins. A Test of the Copernican Principle. *Phys. Rev. Lett.*, 100:191302, 2008.

[196] Pengjie Zhang and Albert Stebbins. Confirmation of the Copernican Principle at Gpc Radial Scale and above from the Kinetic Sunyaev-Zel'dovich Effect Power Spectrum. *Phys. Rev. Lett*, 107(4):041301, July 2011.

[197] Domenico Sapone, Elisabetta Majerotto, and Savvas Nesseris. Curvature versus distances: Testing the FLRW cosmology. *Phys. Rev. D*, 90(2):023012, 2014.

[198] Suman Sarkar and Biswajit Pandey. An information theory based search for homogeneity on the largest accessible scale. *Mon. Not. Roy. Astron. Soc.*, 463(1):L12–L16, 2016.

[199] R.S. Gonçalves, G.C. Carvalho, C.A.P. Bengaly, J.C. Carvalho, and J.S. Alcaniz. Measuring the scale of cosmic homogeneity with SDSS-IV DR14 quasars. *Mon. Not. Roy. Astron. Soc.*, 481(4):5270–5274, 2018.

[200] Chris Clarkson. Establishing homogeneity of the universe in the shadow of dark energy. *Comptes Rendus Physique*, 13:682–718, 2012.

[201] H. P. Robertson. Kinematics and World-Structure. *APJ*, 82:284, November 1935.

[202] H. P. Robertson. Kinematics and World-Structure II. *APJ*, 83:187, April 1936.

[203] H. P. Robertson. Kinematics and World-Structure III. *APJ*, 83:257, May 1936.

[204] A. G. Walker. On Milne's Theory of World-Structure. *Proceedings of the London Mathematical Society*, 42:90–127, January 1937.

[205] Patricio S. Letelier. Anisotropic fluids with two-perfect-fluid components. *Phys. Rev. D*, 22:807–813, Aug 1980.

[206] Hernando Quevedo and Roberto A. Sussman. On the thermodynamics of simple nonisentropic perfect fluids in general relativity. *Class. Quant. Grav.*, 12:859–874, 1995.

[207] Florian Beutler, Chris Blake, Matthew Colless, D. Heath Jones, Lister Staveley-Smith, Lachlan Campbell, Quentin Parker, Will Saunders, and Fred Watson. The 6dF Galaxy Survey: baryon acoustic oscillations and the local Hubble constant. *MNRAS*, 416(4):3017–3032, October 2011.

[208] Ashley J. Ross, Lado Samushia, Cullan Howlett, Will J. Percival, Angela Burden, and Marc Manera. The clustering of the SDSS DR7 main Galaxy sample – I. A 4 per cent distance measure at $z = 0.15$. *Mon. Not. Roy. Astron. Soc.*, 449(1):835–847, 2015.

[209] Shadab Alam et al. The clustering of galaxies in the completed SDSS-III Baryon Oscillation Spectroscopic Survey: cosmological analysis of the DR12 galaxy sample. *Mon. Not. Roy. Astron. Soc.*, 470(3):2617–2652, 2017.

[210] D. J. Fixsen, E. S. Cheng, J. M. Gales, John C. Mather, R. A. Shafer, and E. L. Wright. The Cosmic Microwave Background spectrum from the full COBE FIRAS data set. *Astrophys. J.*, 473:576, 1996.

[211] D. J. Fixsen. The Temperature of the Cosmic Microwave Background. *APJ*, 707(2):916–920, December 2009.

[212] Brent Follin, Lloyd Knox, Marius Millea, and Zhen Pan. First Detection of the Acoustic Oscillation Phase Shift Expected from the Cosmic Neutrino Background. *Phys. Rev. Lett.*, 115(9):091301, 2015.

[213] David H. Weinberg, Jordi Miralda-Escude, Lars Hernquist, and Neal Katz. A Lower bound on the cosmic baryon density. *Astrophys. J.*, 490:564–570, 1997.

[214] Ryan J. Cooke, Max Pettini, and Charles C. Steidel. One Percent Determination of the Primordial Deuterium Abundance. *Astrophys. J.*, 855(2):102, 2018.

[215] Mikhail M. Ivanov, Marko Simonović, and Matias Zaldarriaga. Cosmological Parameters from the BOSS Galaxy Power Spectrum. *JCAP*, 05:042, 2020.

[216] J. H. Jeans. The Stability of a Spherical Nebula. *Philosophical Transactions of the Royal Society of London Series A*, 199:1–53, January 1902.

[217] E. M. Lifshitz. On the gravitational stability of the expanding universe. *Zhurnal Eksperimentalnoi i Teoreticheskoi Fiziki*, 16:587–602, January 1946.

[218] E. R. Harrison. Normal Modes of Vibrations of the Universe. *Reviews of Modern Physics*, 39(4):862–882, October 1967.

[219] George B. Field and L. C. Shepley. Density Perturbations in Cosmological Models. *Astrophysics and Space Science*, 1(3):309–335, May 1968.

[220] E. R. Harrison. Fluctuations at the Threshold of Classical Cosmology. *Phys. Rev. D*, 1(10):2726–2730, May 1970.

[221] Yaa B. Zeldovich. A hypothesis, unifying the structure and the entropy of the Universe. *MNRAS*, 160:1P, January 1972.

[222] P. J. E. Peebles. *The large-scale structure of the universe*. 1980.

[223] James M. Bardeen. Gauge-invariant cosmological perturbations. *Phys. Rev. D*, 22(8):1882–1905, October 1980.

[224] E. Lifshitz. Republication of: On the gravitational stability of the expanding universe. *General Relativity and Gravitation*, 49(2):18, February 2017.

[225] W. H. Press and E. T. Vishniac. Tenacious myths about cosmological perturbations larger than the horizon size. *APJ*, 239:1–11, July 1980.

[226] Hideo Kodama and Misao Sasaki. Cosmological Perturbation Theory. *Progress of Theoretical Physics Supplement*, 78:1, January 1984.

[227] Shoba Veeraraghavan and Albert Stebbins. Causal Compensated Perturbations in Cosmology. *APJ*, 365:37, Dec 1990.

[228] Wayne Hu and Daniel J. Eisenstein. Structure of structure formation theories. *Phys. Rev. D*, 59:083509, Mar 1999.

[229] Ira Wasserman. Degeneracy inherent in the observational determination of the dark energy equation of state. *Phys. Rev. D*, 66:123511, Dec 2002.

[230] Martin Kunz, Andrew R. Liddle, David Parkinson, and Changjun Gao. Constraining the dark fluid. *Phys. Rev. D*, 80:083533, Oct 2009.

[231] Martin Kunz. Degeneracy between the dark components resulting from the fact that gravity only measures the total energy-momentum tensor. *Phys. Rev. D*, 80:123001, Dec 2009.

[232] P. P. Avelino, L. M. G. Beca, and C. J. A. P. Martins. Linear and nonlinear instabilities in unified dark energy models. *Phys. Rev. D*, 77:063515, 2008.

[233] Alejandro Aviles and Jorge L. Cervantes-Cota. Dark degeneracy and interacting cosmic components. *Phys. Rev. D*, 84:083515, 2011. [Erratum: Phys.Rev.D 84, 089905 (2011)].

[234] S. Carneiro and H. A. Borges. On dark degeneracy and interacting models. *JCAP*, 06:010, 2014.

[235] Rodrigo von Marttens, Lucas Lombriser, Martin Kunz, Valerio Marra, Luciano Casarini, and Jailson Alcaniz. Dark degeneracy I: Dynamical or interacting dark energy? *Phys. Dark Univ.*, 28:100490, 2020.

[236] Marc Schumann. Direct Detection of WIMP Dark Matter: Concepts and Status. *J. Phys. G*, 46(10):103003, 2019.

[237] Philippe Brax, Clare Burrage, Christoph Englert, and Michael Spannowsky. LHC Signatures Of Scalar Dark Energy. *Phys. Rev. D*, 94(8):084054, 2016.

[238] P. Brax. What makes the universe accelerate? a review on what dark energy could be and how to test it. *Reports on progress in physics. Physical Society*, 81 1:016902, 2018.

[239] Alexander Yu. Kamenshchik, Ugo Moschella, and Vincent Pasquier. An Alternative to quintessence. *Phys. Lett. B*, 511:265–268, 2001.

[240] M.C. Bento, O. Bertolami, and A.A. Sen. Generalized Chaplygin gas, accelerated expansion and dark energy matter unification. *Phys. Rev. D*, 66:043507, 2002.

[241] H.B. Benaoum. Accelerated universe from modified Chaplygin gas and tachyonic fluid. 5 2002.

[242] L. Amendola, Fabio Finelli, C. Burigana, and D. Carturan. WMAP and the generalized Chaplygin gas. *JCAP*, 07:005, 2003.

[243] Rachel Bean and Olivier Dore. Are Chaplygin gases serious contenders to the dark energy throne? *Phys. Rev. D*, 68:023515, 2003.

[244] Tuomas Multamaki, Marc Manera, and Enrique Gaztanaga. Large scale structure and the generalised Chaplygin gas as dark energy. *Phys. Rev. D*, 69:023004, 2004.

[245] Chan-Gyung Park, Jai-chan Hwang, Jaehong Park, and Hyerim Noh. Observational constraints on a unified dark matter and dark energy model based on generalized Chaplygin gas. *Phys. Rev. D*, 81:063532, 2010.

[246] Oliver F. Piattella. The extreme limit of the generalized Chaplygin gas. *JCAP*, 03:012, 2010.

[247] Mariam Bouhmadi-Lopez, Pisin Chen, and Yen-Wei Liu. Cosmological Imprints of a Generalized Chaplygin Gas Model for the Early Universe. *Phys. Rev. D*, 84:023505, 2011.

[248] R. Aurich and S. Lustig. On the concordance of cosmological data in the case of the generalized Chaplygin gas. *Astropart. Phys.*, 97:118–129, 2018.

[249] Weiqiang Yang, Supriya Pan, Sunny Vagnozzi, Eleonora Di Valentino, David F. Mota, and Salvatore Capozziello. Dawn of the dark: unified dark sectors and the EDGES Cosmic Dawn 21-cm signal. *JCAP*, 11:044, 2019.

[250] Hang Li, Weiqiang Yang, and Liping Gai. Astronomical bounds on the modified Chaplygin gas as a unified dark fluid model. *Astron. Astrophys.*, 623:A28, 2019.

[251] Robert J. Scherrer. Purely Kinetic k Essence as Unified Dark Matter. *Physical Review Letters*, 93(1):011301, Jun 2004.

[252] Daniele Bertacca and Nicola Bartolo. The integrated Sachs Wolfe effect in unified dark matter scalar field cosmologies: an analytical approach. *JCAP*, 2007(11):026, Nov 2007.

[253] T. Padmanabhan and T. Roy Choudhury. Can the clustered dark matter and the smooth dark energy arise from the same scalar field? *Phys. Rev. D*, 66:081301, 2002.

[254] Neven Bilic, Gary B. Tupper, and Raoul D. Viollier. Cosmological tachyon condensation. *Phys. Rev. D*, 80:023515, 2009.

[255] Hoavo Hova and Huanxiong Yang. A dark energy model alternative to generalized Chaplygin gas. *Int. J. Mod. Phys. D*, 27(01):1750178, 2017.

[256] Pierre-Henri Chavanis. The Logotropic Dark Fluid as a unification of dark matter and dark energy. *Phys. Lett. B*, 758:59–66, 2016.

[257] Oliver F. Piattella, Daniele Bertacca, Marco Bruni, and Davide Pietrobon. Unified Dark Matter models with fast transition. *JCAP*, 01:014, 2010.

[258] Iker Leanizbarrutia, Alberto Rozas-Fernández, and Ismael Tereno. Cosmological constraints on a unified dark matter-energy scalar field model with fast transition. *Phys. Rev. D*, 96(2):023503, 2017.

[259] J. S. Farnes. A unifying theory of dark energy and dark matter: Negative masses and matter creation within a modified ΛCDM framework. *Astron. Astrophys.*, 620:A92, 2018.

[260] P.P. Avelino, L.M.G. Beca, J.P.M. de Carvalho, and C.J.A.P. Martins. The lambda-CDM limit of the generalized Chaplygin gas scenario. *JCAP*, 09:002, 2003.

[261] D. M. Scolnic, D. O. Jones, A. Rest, Y. C. Pan, R. Chornock, R. J. Foley, M. E. Huber, R. Kessler, G. Narayan, A. G. Riess, S. Rodney, E. Berger, D. J. Brout, P. J. Challis, M. Drout, D. Finkbeiner, R. Lunnan, R. P. Kirshner, N. E. Sand ers, E. Schlafly, S. Smartt, C. W. Stubbs, J. Tonry, W. M. Wood-Vasey, M. Foley, J. Hand, E. Johnson, W. S. Bur-

gett, K. C. Chambers, P. W. Draper, K. W. Hodapp, N. Kaiser, R. P. Kudritzki, E. A. Magnier, N. Metcalfe, F. Bresolin, E. Gall, R. Kotak, M. McCrum, and K. W. Smith. The Complete Light-curve Sample of Spectroscopically Confirmed SNe Ia from Pan-STARRS1 and Cosmological Constraints from the Combined Pantheon Sample. *APJ*, 859(2):101, June 2018.

[262] Irit Maor, Ram Brustein, and Paul J. Steinhardt. Limitations in using luminosity distance to determine the equation of state of the universe. *Phys. Rev. Lett.*, 86:6, 2001. [Erratum: Phys.Rev.Lett. 87, 049901 (2001)].

[263] James M. Bardeen, J. R. Bond, Nick Kaiser, and A. S. Szalay. The Statistics of Peaks of Gaussian Random Fields. *Astrophys. J.*, 304:15–61, 1986.

[264] Will J. Percival et al. The 2dF Galaxy Redshift Survey: The Power spectrum and the matter content of the Universe. *Mon. Not. Roy. Astron. Soc.*, 327:1297, 2001.

[265] Matthew Colless, Gavin Dalton, Steve Maddox, Will Sutherland, Peder Norberg, Shaun Cole, Joss Bland-Hawthorn, Terry Bridges, Russell Cannon, Chris Collins, Warrick Couch, Nicholas Cross, Kathryn Deeley, Roberto De Propris, Simon P. Driver, George Efstathiou, Richard S. Ellis, Carlos S. Frenk, Karl Glazebrook, Carole Jackson, Ofer Lahav, Ian Lewis, Stuart Lumsden, Darren Madgwick, John A. Peacock, Bruce A. Peterson, Ian Price, Mark Seaborne, and Keith Taylor. The 2dF Galaxy Redshift Survey: spectra and redshifts. *MNRAS*, 328(4):1039–1063, December 2001.

[266] Håvard B. Sandvik, Max Tegmark, Matias Zaldarriaga, and Ioav Waga. The end of unified dark matter? *Phys. Rev. D*, 69(12):123524, Jun 2004.

[267] Beth A. Reid, Will J. Percival, Daniel J. Eisenstein, Licia Verde, David N. Spergel, Ramin A. Skibba, Neta A. Bahcall, Tamas Budavari, Joshua A. Frieman, Masataka Fukugita, J. Richard Gott, James E. Gunn, Željko Ivezić, Gillian R. Knapp, Richard G. Kron, Robert H. Lupton, Timothy A. McKay, Avery Meiksin, Robert C. Nichol, Adrian C. Pope, David J. Schlegel, Donald P. Schneider, Chris Stoughton, Michael A. Strauss, Alexander S. Szalay, Max Tegmark, Michael S. Vogeley, David H. Weinberg, Donald G. York, and Idit Zehavi. Cosmological constraints from the clustering of the Sloan Digital Sky Survey DR7 luminous red galaxies. *MNRAS*, 404(1):60–85, May 2010.

[268] Tamara M. Davis et al. Scrutinizing Exotic Cosmological Models Using ESSENCE Supernova Data Combined with Other Cosmological Probes. *Astrophys. J.*, 666:716–725, 2007.

[269] Hang Li, Weiqiang Yang, and Yabo Wu. Constraint on the generalized Chaplygin gas as an unified dark fluid model after Planck 2015. *Phys. Dark Univ.*, 22:60–66, 2018.

[270] Luis P. Chimento. Extended tachyon field, Chaplygin gas, and solvable k-essence cosmologies. *Physical Review D*, 69(12):123517, Jun 2004.

[271] Y. Sofue, Y. Tutui, M. Honma, A. Tomita, T. Takamiya, J. Koda, and Y. Takeda. Central rotation curves of spiral galaxies. *Astrophys. J.*, 523:136, 1999.

[272] Yoshiaki Sofue and Vera Rubin. Rotation Curves of Spiral Galaxies. *Ann. Rev. Astron. Astrophys.*, 39:137–174, January 2001.

[273] W.J.G. de Blok, F. Walter, E. Brinks, C. Trachternach, S-H. Oh, and Jr. Kennicutt, R.C. High-Resolution Rotation Curves and Galaxy Mass Models from THINGS. *Astron. J.*, 136:2648–2719, 2008.

[274] Dao-Jun Liu and Xin-Zhou Li. CMBR constraint on a modified Chaplygin gas model. *Chin. Phys. Lett.*, 22:1600–1603, 2005.

[275] Amedeo Balbi, Marco Bruni, and Claudia Quercellini. Lambda-alpha DM: Observational constraints on unified dark matter with constant speed of sound. *Phys. Rev. D*, 76:103519, 2007.

[276] Jianbo Lu, Lixin Xu, Jiechao Li, Baorong Chang, Yuanxing Gui, and Hongya Liu. Constraints on modified Chaplygin gas from recent observations and a comparison of its status with other models. *Phys. Lett. B*, 662:87–91, 2008.

[277] P. Thakur, S. Ghose, and B.C. Paul. Modified Chaplygin Gas and Constraints on its B parameter from CDM and UDME Cosmological models. *Mon. Not. Roy. Astron. Soc.*, 397:1935, 2009.

[278] J.C. Fabris, H.E.S. Velten, C. Ogouyandjou, and J. Tossa. Ruling out the Modified Chaplygin Gas Cosmologies. *Phys. Lett. B*, 694:289–293, 2011.

[279] Jianbo Lu, Lixin Xu, Yabo Wu, and Molin Liu. Combined constraints on modified Chaplygin gas model from cosmological observed data: Markov Chain Monte Carlo approach. *Gen. Rel. Grav.*, 43:819–832, 2011.

[280] B.C. Paul, P. Thakur, and A. Saha. Modified Chaplygin gas in Horava-Lifshitz gravity and constraints on its B parameter. *Phys. Rev. D*, 85:024039, 2012.

[281] D. Panigrahi, B.C. Paul, and S. Chatterjee. Constraining Modified Chaplygin gas parameters. *Grav. Cosmol.*, 21:83, 2015.

[282] Dean E. McLaughlin and Ralph E. Pudritz. A model for the internal structure of molecular cloud cores. *Astrophys. J.*, 469:194, 1996.

[283] Dean E. McLaughlin and Ralph E. Pudritz. Gravitational collapse and star formation in logotropic and nonisothermal spheres. *Astrophys. J.*, 476:750, 1997.

[284] Pierre-Henri Chavanis. Is the Universe logotropic? *Eur. Phys. J. Plus*, 130:130, 2015.

[285] Pierre-Henri Chavanis and Suresh Kumar. Comparison between the Logotropic and ΛCDM models at the cosmological scale. *JCAP*, 05:018, 2017.

[286] Abdulla Al Mamon and Subhajit Saha. The Logotropic Dark Fluid: Observational and Thermodynamic Constraints. *Int. J. Mod. Phys. D*, 29:2050097, 2020.

[287] Salvatore Capozziello, Rocco D'Agostino, and Orlando Luongo. Cosmic acceleration from a single fluid description. *Phys. Dark Univ.*, 20:1–12, 2018.

[288] S. D. Odintsov, V. K. Oikonomou, A. V. Timoshkin, Emmanuel N. Saridakis, and R. Myrzakulov. Cosmological Fluids with Logarithmic Equation of State. *Annals Phys.*, 398:238–253, 2018.

[289] Salvatore Capozziello, Rocco D'Agostino, Roberto Giambò, and Orlando Luongo. Effective field description of the Anton-Schmidt cosmic fluid. *Phys. Rev. D*, 99(2):023532, 2019.

[290] Kuantay Boshkayev, Rocco D'Agostino, and Orlando Luongo. Extended logotropic fluids as unified dark energy models. *Eur. Phys. J. C*, 79(4):332, 2019.

[291] H. Anton and P.C. Schmidt. Theoretical investigations of the elastic constants in laves phases. *Intermetallics*, 5(6):449 – 465, 1997.

[292] R. M. Corless, G. H. Gonnet, D. E. G. Hare, D. J. Jeffrey, and D. E. Knuth. On the lambert w function. In *ADVANCES IN COMPUTATIONAL MATHEMATICS*, pages 329–359, 1996.

[293] J. R. Oppenheimer and G. M. Volkoff. On massive neutron cores. *Phys. Rev.*, 55:374–381, Feb 1939.

[294] Richard C. Tolman. Static solutions of einstein's field equations for spheres of fluid. *Phys. Rev.*, 55:364–373, Feb 1939.

[295] F. Donato, G. Gentile, P. Salucci, C. Frigerio Martins, M. I. Wilkinson, G. Gilmore, E. K. Grebel, A. Koch, and R. Wyse. A constant dark matter halo surface density in galaxies. *Mon. Not. Roy. Astron. Soc.*, 397:1169–1176, 2009.

[296] A. Saburova and A. Del Popolo. On the surface density of dark matter haloes. *Mon. Not. Roy. Astron. Soc.*, 445(4):3512–3524, 2014.

[297] G.S. Bisnovatyi-Kogan, A.Y. Blinov, and M. Romanova. *Stellar Physics: 2: Stellar Evolution and Stability.* Astronomy and Astrophysics Library. Springer Berlin Heidelberg, 2011.

[298] D. H. D. H. Lyth and A. A. Riotto. Particle physics models of inflation and the cosmological density perturbation. *Phys. Rept.*, 314(1-2):1–146, Jun 1999.

[299] C. Armendáriz-Picón, T. Damour, and V. Mukhanov. k-Inflation. *Physics Letters B*, 458(2-3):209–218, Jul 1999.

[300] Rouzbeh Allahverdi, Robert Brandenberger, Francis-Yan Cyr-Racine, and Anupam Mazumdar. Reheating in Inflationary Cosmology: Theory and Applications. *Annual Review of Nuclear and Particle Science*, 60:27–51, Nov 2010.

[301] C. Armendariz-Picon, V. Mukhanov, and Paul J. Steinhardt. Essentials of k-essence. *Phys. Rev. D*, 63(10):103510, May 2001.

[302] Jin U. Kang, Vitaly Vanchurin, and Sergei Winitzki. Attractor scenarios and superluminal signals in k-essence cosmology. *Phys. Rev. D*, 76(8):083511, Oct 2007.

[303] Changjun Gao, Yan Gong, Xin Wang, and Xuelei Chen. Cosmological models with Lagrange multiplier field. *Physics Letters B*, 702(2):107–113, Aug 2011.

[304] Lam Hui, Jeremiah P. Ostriker, Scott Tremaine, and Edward Witten. Ultralight scalars as cosmological dark matter. *Phys. Rev. D*, 95(4):043541, Feb 2017.

[305] L. Arturo Ureña López. Brief Review on Scalar Field Dark Matter Models. *Front. Astron. Space Sci.*, 6:47, 2019.

[306] Md. Wali Hossain, R. Myrzakulov, M. Sami, and Emmanuel N. Saridakis. Unification of inflation and dark energy à la quintessential inflation. *International Journal of Modern Physics D*, 24(5):1530014, Mar 2015.

[307] Andrew R. Liddle and L. Arturo Ureña-López. Inflation, Dark Matter, and Dark Energy in the String Landscape. *Phys. Rev. Lett*, 97(16):161301, Oct 2006.

[308] Nilok Bose and A. S. Majumdar. k-essence model of inflation, dark matter, and dark energy. *Phys. Rev. D*, 79(10):103517, May 2009.

[309] Josue de-Santiago and Jorge L. Cervantes-Cota. Generalizing a unified model of dark matter, dark energy, and inflation with a noncanonical kinetic term. *Phys. Rev. D*, 83(6):063502, Mar 2011.

[310] Georges Aad et al. Observation of a new particle in the search for the Standard Model Higgs boson with the ATLAS detector at the LHC. *Phys. Lett.*, B716:1–29, 2012.

[311] Serguei Chatrchyan et al. Observation of a New Boson at a Mass of 125 GeV with the CMS Experiment at the LHC. *Phys. Lett.*, B716:30–61, 2012.

[312] M. S. Madsen. Scalar Fields in Curved Space-times. *Class. Quant. Grav.*, 5:627–639, 1988.

[313] A. H. Taub. Relativistic fluid mechanics. *Annual Review of Fluid Mechanics*, 10:301–332, 1978.

[314] Bernard F. Schutz. Perfect fluids in general relativity: Velocity potentials and a variational principle. *Phys. Rev. D*, 2:2762–2773, Dec 1970.

[315] B. F. Schutz and R. Sorkin. Variational aspects of relativistic field theories, with application to perfect fluids. *Annals of Physics*, 107:1–43, January 1977.

[316] John R. Ray. Lagrangian density for perfect fluids in general relativity. *Journal of Mathematical Physics*, 13(10):1451–1453, 1972.

[317] S. Matarrese. On the Classical and Quantum Irrotational Motions of a Relativistic Perfect Fluid. 1. Classical Theory. *Proc. Roy. Soc. Lond.*, A401:53–66, 1985.

[318] J. David Brown. Action functionals for relativistic perfect fluids. *Class. Quant. Grav.*, 10:1579–1606, 1993.

[319] Christian G. Boehmer, Nicola Tamanini, and Matthew Wright. Interacting quintessence from a variational approach Part I: algebraic couplings. *Phys. Rev. D*, 91(12):123002, 2015.

[320] Christian G. Boehmer, Nicola Tamanini, and Matthew Wright. Interacting quintessence from a variational approach Part II: derivative couplings. *Phys. Rev. D*, 91(12):123003, 2015.

[321] Dario Bettoni, Stefano Liberati, and Lorenzo Sindoni. Extended LCDM: generalized non-minimal coupling for dark matter fluids. *JCAP*, 11:007, 2011.

[322] Dario Bettoni and Stefano Liberati. Dynamics of non-minimally coupled perfect fluids. *JCAP*, 08:023, 2015.

[323] Jibitesh Dutta, Wompherdeiki Khyllep, and Nicola Tamanini. Scalar-fluid interacting dark energy: Cosmological dynamics beyond the exponential potential. *Phys. Rev. D*, 95:023515, Jan 2017.

[324] Tomi S. Koivisto, Emmanuel N. Saridakis, and Nicola Tamanini. Scalar-Fluid theories: cosmological perturbations and large-scale structure. *JCAP*, 09:047, 2015.

[325] Christian G. Böhmer, Nicola Tamanini, and Matthew Wright. Einstein static universe in scalar-fluid theories. *Phys. Rev. D*, 92:124067, Dec 2015.

[326] Philippe Brax and Nicola Tamanini. Extended chameleon models. *Phys. Rev. D*, 93:103502, May 2016.

[327] Nicola Tamanini and Matthew Wright. Cosmological dynamics of extended chameleons. *JCAP*, 04:032, 2016.

[328] Roy Maartens. Causal Thermodynamics in Relativity. *arXiv e-prints*, pages astro–ph/9609119, Sep 1996.

[329] R. K. P. Zia, Edward F. Redish, and Susan R. McKay. Making sense of the Legendre transform. *American Journal of Physics*, 77(7):614–622, Jul 2009.

[330] Frederico Arroja and Misao Sasaki. Note on the equivalence of a barotropic perfect fluid with a k-essence scalar field. *Phys. Rev. D*, 81(10):107301, May 2010.

[331] Sanil Unnikrishnan and L. Sriramkumar. A note on perfect scalar fields. *Phys. Rev. D*, 81(10):103511, May 2010.

[332] Oliver F. Piattella, Júlio C. Fabris, and Neven Bilić. Note on the thermodynamics and the speed of sound of a scalar field. *Classical and Quantum Gravity*, 31(5):055006, Mar 2014.

[333] Olivier Minazzoli and Tiberiu Harko. New derivation of the Lagrangian of a perfect fluid with a barotropic equation of state. *Phys. Rev. D*, 86(8):087502, October 2012.

[334] Orfeu Bertolami, Christian G. Boehmer, Tiberiu Harko, and Francisco S.N. Lobo. Extra force in f(R) modified theories of gravity. *Phys. Rev. D*, 75:104016, 2007.

[335] Thomas P. Sotiriou and Valerio Faraoni. Modified gravity with R-matter couplings and (non-)geodesic motion. *Class. Quant. Grav.*, 25:205002, 2008.

[336] Valerio Faraoni. The Lagrangian description of perfect fluids and modified gravity with an extra force. *Phys. Rev. D*, 80:124040, 2009.

[337] T. Harko. The matter Lagrangian and the energy-momentum tensor in modified gravity with non-minimal coupling between matter and geometry. *Phys. Rev. D*, 81:044021, 2010.

[338] Tahereh Azizi and Emad Yaraie. Cosmological Dynamics of Modified Gravity with a Non-minimal Curvature-Matter Coupling. *Int. J. Mod. Phys. D*, 23:1450021, 2014.

[339] Jacob D. Bekenstein. Fine-structure constant: Is it really a constant? *Phys. Rev. D*, 25(6):1527–1539, March 1982.

[340] Havard Bunes Sandvik, John D. Barrow, and Joao Magueijo. A simple cosmology with a varying fine structure constant. *Phys. Rev. Lett.*, 88:031302, 2002.

[341] Tomi Koivisto. Growth of perturbations in dark matter coupled with quintessence. *Phys. Rev. D*, 72:043516, 2005.

[342] P. P. Avelino. On the cosmological evolution of alpha and mu and the dynamics of dark energy. *Phys. Rev. D*, 78:043516, 2008.

[343] Youness Ayaita, Maik Weber, and Christof Wetterich. Structure formation and backreaction in growing neutrino quintessence. *Phys. Rev. D*, 85:123010, Jun 2012.

[344] A. Pourtsidou, C. Skordis, and E.J. Copeland. Models of dark matter coupled to dark energy. *Phys. Rev. D*, 88(8):083505, 2013.

[345] Bruno J. Barros. Kinetically coupled dark energy. *Phys. Rev. D*, 99(6):064051, 2019.

[346] Ryotaro Kase and Shinji Tsujikawa. Scalar-Field Dark Energy Nonminimally and Kinetically Coupled to Dark Matter. *Phys. Rev. D*, 101(6):063511, 2020.

[347] Joel K. Erickson, R. R. Caldwell, Paul J. Steinhardt, C. Armendariz-Picon, and Viatcheslav F. Mukhanov. Measuring the speed of sound of quintessence. *Phys. Rev. Lett.*, 88:121301, 2002.

[348] Axel de la Macorra and Hector H. Vucetich. Causality, stability and sound speed in scalar field models. 12 2002.

[349] N. Bilić, G. B. Tupper, and R. D. Viollier. Unification of dark matter and dark energy: the inhomogeneous Chaplygin gas. *Physics Letters B*, 535:17–21, May 2002.

[350] L. D. Landau and E. M. Lifshitz. *Fluid Mechanics, Second Edition: Volume 6 (Course of Theoretical Physics)*. Course of theoretical physics / by L. D. Landau and E. M. Lifshitz, Vol. 6. Butterworth-Heinemann, 2 edition, January 1987.

[351] R. Banerjee, S. Ghosh, and S. Kulkarni. Remarks on the generalized Chaplygin gas. *Phys. Rev. D*, 75(2):025008, January 2007.

[352] R. Jackiw. A Particle Field Theorist's Lectures on Supersymmetric, Non-Abelian Fluid Mechanics and d-Branes. *ArXiv Physics e-prints*, October 2000.

[353] C. Ridders. A new algorithm for computing a single root of a real continuous function. *IEEE Transactions on Circuits and Systems*, 26(11):979–980, 1979.

[354] Eugene A. Lim, Ignacy Sawicki, and Alexander Vikman. Dust of Dark Energy. *JCAP*, 05:012, 2010.

[355] Eric V. Linder. Exploring the Expansion History of the Universe. *Phys. Rev. Lett*, 90(9):091301, March 2003.

[356] P. P. Avelino, L. M. Beça, J. P. de Carvalho, C. J. Martins, and E. J. Copeland. Onset of the nonlinear regime in unified dark matter models. *Phys. Rev. D*, 69(4):041301, February 2004.

[357] Neven Bilic, Robert J. Lindebaum, Gary B. Tupper, and Raoul D. Viollier. Nonlinear evolution of dark matter and dark energy in the Chaplygin-gas cosmology. *JCAP*, 2004(11):008, November 2004.

[358] M. F. Shirokov and I. Z. Fisher. Isotropic Space with Discrete Gravitational-Field Sources. On the Theory of a Nonhomogeneous Isotropic Universe. *Sov. Astron. J.*, 6:699, April 1963.

[359] G. F. R. Ellis and W. Stoeger. The 'fitting problem' in cosmology. *Class. Quant. Grav.*, 4:1697–1729, 1987.

[360] R. J. van den Hoogen. Averaging Spacetime: Where do we go from here? In *12th Marcel Grossmann Meeting on General Relativity*, 3 2010.

[361] David L. Wiltshire. What is dust? - Physical foundations of the averaging problem in cosmology. *Class. Quant. Grav.*, 28:164006, 2011.

[362] Stephen R. Green and Robert M. Wald. How well is our universe described by an FLRW model? *Class. Quant. Grav.*, 31:234003, 2014.

[363] T. Buchert et al. Is there proof that backreaction of inhomogeneities is irrelevant in cosmology? *Class. Quant. Grav.*, 32:215021, 2015.

[364] Stephen R. Green and Robert M. Wald. Comments on Backreaction. 6 2015.

[365] Krzysztof Bolejko and Mikołaj Korzyński. Inhomogeneous cosmology and backreaction: Current status and future prospects. *Int. J. Mod. Phys. D*, 26(06):1730011, 2017.

[366] Chris Clarkson, George Ellis, Julien Larena, and Obinna Umeh. Does the growth of structure affect our dynamical models of the universe? The averaging, backreaction and fitting problems in cosmology. *Rept. Prog. Phys.*, 74:112901, 2011.

[367] Timothy Clifton. Back-Reaction in Relativistic Cosmology. *Int. J. Mod. Phys. D*, 22:1330004, 2013.

[368] Vitor Cardoso, Leonardo Gualtieri, Carlos Herdeiro, and Ulrich Sperhake. Exploring New Physics Frontiers Through Numerical Relativity. *Living Rev. Relativity*, 18:1, 2015.

[369] Eloisa Bentivegna and Marco Bruni. Effects of nonlinear inhomogeneity on the cosmic expansion with numerical relativity. *Phys. Rev. Lett.*, 116(25):251302, 2016.

[370] Julian Adamek, David Daverio, Ruth Durrer, and Martin Kunz. General relativity and cosmic structure formation. *Nature Phys.*, 12:346–349, 2016.

[371] Julian Adamek, Chris Clarkson, David Daverio, Ruth Durrer, and Martin Kunz. Safely smoothing spacetime: backreaction in relativistic cosmological simulations. *Class. Quant. Grav.*, 36(1):014001, 2019.

[372] Hayley J. Macpherson, Daniel J. Price, and Paul D. Lasky. Einstein's Universe: Cosmological structure formation in numerical relativity. *Phys. Rev. D*, 99(6):063522, 2019.

[373] William E. East, Radosław Wojtak, and Frans Pretorius. Einstein-Vlasov Calculations of Structure Formation. *Phys. Rev. D*, 100(10):103533, 2019.

[374] Julian Adamek, Cristian Barrera-Hinojosa, Marco Bruni, Baojiu Li, Hayley J. Macpherson, and James B. Mertens. Numerical solutions to Einstein's equations in a shearing-dust Universe: a code comparison. *Class. Quant. Grav.*, 37(15):154001, 2020.

[375] Krzysztof Bolejko. Emerging spatial curvature can resolve the tension between high-redshift CMB and low-redshift distance ladder measurements of the Hubble constant. *Phys. Rev. D*, 97(10):103529, 2018.

[376] Asta Heinesen and Thomas Buchert. Solving the curvature and Hubble parameter inconsistencies through structure formation-induced curvature. *Class. Quant. Grav.*, 37(16):164001, 2020. [Erratum: Class.Quant.Grav. 37, 229601 (2020)].

[377] Thomas Buchert. On average properties of inhomogeneous fluids in general relativity: Perfect fluid cosmologies. *Gen. Rel. Grav.*, 33:1381–1405, 2001.

[378] Christof Wetterich. Cosmon dark matter? *Phys. Rev. D*, 65:123512, 2002.

[379] Bruce A. Bassett, Martin Kunz, David Parkinson, and Carlo Ungarelli. Condensate cosmology - Dark energy from dark matter. *Phys. Rev. D*, 68:043504, 2003.

[380] Youness Ayaita, Maik Weber, and Christof Wetterich. Structure formation and backreaction in growing neutrino quintessence. *Phys. Rev. D*, 85(12):123010, June 2012.

[381] Florian Führer and Christof Wetterich. Backreaction in Growing Neutrino Quintessence. *Phys. Rev. D*, 91(12):123542, 2015.

[382] L. M. G. Beça and P. P. Avelino. Dynamics of perfect fluid unified dark energy models. *Mon.Not.Roy.Astron.Soc.*, 376:1169–1172, April 2007.

[383] Neven Bilic, Robert J. Lindebaum, Gary B. Tupper, and Raoul D. Viollier. Nonlinear evolution of dark matter and dark energy in the Chaplygin-gas cosmology. *JCAP*, 11:008, 2004.

[384] R. A. A. Fernandes, J. P. M. de Carvalho, A. Yu. Kamenshchik, U. Moschella, and A. da Silva. Spherical "top-hat" collapse in general-Chaplygin-gas-dominated universes. *Phys. Rev. D*, 85(8):083501, April 2012.

[385] A. Del Popolo, F. Pace, S. P. Maydanyuk, J. A. S. Lima, and J. F. Jesus. Shear and rotation in Chaplygin cosmology. *Phys. Rev. D*, 87(4):043527, 2013.

[386] Alan Kogut, Jens Chluba, Dale J. Fixsen, Stephan Meyer, and David Spergel. The Primordial Inflation Explorer (PIXIE). In Howard A. MacEwen, Giovanni G. Fazio, Makenzie Lystrup, Natalie Batalha, Nicholas Siegler, and Edward C. Tong, editors, *Space Telescopes and Instrumentation 2016: Optical, Infrared, and Millimeter Wave*, volume 9904 of *Society of Photo-Optical Instrumentation Engineers (SPIE) Conference Series*, page 99040W, July 2016.

[387] Jens Chluba, Rishi Khatri, and Rashid A. Sunyaev. CMB at 2x2 order: The dissipation of primordial acoustic waves and the observable part of the associated energy release. *Mon. Not. Roy. Astron. Soc.*, 425:1129–1169, 2012.

[388] V. S. Berezinsky, V. I. Dokuchaev, and Yu N. Eroshenko. Small-scale clumps of dark matter. *Phys. Usp.*, 57:1–36, 2014.

[389] Masahiro Kawasaki, Naoya Kitajima, and Tsutomu T. Yanagida. Primordial black hole formation from an axionlike curvaton model. *Phys. Rev. D*, 87(6):063519, 2013.

[390] Nelson D. Padilla, Juan Magaña, Joaquín Sureda, and Ignacio J. Araya. Power spectrum of density fluctuations, halo abundances and clustering with primordial black holes. 10 2020.

[391] James S. Bullock and Joel R. Primack. NonGaussian fluctuations and primordial black holes from inflation. *Phys. Rev. D*, 55:7423–7439, 1997.

[392] G. Franciolini, A. Kehagias, S. Matarrese, and A. Riotto. Primordial Black Holes from Inflation and non-Gaussianity. *JCAP*, 03:016, 2018.

[393] P. P. Avelino, K. Bolejko, and G.F. Lewis. Nonlinear Chaplygin Gas Cosmologies. *Phys. Rev. D*, 89(10):103004, 2014.

[394] R. K. Sachs and A. M. Wolfe. Perturbations of a Cosmological Model and Angular Variations of the Microwave Background. *APJ*, 147:73, January 1967.

[395] R.E. Smith, J.A. Peacock, A. Jenkins, S.D.M. White, C.S. Frenk, F.R. Pearce, P.A. Thomas, G. Efstathiou, and H.M.P. Couchmann. Stable clustering, the halo model and nonlinear cosmological power spectra. *Mon. Not. Roy. Astron. Soc.*, 341:1311, 2003.

[396] Ryuichi Takahashi, Masanori Sato, Takahiro Nishimichi, Atsushi Taruya, and Masamune Oguri. Revising the Halofit Model for the Nonlinear Matter Power Spectrum. *Astrophys. J.*, 761:152, 2012.

[397] Benjamin Audren, Julien Lesgourgues, Karim Benabed, and Simon Prunet. Conservative Constraints on Early Cosmology: an illustration of the Monte Python cosmological parameter inference code. *JCAP*, 1302:001, 2013.

[398] Thejs Brinckmann and Julien Lesgourgues. MontePython 3: boosted MCMC sampler and other features. *arXiv e-prints*, page arXiv:1804.07261, Apr 2018.

[399] J. Buchner, A. Georgakakis, K. Nandra, L. Hsu, C. Rangel, M. Brightman, A. Merloni, M. Salvato, J. Donley, and D. Kocevski. X-ray spectral modelling of the AGN obscuring region in the CDFS: Bayesian model selection and catalogue. *Astron. Astrophys.*, 564:A125, 2014.

[400] F. Feroz, M.P. Hobson, and M. Bridges. MultiNest: an efficient and robust Bayesian inference tool for cosmology and particle physics. *Mon. Not. Roy. Astron. Soc.*, 398:1601–1614, 2009.

[401] Andrew Gelman and Donald B. Rubin. Inference from Iterative Simulation Using Multiple Sequences. *Statist. Sci.*, 7:457–472, 1992.

[402] H. Hildebrandt et al. KiDS-450: Cosmological parameter constraints from tomographic weak gravitational lensing. *Mon. Not. Roy. Astron. Soc.*, 465:1454, 2017.

[403] N. Suzuki, D. Rubin, C. Lidman, G. Aldering, R. Amanullah, K. Barbary, L. F. Barrientos, J. Botyanszki, M. Brodwin, N. Connolly, K. S. Dawson, A. Dey, M. Doi, M. Donahue, S. Deustua, P. Eisenhardt, E. Ellingson, L. Faccioli, V. Fadeyev, H. K. Fakhouri, A. S. Fruchter, D. G. Gilbank, M. D. Gladders, G. Goldhaber, A. H. Gonzalez, A. Goobar, A. Gude, T. Hattori, H. Hoekstra, E. Hsiao, X. Huang, Y. Ihara, M. J. Jee, D. Johnston, N. Kashikawa, B. Koester, K. Konishi, M. Kowalski, E. V. Linder, L. Lubin, J. Melbourne, J. Meyers, T. Morokuma, F. Munshi, C. Mullis, T. Oda, N. Panagia, S. Perlmutter, M. Postman, T. Pritchard, J. Rhodes, P. Ripoche, P. Rosati, D. J. Schlegel, A. Spadafora, S. A. Stanford, V. Stanishev, D. Stern, M. Strovink, N. Takanashi, K. Tokita, M. Wagner, L. Wang, N. Yasuda, H. K. C. Yee, and The Supernova Cosmology Project. The Hubble Space Telescope Cluster Supernova Survey. V. Improving the Dark-energy Constraints above z > 1 and Building an Early-type-hosted Supernova Sample. *APJ*, 746(1):85, Feb 2012.

[404] N. Aghanim et al. Planck 2018 results. V. CMB power spectra and likelihoods. 7 2019.

[405] Luca Amendola, Ioav Waga, and Fabio Finelli. Observational constraints on silent quartessence. *JCAP*, 11:009, 2005.

[406] Davide Pietrobon, Amedeo Balbi, Marco Bruni, and Claudia Quercellini. Affine parameterization of the dark sector: costraints from WMAP5 and SDSS. *Phys. Rev. D*, 78:083510, 2008.

[407] Thomas Buchert. On average properties of inhomogeneous fluids in general relativity. 1. Dust cosmologies. *Gen. Rel. Grav.*, 32:105–125, 2000.

[408] Thomas Buchert, Pierre Mourier, and Xavier Roy. On average properties of inhomogeneous fluids in general relativity III: general fluid cosmologies. *Gen. Rel. Grav.*, 52(3):27, 2020.

[409] Alberto Diez-Tejedor. Note on scalars, perfect fluids, constrained field theories, and all that. *Physics Letters B*, 727(1-3):27–30, Nov 2013.

[410] Julien Lesgourgues. The Cosmic Linear Anisotropy Solving System (CLASS) I: Overview. *arXiv e-prints*, page arXiv:1104.2932, April 2011.

[411] Diego Blas, Julien Lesgourgues, and Thomas Tram. The Cosmic Linear Anisotropy Solving System (CLASS). Part II: Approximation schemes. *JCAP*, 2011(7):034, Jul 2011.

[412] Julien Lesgourgues. The Cosmic Linear Anisotropy Solving System (CLASS) III: Comparision with CAMB for LambdaCDM. *arXiv e-prints*, page arXiv:1104.2934, April 2011.

[413] Julien Lesgourgues and Thomas Tram. The Cosmic Linear Anisotropy Solving System (CLASS) IV: efficient implementation of non-cold relics. *JCAP*, 2011(9):032, September 2011.

[414] D.M. Scolnic et al. The Complete Light-curve Sample of Spectroscopically Confirmed SNe Ia from Pan-STARRS1 and Cosmological Constraints from the Combined Pantheon Sample. *Astrophys. J.*, 859(2):101, 2018.

[415] Joachim Harnois-Déraps, Ludovic van Waerbeke, Massimo Viola, and Catherine Heymans. Baryons, Neutrinos, Feedback and Weak Gravitational Lensing. *Mon. Not. Roy. Astron. Soc.*, 450(2):1212–1223, 2015.

[416] Christopher M. Hirata and Uro š Seljak. Intrinsic alignment-lensing interference as a contaminant of cosmic shear. *Phys. Rev. D*, 70:063526, Sep 2004.

[417] Sarah Bridle and Lindsay King. Dark energy constraints from cosmic shear power spectra: impact of intrinsic alignments on photometric redshift requirements. *New Journal of Physics*, 9(12):444–444, dec 2007.

[418] B. Joachimi, R. Mandelbaum, F. B. Abdalla, and S. L. Bridle. Constraints on intrinsic alignment contamination of weak lensing surveys using the MegaZ-LRG sample. *AAP*, 527:A26, March 2011.